Vol. 26, no. 1, 2026 eISSN 2687-1653
PEER-REVIEWED SCIENTIFIC AND PRACTICAL JOURNAL

Advanced Engineering Research (Rostov-on-Don)

Mechanics

Machine Buiding and Machine Science

Information Technology, Computer Science and Management

www.vestnik-donstu.ru
DOI 10.23947/2687-1653

Advanced Engineering Research (Rostov-on-Don)

Peer-reviewed scientific and practical journal

eISSN 2687–1653

Published since 2000

Periodicity – 4 issues per year

DOI: 10.23947/2687–1653

Founder and Publisher — Don State Technical University (DSTU), Rostov-on-Don, Russian Federation

The journal is aimed at informing the readership about the latest achievements and prospects in the field of mechanics, mechanical engineering, computer science and computer technology. The publication is a forum for cooperation between Russian and foreign scientists, it contributes to the convergence of the Russian and world scientific and information space.

The journal is included in the List of the leading peer-reviewed scientific publications (Higher Attestation Commission under the Ministry of Science and Higher Education of the Russian Federation), where basic scientific results of dissertations for the degrees of Doctor and Candidate of Science in scientific specialties and their respective branches of science should be published.

The journal publishes articles in the following fields of science:

– Theoretical Mechanics, Dynamics of Machines (Engineering Sciences)
– Deformable Solid Mechanics (Engineering, Physical and Mathematical Sciences)
– Mechanics of Liquid, Gas and Plasma (Engineering Sciences)
– Mathematical Simulation, Numerical Methods and Program Systems (Engineering Sciences)
– System Analysis, Information Management and Processing, Statistics (Engineering Sciences)
– Automation and Control of Technological Processes and Productions (Engineering Sciences)
– Software and Mathematical Support of Machines, Complexes and Computer Networks (Engineering Sciences)
– Computer Modeling and Design Automation (Engineering, Physical and Mathematical Sciences)
– Computer Science and Information Processes (Engineering Sciences)
– Machine Science (Engineering Sciences)
– Machine Friction and Wear (Engineering Sciences)
– Technology and Equipment of Mechanical and Physicotechnical Processing (Engineering Sciences)
– Engineering Technology (Engineering Sciences)
– Welding, Allied Processes and Technologies (Engineering Sciences)
– Methods and Devices for Monitoring and Diagnostics of Materials, Products, Substances and the Natural Environment (Engineering Sciences)
– Hydraulic Machines, Vacuum, Compressor Equipment, Hydraulic and Pneumatic Systems (Engineering Sciences)

Registration	Extract from the Register of Registered Mass Media ЭЛ № ФС 77 – 78854 dated August 07, 2020, issued by the Federal Service for Supervision of Communications, Information Technology and Mass Media
Indexing and Archiving	Scopus, RSCI, RISC (core), CyberLeninka, CrossRef, Dimensions, DOAJ, EBSCO, Index Copernicus, Internet Archive, Google Scholar
Website	https://vestnik-donstu.ru
Address of the Editorial Office	1, Gagarin sq., Rostov-on-Don, 344003, Russian Federation
E-mail	vestnik@donstu.ru
Telephone	+7 (863) 2–738–372
Date of Publication No.1,2026	30.03.2026

Advanced Engineering Research (Rostov-on-Don)

Рецензируемый научно-практический журнал

eISSN 2687–1653

Издается с 2000 года

Периодичность – 4 выпуска в год

DOI: 10.23947/2687–1653

Учредитель и издатель — Федеральное государственное бюджетное образовательное учреждение высшего образования «Донской государственный технический университет» (ДГТУ), г. Ростов-на-Дону

Создан в целях информирования читательской аудитории о новейших достижениях и перспективах в области механики, машиностроения, информатики и вычислительной техники. Издание является форумом для сотрудничества российских и иностранных ученых, способствует сближению российского и мирового научно-информационного пространства.

Журнал включен в перечень рецензируемых научных изданий (К2), в котором должны быть опубликованы основные научные результаты диссертаций на соискание ученой степени кандидата наук, на соискание ученой степени доктора наук (Перечень ВАК) по следующим научным специальностям:

1.1.7 – Теоретическая механика, динамика машин (технические науки)
1.1.8 – Механика деформируемого твердого тела (технические, физико-математические науки)
1.1.9 – Механика жидкости, газа и плазмы (технические науки)
1.2.2 – Математическое моделирование, численные методы и комплексы программ (технические науки)
2.3.1 – Системный анализ, управление и обработка информации, статистика (технические науки)
2.3.3 – Автоматизация и управление технологическими процессами и производствами (технические науки)
2.3.5 – Математическое и программное обеспечение вычислительных систем, комплексов и компьютерных сетей (технические науки)
2.3.7 – Компьютерное моделирование и автоматизация проектирования (технические, физико-математические науки)
2.3.8 – Информатика и информационные процессы (технические науки)
2.5.2 – Машиноведение (технические науки)
2.5.3 – Трение и износ в машинах (технические науки)
2.5.5 – Технология и оборудование механической и физико-технической обработки (технические науки)
2.5.6 – Технология машиностроения (технические науки)
2.5.8 – Сварка, родственные процессы и технологии (технические науки)
2.5.9 – Методы и приборы контроля и диагностики материалов, изделий, веществ и природной среды (технические науки)
2.5.10 – Гидравлические машины, вакуумная, компрессорная техника, гидро- и пневмосистемы (технические науки)

Регистрация	Выписка из реестра зарегистрированных средств массовой информации ЭЛ № ФС 77 – 78854 от 07 августа 2020 г., выдано Федеральной службой по надзору в сфере связи, информационных технологий и массовых коммуникаций
Индексация и архивация	Scopus, RSCI, РИНЦ (ядро), CyberLeninka, CrossRef, Dimensions, DOAJ, EBSCO, Index Copernicus, Internet Archive, Google Scholar
Сайт	https://vestnik-donstu.ru
Адрес редакции	344003, Российская Федерация, г. Ростов-на-Дону, пл. Гагарина, 1
E-mail	vestnik@donstu.ru
Телефон	+7 (863) 2–738–372
Дата выхода №1,2026 в свет	30.03.2026

Редакционная коллегия

Contents

Содержание

MECHANICS
МЕХАНИКА

UDC 536.21; 517.958
https://doi.org/10.23947/2687-1653-2026-26-1-2242

Original Theoretical Research

Analytical Solution of the Navier–Stokes Equations for Describing Inhomogeneous Couette Flow with a Quadratic Velocity Profile in a Layer with Permeable Boundaries

EDN: ZWPWMM

Kristina V. Gubareva[1] ✉, **Evgenii Yu. Prosviryakov**[2,3], **Anton V. Eremin**[1]
[1] Samara State Technical University, Samara, Russian Federation
[2] Ural Federal University, Ekaterinburg, Russian Federation
[3] Institute of Engineering Science, RAS (Ural Branch), Ekaterinburg, Russian Federation
✉ r.kristina2017@mail.ru

Abstract

Introduction. Flow control in microfluidic systems, membrane technologies, and porous bearings requires an understanding of the synergy between boundary permeability, their spatial inhomogeneity, and the viscosity of the working fluid. Each of these factors is actively studied separately. However, a comprehensive analytical description of their combined effect on the flow is needed. No such publications exist. The presented article fills this gap. Research objectives are as follows: to obtain an analytical solution for the velocity field in Couette flow with permeable boundaries and a nonlinear boundary condition; to study the formation of hydrodynamics under the influence of permeability (α), dynamic viscosity (μ), linear (A) and quadratic (B) inhomogeneity of the boundary condition.

Materials and Methods. The analytical solution is based on the stationary Navier–Stokes equations for an incompressible Newtonian fluid, with a quadratic expansion of velocity along the transverse coordinate. The axial, linear, and quadratic modes of the velocity profile were investigated using numerical modeling in MATLAB. For a stationary, laminar, isothermal flow of a Newtonian viscous incompressible fluid, the distance between permeable plates was h = 1 m. The lower plate was stationary, while the upper plate moved with a velocity of W = 0.3 m/s. The liquid filtration rate was V_w = 0.001 m/s, and μ = 0.01 Pa·s for $A = \pm 0.03$ s^{-1} and $B = \pm 0.005$ m^{-1}·s^{-1}. Water, motor oil, and crude oil were studied at temperatures of 20 °C, 40 °C, or 60 °C. For this case, h = 0.02 m, W = 0.05 m/s, A = 0.1 s^{-1}, B = 0.02 m^{-1}·s^{-1}, V_w = 0.0005 m/s. Depending on the fluid and temperature, μ ranged from 0.05 to $9.15 \cdot 10^{-3}$ Pa·s.

Results. Asymmetry of the flow, deviation from the channel axis, and variability of the vorticity amplitude ω_y were visualized. Zero filtration velocity was observed at the lower plate in the plane z = 0 and increased with this parameter, reaching a maximum at $z = h$ (distance between the plates). For water, the streamlines exhibited minimal deviation from the horizontal, while for oil at 20 °C, they curved near the upper wall. Two-dimensional vorticity fields for water, oil, and petroleum at various temperatures were compared. Weak ω_y and reduced viscosity resulted in negative values ω_y for water and petroleum. For oil, the situation was reversed: positive values corresponded to elevated ω_y.

Discussion. The calculation results allow us to conclude:

– changing the sign of A inverts the directions of the maxima for velocity and vorticity;

– the sign of B determines the curvature of the isolines;

– the thickness of the layer with the maximum velocity gradient changes by two orders of magnitude when transitioning from water to oil.

The identified patterns are explained by the physical meaning of the parameters: A defines the macroscopic flow asymmetry, B governs the distribution of the transverse flow, and viscosity, through α, controls the depth of boundary perturbations.

Conclusion. For the first time, an exact analytical solution to the stationary Navier–Stokes equations was obtained for generalized Couette flow of a Newtonian fluid between permeable plates with a quadratic velocity profile at the boundary. A parametric analysis has shown that coefficient A determines the asymmetry of the velocity and vorticity fields, while B determines their nonlinearity. Viscosity controls the thickness of the shear layer: for high-viscosity media, the velocity drop is localized near the walls, while for low-viscosity media, the profile is linear. The results provide a foundation for applications in microfluidics, membrane technologies, and tribology. Future prospects are associated with accounting for non-Newtonian fluid properties, unsteady regimes, and flow stability.

Keywords: limitations of the Couette model, hydrodynamic structure of the flow, flow velocity profile, fluid filtration rate, vorticity amplitude, dynamic viscosity

Acknowledgements. The authors would like to thank the Editorial board of the journal and the reviewers for their professional analysis of the article and valuable recommendations for its improvement**.**

For Citation. Gubareva KV, Prosviryakov EYu, Eremin AV. Analytical Solution of the Navier–Stokes Equations for Describing Inhomogeneous Couette Flow with a Quadratic Velocity Profile in a Layer with Permeable Boundaries. *Advanced Engineering Research* (*Rostov-on-Don*). 2026;26(1):2242. https://doi.org/10.23947/2687-1653-2026-26-1-2242

Оригинальное теоретическое исследование

Аналитическое решение уравнений Навье – Стокса для описания неоднородного течения Куэтта с квадратичным профилем в слое с проницаемыми границами

К.В. Губарева[1], Е.Ю. Просвиряков[2,3], А.В. Еремин[1]

[1] Самарский государственный технический университет, г. Самара, Российская Федерация

[2] Уральский федеральный университет имени первого Президента России Б.Н. Ельцина, г. Екатеринбург, Российская Федерация

[3] Институт машиноведения имени Э.С. Горкунова Уральского отделения Российской академии наук, г. Екатеринбург, Российская Федерация

✉ r.kristina2017@mail.ru

Аннотация

Введение. Управление структурой потока в микрофлюидных системах, мембранных технологиях и пористых подшипниках требует понимания синергии проницаемости границ, их пространственной неоднородности и вязкости рабочей жидкости. Отдельно каждый из этих факторов активно изучается. Однако необходимо комплексное аналитическое описание их совместного влияния на поток. Таких публикаций нет. Представленная статья восполняет этот пробел. Цели работы: получение аналитического решения для поля скорости в течении Куэтта с проницаемыми границами и нелинейным граничным условием; изучение формирования гидродинамики под влиянием проницаемости (α), динамической вязкости (μ), линейной (A) и квадратичной (B) неоднородности граничного условия.

Материалы и методы. Аналитическое решение базируется на стационарных уравнениях Навье – Стокса для несжимаемой ньютоновской жидкости с квадратичным разложением скорости по поперечной координате. Осевую, линейную и квадратичную моды профиля скорости исследовали методом численного моделирования в Matlab. Для стационарного, ламинарного, изотермического течения ньютоновской вязкой и несжимаемой жидкости расстояние между проницаемыми пластинами h = 1 м. Нижняя пластина неподвижна, верхняя движется со скоростью W = 0,3 м/с. Скорость фильтрации жидкости V_w = 0,001 м/с, μ = 0,01 Па·с для A = ±0,03 с$^{-1}$ и B = ±0,005 м$^{-1}$·с$^{-1}$. Воду, моторное масло и нефть исследовали при 20 °С, 40 °С или 60 °С. В этом случае h = 0,02 м, W = 0,05 м/с, A = 0,1 с$^{-1}$, B = 0,02 м$^{-1}$·с$^{-1}$, V_w = 0,0005 м/с. В зависимости от жидкости и температуры μ — от 0,05 до 9,15·10^{-3} Па·с.

Результаты исследования. Визуализированы асимметрия течения, отклонение от оси канала, вариативность амплитуды завихренности ω_y. Нулевая скорость фильтрации отмечается для нижней пластины в плоскости z = 0 и растет с увеличением этого показателя до максимума при $z = h$ (расстояние между пластинами). Для воды линии тока минимально отклоняются от горизонтали, а для масла при 20 °С — искривляются вблизи верхней стенки. Сопоставляются двумерные поля завихренности для воды, масла и нефти при различных температурах. Слабая ω_y и снижение вязкости обусловили отрицательные показатели ω_y для воды и нефти. Для масла ситуация противоположная: положительные показатели при повышенной ω_y.

Обсуждение. Итоги расчетов позволяют утверждать:

– при изменении знака A инвертируются направления смещения максимумов скорости и завихренности;

– знак B определяет кривизну изолиний;

– толщина слоя с максимальным градиентом скорости меняется на два порядка при переходе от воды к маслу.

Выявленные закономерности объясняются физическим смыслом параметров: A задает макроскопическую асимметрию течения, B управляет распределением поперечного потока, а вязкость через α контролирует глубину граничных возмущений.

Заключение. Впервые было получено точное аналитическое решение стационарных уравнений Навье – Стокса для обобщённого течения Куэтта ньютоновской жидкости между проницаемыми пластинами с квадратичным профилем скорости на границе. Параметрический анализ показал, что коэффициент A определяет асимметрию полей скорости и завихренности, а B — их нелинейность. Вязкость контролирует толщину сдвигового слоя: для высоковязких сред перепад скорости локализуется у стенок, для маловязких — профиль линейный. Результаты создают основу для задач микрофлюидики, мембранных технологий и трибологии. Перспективы связаны с учётом неньютоновских свойств жидкости, нестационарных режимов и устойчивости течений.

Ключевые слова: ограниченность модели Куэтта, гидродинамическая структура течения, профиль скорости течения, скорость фильтрации жидкости, амплитуда завихренности, динамическая вязкость

Благодарности. Авторы выражают благодарность редакционной коллегии журнала и рецензенту за профессиональный анализ статьи и рекомендации для ее корректировки.

Для цитирования. Губарева К.В., Просвиряков Е.Ю., Еремин А.В. Аналитическое решение уравнений Навье – Стокса для описания неоднородного течения Куэтта с квадратичным профилем в слое с проницаемыми границами. *Advanced Engineering Research* (*Rostov-on-Don*). 2026;26(1):2242. https://doi.org/10.23947/2687-1653-2026-26-1-2242

Introduction. Precise control of flow structure in thin layers is critically important for modern technologies — from microfluidic devices to lubrication systems. However, in such cases, some classical hydrodynamic models fail to account for a complex set of technological parameters: wide range of working fluid viscosities, wall permeability, as well as their spatial inhomogeneity (roughness, distributed sources) [1]. An example of such an “incomplete” model is the Couette flow between impermeable plates [2]. The presented study is relevant for the advancement of the following applied areas.

1. *Biomedical microfluidics and so-called labs-on-a-chip*. Efficient mixing of reagents or targeted cell delivery require, firstly, fluid injection through porous membranes ($V_w \neq 0$). Secondly, heterogeneous shear flows generated by wall microtopography (modelled by boundary coefficients A and B) are needed [3].

2. *Energy-efficient membrane technologies (desalination, gas separation)*. In this area, performance is determined by the interaction between the longitudinal flow and transverse filtration through a permeable wall, as well as by the viscous properties of the medium being separated [4].

3. *Tribology of porous and textured bearings*. Pressure distribution, friction, and wear directly depend on the lubricant flow in a microscopic gap with complex topography (A, B) and potential filtration (V_w) through a porous liner [5].

The literature analysis made it possible to systematize approaches to describing the aforementioned factors and revealed a significant gap. Both for model [6] and applied problems [7], the effects of boundary permeability determining nonlinear (exponential) velocity profiles is investigated in detail. The effect of complex (including polynomial) boundary conditions on impermeable walls is well described, which is related to problems of stability, heat and mass transfer, and roughness modeling [8]. The effect of rheological properties, including the wide range of viscosities of real fluids, is deeply studied [9]. Modern numerical [10] and analytical [11] methods are actively used to solve conjugate problems. However, the aforementioned factors have been traditionally studied outside of a systems approach. Analytical solutions either describe permeability under homogeneous boundary conditions [12] or account for boundary nonlinearity only for impermeable walls [13]. Thus, the literature lacks a comprehensive analytical solution that explicitly combines the key dimensionless parameters**:**

– dynamic viscosity (μ);

– permeability ($\alpha = \rho V_w/\mu$);

– linear (A) и quadratic (B) corrections to the boundary velocity profile.

It is this gap that prevents a direct parametric analysis of the synergistic influence of the aforementioned factors on the flow structure. Consequently, it is impossible to purposefully design devices for the applied areas listed above.

The objective of this work is to create and analyze an exact solution for generalized stationary Couette flow of a Newtonian fluid between permeable plates with a quadratic velocity profile at the boundary. The scientific novelty lies in obtaining a closed-form analytical solution that, for the first time, explicitly and comprehensively accounts for the synergy of the parameters α, A, B and μ. The primary advantage of this approach over numerical modeling is the ability to obtain a solution instantly and perform a direct analysis of physical dependences, unmediated by grid approximations. To achieve this objective, four tasks are addressed.

1. Output and rigorous verification of the analytical solution, including checking the limiting transitions to known special cases.

2. Investigation of the effect of the sign and magnitude of the boundary coefficients A and B on the spatial distribution of velocity and vorticity.

3. Quantitative analysis of the effect of the dynamic viscosity of real fluids (water, engine oil, petroleum) on the velocity profile and shear layer thickness.

4. Discussion of the practical significance of the results, model limitations, and promising directions for the model generalization.

Materials and Methods. Let us consider a steady (stationary), laminar, isothermal flow of a Newtonian viscous and incompressible fluid in a channel formed by two infinite, parallel, flat plates (Fig. 1).

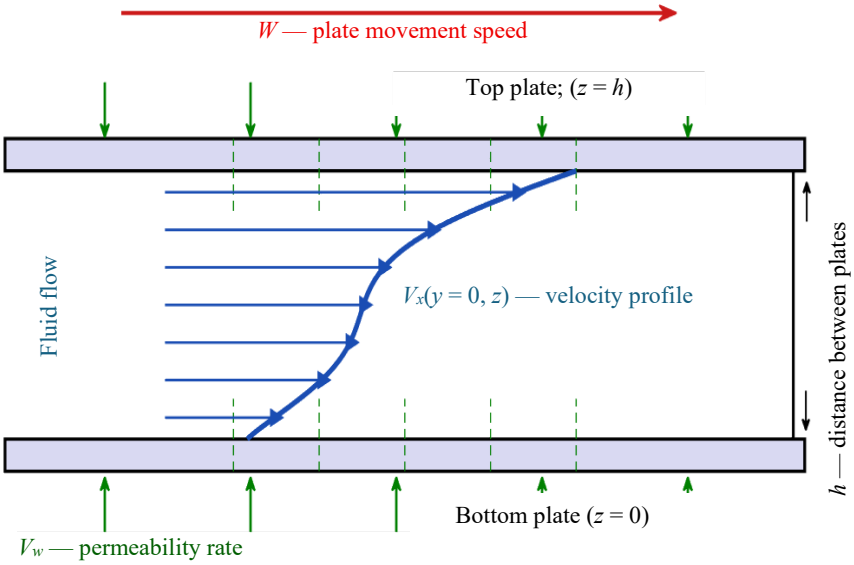

Fig. 1. Schematic diagram of Couette flow between permeable plates

The distance between the plates is constant and equal to h. The bottom plate is stationary and located in the plane $z = 0$. The top plate is located in the plane $z = h$ and moves with constant velocity W in the positive x direction.

A key feature of this problem is the permeability of both plates, which enables fluid filtration in the direction normal to their surfaces [6]. It is assumed that this normal velocity (V_w) is constant over the entire surface of each plate and is the same for both plates. If $V_w > 0$, fluid enters the channel through the bottom plate and exits through the top plate; if $V_w < 0$, the flow direction through the walls is reversed.

The longitudinal velocity component V_x is specified as a quadratic expansion in the transverse coordinate y. This generalization of the classical Couette profile allows for more complex boundary conditions on the top plate [5]:

$$V_x(y,z) = U(z) + yu_1(z) + \frac{y^2}{2}u_2(z). \quad (1)$$

Here, functions $U(z)$, $u_1(z)$ and $u_2(z)$ represent the primary (axial), linear, and quadratic modes of the velocity profile, respectively, depending only on the coordinate z.

Boundary conditions are formulated on the basis of the no-slip condition. On the stationary bottom plate ($z = 0$), a complete absence of motion is specified:

$$U(0) = 0,\ u_1(0) = 0,\ u_2(0) = 0. \quad (2)$$

On the top plate ($z = h$), a generalized velocity profile is specified:

$$U(h) = W,\ u_1(h) = A,\ u_2(h) = B, \quad (3)$$

where W — rate of translational motion of the plate; A — coefficient determining the linear velocity gradient along y; B — coefficient determining the profile curvature.

Unknown functions $U(z)$, $u_1(z)$ and $u_2(z)$ can be found from the Navier–Stokes equation for the x-component of velocity. Under the assumption of stationarity, it takes the form [2]:

$$\rho\left(V_x\frac{\partial V_x}{\partial x}\middle|V_y\frac{\partial V_x}{\partial y}\middle|V_z\frac{\partial V_x}{\partial z}\right) = -\frac{\partial p}{\partial x} + \mu\left(\frac{\partial^2 V_x}{\partial x^2}\middle|\frac{\partial^2 V_x}{\partial y^2}\middle|\frac{\partial^2 V_x}{\partial z^2}\right). \quad (4)$$

The flow under consideration is a generalization of pure Couette flow, which is characterized by the absence of a pressure gradient along the channel ($\partial p/\partial x = 0$). Taking this condition into account, as well as the facts that V_x is independent of x, $V_y = 0$ and $V_z = V_w = const$ [3]. In this case, equation (4) is simplified significantly:

$$\rho V_w \frac{\partial V_x}{\partial z} = \mu\left(\frac{\partial^2 V_x}{\partial y^2} | \frac{\partial^2 V_x}{\partial z^2}\right). \tag{5}$$

Substituting (1) into (5) and computing the corresponding derivatives yields an equation that must hold for all values of y. Equating coefficients of like powers of y gives a system of three independent ordinary differential equations (ODE) [11]:

$$\mu u_1'' - \rho V_w u_1' = 0, \tag{6}$$

$$u_2'' - \rho V_w u_2' = 0, \tag{7}$$

$$\mu U'' - \rho V_w U' = -\mu u_2. \tag{8}$$

Expressions (6) and (7) are second-order linear homogeneous ordinary differential equations (ODE) with constant coefficients. To solve them, the dimensionless permeability parameter $\alpha = \rho V_w / \mu$ is introduced, which physically represents the ratio of inertial forces to viscous forces in the normal direction. Dividing (6) and (7) by μ gives the canonical form:

$$u_1'' - \alpha u_1' = 0, \quad u_2'' - \alpha u_2' = 0. \tag{9}$$

The general solutions to these equations are:

$$u_1(z) = C_1^{(1)} + C_2^{(1)} e^{\alpha z}, \quad u_2(z) = C_1^{(2)} + C_2^{(2)} e^{\alpha z}. \tag{10}$$

Using boundary conditions (2) and (3) allows us to determine the integration constants. For function $u_1(z)$, the conditions $u_1(0) = 0$ and $u_1(h) = A$ yield:

$$C_1^{(1)} = -C_2^{(1)}, \quad C_2^{(1)} = \frac{A}{e^{\alpha h} - 1}. \tag{11}$$

Similarly, for $u_2(z)$ from the conditions $u_2(0) = 0$ and $u_2(h) = B$, we find:

$$C_1^{(2)} = -C_2^{(2)}, \quad C_2^{(2)} = \frac{B}{e^{\alpha h} - 1}. \tag{12}$$

Final expressions for the linear and quadratic modes of the velocity profile:

$$u_1(z) = \frac{A}{e^{\alpha h} - 1}\left(e^{\alpha z} | 1\right), \tag{13}$$

$$u_2(z) = \frac{B}{e^{\alpha h} - 1}\left(e^{\alpha z} | 1\right). \tag{14}$$

Equation (8) for the fundamental mode $U(z)$ is inhomogeneous. We substitute into it the expression found for $u_2(z)$ (14) and divide by μ:

$$U'' - \alpha U' = -\frac{B}{e^{\alpha h} - 1}\left(e^{\alpha z} | 1\right). \tag{15}$$

For equation (15), the method of undetermined coefficients [13] is applied. Its general solution is the sum of the general solution to the homogeneous equation and a particular solution to the non-homogeneous equation. After determining the constants of integration from the boundary conditions (2) and (3), the final expression for the primary mode takes the form [14]:

$$U(z) = \left[\frac{W}{e^{\alpha h} - 1} | \frac{Bh\left(e^{\alpha h} + 1\right)}{\alpha\left(e^{\alpha h} - 1\right)^2}\right]\left(e^{\alpha z} | 1\right) - \frac{B}{\alpha\left(e^{\alpha h} - 1\right)} z\left(e^{\alpha z} | 1\right). \tag{16}$$

Thus, substituting (13), (14), and (16) into the original ansatz (1) yields the full field of the longitudinal velocity component. The analytical solution obtained satisfies both the equation of motion (5) and all boundary conditions, i.e., (2) and (3).

To confirm the physical validity of the solution, let us consider the limiting transition $V_w \to 0$, which is equivalent to $\alpha \to 0$. In this limit, using the Taylor series expansion of the exponential, we obtain for the quadratic mode:

$$u_2(z) \to \frac{Bz}{h}, \quad \alpha \to 0. \tag{17}$$

Similarly for the linear mode:

$$u_1(z) \to \frac{Az}{h}, \quad \alpha \to 0. \tag{18}$$

For the fundamental mode:

$$(z) \to \frac{Wz}{h} + \frac{B}{6h}\left(h^2 z \mid z^3\right), \quad \alpha \to 0. \tag{19}$$

Numerical modeling. At this stage, the following is performed:

– verification and analysis of the obtained solution;

– investigation of the effect of physical parameters on the flow structure.

To this end, the authors of the presented article conducted comprehensive numerical modeling in the MATLAB environment. The primary objectives of the software implementation were:

– visual representation of velocity fields;

– quantitative comparison of flow characteristics for various fluid types and boundary conditions.

The central element of the code is *solve_couette_full* function, which implements formulas (13), (14), and (16).

The inputs are:

– physical properties of the fluid (density ρ and dynamic viscosity μ);

– geometric parameters of the problem (distance between the plates h);

– kinematic characteristics (W, A, B, V_w);

– z-coordinate grid.

The output is the basic functions $U(z)$, $u_1(z)$, $u_2(z)$ and their derivatives with respect to z for the subsequent calculation of such important hydrodynamic quantities as shear stress and vorticity.

The modeling was conducted in two stages. In the first stage, a basic calculation was performed for a standard set of parameters. This allowed for verification of the boundary conditions. The maximum deviation of the velocity from the specified values at the boundaries $z = 0$ and $z = h$ did not exceed 10^{-12}, which confirmed the high accuracy of the analytical approach and the correctness of the software implementation.

In the second stage, the code was extended to analyze two key aspects. First, the effect of the signs and magnitudes of the coefficients A and B in the boundary velocity profile on the top plate was investigated in detail. Four combinations were considered: $A > 0$, $B > 0$; $A > 0$, $B < 0$; $A < 0$, $B > 0$; $A < 0$, $B < 0$. This allowed for the simulation of several physical scenarios (from flow acceleration toward the channel center to its deceleration near the walls), as well as the transition from convex to concave velocity profiles. For each combination, two-dimensional maps of the velocity distribution $V_x(y, z)$ and velocity profiles along the normal to the plates at fixed values of the transverse coordinate y were constructed. This provided a clear visual representation of how changing the sign of the quadratic term B altered drastically the shape of the velocity isolines, and how the sign of the linear coefficient A determined the asymmetry of the profile relative to the plane $y = 0$.

Secondly, the flow for various fluids was calculated. The model incorporated the physical properties of water SAE 30[1] engine oil, and petroleum at temperatures of 20°C, 40°C, or 60°C [14]. The use of reference data for dynamic viscosity and density made it possible to move from an abstract mathematical model to practically significant engineering calculations. For each fluid, the Reynolds number $Re=Wh/\nu$ was automatically determined, which made it possible to assess the flow regime. As expected, for water at room temperature, the Reynolds number reached $Re\approx1000$. At the same time, the flow remained laminar, which was consistent with the known stability of classical Couette flow. For oil and petroleum, the flow remained deeply laminar ($Re < 20$).

Particular attention was paid to the calculation of derived quantities. For each value of the coordinate y, the shear stress $\tau_{xz} = \mu\partial V_x/\partial z$ and the vorticity $\omega_y = -\partial V_x/\partial z$ were computed analytically. This made it possible to avoid errors of numerical differentiation [15] and ensured high accuracy in constructing the distributions of the specified quantities both along the gap between the plates and as a function of the transverse coordinate y.

Thus, the program developed in MATLAB is a tool for the comprehensive analysis of generalized Couette flow. It can be used to:

– verify the correctness of the analytical solution;

– conduct an in-depth study of the effect of the physical properties of the working medium and complex boundary conditions on the flow hydrodynamics;

– obtain extensive visual and quantitative data for further analysis.

[1] From the name of the American organization Society of Automotive Engineers — Association of Automotive Engineers.

Functions $u_1(z)$, $u_2(z)$, $U(z)$ were parametrically investigated using the numerical modeling method in MATLAB based on the analytical solution derived from (13), (14), and (16). The calculations were performed with the following fixed parameters (Figs. 2–5): $h = 1.0$ m, $W = 0.3$ m/s, $V_w = 0.001$ m/s, $\mu = 0.01$ Pa·s, for four combinations of signs: $A = \pm 0.03$ s^{-1} and $B = \pm 0.005$ m^{-1}·s^{-1}.

For real fluids, calculations were performed with $h = 0.02$ m, $W = 0.05$ m/s, $A = 0.1$ s^{-1}, $B = 0.02$ m^{-1}·s^{-1}, $V_w = 0.0005$ m/s. The following were used: water at 20°C ($\mu = 1.002 \cdot 10^{-3}$ Pa·s) and 40°C ($\mu = 0.653 \cdot 10^{-3}$ Pa·s); petroleum at 20°C ($\mu = 9.15 \cdot 10^{-3}$ Pa·s) and 40°C ($\mu = 4.72 \cdot 10^{-3}$ Pa·s);); SAE 30 oil at 20°C ($\mu = 0.290$ Pa·s) and 60°C ($\mu = 0.050$ Pa·s).

Research Results. Figure 2 shows the vorticity fields ω_y. For $A > 0$, the maximum positive values ω_y are located in the region of positive coordinates y. For $A < 0$, maxima ω_y are shifted to the region $y < 0$. The amplitude of the values ω_y varies with changes in coefficient B.

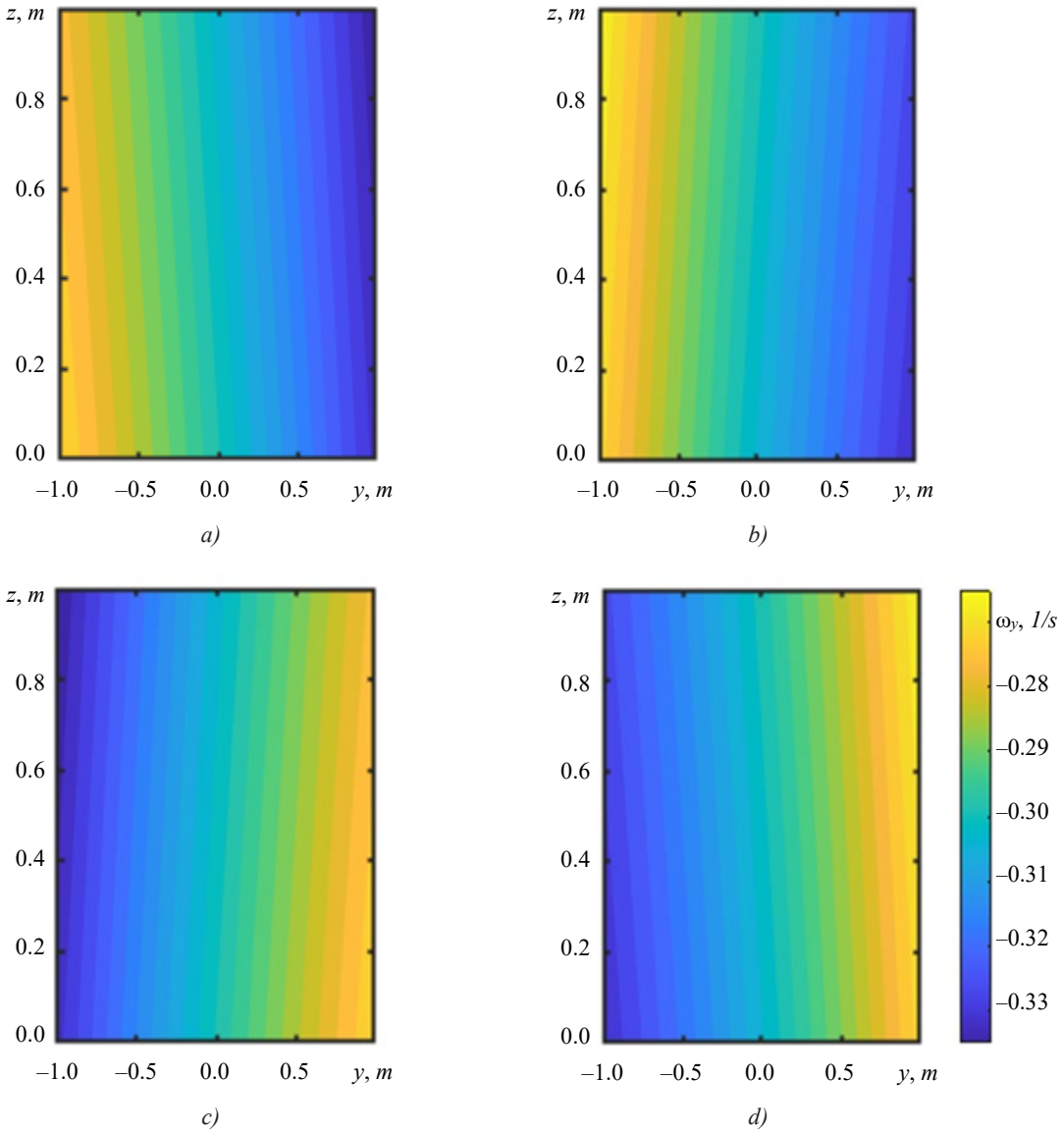

Fig. 2. Distribution of vorticity ω_y for different combinations of parameter signs A and B:
a — $A > 0$, $B > 0$; *b* — $A > 0$, $B < 0$; *c*— $A < 0$, $B > 0$; *d* — $A < 0$, $B < 0$

Figure 3 shows the velocity magnitude field $|V|$ and the vector field for two combinations of the signs of parameters A and B. For $A > 0$, the vectors are longer in the region $y > 0$, indicating a shift of the velocity maximum towards the positive transverse coordinate region. For $A < 0$, the opposite pattern is observed: the vectors are longer in the region $y < 0$, which indicates a shift of the maximum towards the negative region. This is a manifestation of flow asymmetry caused by the linear term A in the boundary condition. The shape of isolines $|V|$ differs for the cases $B > 0$ and $B < 0$, which is related to the effect of the quadratic term B.

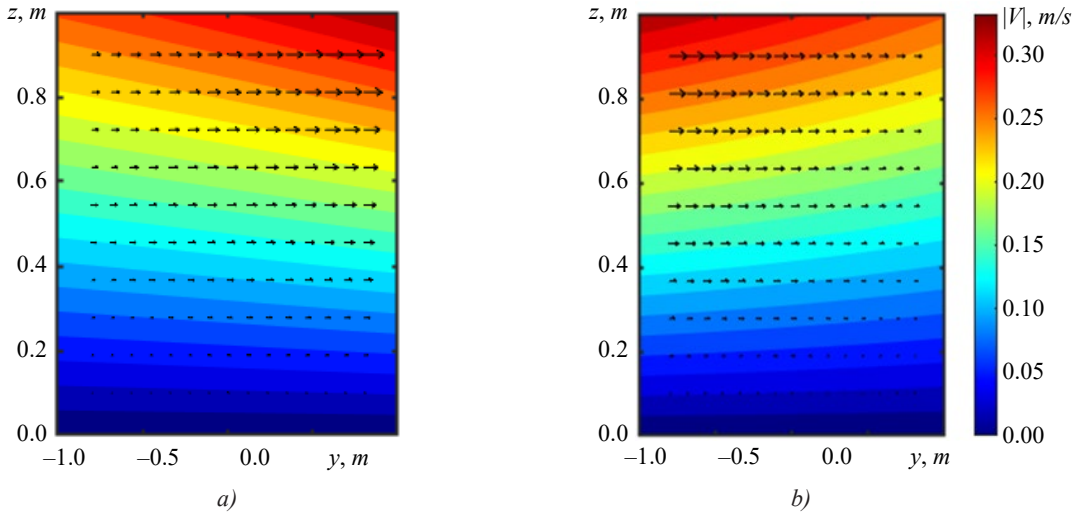

Fig. 3. Velocity modulus field and vector field for different combinations of parameter signs A and B:
a — $A > 0$, $B > 0$; $A > 0$, $B < 0$; b — $A < 0$, $B > 0$; $A < 0$, $B < 0$

Figure 4 presents the isolines of the longitudinal velocity V_x and the streamlines. The streamlines deviate from the direction of the channel axis. The direction of the deviation is determined by the sign A. The isolines V_x for $B > 0$ and $B < 0$ have different curvatures.

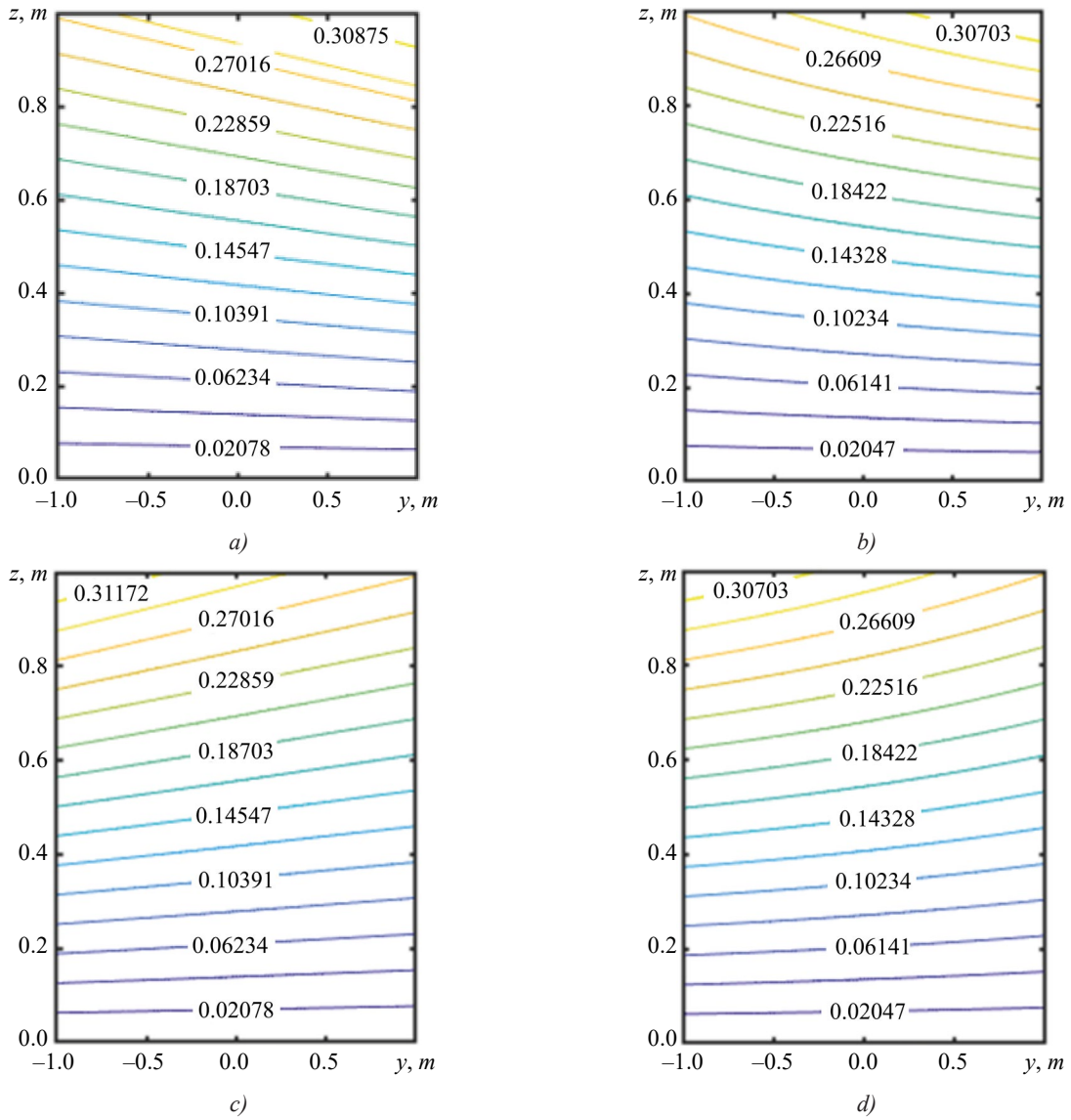

Fig. 4. Isolines of the velocity component V_x and streamlines for different combinations of parameter signs A and B:
a — $A > 0$, $B > 0$; b — $A > 0$, $B < 0$; c — $A < 0$, $B > 0$; d — $A < 0$, $B < 0$

Figure 5 shows the profiles $V_x(y)$ at different levels, i.e., at $z = 0$, h, $h/4$, $h/2$ and $3h/4$. At $z = 0$, the velocity V_x is zero. As z increases, the variation V_x with y increases and reaches the maximum at $z = h$, where the profile is determined by parameters A and B. At $z = h/2$, the profile is close to linear.

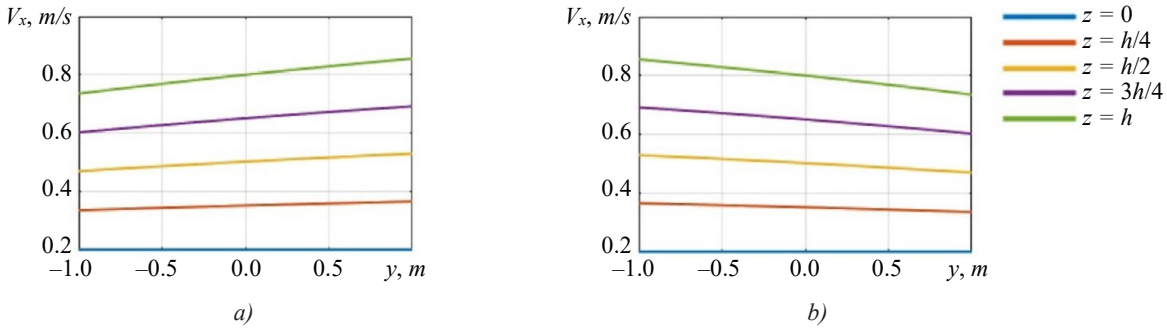

Fig. 5. Distribution of the velocity component V_x along the transverse coordinate y at different channel height levels:

a — $A > 0$, $B > 0$; $A > 0$, $B < 0$; b — $A < 0$, $B > 0$; $A < 0$, $B < 0$

The calculations were performed for real fluids with $h = 0.02$ m, $W = 0.05$ m/s, $A = 0.1$ s^{-1}, $B = 0.02$ m^{-1}·s^{-1}, $V_w = 0.0005$ m/s (Figs. 6–8). The following were used: water at 20°C ($\mu = 1.002 \cdot 10^{-3}$ Pa·s) and 40°C ($\mu = 0.653 \cdot 10^{-3}$ Pa·s); petroleum at 20°C ($\mu = 9.15 \cdot 10^{-3}$ Pa·s) and 40°C ($\mu = 4.72 \cdot 10^{-3}$ Pa·s); SAE 30 oil at 20°C ($\mu = 0.290$ Pa·s) and 60°C ($\mu = 0.050$ Pa·s).

Figure 6 shows the profiles $V_x(z)$ at $y = 0$. All profiles are plotted within the range $z \in [0, 20]$ mm, which corresponds to the layer thickness.

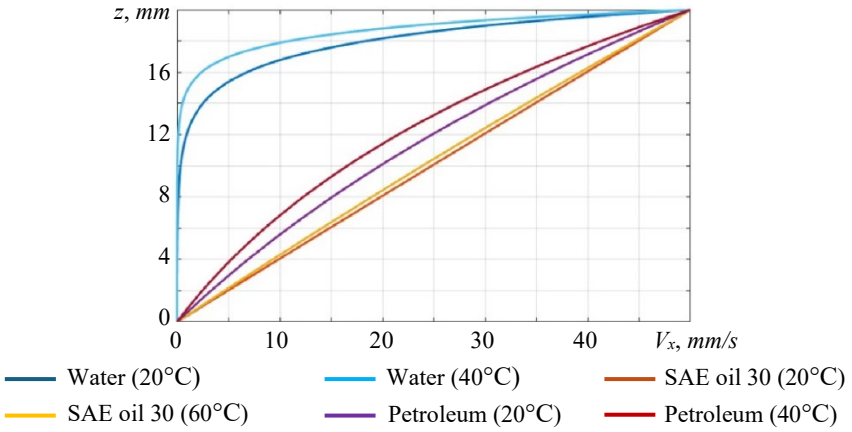

Fig. 6. Comparison of velocity profiles V_x(z) at $y = 0$ for various fluids

Figure 7 displays the isolines $|V|$ For water, the streamlines show minimal deviation from the horizontal, while for petroleum at 20°C, they are significantly curved near the upper wall.

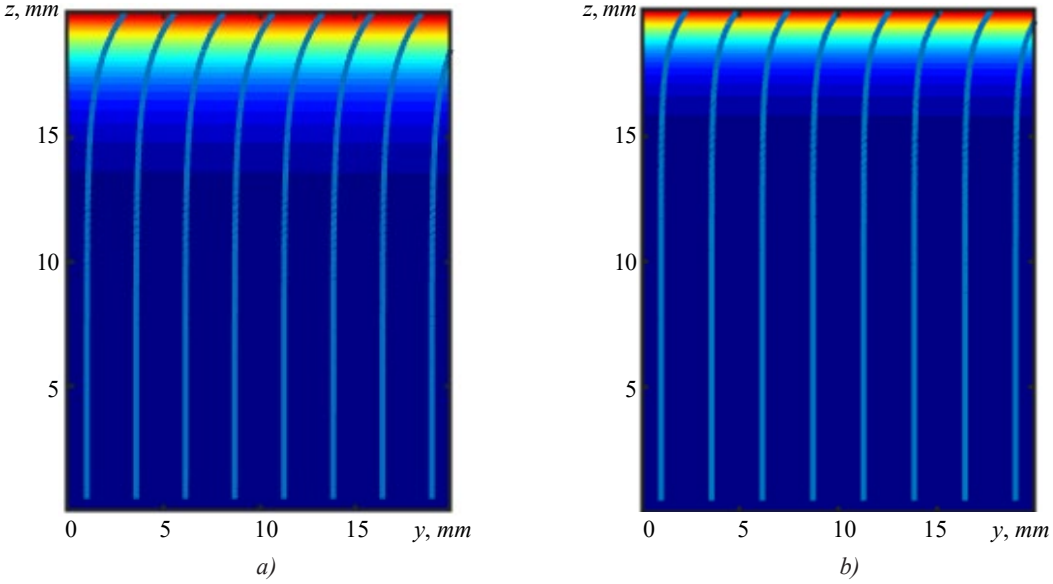

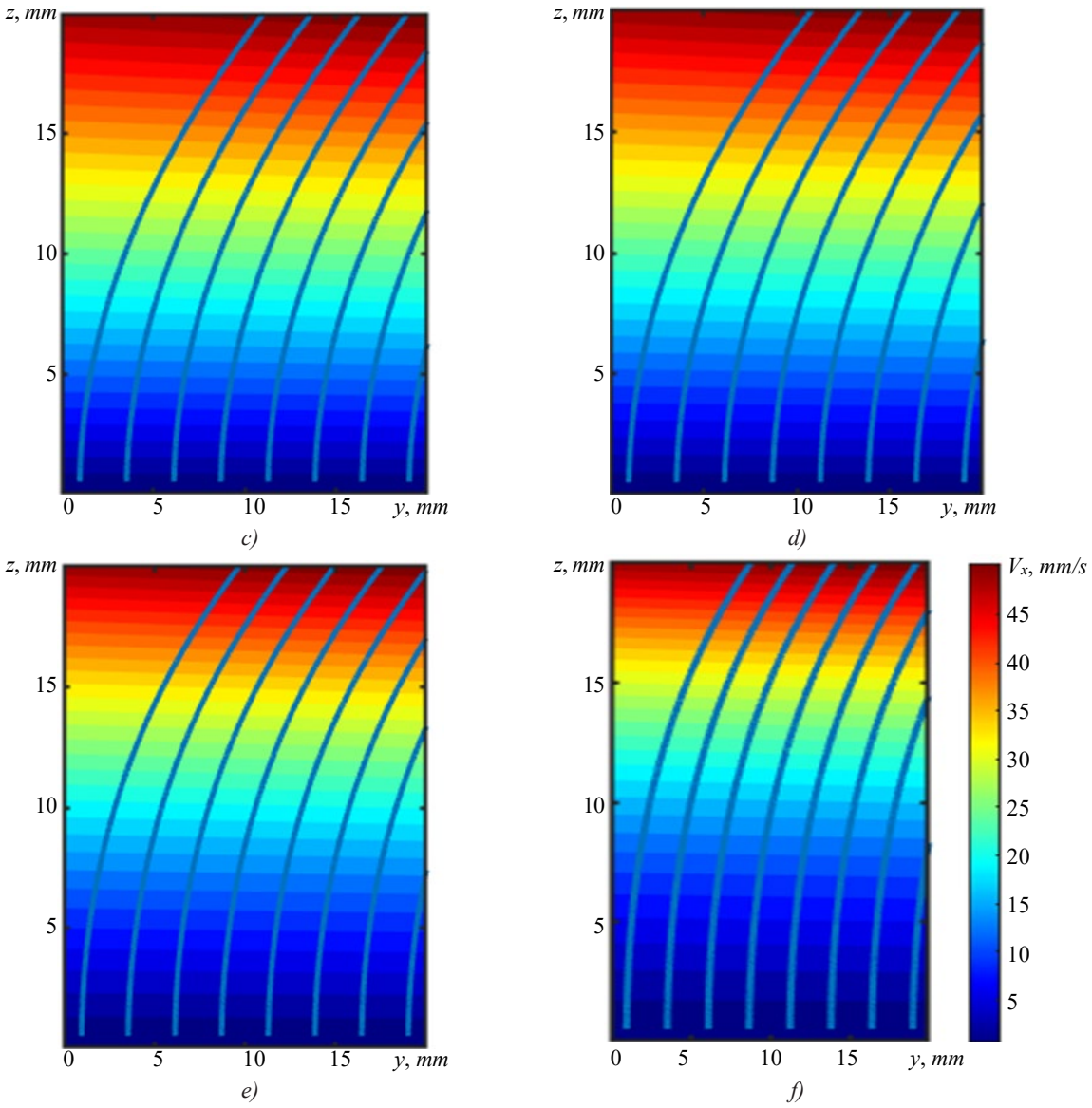

Fig. 7. Isolines of the velocity module $|\vec{V}|$ and streamlines for various fluids:
a — water (20°C); *b* — water (40°C); *c* —SAE oil (20°C); *d* — SAE oil (60°C);
e — petroleum (20°C); *f* — petroleum (40°C)

Figure 8 shows two-dimensional vorticity fields ω_y for various fluids.

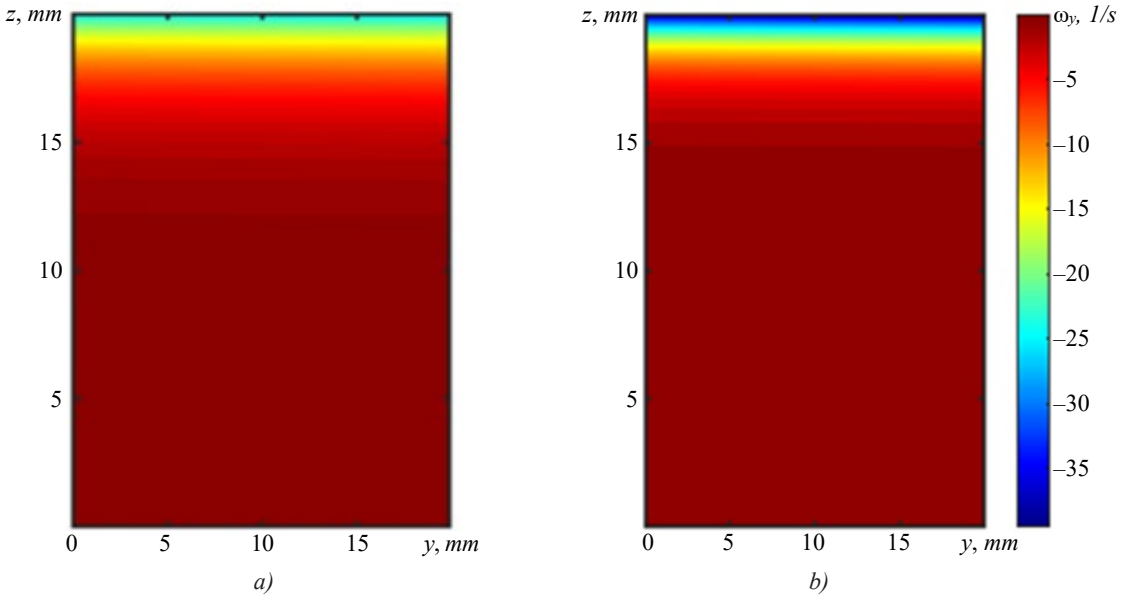

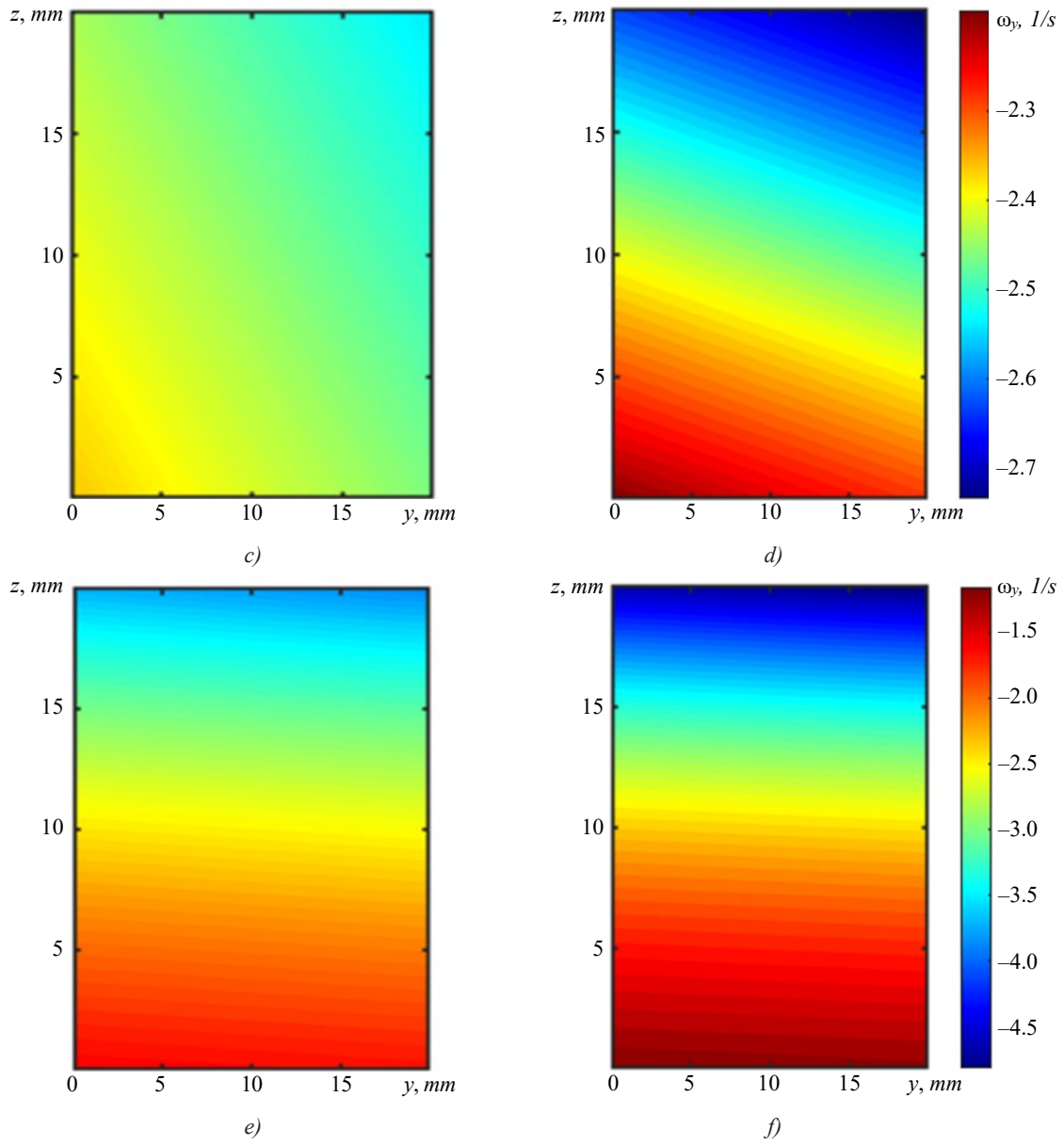

Fig. 8. Two-dimensional vorticity fields ω_y for various fluids: *a* — water (20°C); *b* — water (40°C); *c* — SAE oil (20°C); *d* — SAE oil (60°C); *e* — petroleum (20°C); *f* — petroleum (40°C)

Discussion. According to the data in Figure 6, for water at 20°C, the profile $V_x(z)$ exhibits a weak deviation from the linear law, which is associated with its low viscosity. When the temperature increases to 40°C, this deviation becomes even less pronounced, and the overall slope of the profile slightly decreases. For SAE 30 oil (20°C), a moderate non-linearity of the profile is observed, which weakens significantly upon heating to 60°C. In this case, the profile approaches the linear one, which corresponds to a decrease in viscosity with increasing temperature. For petroleum (20°C), the profile is characterized by a pronounced non-linearity. When the temperature increases to 40°C, the curve becomes closer to the linear one, which is also consistent with a decrease in viscosity.

As shown in Figure 8, for water at 20°C and 40°C, the vorticity is negative and varies in the range from –35 to –5 s^{-1}, which corresponds to weak vorticity throughout the channel. For SAE 30 oil at 20°C, a localized region of elevated vorticity magnitude ($|\omega_y| > 2{,}3$ c^{-1}), is observed, concentrated near the upper wall. Upon heating to 60°C, the region of elevated vorticity expands, and its magnitude decreases, which is consistent with the reduction in viscosity. For petroleum at 20°C, vorticity reaches values up to –4.5 s^{-1}, and at 40°C up to –1.5 s^{-1}, which also corresponds to a decrease in viscosity.

The research results allow us to assert that the combined action of permeability, nonlinear boundary conditions and viscosity, determines qualitatively new flow regimes that cannot be reduced to a simple superposition of known effects [5].

The decisive influence of the sign of coefficient *A* on flow asymmetry (Figs. 2–5) is explained by its physical meaning as the velocity gradient $\partial V_x/\partial y$ at the boundary. This gradient, specified at the upper wall, generates a transverse flow component throughout the entire volume due to viscous diffusion, leading to a shift in streamlines and vorticity maxima. Coefficient *B*,

governing the curvature of the profile ($\partial^2 V_x/\partial y^2$), determines the distribution of this transverse flow across the channel width, which is reflected in the change in the shape of the velocity isolines (Figs. 3, 4). The weakening of the effect of the boundary coefficients with distance from the upper wall (Fig. 5) is quantitatively described by the exponential dependences (13) and (14), which is consistent with the concept of disturbance damping from the boundary in a viscous fluid [16].

The dimensionless permeability parameter α depends on the dynamic viscosity μ ($\alpha = \rho V_w / \mu$). This explains the pronounced difference between the flow of water and petroleum (Figs. 6, 8).

For high-viscosity fluids (low α values), the solution far from the boundaries tends to a linear profile. However, the inhomogeneity in equation (8) for $U(z)$, caused by the term with B, leads to the concentration of shear in a thin near-wall layer, whose thickness is inversely proportional to $|\alpha|$. Thus, viscosity is not merely a multiplicative factor but a parameter governing the spatial localization of shear deformation. This has significant practical implications, for example, in calculating friction in bearings with porous lubrication [17].

The obtained solution is verified, as it correctly reproduces known limiting cases. For $\alpha \to 0$, it transforms into the solution for flow with a quadratic condition on an impermeable wall [18]. For $A, B \to 0$, it reduces to the classical exponential profile for permeable walls [19]. The simultaneous transition $\alpha, A, B \to 0$ yields the linear profile of classical Couette flow [2].

The explicit form of the solution allows for direct assessment of the effect of each parameter on the flow field, which is valuable for engineering design. For example, in a microfluidic mixer, the microrelief of the wall can be varied (via A and B) to generate a specific vortex structure that enhances mixing [20]. In the problem of porous bearing lubrication, the model enables an analytical connection between oil viscosity, seepage rate, and surface roughness (via A, B), and the distribution of shear stress and energy dissipation [21].

The basic limitation of the model is its assumptions of steady, laminar, and Newtonian flow behavior. Extending the model to account for turbulence is beyond the scope of this research. This represents a separate complex problem, requiring a transition to the Reynolds-averaged Navier-Stokes equations (RANS) or Large Eddy Simulation (LES) models. [20]. Another promising direction is generalization for non-Newtonian fluids [21] and unsteady regimes [22]. This would allow for the modeling of a wider class of applied problems, such as pulsating flows in biomedical devices.

Conclusion. For the first time, an exact analytical solution to the stationary Navier-Stokes equations has been obtained, describing generalized Couette flow of a Newtonian fluid between permeable plates with a quadratic velocity profile at the boundary.

The parametric analysis has revealed that the linear coefficient A of the boundary condition determines the direction of asymmetry in the velocity and vorticity fields, while the quadratic coefficient B determines the degree of their spatial nonlinearity.

Dynamic viscosity is shown to be a key parameter controlling the thickness of the shear layer. For high-viscosity media, the main velocity gradient is localized in a thin near-wall region, whereas for low-viscosity fluids, the velocity profile is close to linear across the entire channel height.

The results of this research provide an analytical foundation for solving applied problems in microfluidics, membrane technologies, and tribology, where flow control under conditions of boundary permeability and complex boundary conditions is required.

Further research is related to refining and expanding the model. In perspective, it could be extended to account for the non-Newtonian properties of the fluid, unsteady regimes, and flow stability.

References

1. Papanastasiou T, Georgios G, Alexandrou AN. *Viscous Fluid Flow*. Boca Raton FL: CRC Press; 2021. 434 p. https://doi.org/10.1201/9780367802424

2. Temam R. *Navier-Stokes Equations: Theory and Numerical Analysis*, 3rd rev. ed. Providence, RI: AMS; 2001. 500 p.

3. Ganie AH, Memon AA, Memon MA, Al-Bugami AM, Bhatti K, Khan I. Numerical Analysis of Laminar Flow and Heat Transfer through a Rectangular Channel Containing Perforated Plate at Different Angles. *Energy Reports*. 2022;8:539–550. https://doi.org/10.1016/j.egyr.2021.11.232

4. Vafai K. *Handbook of Porous Media.* Boca Raton, FL: CRC Press; 2015. 959 p. https://doi.org/10.1201/B18614

5. Wang FZ, Animasaun IL, Muhammad T, Okoya SS. Recent Advancements in Fluid Dynamics: Drag Reduction, Lift Generation, Computational Fluid Dynamics, Turbulence Modelling, and Multiphase Flow. *Arabian Journal for Science and Engineering*. 2024;49(8):10237–10249. https://doi.org/10.1007/s13369-024-08945-3

6. Almuthaybiri SS, Tisdell CC. Laminar Flow in Channels with Porous Walls: Advancing the Existence, Uniqueness and Approximation of Solutions via Fixed Point Approaches. *Journal of Fixed Point Theory and Applications*. 2022;24:55. https://doi.org/10.1007/s11784-022-00971-8

7. Shvarts KG. Plane-Parallel Adjective Flow in a Horizontal Incompressible Fluid Layer with an Internal Linear Heat Source. *Fluid Dynamics*. 2019;53(1):524-528.

8. Waqas H, Farooq U, Dong Liu, Abid M, Imran M, Muhammad T. Heat Transfer Analysis of Hybrid Nanofluid Flow with Thermal Radiation through a Stretching Sheet: A Comparative Study. *International Communications in Heat and Mass Transfer*. 2022;138:106303. https://doi.org/10.1016/j.icheatmasstransfer.2022.106303

9. Karmakar S, Usha R, Chattopadhyay G, Millet S, Ramana Reddy JV, Shukla P. Stability of a Plane Poiseuille Flow in a Channel Bounded by Anisotropic Porous Walls. *Physics of Fluids*. 2022;34(3):034111. https://doi.org/10.1063/5.0083217

10. Mirzaei A, Jalili P, Afifi MD, Jalili B, Ganji DD. Convection Heat Transfer of MHD Fluid Flow in the Circular Cavity with various obstacles: Finite element approach. *International Journal of Thermofluids*. 2023;20:100522. https://doi.org/10.1016/j.ijft.2023.100522

11. Gubareva KV, Eremin AV. Numerical Solution to the Problem of Thermal Conductivity in a Porous Plate with a Topology of Triply Periodic Minimal Surfaces. *Advanced Engineering Research* (*Rostov-on-Don*). 2025;25(1):23–31. https://doi.org/10.23947/2687-1653-2025-25-1-23-31

12. Goruleva LS, Prosviryakov EYu. Exact Solutions to the Navier-Stokes Equations for Describing Inhomogeneous Isobaric Vertical Vortex Fluid Flows in Regions with Permeable Boundaries. *Diagnostics*, *Resource and Mechanics of Materials and Structures*. 2023;1:41–53. https://doi.org/10.17804/2410-9908.2023.1.041-053

13. Polyanin AD, Zaitsev VF. *Handbook of Exact Solutions for Ordinary Differential Equations,* 2nd ed. Boca Raton, FL: CRC Press; 2003. 816 p.

14. Goruleva LS, Prosviryakov EYu. Unidirectional Steady-State Inhomogeneous Couette Flow with a Quadratic Velocity Profile Along a Horizontal Coordinate. *Diagnostics*, *Resource and Mechanics of Materials and Structures*. 2022;3:47–60. https://doi.org/10.17804/2410-9908.2022.3.047-060

15. Roache PJ. *Verification and Validation in Computational Science and Engineering.* Albuquerque, NM: Hermosa Publishers; 1998. 446 p.

16. Peiqing Liu. Boundary Layer Theory and Its Approximation. In book: *Aerodynamics*. New York, NY: Springer; 2022. P. 307–393 https://doi.org/10.1007/978-981-19-4586-1_6

17. Zhixiang Feng, Qingqing Ye. Turbulent Boundary Layer over Porous Media with Wall-Normal Permeability. *Physics of Fluids.* 2023;35(9):095111. https://doi.org/10.1063/5.0160773

18. Kulikovsky A. Laminar Flow in a PEM Fuel Cell Cathode Channel. *Journal of The Electrochemical Society.* 2023;170(2):024510. https://doi.org/10.1149/1945-7111/acba47

19. Nield DA, Bejan A. *Convection in Porous Media.* New York, NY: Springer; 2017. 640 p. https://doi.org/10.1007/978-3-319-49562-0

20. Pope SB. *Turbulent Flows.* Cambridge: Cambridge University Press; 2000. 807 p.

21. Das D, Mondal K, Poddar N, Ping Wang. Transient Dispersion of a Reactive Solute in an Oscillatory Couette Flow through an Anisotropic Porous Medium. *Physics of Fluids*. 2024;36(2):023610. https://doi.org/10.1063/5.0184921

22. Lemarie-Rieusset PG. *The Navier-Stokes Problem in the 21st Century*, 2nd ed. New York: Chapman and Hall/CRC; 2023. 778 p. https://doi.org/10.1201/9781003042594

About the Authors:

Kristina V. Gubareva, Cand.Sci. (Eng.), Associate Professor of the Department of Industrial Thermal Power Engineering, Samara State Technical University (244, Molodogvardeyskaya Str., Samara, 443100, Russian Federation), SPIN-code, ORCID, ScopusID, r.kristina2017@mail.ru

Evgenii Yu. Prosviryakov, Dr.Sci. (Phys.-Math.), Associate Professor of the Department of Information Technology and Control Systems, Ural Federal University (19, Mira Str., Ekaterinburg, 620002, Russian Federation), Head of the Nonlinear Vortex Hydrodynamics Sector, Institute of Engineering Science, RAS (Ural Branch) (34, Komsomolskaya Str., Ekaterinburg, 620049, Russian Federation), SPIN-code, ORCID, ScopusID, ResearcherID, evgen_pros@mail.ru

Anton V. Eremin, Dr.Sci. (Eng.), Associate Professor, Vice-Rector for Scientific Work, Head of the Department of Industrial Thermal Power Engineering, Samara State Technical University (244, Molodogvardeyskaya Str., Samara, 443100, Russian Federation), SPIN-code, ORCID, ScopusID, ResearcherID, a.v.eremin@list.ru

Claimed Contributorship:

KV Gubareva: investigation, software, writing – original draft preparation, visualization.
EYu Prosviryakov: conceptualization, data curation, methodology, writing – review & editing.
AV Eremin: formal analysis, validation, writing – review & editing.

Conflict of Interest Statement: **the authors declare no conflict of interest.**

All authors have read and approved the final manuscript.

Об авторах:

Кристина Владимировна Губарева, кандидат технических наук, доцент кафедры «Промышленная теплоэнергетика» Самарского государственного технического университета (443100, Российская Федерация, г. Самара, ул. Молодогвардейская, 244), SPIN-код, ORCID, ScopusID, r.kristina2017@mail.ru

Евгений Юрьевич Просвиряков, доктор физико-математических наук, доцент, профессор кафедры «Информационные технологии и системы управления» Уральского федерального университета имени первого Президента России Б.Н. Ельцина (620062, Российская Федерация, г. Екатеринбург, ул. Мира, 19), заведующий сектором нелинейной вихревой гидродинамики Института машиноведения имени Э.С. Горкунова Уральского отделения Российской академии наук (620049, Российская Федерация, г. Екатеринбург, ул. Комсомольская, 34), SPIN-код, ORCID, ScopusID, ResearcherID, evgen_pros@mail.ru

Антон Владимирович Еремин, доктор технических наук, доцент, проректор по научной работе, заведующий кафедрой «Промышленная теплоэнергетика» Самарского государственного технического университета (443100, г. Самара, ул. Молодогвардейская, 244). SPIN-код, ORCID, ScopusID, ResearcherID, a.v.eremin@list.ru

Заявленный вклад авторов:

К.В. Губарева: проведение исследования, разработка программного обеспечения, написание черновика рукописи, визуализация.

Е.Ю. Просвиряков: разработка концепции, курирование данных, разработка методологии, написание рукописи — внесение замечаний и исправлений.

А.В. Еремин: формальный анализ, валидация результатов, написание рукописи — внесение замечаний и исправлений.

Конфликт интересов: **авторы заявляют об отсутствии конфликта интересов.**

Все авторы прочитали и одобрили окончательный вариант рукописи.

Received / **Поступила в редакцию** 04.12.2025
Reviewed / Поступила после рецензирования 22.12.2025
Accepted / **Принята к публикации** 14.01.2026

MECHANICS
МЕХАНИКА

UDC 534.1, 539.3, 539.5
https://doi.org/10.23947/2687-1653-2026-26-1-2272

Original Theoretical Research

Applied Theory of Transverse Vibrations of Layered Structure with Polymer Matrices and Inclusions of Porous Piezoceramic Rods Arranged along the Layer

Arkadiy N. Soloviev[1,2] ✉, Maria S. Germanchuk [1,3], Pavel A. Oganesyan[4]

[1] Crimean Engineering and Pedagogical University named after Fevzi Yakubov, Simferopol, Republic of Crimea

[2] Research and Production Center for Engineering Technologies, Crimean Engineering and Pedagogical University named after Fevzi Yakubov, Simferopol, Republic of Crimea

[3] V.I. Vernadsky Crimean Federal University, Simferopol, Republic of Crimea

[4] Southern Federal University, Rostov-on-Don

✉ solovievarc@gmail.com

EDN: OLMHAS

Abstract

Introduction. The development of ultrasonic technology requires the creation of piezoelectric transducers with improved operational and metrological characteristics. One of the most promising directions is the use of composite materials. As shown in the literature, porous piezoceramics possess a unique property: their piezoelectric modulus d_{33} is practically independent of porosity, whereas the elastic moduli noticeably decrease as porosity increases. This opens up possibilities for the design of high-performance devices, particularly composites with a polymer matrix and porous piezoelectric ceramic rods with axial polarization. However, despite the sufficient study of their static properties, theoretical analysis of the dynamic behavior of such structures, including their simplified two-dimensional models, under bending vibrations and longitudinal polarization, is virtually absent in the scientific literature. In this regard, the objective of the work is to develop a simplified mathematical model for the analysis of bending vibrations of a layered plate of the specified composite and to identify the effect of porosity on its dynamic characteristics.

Materials and Methods. The structure is made of a piezoelectric composite consisting of several layers. Each layer is 1–3 piezoelectric composite, formed by a polymer matrix and porous longitudinally polarized piezoceramic rods. The mathematical formulation of the boundary value problems is performed within the framework of the linear theory of electroelasticity. Based on Kirchhoff-Love hypotheses and assumptions regarding the electric potential distribution, an applied method for calculating steady-state bending vibrations of a layered plate is proposed. The adequacy of the approach is verified through its comparison with the results of finite element modeling implemented in the ACELAN package.

Results. The key outcome of the study was the development and successful testing of an applied theory that reduced the three-dimensional boundary-value problem of electroelasticity for layered piezoelectric elements to a simpler two-dimensional formulation. This significantly reduced calculation time compared to traditional finite element methods while maintaining the required accuracy. To verify the proposed model, numerical testing was performed by comparing it with calculations in the ACELAN software package. The comparative analysis showed almost complete agreement between the results in the low-frequency range, including the precise determination of the first bending mode frequency. The obtained correspondence confirmed the high adequacy and reliability of the developed method, demonstrating its applicability as an efficient tool for the analysis and optimal design of piezoelectric devices.

Discussion. One of the key challenges in the design of layered piezoelectric transducers is the high resource intensity of three-dimensional modeling without transitioning to efficient characteristics, which significantly limits optimization possibilities. The proposed approach, based on reducing the three-dimensional problem to a two-dimensional one, represents a significant step forward in addressing this issue**.** Its main advantage is the reduction in computational costs

and the possibility of using simpler software tools compared to “heavy” CAE packages in numerical analysis. This opens the way to multiple runs, including those employing evolutionary algorithms, in the process of searching for the optimal geometry and structure of the piezoelectric element. Validation of the model based on comparison with calculations in the ACELAN finite element package has shown a high degree of correspondence in the low-frequency region, which confirms its adequacy for practical application. At the same time, the identified limitations related to the frequency range and differences in the elastic properties of the layers outline the boundaries of applicability and set directions for subsequent research.

Conclusion. As a result of the conducted research, an efficient calculation method has been developed and tested. It reduces the three-dimensional boundary value problem of electroelasticity for layered piezoelectric elements to a two-dimensional formulation. The main outcome is a significant acceleration of numerical modeling while maintaining accuracy. It is shown that the proposed theory provides high correctness of results in the low-frequency range, up to the first flexural mode, which has been confirmed by comparison with reference data from finite element analysis in ACELAN. This demonstrates the practical significance of the method as an efficient tool for the iterative search for the optimal design of converters. Prospects are opening up for its application in engineering practice when designing new types of piezoceramic devices, as well as for the further development of applied theory — in the direction of expanding the frequency range and adapting to more complex multilayer structures.

Keywords: composite materials, porous piezoceramics, layered plate, bending, applied theory, finite element method

Acknowledgements. The authors would like to thank the editorial board and reviewers for their attentive attitude towards the article.

Funding Information. The research is done with the financial support from RFFI (grant no. 22–11–00302 П) at the Southern Federal University. https://rscf.ru/project/22-11-00302/

For Citation. Soloviev AN, Germanchuk MS, Oganesyan PA. Applied Theory of Transverse Vibrations of Layered Structure with Polymer Matrices and Inclusions of Porous Piezoceramic Rods Arranged along the Layer. *Advanced Engineering Research (Rostov-on-Don).* 2026;26(1):2272. https://doi.org/10.23947/2687-1653-2026-26-1-2272

Оригинальное теоретическое исследование

Прикладная теория поперечных колебаний слоистой конструкции с полимерными матрицами и включениями из расположенных вдоль слоя пористых пьезокерамических стержней

А.Н. Соловьев[1,2] ✉, М.С. Германчук[1,3], П.А. Оганесян[4]

[1] Крымский инженерно-педагогический университет имени Февзи Якубова, г. Симферополь, Республика Крым

[2] Научно-производственный центр инжиниринговых технологий, Крымский инженерно-педагогический университет имени Февзи Якубова, г. Симферополь, Республика Крым

[3] Крымский федеральный университет им. В.И. Вернадского, г. Симферополь, Республика Крым

[4] Южный федеральный университет, г. Ростов-на-Дону, Российская Федерация

✉ solovievarc@gmail.com

Аннотация

Введение. Развитие ультразвуковой техники требует создания пьезоэлектрических преобразователей с улучшенными эксплуатационными и метрологическими характеристиками. Одним из наиболее перспективных направлений является применение композиционных материалов. Как показано в литературе, пористая пьезокерамика обладает уникальным свойством: ее пьезомодуль d_{33} практически не зависит от пористости, тогда как модули упругости заметно убывают при её увеличении. Это открывает возможности для проектирования высокоэффективных устройств, в частности композитов с полимерной матрицей и пористыми пьезокерамическими стержнями с осевой поляризацией. Однако, несмотря на достаточную изученность статических свойств, теоретический анализ динамического поведения таких структур, включая их упрощённые двумерные модели, при изгибных колебаниях и продольной поляризации в научной литературе практически отсутствует. В этой связи целью работы является разработка упрощённой математической модели для анализа изгибных колебаний слоистой пластины указанного композита и выявление влияния пористости на её динамические характеристики.

Материалы и методы. Материал конструкции — пьезоэлектрический композит, состоящий из нескольких слоёв. Каждый слой представляет собой пьезокомпозит связности 1–3, образованный полимерной матрицей и пористыми продольно поляризованными пьезокерамическими стержнями. Математическая постановка краевых задач выполнена в рамках линейной теории электроупругости. На основе гипотез типа Кирхгоффа-Лява и предположений о распределении электрического потенциала предложен прикладной метод расчёта установившихся изгибных колебаний слоистой пластины. Адекватность подхода проверена сопоставлением с результатами конечно-элементного моделирования, реализованного в пакете ACELAN.

Результаты исследования. Ключевым итогом работы стала разработка и успешная апробация прикладной теории, позволяющей свести трёхмерную краевую задачу электроупругости для слоистых пьезоэлементов к более простой двумерной постановке. Это обеспечило существенное сокращение времени расчёта по сравнению с традиционными методами конечных элементов при сохранении требуемой точности. Для верификации предложенной модели выполнено численное тестирование путём сравнения с расчётами в программном комплексе ACELAN. Сравнительный анализ показал практически полное совпадение результатов в низкочастотном диапазоне, включая точное определение частоты первой изгибной моды. Полученное соответствие подтверждает высокую адекватность и достоверность разработанного метода, демонстрируя его применимость в качестве эффективного инструмента для анализа и оптимального проектирования пьезоэлектрических устройств.

Обсуждение. Одной из ключевых проблем при проектировании слоистых пьезоэлектрических преобразователей является высокая ресурсоёмкость трёхмерного моделирования без перехода к эффективным характеристикам, что существенно ограничивает возможности оптимизации. Предложенный подход, основанный на сведении трёхмерной задачи к двумерной, представляет значимый шаг вперёд в решении этой проблемы. Его основное преимущество — снижение вычислительных затрат и возможность использования более простого программного инструментария по сравнению с «тяжёлыми» CAE-пакетами при численном анализе, что открывает путь к множественным прогонкам, в том числе с применением эволюционных алгоритмов, в процессе поиска оптимальной геометрии и структуры пьезоэлемента. Валидация модели на основе сравнения с расчётами в конечно-элементном пакете ACELAN показала высокую степень соответствия в низкочастотной области, что подтверждает её адекватность для практического применения. Вместе с тем выявленные ограничения, связанные с частотным диапазоном и различиями в упругих свойствах слоёв, очерчивают границы применимости и задают направления для последующих исследований.

Заключение. В результате проведённого исследования создан и апробирован эффективный метод расчёта, сводящий трёхмерную краевую задачу электроупругости для слоистых пьезоэлементов к двумерной постановке. Главный итог — существенное ускорение численного моделирования при сохранении точности. Показано, что предложенная теория обеспечивает высокую корректность результатов в низкочастотном диапазоне, вплоть до первой изгибной моды, что подтверждено сравнением с эталонными данными конечно-элементного анализа в ACELAN. Тем самым продемонстрирована практическая значимость метода как эффективного инструмента для итерационного поиска оптимальной конструкции преобразователей. Открываются перспективы его применения в инженерной практике при проектировании новых типов пьезокерамических устройств, а также для дальнейшего развития прикладной теории — в направлении расширения частотного диапазона и адаптации к более сложным многослойным структурам.

Ключевые слова: композитные материалы, пористая пьезокерамика, слоистая пластина, изгиб, прикладная теория, метод конечных элементов

Благодарности. Авторы выражают благодарность редакции журнала и рецензентам за внимательное отношение к статье.

Финансирование. Исследование выполнено при финансовой поддержке гранта РНФ (№ 22–11–00302 П) в Южном федеральном университете, https://rscf.ru/project/22-11-00302/

Для цитирования. Соловьев А.Н., Германчук М.С., Оганесян П.А. Прикладная теория поперечных колебаний слоистой конструкции с полимерными матрицами и включениями из расположенных вдоль слоя пористых пьезокерамических стержней. *Advanced Engineering Research (Rostov-on-Don).* 2026;26(1):2272. https://doi.org/10.23947/2687-1653-2026-26-1-2272

Introduction. To improve the efficiency of piezoelectric transducers, research is being conducted to find the optimal configuration of the device — its size, shape, electroplating pattern, loading methods, and the materials used. Despite a significant amount of work having been carried out, the task of determining efficient designs for piezoelectric generators and selecting piezo-materials with improved characteristics for energy storage devices remains a challenge. One of the

most promising ways to improve the performance of such transducers is the use of piezocomposite materials. The most well-known and thoroughly studied are fibrous piezocomposites, or systems with a 1–3 connectivity pattern according to Newnham's terminology [1], in which rod-shaped piezoceramic elements are embedded in an elastic dielectric matrix. Among numerous papers devoted to 1–3 composites, we should note [2], which examines applications for hydrophones. In [3], the efficient properties are calculated through solving boundary value problems by the finite element method for a unit cell with periodic boundary conditions. In [4], the corresponding coefficients are presented in closed form. In [5], formulas are derived based on asymptotic averaging, and comparison with experiment shows good agreement. Homogenization theory for the design of optimal piezocomposites is applied in [6]. In [7], analytical expressions for the effective constants are also obtained under the condition that the structure period is significantly smaller than the elastic wavelength, and new composites with improved global properties for biomedical imaging are proposed. An analysis of electroelastic composites using self-consistent methods and asymptotic homogenization is performed in [8]. In [9], a theoretical framework for designing piezocomposites with specified generalized characteristics is presented. Additional information is gathered in review [10]. 1–3 composites provide high values for a number of key parameters important for applications — the hydrostatic piezoelectric charge coefficient, the hydrostatic voltage coefficient, the thickness electromechanical coupling coefficient, the hydrostatic Q-factor, and others.

Macro fiber composites, originally developed for the aerospace industry, are also successfully used in energy harvesting systems. These miniature, low-power generators are thin beams and include piezoelectric fibers placed in a dielectric medium. The fibers are integrated into a single multilayer structure with interdigital electrodes on the lateral surfaces of the beams on both sides. The objective of [11] was to assess the effect of the uncertainty in the physical properties of both the piezoelectric fibers and the epoxy matrix on the model response, and to identify the parameters that determine the greatest variability in the output data. In [12], a potential technology is proposed for integrating energy harvesting sources into complex airframe structures in aerospace engineering, enabling the generation of the energy required for monitoring environmental conditions or controlled structural characteristics. A comparative analysis of generators made from monolithic and composite piezoceramics, conducted in [13], showed the high efficiency of using macro fiber composites. Study [14] presents the development of a microgenerator based on microcomposite piezoelectric materials for energy harvesting in glove structures. The devices described consist of piezoelectric fibers with a diameter of 90–250 μm, aligned in a unidirectional order and embedded in a composite structure.

To improve the performance of 1–3 composites, it is possible to vary the materials of the piezoelectric fibers and the elastic dielectric matrix. In particular, porous materials with a reduced Young's modulus and a significantly varying Poisson's ratio can be used as the matrix [2, 14]. In [15, 16], the Mori-Tanaka method is used to determine the effective moduli first for the porous matrix, after which an analysis of 1–3 composites is performed. In [15, 16], additional options for pore orientation relative to the polarization direction are considered, which, however, is difficult to implement in practice. In [2], approximations of the effective environmental method are used. In [17, 18] a topological optimization of the porous structure of the matrix is performed based on the approaches from [2]. In [19], a modeling of a 0–3 composite with piezoelectric particles in a porous matrix is performed. It is also shown that the use of a porous matrix does not lead to an improvement in the electromechanical properties of a 0–3 system. However, the piezoelectric sensitivity coefficients are not analyzed in that study.

Another direction of modification is related to the use of porous piezoceramics, which in recent years have been considered a promising active material for energy storage devices. Compared with dense ceramics, porous materials are characterized by reduced acoustic impedance, increased piezoelectric sensitivity, and a number of high-quality indicators. Thus, in [20], a Rosen-type piezoelectric element utilizing the longitudinal piezoelectric modulus is investigated. In [21], it is shown that introducing a porous layer into a multilayer element based on barium titanate significantly improves performance in piezoelectric energy harvesting. Experimental study [22] describes a piezoelectric generator manufactured using porous ceramics. In [23], a review of the current state and prospects for the use of porous piezoceramics is given.

The present study builds upon the results of [20, 24] and, to a certain extent, combines approaches to the introduction of porous piezoelectric ceramics as an active phase in 1–3 composite fibers and to varying matrix materials with different stiffness. In other words, it examines 1–3 piezoelectric composites in which porous piezoceramics are used as the piezoelectrically active material.

Thus, an analysis of the literature shows that the main efforts of researchers are focused on determining the efficient electroelastic properties of 1–3 composites. A wide range of methods has been developed — from analytical formulas to detailed numerical procedures — that make it possible to predict with high accuracy the homogenized (averaged) characteristics of the material depending on the properties of the constituent phases: the fibers and the matrix. This information is undoubtedly important, but it describes the behavior of the material as a whole, rather than that of the final structural element, which is the goal of engineering design.

The transition from efficient properties to the analysis of the dynamics of real structures, such as plates and shells, represents an independent and non-trivial problem. Although the finite element method (FEM) is applicable for high-precision analysis, as implemented in numerous software packages, full-scale three-dimensional modeling at the stages of preliminary design and optimization often proves to be excessively resource-intensive. At the same time, the development of applied two-dimensional theories (theories of plates and shells) that take into account the specific features of 1–3 composites (particularly in the presence of porous 3–0 and 3–3 components) would significantly simplify and speed up calculations, while maintaining accuracy sufficient for engineering applications. In the scientific literature, there is a distinct lack of such models capable of acting as a bridge between the micromechanics of the material and the macromechanics of the structure.

The objective of this work is to construct an applied two-dimensional theory for calculating the transverse vibrations of layered plates made of 1–3 piezoelectric composite, followed by validation of the results obtained using the proposed theory through comparing them with a solution from the ACELAN finite element package.

Materials and Methods. The development of a mathematical model based on the linear theory of electroelasticity and a computer model of a multilayer transducer with polarization along the layers is performed in the ACELAN finite element package. The computer model of the device is subsequently used to validate the adequacy of the developed applied theory.

Mathematical model

The paper considers models of piezoelectric transducers consisting of electroelastic composite materials, whose properties are specified by effective constants [20, 24]. Let us introduce index j for numbering the bodies and write down the equations and constitutive relations [25]:

$$\begin{gathered}\rho_j\omega^2\ddot{\mathbf{u}}+\alpha_j\rho_j\dot{\mathbf{u}}-\nabla\cdot\boldsymbol{\sigma}=f_j;\nabla\cdot\mathbf{D}=0;\\ \boldsymbol{\sigma}=\mathbf{c}_j^E\cdot\cdot(\boldsymbol{\varepsilon}+\beta_{dj}\dot{\boldsymbol{\varepsilon}})-\mathbf{e}_j^T\cdot\mathbf{E};\mathbf{E}=-\nabla\varphi;\\ \mathbf{D}+\varsigma_d\dot{\mathbf{D}}=\mathbf{e}_j\cdot\cdot(\boldsymbol{\varepsilon}+\varsigma_d\dot{\boldsymbol{\varepsilon}})+\mathfrak{э}_j^S\cdot\mathbf{E};\boldsymbol{\varepsilon}=(\nabla\mathbf{u}+\nabla\mathbf{u}^T)/2,\end{gathered}\tag{1}$$

where $\boldsymbol{\sigma}$ — stress tensor; ρ_j — density of the body; $\boldsymbol{\varepsilon}$ — strain tensor; $\mathbf{u}$ — displacement vector; $\mathbf{D}$ — electric induction vector; $\mathbf{E}$— electric field strength vector; $\mathbf{f}_j$ — vector of mass forces; φ — electric potential; α, β, ς, β_{dj}, ς_d — damping coefficients; $\mathbf{c}_j^E$, $\mathbf{e}_j^T$, $\mathfrak{э}_j^S$ — tensors of elastic constants, piezo moduli and permittivity; index j corresponds to the number of the body in the model.

System (1) is supplemented with the corresponding mechanical and electrical boundary conditions. In particular, the value of the electric potential φ is specified on the electrodes, and on the non-electrode part of the surface — the no-charge condition is set, i.e., the normal component of the electric induction vector $\mathbf{D}$ is equal to zero. In the case of free electrode S_E, potential V_0 on it is unknown and is determined from an additional condition:

$$\int_{S_E}\dot{D}_n\,ds=0.\tag{2}$$

The same condition is applied when determining the antiresonance frequencies.

To analyze the efficiency of the device, the values of the output electric potential, mechanical stresses, and the electromechanical coupling coefficient (EMCC) are used. This is calculated from the formula:

$$k=\sqrt{1-\left(f_r/f_a\right)^2},\tag{3}$$

where f_r and f_a — resonance and antiresonance frequencies, respectively.

The calculation of the damping coefficients when determining the output potential at resonant frequencies was performed using the approach from [25], for which a constant quality factor Q was assumed at the first two resonant frequencies:

$$\alpha_d=\frac{2\pi f_{r1}f_{r2}}{Q\left(f_{r1}+f_{r2}\right)},\quad \beta_d=\varsigma_d=\frac{1}{2\pi Q\left(f_{r1}+f_{r2}\right)}.\tag{4}$$

The operating frequencies (f_{r1}) and the next closest ones (f_{r2}) are selected as such resonant frequencies. For the structures under consideration, the operating frequency is the first bending mode.

When modeling porous composites, the efficient moduli obtained for porous PZT-4 piezoceramics by the averaging method [20, 26] in the ACELAN-COMPOS package were used. Data were obtained for materials with porosity up to 80%. The efficient moduli used in the numerical experiments are given in Table 1.

Table 1

Efficient Porous Ceramic Modules [20]

Porosity, %	0	10	20	30	40	50	60	70	80
ρ, kg/m^3	7500	6750	6000	5250	4500	3750	3000	2250	1500
c_{11}^E, GPa	139	115.6	92.5	68.5	50.5	33.4	20.7	12.6	6.8
c_{12}^E, GPa	77.8	61.5	46.6	31.4	21	11.6	6.2	2.8	1.3
c_{13}^E, GPa	74.3	58.2	42.5	28.2	18.7	10.6	5.2	2.4	1
c_{33}^E, GPa	115	95.3	72.3	54.2	39.1	27.2	16.3	9.1	4.7
c_{44}^E, GPa	25.6	22.3	18.3	14.4	11	7.4	4.4	2.3	1
e_{31}, C/m^2	–5.2	–4.23	–3.14	–2.07	–1.32	–0.75	–0.43	–0.21	–0.1
e_{33}, C/m^2	15.1	13.38	11.37	9.59	7.68	5.93	3.93	2.3	1.25
e_{15}, C/m^2	12.7	10.96	8.96	6.91	5	3.3	1.95	1	0.44
$\mathfrak{э}_{11}^S / \varepsilon_0$	730	663	582	509	439	349	263	191	122
$\mathfrak{э}_{33}^S / \varepsilon_0$	635	567	492	413	345	270	199	130	75

When modeling a 1–3 composite (Fig. 1), the effective properties (Tables 2, 3) are taken from [24].

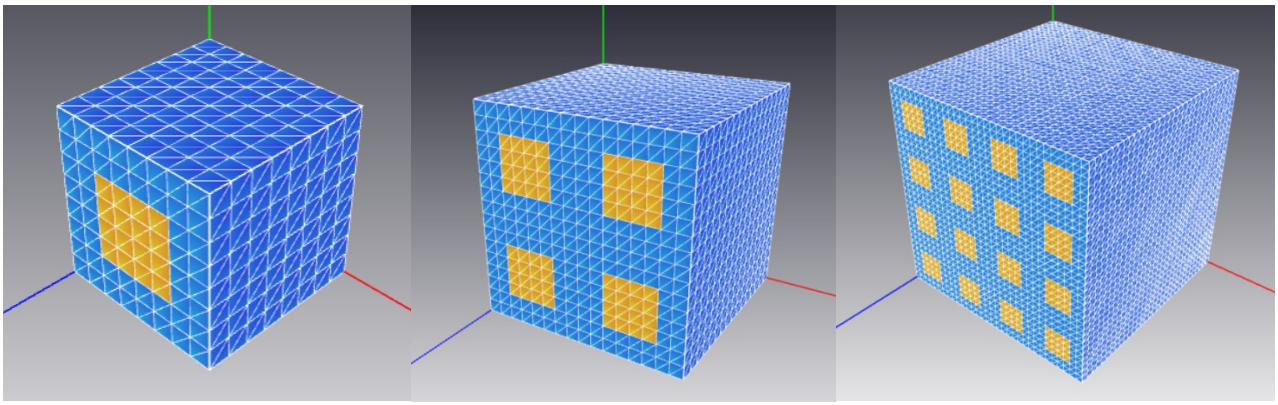

Fig. 1. Examples of representative 1–3 composite volumes, constructed in ACELAN-COMPOS complex

Table 2

Material Properties of Composite 1–3 with Matrix 1

Percentage of porosity	0	10	20	30	40	50	60	70	80
ρ, kg/m^3	5250	5060	4880	4690	4500	4310	4130	3940	3750
$c_{11}^{E\,\mathrm{eff}}$, 10^{10}, N/m^2	6.36	6.12	5.83	5.44	5.05	4.54	4.05	3.63	3.27
$c_{12}^{E\,\mathrm{eff}}$, 10^{10}, N/m^2	2.77	2.66	2.52	2.31	2.09	1.8	1.53	1.28	1.09
$c_{13}^{E\,\mathrm{eff}}$, 10^{10}, N/m^2	2.82	2.67	2.48	2.25	2.03	1.78	1.54	1.36	1.22
$c_{33}^{E\,\mathrm{eff}}$, 10^{10}, N/m^2	6.22	5.89	5.51	5.12	4.76	4.43	4.08	3.83	3.67
$c_{44}^{E\,\mathrm{eff}}$, 10^{10}, N/m^2	1.64	1.58	1.51	1.43	1.35	1.25	1.16	1.08	1.02
e_{33}^{eff}, C/m^2	–1.3	–1.05	–0.785	–0.523	–0.33	–0.185	–0.108	–0.053	–0.025
e_{31}^{eff}, C/m^2	3.77	3.35	2.86	2.4	1.93	1.49	0.972	0.58	0.31
e_{31}^{eff}, C/m^2	3.66	3.26	2.81	2.31	1.83	1.3	0.845	0.465	0.221
$\mathfrak{э}_{11}^{S\,\mathrm{eff}} / \varepsilon_0$	51.4	46.5	40.7	35.2	30.1	24.1	18.3	13.1	8.61
$\mathfrak{э}_{33}^{S\,\mathrm{eff}} / \varepsilon_0$	159	142	124	104	86.9	68.2	50.5	33.2	19.5

Table 3

Material Properties of Composite 1–3 with Matrix 2

Percentage of porosity	0	10	20	30	40	50	60	70	80
ρ, kg/m^3	3000	2810	2630	2440	2250	2060	1880	1690	1500
$c_{11}^{E\text{eff}}$, 10^{10}, N/m^2	1.15	1.13	1.1	1.06	1.02	0.956	0.882	0.796	0.685
$c_{12}^{E\text{eff}}$, 10^{10}, N/m^2	0.237	0.233	0.228	0.222	0.214	0.202	0.186	0.158	0.133
$c_{13}^{E\text{eff}}$, 10^{10}, N/m^2	0.332	0.315	0.294	0.269	0.246	0.219	0.184	0.155	0.125
$c_{33}^{E\text{eff}}$, 10^{10}, N/m^2	2.25	2.03	1.78	1.54	1.32	1.12	0.904	0.74	0.632
$c_{44}^{E\text{eff}}$, 10^{10}, N/m^2	0.425	0.415	0.403	0.388	0.369	0.341	0.304	0.261	0.219
e_{33}^{eff}, C/m^2	–1.3	–1.05	–0.785	–0.523	–0.33	–0.185	–0.108	–0.053	–0.025
e_{31}^{eff}, C/m^2	3.77	3.35	2.86	2.39	1.93	1.49	0.972	0.58	0.31
e_{31}^{eff}, C/m^2	1.44	1.35	1.24	1.1	0.959	0.783	0.591	0.381	0.209
$э_{11}^{S\text{eff}} / \varepsilon_0$	14.1	12.9	11.5	10.1	8.9	7.39	5.93	4.62	3.47
$э_{33}^{S\text{eff}} / \varepsilon_0$	159	142	123	104	86.9	68.2	50.5	33.2	19.5

Layered plate structures and finite element model

The piezoelectric element under consideration is a layered plate (Fig. 2), in which each layer is a 1–3 piezocomposite, with the piezoceramic rods (marked by black circles in Fig. 2) made of porous piezoceramics. It is noteworthy that two layers symmetric with respect to the midsurface have opposing longitudinal polarization.

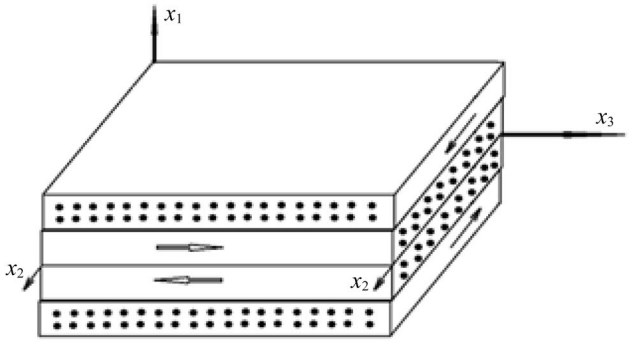

Fig. 2. Layered plate structures

In the case where the piezoelectric element consists of two layers, its finite element model is constructed. Figure 3 *a* presents the geometric model with two oppositely polarized layers (red and yellow colors), and Figure 3 *b* shows the mesh of triangular quadratic finite elements (1350 finite elements, 2839 nodes).

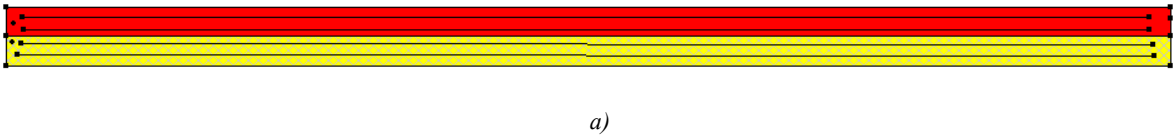

a)

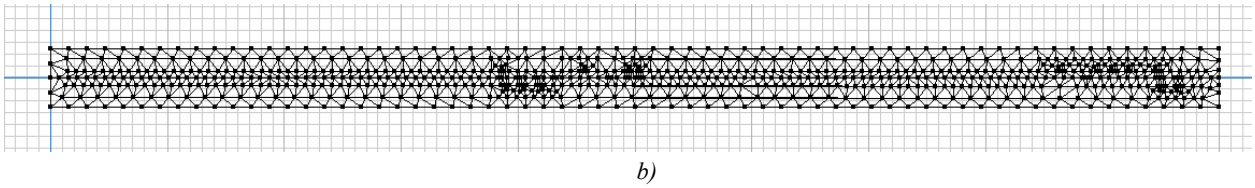

b)

Fig. 3. Two-layer piezoelectric element: *a* — geometric model; *b* — finite element mesh

The finite element model constructed in this section was used to validate the adequacy of the applied theory in calculations in the following sections.

Research Results

Development of an applied theory for calculating transverse vibrations of a layered structure with polarization of layers in the plane of the plate

The applied theory of bending vibrations of the plate under consideration, consisting of four layers, in which the upper and lower layers are isotropic (thicknesses H with Lamé coefficients λ, μ), and the internal electroelastic thickness h is constructed on the basis of Kirchhoff-Love-type hypotheses. The first hypothesis is that normal stresses are equal to zero throughout the entire volume of the plate $\sigma_{11} = 0$, which makes it possible to express longitudinal deformations:

$$\varepsilon_{11} = -\frac{e_{31}\dfrac{\partial}{\partial z}\phi(x,y,z) + c_{12}\varepsilon_{22} + c_{13}\varepsilon_{33}}{c_{11}}. \tag{5}$$

The second hypothesis shows that the distribution of the components of the displacement vector and the electric potential has the form:

$$\begin{gathered} u_1(x,y,z) = UX(y,z),\ u_2(x,y,z) = -\left(\frac{\partial}{\partial y}UX(y,z)\right)x,\ u_3(x,y,z) = -\left(\frac{\partial}{\partial z}UX(y,z)\right)x, \\ \phi(x,y,z) = \Phi(y,z),\ \varepsilon_{22} = -\left(\frac{\partial^2}{\partial y^2}UX(y,z)\right)x,\ \varepsilon_{33} = -\left(\frac{\partial^2}{\partial z^2}UX(y,z)\right)x, \end{gathered} \tag{6}$$

where $UX(y, z)$ — deflection of the midsurface, $x_1 = x$, $x_2 = y$, $x_3 = z$.

Taking into account relations (5) and (6) in system (1) in the case of steady-state vibrations with circular frequency ω leads to a system of equations for two unknown functions $\Phi(y, z)$, $UX(y, z)$.

$$\begin{gathered} \left(-\frac{1}{2}\left(2e_{31} - \frac{2c_{12}e_{31}}{c_{11}}\right)\left(\left(\frac{1}{2}h+H\right)^2 - \frac{1}{4}h^2\right) - 2e_{15}\left(\left(\frac{1}{2}h+H\right)^2 - \frac{1}{4}h^2\right)\right)\times \\ \times\left(\frac{\partial^3}{\partial z\partial y^2}\Phi(y,z)\right) - \frac{1}{2}\left(-\frac{2c_{13}e_{31}}{c_{11}} + 2e_{33}\right)\left(\left(\frac{1}{2}h+H\right)^2 - \frac{1}{4}h^2\right)\times \\ \times\left(\frac{\partial^3}{\partial z\partial y^2}\Phi(y,z)\right) - \frac{1}{2}\left(-\frac{2c_{13}e_{31}}{c_{11}} + 2e_{33}\right)\left(\left(\frac{1}{2}h+H\right)^2 - \frac{1}{4}h^2\right)\left(\frac{\partial^3}{\partial z^3}\Phi(y,z)\right) + \\ + \left(-\frac{1}{3}\left(\frac{2c_{12}^2}{c_{11}} - 2c_{11}\right)\left(\left(\frac{1}{2}h+H\right)^3 - \frac{1}{8}h^3\right) - \frac{1}{24}\left(-2\lambda - 4\mu + \frac{2\lambda^2}{\lambda+2\mu}\right)h^3\right)\times \\ \times\left(\frac{\partial^4}{\partial y^4}UX(y,z)\right) + \left(\frac{1}{3}\mu h^3 + \frac{8}{3}c_{44}\left(\left(\frac{1}{2}h+H\right)^3\right) - \frac{1}{8}h^3\right) - \frac{2}{3}\left(\frac{2c_{12}c_{13}}{c_{11}} - 2c_{13}\right)\times \\ \times\left(\left(\frac{1}{2}h+H\right)^3 - \frac{1}{8}h^3\right) - \frac{1}{12}\left(\frac{2\lambda^2}{\lambda+2\mu} - 2\lambda\right)h^3\left(\frac{\partial^4}{\partial z^2\partial y^2}UX(y,z)\right) + \\ + \left(-\frac{1}{3}\left(\frac{2c_{13}^2}{c_{11}} - 2c_{33}\right)\left(\left(\frac{1}{2}h+H\right)^3 - \frac{1}{8}h^3\right) - \frac{1}{24}\left(-2\lambda - 4\mu + \frac{2\lambda^2}{\lambda+2\mu}\right)h^3\right)\times \\ \times\left(\frac{\partial^4}{\partial z^4}UX(y,z)\right) - \omega^2\rho h UX(y,z) - p(y,z) = 0. \\ -2g_{11}\left(\frac{\partial^2}{\partial y^2}\Phi(y,z)\right) + \left(-\frac{2e_{31}^2}{c_{11}} - 2g_{33}\right)\left(\frac{\partial^2}{\partial z^2}\Phi(y,z)\right) + \\ + \frac{1}{H}\left(\left(\frac{c_{12}e_{31}}{c_{11}} - 2e_{15} - e_{31}\right)\left(\left(\frac{1}{2}h+H\right)^2 - \frac{1}{4}h^2\right)\left(\frac{\partial^3}{\partial z\partial y^2}UX(y,z)\right)\right) + \\ + \frac{1}{H}\left(\left(\frac{c_{13}e_{31}}{c_{11}} - e_{33}\right)\left(\left(\frac{1}{2}h+H\right)^2 - \frac{1}{4}h^2\right)\left(\frac{\partial^3}{\partial z^3}UX(y,z)\right)\right) = 0. \end{gathered} \tag{7}$$

Bending moments and shear forces have the form:

$$M_{22}=\frac{1}{24}\left(-2(\lambda+2\mu)\left(\frac{\partial^2}{\partial y^2}UX(y,z)\right)-\right.$$
$$-\frac{1}{\lambda+2\mu}\left(2\lambda\left(-\left(\frac{\partial^2}{\partial y^2}UX(y,z)\right)\lambda-\lambda\left(\frac{\partial^2}{\partial z^2}UX(y,z)\right)\right)\right)-2\lambda\left(\frac{\partial^2}{\partial z^2}UX(y,z)\right)\Bigg)\times$$
$$-2c_{13}\left(\frac{\partial^2}{\partial z^2}UX(y,z)\right)-2c_{11}\left(\frac{\partial^2}{\partial y^2}UX(y,z)\right)\Bigg)\left(\left(\frac{1}{2}h+H\right)^3-\frac{1}{8}h^3\right)+$$
$$+\frac{1}{2}\left(2e_{31}\left(\frac{\partial}{\partial z}\Phi(y,z)\right)-\frac{2c_{12}e_{31}\left(\frac{\partial}{\partial z}\Phi(y,z)\right)}{c_{11}}\right)\left(\left(\frac{1}{2}h+H\right)^2-\frac{1}{4}h^2\right).$$

$$M_{33}=\frac{1}{24}\left(-\frac{1}{\lambda+2\mu}\left(2\lambda\left(-\left(\frac{\partial^2}{\partial y^2}UX(y,z)\right)\lambda-\lambda\left(\frac{\partial^2}{\partial z^2}UX(y,z)\right)\right)\right)-\right.$$
$$-2\left(\frac{\partial^2}{\partial y^2}UX(y,z)\right)\lambda-2(\lambda+2\mu)\left(\frac{\partial^2}{\partial z^2}UX(y,z)\right)\Bigg)h^3+$$
$$+\frac{1}{3}\left(-\frac{1}{c_{11}}\left(2c_{13}\left(-\left(\frac{\partial^2}{\partial y^2}UX(y,z)\right)c_{12}-c_{13}\left(\frac{\partial^2}{\partial z^2}UX(y,z)\right)\right)\right)-\right.$$
$$-2c_{13}\left(\frac{\partial^2}{\partial y^2}UX(y,z)\right)-2c_{33}\left(\frac{\partial^2}{\partial z^2}UX(y,z)\right)\Bigg)\left(\left(\frac{1}{2}h+H\right)^3-\frac{1}{8}h^3\right)+$$
$$+\frac{1}{2}\left(-\frac{2c_{13}e_{31}\left(\frac{\partial}{\partial z}\Phi(y,z)\right)}{c_{11}}+2e_{33}\left(\frac{\partial}{\partial z}\Phi(y,z)\right)\right)\left(\left(\frac{1}{2}h+H\right)^2-\frac{1}{4}h^2\right).$$

$$M_{23}=-\frac{1}{6}\mu\left(\frac{\partial^2}{\partial z\partial y}UX(y,z)\right)h^3-\frac{4}{3}\left(\frac{\partial^2}{\partial z\partial y}UX(y,z)\right)c_{44}\left(\left(\frac{1}{2}h+H\right)^3-\frac{1}{8}h^3\right)+$$
$$+e_{15}\left(\frac{\partial}{\partial y}\Phi(y,z)\right)\left(\left(\frac{1}{2}h+H\right)^2-\frac{1}{4}h^2\right).$$

$$Q_2=\frac{1}{6}\mu\left(\frac{\partial^3}{\partial z^2\partial y}UX(y,z)\right)h^3+\frac{4}{3}\left(\frac{\partial^3}{\partial z^2\partial y}UX(y,z)\right)c_{44}\left(\left(\frac{1}{2}h+H\right)^3-\frac{1}{8}h^3\right)-$$
$$-e_{15}\left(\frac{\partial^2}{\partial z\partial y}\Phi(y,z)\right)\left(\left(\frac{1}{2}h+H\right)^2-\frac{1}{4}h^2\right)-\frac{1}{24}\left(-2(\lambda+2\mu)\left(\frac{\partial^3}{\partial y^3}UX(y,z)\right)-\right.$$
$$-\frac{1}{\lambda+2\mu}\left(2\lambda\left(-\left(\frac{\partial^3}{\partial y^3}UX(y,z)\right)\lambda-\lambda\left(\frac{\partial^3}{\partial z^2\partial y}UX(y,z)\right)\right)\right)-2\lambda\left(\frac{\partial^3}{\partial z^2\partial y}UX(y,z)\right)\Bigg)h^3-$$
$$-\frac{1}{3}\left(-\frac{1}{c_{11}}\left(2c_{12}\left(-\left(\frac{\partial^3}{\partial y^3}UX(y,z)\right)c_{12}-c_{13}\left(\frac{\partial^3}{\partial z^2\partial y}UX(y,z)\right)\right)\right)-\right.$$
$$-2c_{13}\left(\frac{\partial^3}{\partial z^2\partial y}UX(y,z)\right)-2c_{11}\left(\frac{\partial^3}{\partial y^3}UX(y,z)\right)\Bigg)\left(\left(\frac{1}{2}h+H\right)^3-\frac{1}{8}h^3\right)-$$
$$-\frac{1}{2}\left(2e_{31}\left(\frac{\partial^2}{\partial z\partial y}\Phi(y,z)\right)-\frac{2c_{12}e_{31}\left(\frac{\partial^2}{\partial z\partial y}\Phi(y,z)\right)}{c_{11}}\right)\left(\left(\frac{1}{2}h=H\right)^2-\frac{1}{4}h^2\right).$$

$$Q_3 = -\frac{1}{24}\left(-\frac{1}{\lambda+2\mu}\left(2\lambda\left(-\left(\frac{\partial^3}{\partial z\partial y^2}UX(y,z)\right)\lambda-\lambda\left(\frac{\partial^3}{\partial z^3}UX(y,z)\right)\right)\right)-\right.$$
$$\left.-2\left(\frac{\partial^3}{\partial z\partial y^2}UX(y,z)\right)\lambda-2(\lambda+2\mu)\left(\frac{\partial^3}{\partial z^3}UX(y,z)\right)\right)h^3-$$
$$-\frac{1}{3}\left(-\frac{1}{c_{11}}\left(2c_{13}\left(-\left(\frac{\partial^3}{\partial z\partial y^2}UX(y,z)\right)c_{12}-c_{13}\left(\frac{\partial^3}{\partial z^3}UX(y,z)\right)\right)\right)-\right.$$
$$\left.-2c_{13}\left(\frac{\partial^3}{\partial z\partial y^2}UX(y,z)\right)-2c_{33}\left(\frac{\partial^3}{\partial z^3}UX(y,z)\right)\right)\left(\left(\frac{1}{2}h+H\right)^3-\frac{1}{8}h^3\right)-$$
$$-\frac{1}{2}\left(-\frac{2c_{13}e_{31}\left(\frac{\partial^2}{\partial z^2}\Phi(y,z)\right)}{c_{11}}+2e_{33}\left(\frac{\partial^2}{\partial z^2}\Phi(y,z)\right)\right)\left(\left(\frac{1}{2}h+H\right)^2-\frac{1}{4}h^2\right)+$$
$$+\frac{1}{6}\mu\left(\frac{\partial^3}{\partial z\partial y^2}UX(y,z)\right)h^3+\frac{4}{3}\left(\frac{\partial^3}{\partial z\partial y^2}UX(y,z)\right)c_{44}\left(\left(\frac{1}{2}h+H\right)^3-\frac{1}{8}h^3\right)-$$
$$-e_{15}\left(\frac{\partial^2}{\partial y^2}\Phi(y,z)\right)\left(\left(\frac{1}{2}h+H\right)^2-\frac{1}{4}h^2\right).$$

For the case of a panel consisting of two internal layers (Fig. 2 and 3 *a*), the second equation of system (7) is reduced to the form:

$$\frac{1}{4}\left(\frac{c_{13}e_{31}}{c_{11}}-e_{33}\right)h\left(\frac{d}{dz}UX(z)\right)+\left(-\frac{e_{31}^2}{c_{11}}-g_{33}\right)\Phi(z)+C_1z+C_2=0, \tag{8}$$

from which the electric potential is expressed:

$$\Phi(z)=\frac{1}{4}\frac{\left(-c_{11}e_{33}h+c_{13}e_{31}h\right)\left(\frac{d}{dz}UX(z)\right)}{g_{33}c_{11}+e_{31}^2}+\frac{1}{4}\frac{4C_1c_{11}z+4C_2c_{11}}{g_{33}c_{11}+e_{31}^2}. \tag{9}$$

After this, the first equation (7) is reduced to the form:

$$\left(-\frac{1}{24}\left(\frac{2c_{13}^2}{c_{11}}-2c_{33}\right)h^3-\frac{1}{32}\frac{1}{c_{11}g_{33}+e_{31}^2}\left(\left(-\frac{2c_{13}e_{31}}{c_{11}}+2e_{33}\right)h^2\left(-c_{11}e_{33}h+c_{13}e_{31}h\right)\right)\right)\times$$
$$\times\left(\frac{d^4}{dz^4}UX(z)\right)-\omega^2\rho hUX(z)-p(z)=0. \tag{10}$$

System of equations (7) is generally solved numerically, whereas equation (10) can be solved analytically.

Validation of the proposed method for adequacy based on a comparison of the results with calculations in the ACELAN package

To test the applicability of the proposed applied theory, two problems for a two-layer panel are solved: determining the first resonant frequency of the bending mode, and the problem of steady-state vibrations at a frequency of 200 Hz under a uniformly distributed load on the upper plane of the plate with an amplitude of 1000 Pa. The plate length is 0.1 m, the thickness of each layer is 0.0025 m, and the material is PZT-4. The plate is fixed at the left end and hinged at the right (Fig. 3 *a*).

The self-resonant frequency of the first bending mode (Fig. 4) in the ACELAN package calculation is 1348.68 Hz, while the applied theory calculation is 1360 Hz, i.e., the error is 0.8%.

The forced vibration calculation has yielded the following results: Figure 4 shows the distribution of vertical displacements on the deformed plate.

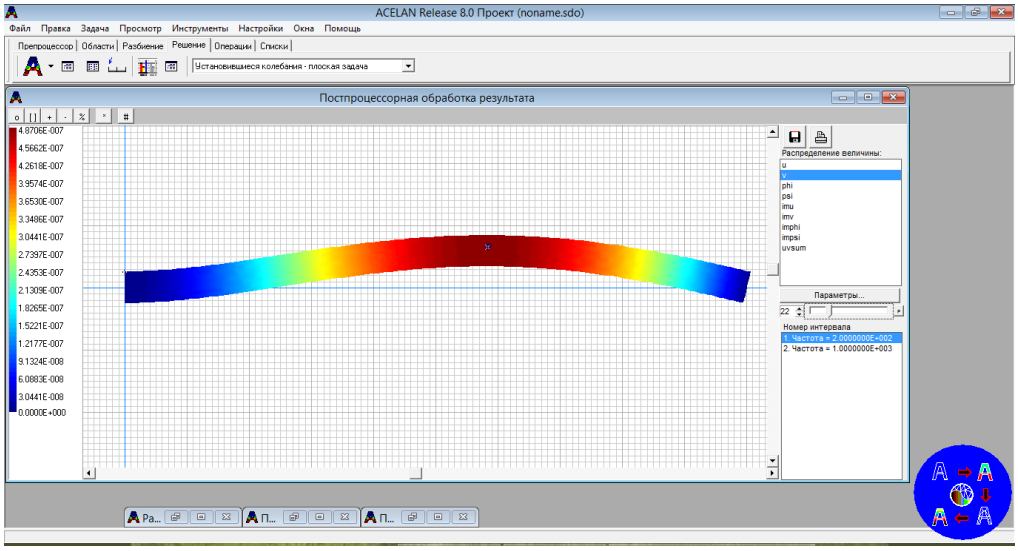

Fig. 4. Distribution of vertical displacement at a frequency of 200 Hz

Figure 5 shows the graphs of the deflection of the midsurface of the plate.

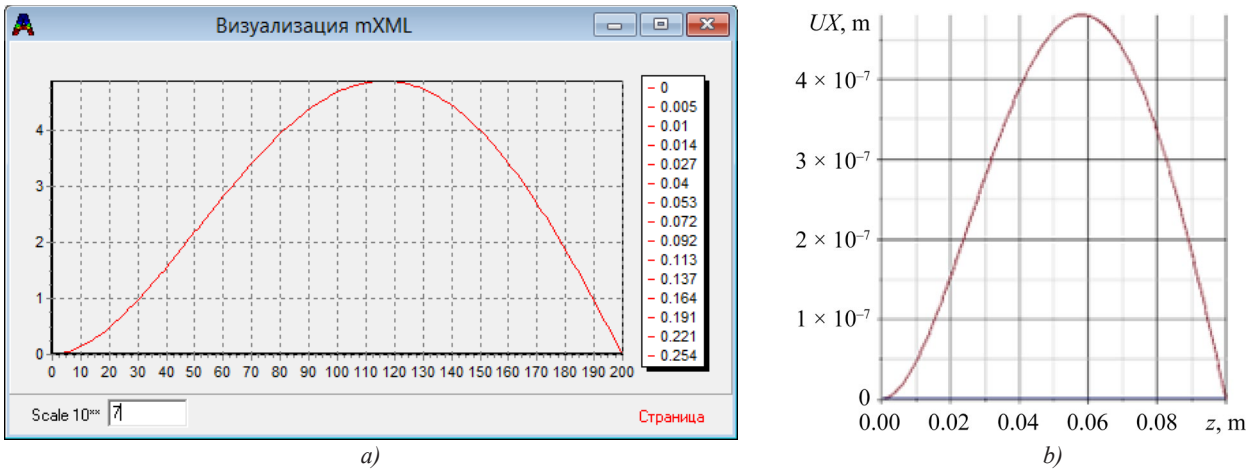

a) *b)*

Fig. 5. Plate deflection: *a* — ACELAN; *b* — applied theory of equation (8)–(10)

Figures 6 and 7 present similar results for horizontal displacement, and Figures 8 and 9 show them for electric potential.

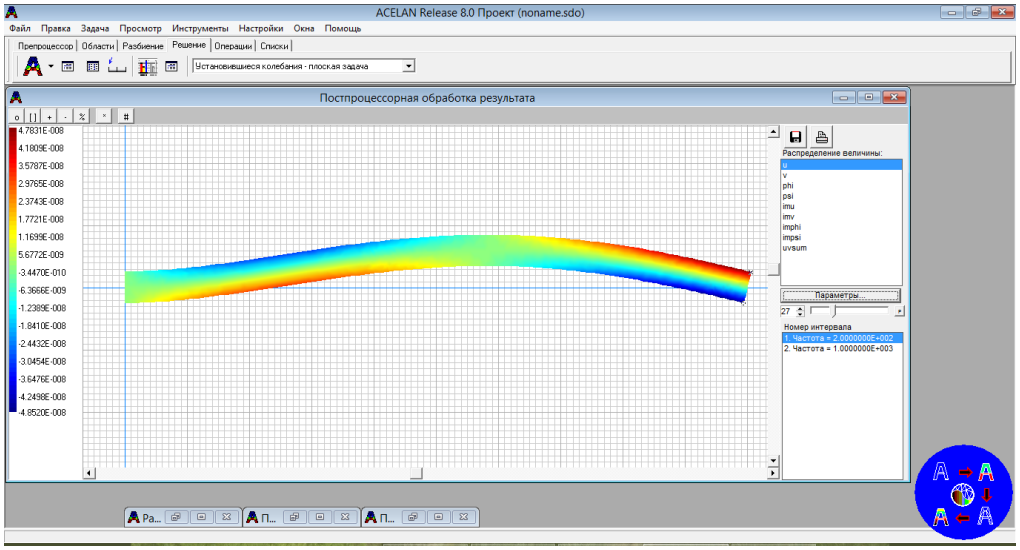

Fig. 6. Distribution of horizontal displacement at a frequency of 200 Hz

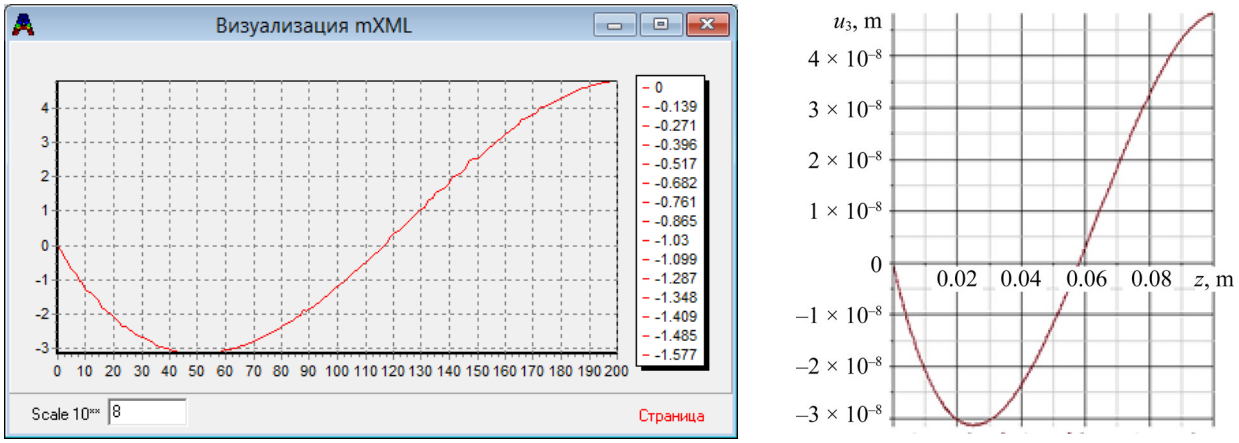

a) *b)*

Fig. 7. Horizontal displacement on the plate surface:
a — ACELAN; *b* — applied theory

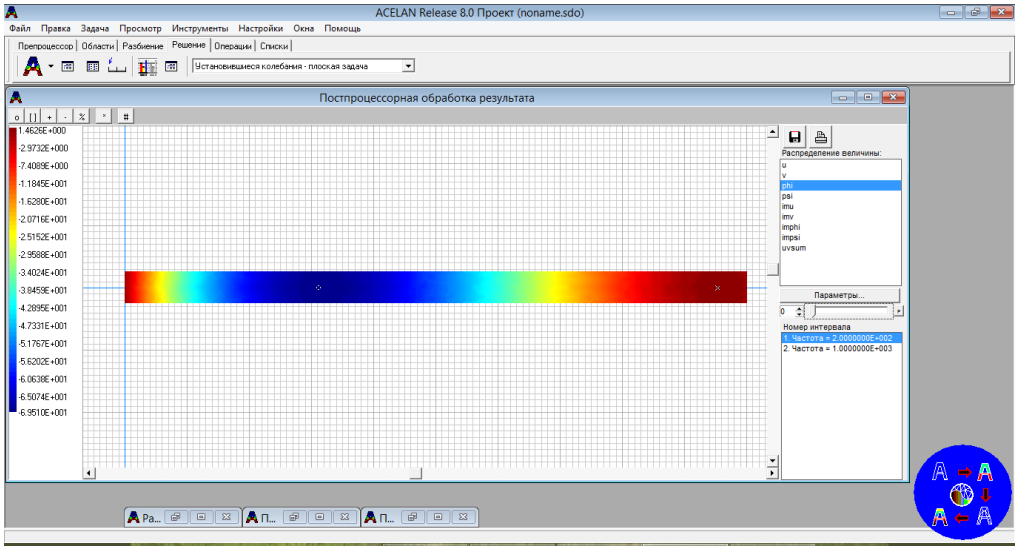

Fig. 8. Distribution of electric potential at a frequency of 200 Hz

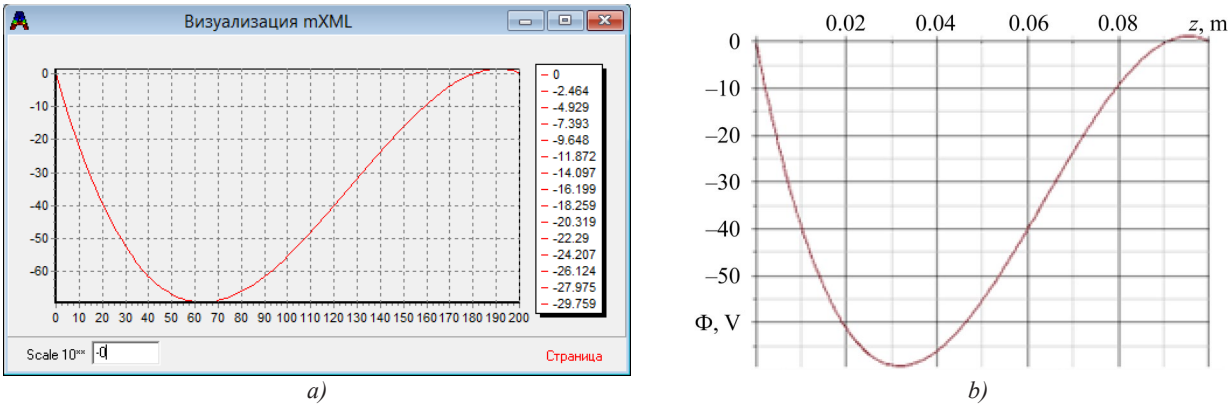

a) *b)*

Fig. 9. Electric potential in the plate: *a* — ACELAN; *b* — applied theory

Discussion. The key result of this research is an applied two-dimensional theory and the demonstration of a high degree of agreement between the solutions obtained from it and the simulation data in the ACELAN finite element package. The deviation in the calculation of the first resonant frequency is only 0.8%, which is more than sufficient for engineering applications. Visual and quantitative comparison of the graphs of deflections, horizontal displacements, and the distribution of electric potential under forced vibrations also shows their almost complete agreement (Figs. 5, 7, 9), which confirms the proposed model adequacy in the frequency range under consideration.

The primary application of the developed theory is the low-frequency range. The structural geometry is thin plates. The range of variation of the material parameters of the layers is relatively small. For wider property ranges, when constructing the applied theory, it will be necessary to take into account the broken normal and use a higher order of approximation for the characteristics of the mechanical and electrical fields across the thickness of the structure.

The proposed theory eliminates resource-intensive 3D modeling at the preliminary design stages. The practical significance of the results is in the creation of an efficient and fast tool for engineers and researchers: instead of time-consuming calculations in "heavy" CAE packages, analytical or numerically analytical solutions of equations (7)–(10) can be used to quickly evaluate dynamic characteristics, conduct parametric studies, and optimize the designs of piezoelectric transducers, sensors, and energy harvesting devices.

Conclusion. Within the framework of the study, the problem of constructing and validating an applied two-dimensional theory for calculating the transverse vibrations of layered plates made of a 1–3 piezocomposite and porous piezoactive 3–0 and 3–3 elements is successfully solved.

A mathematical model based on the Kirchhoff-Love hypothesis is developed to describe the dynamic behavior of a thin layered electroelastic plate with opposing longitudinal polarization of the layers.

A system of differential equations is derived, which, for the particular case of a two-layer panel, reduces to a single equation that admits an analytical solution.

The proposed theory is validated through comparing its results with numerical simulation data in the ACELAN finite element package. The error in determining the first resonant frequency does not exceed 0.8%.

The adequacy of the theory in calculating forced vibrations is proven: the profiles of vertical and horizontal displacements, as well as the distribution of electric potential, calculated using the applied theory, almost completely coincides with the results of finite element modeling.

Thus, it is shown that the proposed two-dimensional theory is an effective and computationally efficient tool for the analysis and design of thin-walled structures made of piezocomposite materials, which allows for a significant acceleration of development compared with the use of universal finite element packages.

Prospects for further research are related to the development of the next level of homogenization — the transition to the efficient properties of a 2–2 composite with subsequent consideration of a two-layer plate — as well as with more complex approximations of mechanical and electrical fields, including consideration of edge effects. However, when complicating the model, it should be remembered that the primary practical purpose of such theories is the calculation of the output integral characteristics of devices: resonant frequencies, output electrical potential, power, etc.

References

1. Newnham RE, Skinner DP, Cross LE. Connectivity and Piezoelectric-Pyroelectric Composites. *Materials Research Bulletin.* 1978;13(5):525–536. https://doi.org/10.1016/0025-5408(78)90161-7

2. Avellaneda M, Swart PJ. Calculating the Performance of 1–3 Piezocomposite for Hydrophone Applications: An Effective Medium Approach. *The Journal of the Acoustical Society of America.* 1998;103(3):1449–1467. http://doi.org/10.1121/1.421306

3. Berger H, Kari S, Gabbert U, Rodriguez-Ramos R, Guinovart-Diaz R, Otero JA, et al. An Analytical and Numerical Approach for Calculating Effective Material Coefficients of Piezoelectric Fiber Composites. *International Journal* of *Solids* and *Structures*. 2005;42(21–22):5692–5714. http://doi.org/10.1016/j.ijsolstr.2005.03.016

4. Bravo-Castillero J, Guinovart-Díaz R, Sabina FJ, Rodríguez-Ramos R. Closed-Form Expressions for the Effective Coefficients of a Fiber-reinforced Composite with Transversely Isotropic Constituents – II. Piezoelectric and Square Symmetry. *Mechanics of Materials.* 2001;33(4):237–248. http://doi.org/10.1016/S0167-6636(00)00060-0

5. Castillero JB, Diaz RG, Hernandez JAO, Ramos RR. Electromechanical Properties of Continuous Fibre-reinforced Piezoelectric Composites. *Mechanics of Composite Materials.* 1997;33:475–482. https://doi.org/10.1007/BF02256903

6. Gibiansky LV, Torquato S. On the Use of Homogenization Theory to Design Optimal Piezocomposites for Hydrophone Applications. *Journal of the Mechanics and Physics of Solids.* 1997;45(5):689–708. https://doi.org/10.1016/S0022-5096(96)00106-8

7. Guinovart-Dıaz R, Bravo-Castillero J, Rodrıguez-Ramos R, Sabina FJ, Martınez-Rosado R. Overall Properties of Piezocomposite Materials 1–3. *Materials Letters.* 2001;48(2):93–98. http://doi.org/10.1016/S0167-577X(00)00285-8

8. Levin VM, Sabina FJ, Bravo-Castillero J, Guinovart-Díaz R, Rodríguez-Ramos R, Valdiviezo-Mijangos OC. Analysis of Effective Properties of Electroelastic Composites Using the Self-Consistent and Asymptotic Homogenization Methods. *International Journal of Engineering Science.* 2008;46(8):818–834. http://doi.org/10.1016/j.ijengsci.2008.01.017

9. Sevostianov I, Levin V, Kachanov M. On the Modeling and Design of Piezocomposites with Prescribed Properties. *Archive of Applied Mechanics.* 2001;71:733–747. http://doi.org/10.1007/s004190100181

10. Pramanik R, Arockiarajan A. Effective Properties and Nonlinearities in 1–3 Piezocomposites: A Comprehensive Review. *Smart Materials and Structures*. 2019;28(10):103001. https://doi.org/10.1088/1361-665X/ab350a

11. Aloui R, Larbi W, Chouchane M. Uncertainty Quantification and Global Sensitivity Analysis of Piezoelectric Energy Harvesting Using Macro Fiber Composites. *Smart Materials* and *Structures*. 2020;29(9):095014. http://doi.org/10.1088/1361-665X/ab9f12

12. Yu Shi, Hallett SR, Meiling Zhu. Energy Harvesting Behaviour for Aircraft Composites Structures Using Macro-Fibre Composite: Part I – Integration and Experiment. *Composite Structures.* 2017;160:1279–1286. https://doi.org/10.1016/j.compstruct.2016.11.037

13. Hyun J Song, Young-Tai Choi, Wereley NM, Purekar A. Comparison of Monolithic and Composite Piezoelectric Material–based Energy Harvesting Devices. *Journal of Intelligent Material Systems and Structures.* 2014;25(14):1825–1837. http://doi.org/10.1177/1045389X14530592

14. Swallow LM, Luo JK, Siores E, Patel I, Dodds D. A Piezoelectric Fibre Composite Based Energy Harvesting Device for Potential Wearable Applications. *Smart Materials* and *Structures*. 2008;17(2):025017. http://doi.org/10.1088/0964-1726/17/2/025017

15. Della CN, Dongwei Shu. Performance of 1–3 Piezoelectric Composites with Porous Piezoelectric Matrix. *Applied Physics Letters*. 2013;103:132905. https://doi.org/10.1063/1.4822109

16. Della ChN, Dongwei Shu. The Performance of 1–3 Piezoelectric Composites with a Porous Non-piezoelectric Matrix. *Acta Materialia.* 2008;56(4):754–761. https://doi.org/10.1016/j.actamat.2007.10.022

17. Gibiansky LV, Torquato S. On the Use of Homogenization Theory to Design Optimal Piezocomposites for Hydrophone Applications. *Journal of the Mechanics and Physics of Solids.* 1997;45(5):689–708. https://doi.org/10.1016/S0022-5096(96)00106-8

18. Sigmund O, Torquato S, Aksay IA. On the Design of 1–3 Piezocomposites Using Topology Optimization. *Journal of Materials Research.* 1998;13:1038–1048. https://doi.org/10.1557/JMR.1998.0145

19. Sladek J, Novak P, Bishay PL, Sladek V. Effective Properties of Cement-based Porous Piezoelectric Ceramic Composites. *Construction and Building Materials.* 2018;190:1208–1214. https://doi.org/10.1016/j.conbuildmat.2018.09.127

20. Nasedkin AV, Oganesyan PA, Soloviev AN. Analysis of Rosen Type Energy Harvesting Devices from Porous Piezoceramics with Great Longitudinal Piezomodulus. *Zeitschrift für Angewandte Mathematik und Mechanik.* 2021;101(3):e202000129. http://doi.org/10.1002/zamm.202000129

21. Roscow JI, Lewis RWC, Taylor J, Bowen CR. Modelling and Fabrication of Porous Sandwich Layer Barium Titanate with Improved Piezoelectric Energy Harvesting Figures of Merit. *Acta Materialia*. 2017;128:207–217. http://doi.org/10.1016/j.actamat.2017.02.029

22. Rybyanets AN, Naumenko AA, Lugovaya MA, Shvetsova NA. Electric Power Generations from PZT Composite and Porous Ceramics for Energy Harvesting Devices. *Ferroelectrics.* 2015;484(1):95–100. https://doi.org/10.1080/00150193.2015.1060065

23. Mingyang Yan, Zhida Xiao, Jingjing Ye, Xi Yuan, Zihe Li, Chris Bowen, et al. Porous Ferroelectric Materials for Energy Technologies: Current Status and Future Perspectives. *Energy & Environmental Science.* 2021;14(12):6158–6190. http://doi.org/10.1039/d1ee03025f

24. Do TB, Nasedkin A, Oganesyan P, Soloviev A. Multilevel Modeling of 1-3 Piezoelectric Energy Harvester Based on Porous Piezoceramics. *Journal of Applied and Computational Mechanics.* 2023;9(3):763–774. http://doi.org/10.22055/jacm.2023.42264.3900

25. Belokon' AV, Nasedkin AV, Solov'ev AN. New Schemes for the Finite-Element Dynamic Analysis of Piezoelectric Devices. *Journal of Applied Mathematics and Mechanics.* 2002;66(3):481–490. http://doi.org/10.1016/S0021-8928(02)00058-8

26. Oganesyan PA, Shtein OO. Implementation of Basic Operations for Sparse Matrices when Solving a Generalized Eigenvalue Problem in the ACELAN-COMPOS Complex. *Advanced Engineering Research (Rostov-on-Don).* 2023;23(2):121–129. https://doi.org/10.23947/2687-1653-2023-23-2-121-129

About the Authors:

Arkadiy N. Soloviev, Dr.Sci. (Phys.-Math.), Professor of the Mathematics and Physics Department, Crimean Engineering and Pedagogical University named after Fevzi Yakubov (8, Uchebnyi Lane, Simferopol, 295015, Republic of Crimea), Chief Researcher of the Research and Production Center for Engineering Technologies, Crimean Engineering and Pedagogical University named after Fevzi Yakubov (8, Uchebnyi Lane, Simferopol, 295015, Republic of Crimea), SPIN-code, ORCID, ScopusID, ResearcherID, solovievarc@gmail.com

Maria S. Germanchuk, Cand.Sci. (Phys.-Math.), Associate Professor of the Informatics Department, V.I. Vernadsky Crimean Federal University (4, Vernadskogo Prospect, Simferopol, 295007, Republic of Crimea), Associate Professor of the Mathematics and Physics Department, Crimean Engineering and Pedagogical University named after Fevzi Yakubov (8, Uchebnyi Lane, Simferopol, 295015, Republic of Crimea**)**, SPIN-code, ORCID, ScopusID, ResearcherID, m.german4uk@yandex.ru

Pavel A. Oganesyan, Cand.Sci. (Phys.-Math.), Associate Professor of the Mathematical Modeling Department, Vorovich Institute for Mathematics, Mechanics, and Computer Science, Southern Federal University (8a, Milchakova Str., Rostov-on-Don, 344058, Russian Federation), SPIN-code, ORCID, ScopusID, poganesyan@sfedu.ru

Claimed Contributorship:

AN Soloviev: conceptualization, supervision, funding acquisition, methodology, writing – original draft preparation, writing – review & editing.

MS Germanchuk: formal analysis, validation, visualization.

PA Oganesyan: investigation, software, funding acquisition, visualization.

***Conflict of Interest Statement*: the authors declare no conflict of interest.**

All authors have read and approved the final version of the manuscript.

Об авторах:

Аркадий Николаевич Соловьев, доктор физико-математических наук, профессор кафедры «Математика и физика» Крымского инженерно-педагогического университета имени Февзи Якубова (295015, Республика Крым, г. Симферополь, пер. Учебный, д. 8), главный научный сотрудник Научно-производственного центра инжиниринговых технологий Крымского инженерно-педагогического университета имени Февзи Якубова (295015, Республика Крым, г. Симферополь, пер. Учебный, д. 8), SPIN-код, ORCID, ScopusID, ResearcherID, solovievarc@gmail.com

Мария Сергеевна Германчук, кандидат физико-математических наук, доцент кафедры «Информатика» Крымского федерального университета им. В.И. Вернадского, (295007, Республика Крым, г. Симферополь, пр. Вернадского, д. 4), SPIN-код, ORCID, ScopusID, ResearcherID, m.german4uk@yandex.ru

Павел Артурович Оганесян, кандидат физико-математических наук, доцент кафедры «Математическое моделирование» Южного федерального университета. (344058 г. Ростов-на-Дону, ул. Мильчакова 8а, ИММиК), SPIN-код, ORCID, ScopusID, poganesyan@sfedu.ru

Заявленный вклад авторов:

А.Н. Соловьев: разработка концепции, научное руководство, получение финансирования, разработка методологии, написание черновика рукописи, написание рукописи — внесение замечаний и исправлений.

М.С. Германчук: формальный анализ, валидация результатов, создание и подготовка рукописи, визуализация.

П.А. Оганесян: проведение исследования, разработка программного обеспечения, получение финансирования, визуализация.

***Конфликт интересов:* авторы заявляют об отсутствии конфликта интересов.**

Все авторы прочитали и одобрили окончательный вариант рукописи.

Received / Поступила в редакцию 01.12.2025
Reviewed / Поступила после рецензирования 18.12.2025
Accepted / Принята к публикации 12.01.2026

MACHINE BUILDING AND MACHINE SCIENCE
МАШИНОСТРОЕНИЕ И МАШИНОВЕДЕНИЕ

UDC 673.7
https://doi.org/10.23947/2687-1653-2026-26-1-2199

Original Empirical Research

Creating Insulation Materials from Unsaturated Polyester and Recycled Tire Rubber

Imad R. Antypas ✉, **Tatyana P. Savostina**
Don State Technical University, Rostov-on-Don, Russian Federation
✉ Imad.antypas@mail.ru

EDN: RAQDMY

Abstract

Introduction. The disposal of automotive tires typically involves landfilling, stockpiling, or incineration. As a result, this causes soil and atmospheric pollution. Scientists have long and actively discussed the recycling of tire rubber as one of the approaches to solving environmental problems. It is known that the use of rubber crumb in composites can reduce their weight and thermal conductivity. However, materials based on unsaturated polyester containing rubber waste have been insufficiently studied. There are contradictions in the assessment of their mechanical and thermal insulation properties. Moreover, the optimal rubber content in the composite is unknown. The presented work addresses these gaps. The research objectives include the development and analysis of new materials based on unsaturated polyester with justification for the required proportion of rubber waste.

Materials and Methods. During the processing of tire rubber, a multistage grinding process was carried out, followed by magnetic and air separation. A powder with a density of 500 kg/m³ was obtained. The minimum particle size was 0.1 mm, and the maximum was up to 1 mm. The composite matrix was unsaturated polyester with a density of 1160 kg/m³. To fabricate the specimens, 0, 10, 20, 30, 40, and 50% rubber filler were added to it. Stable geometry was achieved through curing at room temperature and subsequent mechanical processing. For each composition, three specimens with an area of 0.021 m² and a thickness of 0.01 m were produced.

Results. The dependence of density, water absorption, and thermal conductivity of the samples on the volume of recycled tire rubber was shown. As its proportion increased, a noticeable decrease in density was recorded: at 0% — 1160 kg/m³; at 10% — 1074.3; at 20% — 1037.2; at 30% — 1017.8; at 40% — 963.7; at 50% — 905. Water absorption dynamics were determined by the weight of the samples after immersion in water. It took more than 8 hours for changes (even minor ones) to occur. The indicator in percentage terms increased from 0.024% to 0.47%, meaning the absolute maximum was <0.5%. As the rubber content increased, thermal conductivity decreased. The value for pure polyester was 0.254854 W/(m·K); for the composite with 10% rubber — 0.2510574; with 20% — 0.245156; with 30% — 0.238484; with 40% — 0.223062; with 50% — 0.207039. All samples withstood a load of 1300 kN.

Discussion. The incorporation of 50% rubber into unsaturated polyester results in a 22% reduction in sample density and a 19% decrease in thermal conductivity, with water absorption remaining under 0.5%. These properties suggest the suitability of the composite as an efficient insulation material, even in environments with elevated humidity. Its high compressive strength (>61.83 MPa) allows for its use in structures subjected to significant loads. Varying the rubber content will provide an optimal balance between mechanical properties and moisture resistance.

Conclusion. This work presents an approach for the sustainable recycling of tires to produce effective insulation materials. Promising directions for future study include investigating composites with larger rubber particles (>1 mm), evaluating their acoustic insulation properties, and assessing their fire resistance and chemical stability.

Keywords: tire recycling, unsaturated polyester, properties of polyester-rubber composites, low-absorption materials

Acknowledgements. The authors would like to thank the team of the Composite Materials Laboratory, Faculty of Mechanical Engineering, Aleppo University, for their technical assistance in conducting the experiments.

For Citation. Antypas IR, Savostina TP. Creating Insulation Materials from Unsaturated Polyester and Recycled Tire Rubber. *Advanced Engineering Research* (*Rostov-on-Don*). 2026;26(1):2199. https://doi.org/10.23947/2687-1653-2026-26-1-2199

Оригинальное эмпирическое исследование

Создание изоляционных материалов из ненасыщенного полиэфира и переработанной шинной резины

И.Р. Антибас ✉, **Т.П. Савостина**
Донской государственный технический университет, г. Ростов-на-Дону, Российская Федерация
✉ Imad.antypas@mail.ru

Аннотация

Введение. Утилизация автомобильных шин обычно предполагает их складирование, захоронение или сжигание. Как следствие, загрязняются почва и атмосфера. Ученые давно и активно обсуждают переработку шинной резины как один из подходов к решению экологических проблем. Известно, что использование резиновой крошки в композитах позволяет снизить их массу и теплопроводность. Однако мало изучены материалы с резиноотходами на основе ненасыщенного полиэфира. Есть противоречия в оценке их механических и теплоизоляционных свойств. Кроме того, неизвестно оптимальное содержание резины в композите. Представленная работа восполняет эти пробелы. Цели исследования: создание и анализ новых материалов из ненасыщенного полиэфира с обоснованием необходимой доли резиноотходов.

Материалы и методы. При обработке шинной резины провели многоступенчатое измельчение, магнитную и воздушную сепарацию. Получили порошок плотностью 500 кг/м^3. Минимальная фракция — 0,1 мм, максимальная — до 1 мм. База композита — ненасыщенный полиэфир плотностью 1160 кг/м^3. Для изготовления образцов к нему добавляли 0, 10, 20, 30, 40 и 50 % резинового наполнителя. Стабильной геометрии добивались отверждением при комнатной температуре и механической обработкой. Для каждого состава изготовили по три образца площадью 0,021 м^2 и толщиной 0,01 м.

Результаты исследования. Показана зависимость плотности, водопоглощения и теплопроводности образцов от объема переработанной шинной резины. С увеличением ее доли фиксируется заметное снижение плотности: при 0 % — 1160 кг/м^3; при 10 % — 1074,3; при 20 % — 1037,2; при 30 % — 1017,8; при 40 % — 963,7; при 50 % — 905. Динамику водопоглощения определяли по весу образцов после пребывания в воде. Для изменений (причем несущественных) потребовалось более 8 часов. Показатель в процентном отношении растет с 0,024 до 0,47 %, то есть абсолютный максимум <0,5 %. С увеличением доли резины снижается теплопроводность. Показатель для чистого полиэфира — 0,254854 Вт/(м · К); для композита с 10 % резины — 0,2510574; с 20 % — 0,245156; с 30 % — 0,238484; с 40 % — 0,223,062; с 50 % — 0,207039. Все образцы выдержали нагрузку 1300 кН.

Обсуждение. При добавлении в ненасыщенный полиэфир 50 % резины плотность образца снижается на 22 %, коэффициент теплопроводности — на 19 %, а водопоглощение не превышает 0,5 %. Значит, композит будет хорошим изолирующим материалом даже при повышенной влажности. Высокая прочность на сжатие (>61,83 МПа) позволяет использовать его в конструкциях, испытывающих серьезные нагрузки. Варьирование содержания резины даст оптимальный баланс механических свойств и влагостойкости.

Заключение. Предложено решение для экологичной утилизации шин и создания качественных изоляционных материалов. В перспективе можно изучить более крупные частицы резины (от 1 мм) в композите, звукоизоляционный потенциал таких материалов, их стойкость к огню и химическим веществам.

Ключевые слова: переработка автомобильных шин, ненасыщенный полиэфир, свойства композита из полиэфира и резины, материалы с низким водопоглощением

Благодарности. Авторы выражают благодарность коллективу лаборатории композиционных материалов механического факультета Университета Алеппо за техническую поддержку при проведении экспериментов.

Для цитирования. Антибас И.Р., Савостина Т.П. Создание изоляционных материалов из ненасыщенного полиэфира и переработанной шинной резины. *Advanced Engineering Research* (*Rostov-on-Don*). 2026;26(1):2199. https://doi.org/10.23947/2687-1653-2026-26-1-2199

Introduction. The accumulation of automobile tire waste is a global environmental problem. According to [1], approximately 1.5 billion tires are produced worldwide each year, with over 17 million tons being disposed [1]. It is expected that by 2030, the number of end-of-life tires will reach 1.2 billion units. Currently, a significant portion of discarded tires is sent to landfills. As a result:

– the risks of fires and environmental pollution increase;

– the shortage of cheap insulation materials for construction is exacerbated.

It is known that about 40% of global energy consumption is attributable to the construction sector [2]. The industry has a critical need for effective thermal insulation materials to improve the energy efficiency of buildings. Therefore, the development of innovative composites is essential both for enhancing the recycling of rubber waste and for creating much-needed thermal insulation [2].

Unsaturated polyester was selected as the composite matrix due to its thermosetting properties. When mixed with a curing agent, unsaturated polyester forms a rigid polymer structure, allowing the desired shape and porosity to be imparted to the composition. Rubber waste, in turn, serves as an effective dispersed filler. Incorporating rubber crumb into the composite substantially lowers its thermal conductivity. This reduction is attributed to two factors: firstly, the intrinsically low thermal conductivity of rubber (~0.1–0.2 W/(m·K)), and secondly, its particles, dispersed in the polymer matrix, create additional air cavities and a complex network of so-called “thermal bridges” [3].

There are publications on the use of tire rubber and other industrial waste to create materials with high sound-absorbing properties [4]. In [5], the sound transmission loss of three composite panels was measured: made from waste tire rubber, composite wood board, and particleboard. The conditions under which the use of tire rubber improves sound insulation have been determined.

The University of Wisconsin-Milwaukee studied the use of rubber concrete in railway construction [6]. The authors [6] compared the performance of a rubber suspension to a standard mix and revealed its higher strength and ductility. The research also explored the potential of using this waste-derived material for trench backfilling and filling voids in bridge abutments.

In [7], unsaturated polyester composites containing 5–40% recycled rubber glove filler are investigated. It has been found that the additive increases the impact strength of the compound, but reduces tensile and flexural strength. This is explained by weak rubber adhesion and the formation of pores at high levels.

Study [8] shows how the addition of rubber waste to unsaturated polyester reduces the flexural strength of the base polymer material. The reason is the presence of contaminant particles, which impair the mechanical properties of the mixture. It is further revealed that pre-treatment of the rubber waste enhances material stiffness, while pre-heating the rubber prior to incorporation improves the flexural strength of the resulting composite.

In [9], it is demonstrated that incorporating rubber waste particles of varying sizes into unsaturated polyester yields an insulating material with reduced density, thermal conductivity, and water absorption.

The mechanical properties of unsaturated polyester with different rubber waste loadings are reported in [10]. For example, tensile strength ranges from 1.25 to 22.8 MPa, and compressive strength ranges from 8.25 to 79.5 MPa. Thus, the material described is suitable for insulation applications where high mechanical performance is not required.

Study [11] investigated the effect of incorporating 2–4 mm rubber crumb particles on the compressive strength and elasticity of the composite. Both properties improved, particularly following pre-treatment of the rubber waste with synthetic resins. Under these conditions, compressive strength increased by 12% and elasticity by 40%.

The addition of rubber reduces tensile and flexural strength [10], which is caused by pore formation and weak adhesion at the polymer–rubber interface. However, it simultaneously increases impact toughness [7] and elasticity [11].

The negative impact on strength can be reduced. For this purpose, pre-treating the rubber is recommended. Scientists suggest techniques such as cleaning, heating, or resin treatment. All of these improve adhesion and partially restore the mechanical properties of the compound [11].

Despite active and multifaceted interest from researchers in the topic under consideration, some key questions remain unresolved. It is still unknown, for example, how the properties of composites based on unsaturated polyester depend on the concentration and particle size distribution of rubber waste. This concerns parameters such as thermal conductivity, density, water absorption, and flexural and compressive strength.

No optimization criteria have been developed for the composition required to produce an efficient thermal insulation material for construction. In this case, it is important to balance processability, low thermal conductivity, and mechanical properties suitable for the installation and operation of the structure.

The targeted development of such materials requires a deeper understanding of the processes occurring in the unsaturated polyester–rubber crumb system. It is necessary to examine in detail the formation of the porous structure and the mechanism behind the reduction in thermal conductivity. The presented scientific work aims to address this challenge. The research objectives include the creation and comprehensive study of new composites based on unsaturated polyester, with justification for the required proportion of rubber waste.

Materials and Methods. Polymer insulating composites were prepared through blending rubber waste and unsaturated polyester at different weight ratios. The experimental study was conducted in three consecutive stages.

1. Preparation of raw materials and equipment

This phase assessed the feasibility and efficiency of mechanical recycling of end-of-life tires for producing rubber powder with predefined characteristics. The study included an analysis of the processing steps, parametric monitoring at each stage, and final quality control of the resulting material.

In the raw material preparation phase, steel bead wires were first stripped from the tire sidewalls. Primary size reduction was performed using a shredder operating at 80 rpm for 2 minutes, producing particles in the 50–300 mm range. Subsequent grinding in a rotary crusher at 1500 rpm for 5 minutes further reduced the particle size to 10–50 mm.

A critical step in the preparation process involved separation of the ground material. Ferrous residues were extracted using drum magnetic separators operating at 25 rpm with a magnetic induction of 500 mT. Textile fibers were subsequently removed by means of vortex air classifiers operating at an airflow velocity of 15 m/s and a material feed angle of 30°.

The cleaned rubber feedstock was further processed in a roll granulator, yielding granules in the 1–10 mm size range. Subsequently, the material was subjected to fine milling in a ball mill operating at 45 rpm for 60 minutes to achieve a homogeneous powder.

The multistage grinding and separation process yielded a homogeneous rubber powder with a bulk density of 500 kg/m^3. Sieve analysis was conducted to verify its particle size distribution. The results confirmed that all particles were smaller than 1 mm (Table 1), meeting the specified maximum particle size. Notably, 85% of the particles were found to be below 0.37 mm, indicating a predominantly fine-grained fraction suitable for composite fabrication.

Table 1

Sieve Analysis Results for Rubber Powder

Sieve passage of powder, %	100	99.5	99	98	97	95	92	85	30	15	5
Sieve cell, mm	1.0	0.91	0.82	0.73	0.64	0.55	0.46	0.37	0.28	0.19	0.10

Unsaturated polyester resin supplied by SABIC (Saudi Arabia) served as the polymer matrix. The material, a pinkish transparent liquid with a characteristic pungent odor, cured at ambient temperature upon initiator addition. Its density, determined at 25±2°C, was found to be 1160 kg/m³.

Methyl ethyl ketone peroxide (MEKP) produced by Haihang Industry (China) was used as a polymerization initiator.

2. Specimen fabrication

Test specimens were prepared using silicone molds, which allowed for convenient demolding after curing. The mold cavity dimensions of 145 mm × 145 mm × 10 mm were selected to comply with ASTM D695 standard requirements while also matching the measurement capabilities of the available testing instrumentation.

The volumes of rubber waste in the specimens were 0, 10, 20, 30, 40 and 50%.

Following demolding, all specimens were surface-ground for dimensional stability and eliminating any surface irregularities.

For each composition (0, 10, 20, 30, 40, and 50 vol.% rubber waste), three replicate specimens were prepared and tested to ensure statistically reliable results.

3. Testing

In accordance with international standards, a series of physical, thermal, and mechanical tests were conducted at the Composite Materials Laboratory of the Faculty of Mechanical Engineering, University of Aleppo.

3.1. Physical tests

Specimen density was measured in accordance with ISO 1183-1:2019. The standardized procedure comprised four key steps. During the preparatory stage, appropriate equipment was selected and specimens were conditioned for testing. At the experimental stage, direct mass and volume measurements were conducted. Specimen mass was determined using a balance with a precision of 0.01 g.

Linear dimensions — length, width, and height — were measured using a hardened stainless steel digital caliper with a precision of 0.01 mm.

Specimen volume was determined from the geometric measurements. Density was calculated according to the formula: $\rho = m/V$, where m — specimen mass, V — its volume.

3.2. Water absorption test (ISO 62:2008)

Specimens were submerged in water for 24 hours, with weight measurements recorded at two-hour intervals. Water absorption was calculated from the formula:

$$WR\% = \frac{W - W_1}{W_1} \cdot 100,$$

where W — wet specimen mass after immersion, g; W_1 — dry specimen mass before immersion, g.

3.3. Thermal conductivity test (ISO 8301:1991)

Thermal conductivity measurements were performed using a DRX thermal conductivity analyzer (China). The instrument has a measurement range of 0.01 to 2 W/(m·K) and an accuracy of ±3%. Testing was carried out over a temperature range of 15–100°C, following the Chinese standard GB/T 10295-2008, which corresponds to ISO 8301:1991.

During testing, the heat source was supplied with a constant voltage of 8 V, maintaining a current of 1.18 A and a source temperature of 15°C. Temperature measurements were taken at equal time intervals throughout the experiment. The thermal conductivity coefficient was determined according to Fourier's law:

$$Q = P = \frac{dH}{dt} = V \cdot I = \frac{k \cdot A \cdot \Delta T}{d} \Rightarrow k = \frac{V \cdot I \cdot d}{A \cdot \Delta T},$$

where Q — heat flux; P — thermal power, W; d — specimen thickness, m; H — enthalpy, J; t — time; V — heater supply voltage, V; I — current from the voltage source, A; k — thermal conductivity coefficient, W/(m·K); A — specimen surface area, m^2; ΔT — temperature difference between specimen surfaces, K.

Prior to testing, the thermal conductivity analyzer was calibrated using reference specimens provided by the manufacturer. For each standard specimen, the correlation between nominal (theoretical) and measured thermal conductivity values was established. This allowed for the derivation of a calibration equation and subsequent correction of the experimental thermal conductivity data (Fig. 1).

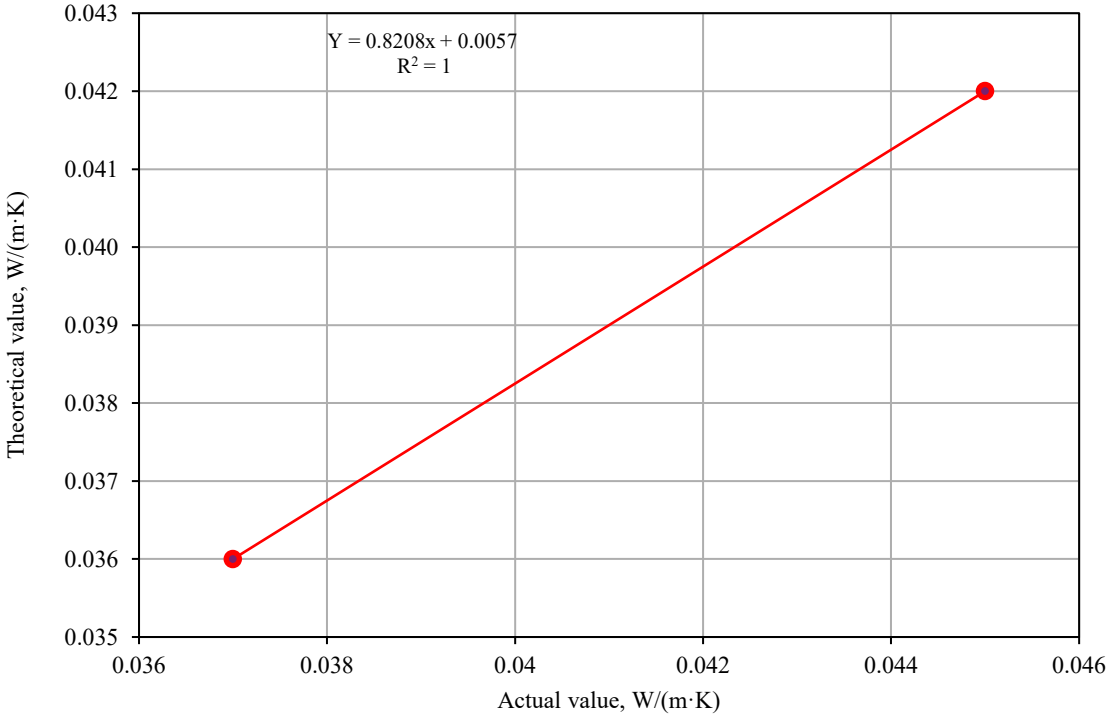

Fig. 1. Calibration curve of the thermal conductivity measuring device: R — coefficient of determination; Y — theoretical thermal conductivity; x — actual value

3.4. Compression testing (ISO 604:2002)

A brief description of the compression testing machine operation is as follows. The upper movable plate applies pressure to square specimens (25 mm thick) placed on the lower plate. The axial load is gradually increased.

Research Results. The density of the specimens was calculated from their mass and volume (Table 2). The obtained data allowed for an analysis of density variation as a function of composition and the physical-mechanical characteristics of the material.

Table 2

Specimen Density Calculation Results

Rubber waste volume, %	Specimen parameters			Density, kg/m^3
	Dry mass, kg·10^{-3}	Area, m^2	Thickness, m	
0	232.00	0.021	0.01	1160
10	225.60			1074.333
20	217.52			1037.238
30	213.73			1017.761
40	202.59			963.714
50	190.06			905.047

Figure 2 shows the density of the specimens as a function of rubber volume fraction.

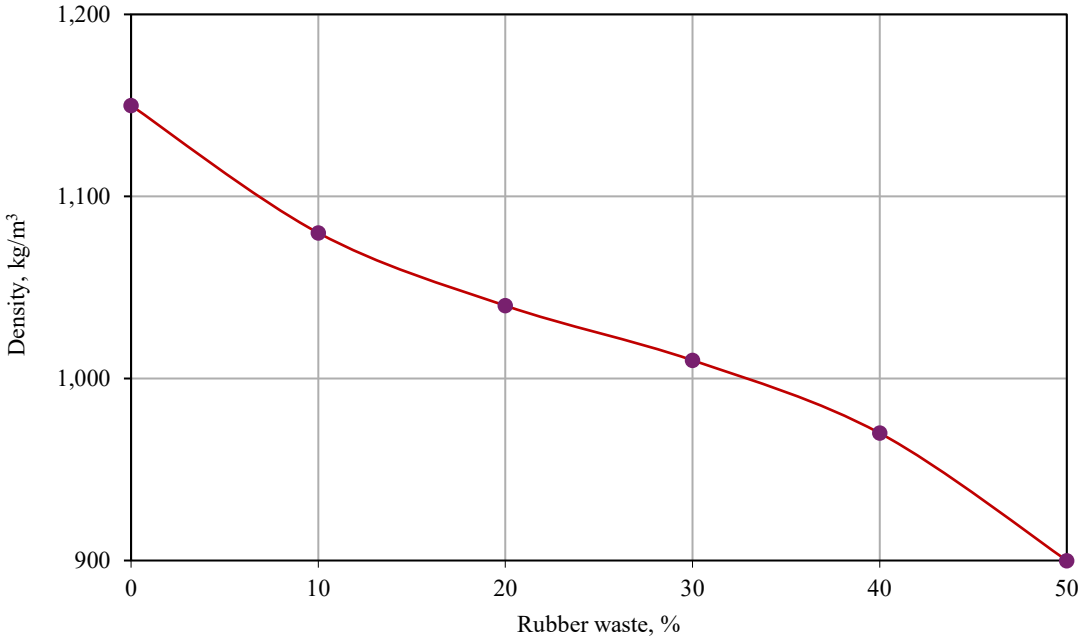

Fig. 2. Density as a function of rubber content

Water absorption behavior was evaluated through monitoring the weight change of specimens after 2 to 24 hours of immersion in water (Table 3).

Table 3

Specimen Water Absorption Behavior

Rubber waste volume, %	Weight before immersion, k·10^{-3}	Weight after immersion, kg·10^{-3}				
		in 2 hours	in 4 hours	in 6 hours	in 8 hours	in 24 hours
0	201.47	201.47	201.47	201.47	201.50	201.52
10	271.39	271.39	271.40	271.47	271.49	271.66
20	289.14	289.18	289.19	289.26	289.34	289.76
30	287.81	287.86	287.99	288.03	288.06	288.60
40	304.66	304.71	304.83	304.94	304.97	305.56
50	271.78	271.18	272.18	272.28	272.39	273.08

Figure 3 shows water absorption as a function of rubber volume fraction.

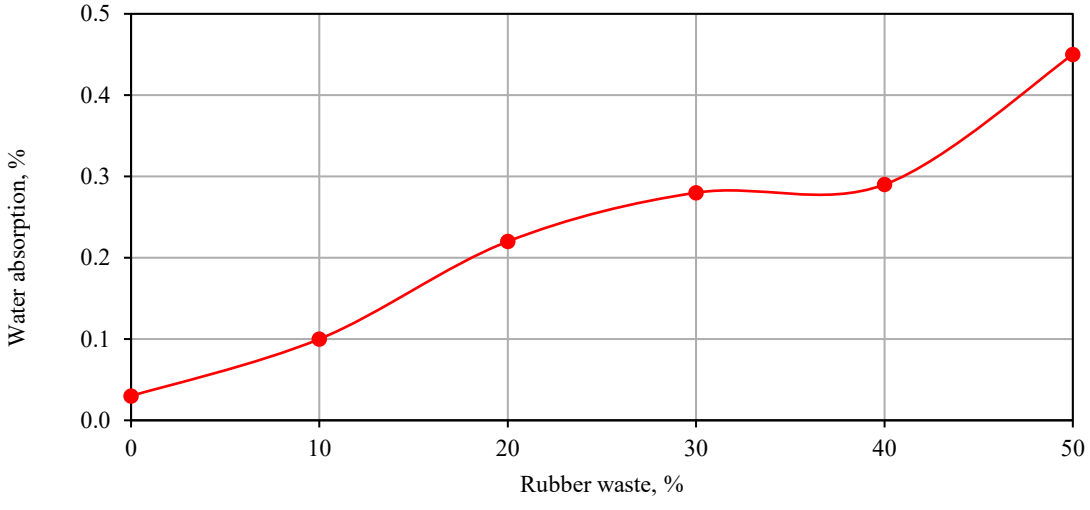

Fig. 3. Dependence of water absorption on rubber loading

Table 4 presents the results of measuring the thermal conductivity coefficient of the specimens.

Table 4

Thermal Conductivity Measurement Results

Rubber waste volume, %	Heat flow, $V \cdot I$, W	Temperature,°C	Specimen area, m^2	Specimen thickness, m	Thermal conductivity coefficient, W/(m·K)
0	8·1.15	17.90	0.021	0.01	0.2548540
10		17.45			0.2510574
20		17.78			0.2451560
30		18.37			0.2384840
40		19.64			0.2230620
50		21.16			0.2070390

Figure 4 shows the thermal conductivity coefficient as a function of rubber waste content.

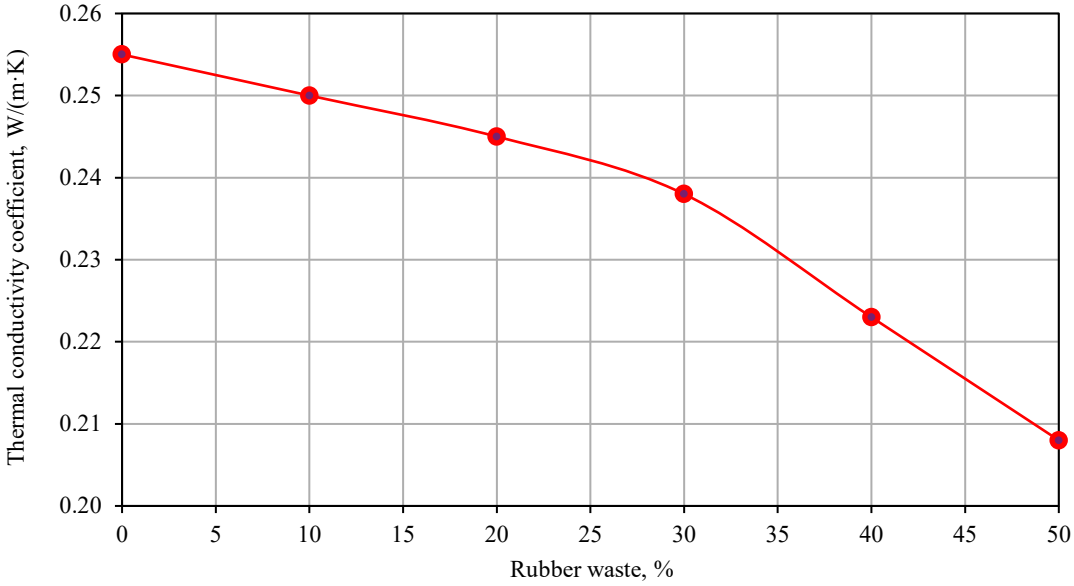

Fig. 4. Thermal conductivity as a function of rubber content

Table 5 shows the compression test results.

Table 5

Compression Test Results

Rubber waste volume, %	Specimen area, m^2	Maximum load, kN	Maximum compressive stress, MPa
0	0.145·0.145	1300	61.83
10			
20			
30			
40			
50			

Discussion. As shown in Table 2 and Figure 2, specimen density decreases as the rubber waste content increases. This is because the rubber has a lower density (500 kg/m³) than unsaturated polyester (1160 kg/m³). The specimen with 50% rubber waste exhibited the lowest density (905.05 kg/m³), representing a reduction of nearly 22% compared to the pure polymer. This density reduction corresponds to a decrease in specimen mass from 232 g to 190 g, with the geometric dimensions held constant (thickness: 0.01 m; area: 0.021 m²).

The discrepancies between the present results and those reported in [10] are minor and can be attributed to differences in the characteristics of the polymer matrix and the recycled tire rubber [12]. These findings confirm that rubber waste serves as an efficient filler. It allows for a reduction in composite weight and controlled adjustment of the final density to meet specific performance requirements.

As shown in Table 3, specimen mass remained virtually unchanged during the first hours following water immersion. Detectable changes occurred only after 8–24 hours of exposure. Figure 3 demonstrated that incorporating rubber waste into the unsaturated polyester matrix did not substantially affect water absorption in absolute terms. The values increased marginally from 0.024% for pure polyester to a maximum of 0.47% for the composition with 50% rubber waste. Thus, water absorption below 0.5% can be regarded as negligible. In this case, the low water absorption can be attributed to two factors:

– hydrophobic nature of rubber relative to unsaturated polyester;

– microscopic pores formed during the mixing process.

The low water absorption makes these materials promising for applications requiring moisture resistance, such as protective coatings, thermal insulation, and machinery components exposed to humid conditions. Further enhancement of performance could be achieved through chemical surface modification of the rubber particles or by limiting the rubber content to 20–30%, thereby attaining an optimal balance between mechanical integrity and moisture resistance.

According to Table 4 and Figure 4, increasing the rubber waste content to 50% reduces the thermal conductivity coefficient by approximately 19%, thereby enhancing the thermal insulation performance of the specimens. This trend is attributed to the inherently low thermal conductivity of rubber. The composite with 50% rubber waste exhibits a thermal conductivity of 0.2070 W/(m·K), which lies within the range of values reported in previous comparative studies [10]. Minor discrepancies between the present results and those in the literature may arise from differences in measurement techniques or the specific characteristics of the materials employed [13, 14].

Compression testing (Table 5) did not yield precise compressive strength values for the developed composites, as all specimens remained intact up to the maximum load capacity of the testing machine (1300 kN). The corresponding compressive stress at this load was calculated to be 61.83 MPa, which was considered to fall within the acceptable strength range for insulation materials.

Conclusion. This study shows that the incorporation of rubber waste into unsaturated polyester yields composites with enhanced properties suitable for construction applications.

The composition with 50% rubber waste was identified as optimal, exhibiting reduced density and thermal conductivity — key characteristics for thermal insulation materials. Although water absorption increased marginally with higher rubber content, it remained at a very low level (maximum 0.47%), making the composite suitable for use in humid environments.

The tests confirmed the high mechanical strength of the developed composites. All specimens withstood compressive loads of up to 1300 kN without failure, indicating their suitability for use in structural components exposed to mechanical stress.

Thus, the developed composites can contribute to solving two problems:

– environmentally sustainable disposal of substantial quantities of rubber waste;

– fabrication of efficient thermal insulation materials with high structural integrity.

Future work will focus on three main aspects.

1. Investigation of the effect of larger rubber particles (from 1 mm) on the properties of composites.

2. Evaluation of the sound insulation potential of the materials. This requires studying the microstructure, clarifying the proportion of air voids, and their effect on acoustics and mechanical properties.

3. Conducting experiments to study the resistance of the specimens to fire and chemicals.

References

1. Hashamfirooz M, Dehghani MH, Khanizadeh M, Aghaei M, Bashardoost P, Hassanvand MS, et al. A Systematic Review of the Environmental and Health Effects of Waste Tires Recycling. *Heliyon*. 2025;11(2):e41909. https://doi.org/10.1016/j.heliyon.2025.e41909

2. Antipas IR. Effect of Glass Fiber Reinforcement on the Mechanical Properties of Polyester Composites. *Advanced Engineering Research* (*Rostov-on-Don*). 2023;23(4):387–397. https://doi.org/10.23947/2687-1653-2023-23-4-387-397

3. Van de Lindt JW, Carraro JAH, Heyliger PR, Choi C. Application and Feasibility of Coal Fly Ash and Scrap Tire Fiber as Wood Wall Insulation Supplements in Residential Buildings. *Resources, Conservation and Recycling.* 2008;52(10):1235–1240. https://doi.org/10.1016/j.resconrec.2008.07.004

4. Fedoseev IV, Barkan MSh, Prokhotsky YuM, Laskina NE, Loginova AYu. Technology for Recycling Waste Rubber Products. *ChemChemTech*. 2013;56(2):117–120. (In Russ.)

5. Zhao J, Wang X-M, Chang JM, Yao Y, Cui Q. Sound Insulation Property of Wood-Waste Tire Rubber Composite. *Composites Science and Technology*. 2010;70(14):2033–2038. https://doi.org/10.1016/j.compscitech.2010.03.015

6. Siddique R, Naik TR. Properties of Concrete Containing Scrap-Tire Rubber — An Overview. *Waste Management*. 2004;24(6):563–569. https://doi.org/10.1016/j.wasman.2004.01.006

7. Nuzaimah M, Saruan SM, Nadlene N, Jawaid M. Microstructure and Mechanical Properties of Unsaturated Polyester Composites Filled with Waste Rubber Glove Crumbs. *Fibers and Polymers.* 2019;20(6):1290–1300.

8. Paulo JRO Nóvoa, Antonio Ferreira, António Torres Marques. Mechanical Performance of Unsaturated Polyester Resins. *Materials Science Forum.* 2006;514–516:662–665. https://doi.org/10.4028/www.scientific.net/MSF.514-516.662

9. Abu-Jdayil B, Mourad A-H, Hussain A. Thermal and Physical Characteristics of Polyester-Scrap Tire Composites. *Construction and Building Materials.* 2016;105:472–479. https://doi.org/10.1016/j.conbuildmat.2015.12.180

10. Abu-Jdayil B, Mourad A-H, Hussain A. Investigation on the Mechanical Behavior of Polyester-Scrap Tire Composites. *Construction and Building Materials.* 2016;127:896–903. https://doi.org/10.1016/j.conbuildmat.2016.09.138

11. Hanbing Liu, Xianqiang Wang, Yubo Jiao, Tao Sha. Experimental Investigation of the Mechanical and Durability Properties of Crumb Rubber Concrete. *Materials.* 2016;9(3):172. https://doi.org/10.3390/ma9030172

12. Abo Elenien KF, Azab NA, Bassioni G, Abdellatif MH. The Effect of Tire Rubber Particles on the Mechanical and Physical Properties of Polyester. *IOP Conference Series: Materials Science and Engineering.* 2020;973:012019. https://doi.org/10.1088/1757-899X/973/1/012019

13. Fedroff D, Ahmad S, Savas BZ. Mechanical Properties of Concrete with Ground Waste Tire Rrubber. *Transportation Research Record: Journal of Transportation Research Board*. 1996;1532(1):66–72. https://doi.org/10.1177/0361198196153200110

14. Rybak AT, Teplyakova SV, Olshevskaya AV, Prutskov AS. A Method for Monitoring the Reliability of Technical Systems by Identifying the Entropy of the Causes of Their Failures. *Advanced Engineering Research (Rostov-on-Don).* 2025;25(2):112–119. https://doi.org/10.23947/2687-1653-2025-25-2-112-119

About the Authors:

Imad Rizakalla Antipas, Cand.Sci. (Eng.), Associate Professor of the Fundamentals of Machinery Design Department, Don State Technical University (1, Gagarin sq., Rostov-on-Don, 344003, Russian Federation), SPIN-code, ORCID, ScopusID, ResearchID, imad.antypas@mail.ru

Tatyana P. Savostina, Senior Lecturer of the Fundamentals of Machinery Design Department, Don State Technical University (1, Gagarin sq., Rostov-on-Don, 344003, Russian Federation), SPIN-code, ORCID, ScopusID, kovtanya@yandex.ru

Claimed Contributorship:

IR Antipas: conceptualization, data curation, formal analysis, investigation, methodology, resources, supervision, validation, visualization, writing – original draft preparation, writing — review & editing.

TP Savostina: project administration, visualization, writing — original draft preparation,

Conflict of Interest Statement: **the authors declare no conflict of interest.**

All authors have read and approved the final version of the manuscript.

Об авторах:

Имад Ризакалла Антибас, кандидат технических наук, доцент кафедры «Основы конструирования машин» Донского государственного технического университета (344003, Российская Федерация, г. Ростов-на-Дону, пл. Гагарина, 1), SPIN-код, ORCID, ScopusID, ResearchID, imad.antypas@mail.ru

Татьяна Петровна Савостина, старший преподаватель кафедры «Основы конструирования машин» Донского государственного технического университета (344003, Российская Федерация, г. Ростов-на-Дону, пл. Гагарина, 1), SPIN-код, ORCID, ScopusID, kovtanya@yandex.ru

Заявленный вклад авторов:

И.Р. Антибас: разработка концепции, курирование данных, формальный анализ, проведение исследования, разработка методологии, предоставление ресурсов, научное руководство, валидация результатов, визуализация, написание черновика рукописи, написание рукописи — внесение замечаний и исправлений.

Т.П. Савостина: административное руководство исследовательским проектом, визуализация, написание черновика рукописи.

Конфликт интересов: **авторы заявляют об отсутствии конфликта интересов.**

Все авторы прочитали и одобрили окончательный вариант рукописи.

Received / **Поступила в редакцию** 25.12.2025
Reviewed / Поступила после рецензирования 20.01.2026
Accepted / **Принята к публикации** 27.01.2026

MACHINE BUILDING AND MACHINE SCIENCE
МАШИНОСТРОЕНИЕ И МАШИНОВЕДЕНИЕ

UDC 620.1
https://doi.org/10.23947/2687-1653-2026-26-1-2250

Original Empirical Research

Experimental Study and Modeling of Thermal Response in Turning a 3.5 mm Thick Shell of Metal Composite System

Nickolai S. Lyubimyi, Boris S. Chetverikov ✉, Michail S. Gerasimov, Mikhail V. Bytsenko, Andrei A. Pol'shin, Ardalion K. Mal'tsev
Belgorod State Technological University named after V.G. Shukhov, Belgorod, Russian Federation
✉ await_rescue@mail.ru

EDN: SNBJCR

Abstract

Introduction. Modern technologies of tool and mold production increasingly use metal-composite systems (MCS), which combine additively manufactured metal shells and metal-polymer fillers. This corresponds to priority areas of scientific and technological progress, such as digitalization and additive manufacturing (in accordance with the Federal Project "Development of Materials and Production Technologies" within the framework of the national program "Scientific and Technological Development"). The scope of application of MCS in industry is growing: according to industry reviews, their share in the production of high-precision components for the aerospace and automotive industries has increased by 25–30% over the past five years, providing economic benefits due to a 15–20% reduction in the weight of structures and improvement of the energy efficiency of processes. Such systems combine the strength and thermal conductivity of metal with the damping properties of polymers, yet exhibit high sensitivity to overheating during machining. Consequently, the temperature at the metal–MCPM (metal-polymer composite material) interface during turning may exceed the thermal stability threshold (170°C), resulting in thermal degradation, loss of adhesion, and shell deformation. In the literature, the problem of MCS thermal stability in turning is addressed only fragmentarily: existing studies focus on monolithic composites or general heat-transfer models, lacking detailed analysis of interfacial heating in additively manufactured systems featuring low-conductivity fillers. Therefore, research is needed to quantify the thermal response during the machining of such systems and to determine the cutting parameters that provide their thermal stability. The objective of this work is to experimentally study the temperature response during turning of MCS with a shell thickness of $\delta = 3.5$ mm and to construct a second-order regression model linking the temperature at the metal – MPCM interface with the cutting parameters.

Materials and Methods. A hardware-software measurement unit simulating the MCS structure was developed for the study. It included a replaceable bushing made of 12Kh18N10T steel, an internal insert made of Ferro-Chromium metal-polymer, three built-in type K thermocouples, and a data acquisition module based on an ESP32-WROOM microcontroller with MAX6675 converters, providing temperature recording at 5 Hz and data transmission via Wi-Fi. The accuracy of the measurements was confirmed by thermal imaging verification using FLUKE Ti400. The experiment was conducted according to the full factorial design (FFD) $2^3 + n_0$, in which cutting speed V, feed S and cutting depth t were varied. Data processing was performed by the least-squares method with adequacy validation using Fisher's F-test and coefficient significance by Student's t-test. Based on the results of processing in real physical units, a second-order regression model was constructed — model 3.5TP, designed for engineering prediction.

Results. The analysis of the experimental data showed that the thermal response of the metal–composite system was nonlinear. The depth of cut t was the dominant factor increasing the temperature, whereas within the investigated range, an increase in the feed rate S and cutting speed V led to a decrease in the interface temperature due to a shorter thermal exposure time and more intensive heat removal with the chip flow. The resulting 3.5TP model was characterized by the coefficient of determination $R^2 = 0.9513$, Fisher criterion value $F = 364.31$ and the significance level $p < 10^{-5}$, which validated its adequacy. Interpretation of the regression coefficients indicated that the depth of cut (t) had the strongest impact on the temperature rise, the feed rate (S) showed a moderate effect, and the cutting speed (V) had the least sensitivity within the investigated range. The constructed response surfaces and contour maps identified the "safe zones" of cutting conditions that satisfied the constraint $T \leq 170$°C, corresponding to the thermal stability limit of the metal–polymer filler. The average deviation between the experimental and calculated data did not exceed 7°C, that confirmed the high accuracy and predictive capability of the proposed model.

Discussion. The constructed 3.5TP model revealed the relationship between geometric and technology factors that determine the thermal load of the MCS during turning. The dominant impact of the depth of processing was due to the increase in the volume of the cut layer and heat generation in the contact zone, while the increase in feed and cutting speed was accompanied by compensating effects due to a decrease in the time of thermal contact and more intense heat removal with the chips. The results obtained indicated the need to optimize processing modes taking into account the shell thickness δ. Directions for further research were identified.

Conclusion. The conducted study demonstrates that the developed experimental setup reproduces accurately the thermal behavior of a metal–composite system composed of an additively manufactured metal shell and a metal–polymer filler. The constructed 3.5TP regression model adequately describes the temperature response during turning and can be used for engineering prediction of mechanical processing modes.

Keywords: additive technologies, metal polymer, cutting temperature, interfacial boundary

Acknowledgements. The authors would like to thank the management of the High Technology Center at the BSTU named after V.G. Shukhov for providing components and equipment for testing. The authors appreciate the anonymous reviewers.

Funding Information. This study was supported by grant no. 23–79–10022 from the Russian Science Foundation, https://rscf.ru/project/23-79-10022/

For Citation. Lyubimyi NS, Chetverikov BS, Gerasimov MD, Bytsenko MV, Pol'shin AA, Mal'tsev AK. Experimental Study and Modeling of Thermal Response in Turning a 3.5 mm Thick Shell of Metal Composite Systems. *Advanced Engineering Research (Rostov-on-Don)*. 2026;26(1):2250. https://doi.org/10.23947/2687-1653-2026-26-1-2250

Оригинальное эмпирическое исследование

Экспериментальное исследование и моделирование теплового отклика металл-композитной системы при точении оболочки толщиной 3,5 мм

Н.С. Любимый, Б.С. Четвериков✉, М.Д. Герасимов, М.В. Быценко, А.А. Польшин, А.К. Мальцев

Белгородский государственный технологический университет им. В.Г. Шухова, г. Белгород, Российская Федерация

✉ await_rescue@mail.ru

Аннотация

Введение. Современные технологии инструментального и формообразующего производства всё чаще используют металл-композитные системы (МКС), сочетающие аддитивно изготовленные металлические оболочки и металлополимерные наполнители, что соответствует приоритетным направлениям научно-технического прогресса, таким как цифровизация и аддитивное производство (в соответствии с Федеральным проектом «Развитие технологий материалов и производства» в рамках национальной программы «Научно-технологическое развитие»). Масштабы применения МКС в промышленности растут: по данным отраслевых обзоров, их доля в производстве высокоточных компонентов для авиакосмической и автомобильной отраслей увеличилась на 25–30% за последние пять лет, обеспечивая экономическую выгоду за счет снижения массы конструкций на 15–20 % и повышения энергоэффективности процессов. Такие системы сочетают прочность и теплопроводность металла с демпфирующими свойствами полимера, но характеризуются высокой чувствительностью к перегреву при механической обработке. Вследствие этого температура на границе «металл – МПКМ» при точении может превышать порог термостойкости (170°C), приводя к термодеструкции, потере адгезии и деформации оболочки. В литературе проблема термостабильности МКС при точении освещена фрагментарно: существующие работы фокусируются на монолитных композитах или общих моделях теплопереноса, без детального анализа межфазного нагрева в аддитивно-формованных системах с низкой теплопроводностью наполнителя. Поэтому необходимы исследования, позволяющие количественно описать тепловой отклик при обработке таких систем и определить параметры резания, обеспечивающие их термостабильность. Цель настоящей работы — экспериментальное исследование температурного отклика при точении МКС с толщиной оболочки δ = 3,5 мм и построение регрессионной модели второго порядка, связывающей температуру на границе «металл – МПКМ» с параметрами резания.

Материалы и методы. Для исследования был разработан программно-аппаратный измерительный узел, моделирующий структуру МКС. Он включал сменную втулку из стали 12Х18Н10Т, внутреннюю вставку из металлополимера «Ферро-хром», три встроенные термопары типа K и модуль сбора данных на микроконтроллере ESP32-WROOM с преобразователями MAX6675, обеспечивающий регистрацию температуры с частотой 5 Гц и передачу данных по Wi-Fi. Корректность измерений подтверждена тепловизионной верификацией с использованием FLUKE Ti400. Эксперимент проводился по плану полного факторного эксперимента (ПФЭ) $2^3 + n_0$, в котором варьировались скорость резания V, подача S и глубина резания t. Обработка данных выполнялась методом наименьших квадратов с проверкой адекватности по F-критерию Фишера и значимости коэффициентов по t-критерию Стьюдента. По результатам обработки в реальных физических единицах построена регрессионная модель второго порядка — модель 3.5ТР, предназначенная для инженерного прогнозирования.

Результаты исследования. Анализ экспериментальных данных показал, что температурный отклик МКС имеет нелинейный характер, при этом глубина резания t является доминирующим фактором повышения температуры, тогда как в исследованном диапазоне увеличение подачи S и скорости резания V сопровождается снижением температуры на межфазной границе за счёт сокращения времени теплового воздействия и более интенсивного выноса тепла со стружкой. Полученная модель 3.5ТР характеризуется коэффициентом детерминации $R^2 = 0{,}9513$, значением критерия Фишера $F = 364{,}31$ и уровнем значимости $p < 10^{-5}$, что подтверждает её адекватность. Интерпретация коэффициентов выявила, что глубина резания t оказывает наибольшее влияние на рост температуры, подача S — умеренное воздействие, а скорость резания V — минимальное. Построенные поверхности отклика и контурные карты позволили выделить «безопасные зоны» режимов, удовлетворяющих условию $T \leq 170$°C. Средние расхождения между экспериментальными и расчётными данными не превышали 7°C, что подтверждает высокую точность модели.

Обсуждение. Построенная модель 3.5ТР раскрыла взаимосвязь геометрических и технологических факторов, определяющих термонагруженность МКС при точении. Доминирующее влияние глубины обработки обусловлено увеличением объёма срезаемого слоя и тепловыделения в зоне контакта, тогда как рост подачи и скорости резания сопровождается компенсирующими эффектами за счёт уменьшения времени теплового контакта и более интенсивного выноса тепла со стружкой. Полученные результаты свидетельствуют о необходимости оптимизации режимов обработки с учётом толщины оболочки δ. Определены направления дальнейших исследований.

Заключение. Проведённое исследование доказало, что разработанная экспериментальная установка корректно воспроизводит тепловое поведение металл-композитной системы с аддитивной оболочкой и металлополимерным заполнителем. Построенная регрессионная модель 3.5ТР адекватно описывает температурный отклик при точении и может использоваться для инженерного прогнозирования режимов механической обработки.

Ключевые слова: аддитивные технологии, металлополимер, температура резания, межфазная граница

Благодарности. Авторы благодарят руководство Центра высоких технологий БГТУ им. В.Г. Шухова за предоставленные образцы и оборудование для испытаний. Авторы выражают признательность анонимным рецензентам.

Финансирование. Исследование выполнено при поддержке гранта Российского научного фонда № 23–79–10022, https://rscf.ru/project/23-79-10022

Для цитирования. Любимый Н.С., Четвериков Б.С., Герасимов М.Д., Быценко М.В., Польшин А.А., Мальцев А.К. Экспериментальное исследование и моделирование теплового отклика металл-композитной системы при точении оболочки толщиной 3,5 мм. *Advanced Engineering Research (Rostov-on-Don).* 2026;26(1):2250. https://doi.org/10.23947/2687-1653-2026-26-1-2250

Introduction. The modern development of tool and form-forming production, particularly in the aircraft and machine-building industries, is characterized by a transition to hybrid structural solutions that combine metal and composite components. One of the promising areas in this field is the development of metal-composite systems (MCS), in which thin-walled metal shells are combined with fillers made of metal-polymer composite materials (MPCM). This provides an optimal balance of strength, thermal conductivity and damping properties [1].

In recent years, additive manufacturing (AM) technologies [2] have become widespread, allowing for the formation of complex topologically optimized (TO) shells, including structures with conformal cooling channels that provide targeted heat dissipation and increased thermal stability of products [3]. This approach is particularly important for tooling products, for example**,** indexable drills with internal cooling channels (Fig. 1), manufactured through selective laser melting (SLM). They improve heat dissipation from the cutting zone and increase the durability of carbide heads [4].

Fig. 1. Indexable drill: *a* — model of a topologically optimized part of a drill body with a setting head and curved cooling channels of the body; *b* — model of the TO drill body with a thin-walled shell forming the chip grooves and shank; *c* — physical sample of TO metal-composite indexable drill (cavity after TO is filled with MPCM), manufactured using SLM technology: 1 — machined metal-composite shank; 2 — chip grooves; 3 — cutting head of the indexable drill

The transition to hybrid metal-composite structures, despite obvious advantages, is accompanied by new technological constraints. The most significant of these are thermal processes during finishing machining, where local temperature distribution determines the strength of interfacial adhesion, geometric stability, and durability of the product. Unlike monolithic metal workpieces, the heat flow during turning of hybrid metal-composite structures is concentrated at the metal – MPCM interface, where the materials differ sharply in thermal conductivity and heat capacity [5]. Since the metal polymer is characterized by low thermal conductivity and limited heat resistance (up to 170°C), even short-term overheating can cause thermal destruction, reduced adhesion, and deformation of the shell. [6].

The analysis of the literature data shows that existing research in the field of thermal loading during cutting covers mainly homogeneous metal alloys [7] or metal-matrix composites [6], where the temperature field is described through the mechanisms of friction and hardening of surface layers. In studies on thin-walled parts [8], the main focus is on increasing rigidity and vibration resistance due to special basing systems and devices [9]. At the same time, hybrid metal-polymer structures remain virtually unexplored in terms of heat transfer patterns during turning.

Furthermore, traditional analytical and numerical heat transfer models used in cutting simulations are developed for materials with uniform thermal properties and do not take into account the discontinuity in thermal conductivity at the interphase boundary [8]. This makes it impossible to directly use known relationships to predict the temperature in the MCS where the metal and metal-polymer components interact.

Cooling and lubrication conditions, and the selection of tool materials and coatings also have an additional impact on thermal loading. It is known that the use of PVD coatings in combination with optimized conditions increases tool life when machining heat-resistant alloys [10], and modification of metalworking fluids (MWF) can reduce contact temperatures when turning titanium and aluminum alloys [11]. For additive materials obtained by surfacing, an increase in temperature gradients was noted due to differences in the thermal conductivity of the layers [12]. These effects are particularly significant when processing products with a combined metal-polymer structure.

Additively produced shells are also characterized by increased roughness and residual stresses [13], which affect local heat transfer and the generation of contact temperature [14]. This further complicates the selection of rational processing modes, requiring the construction of experimentally verified thermal response models.

Thus, in the modern scientific picture, there is a gap in knowledge due to the lack of experimentally confirmed data and validated regression models describing the temperature response of metal-composite systems during finishing. The effect of the metal shell thickness on the efficiency of heat dissipation and the nature of the temperature gradient in the metal – MPCM contact zone remains particularly understudied.

The objective of this study is to experimentally determine the temperature response of a metal-composite system with a metal shell thickness of 3.5 mm during turning, as well as to construct a regression model of the dependence of the temperature at the interphase boundary on cutting conditions (V, S, t).

To achieve this objective, the following tasks were completed:

– development and production of a hardware-software stand for real-time temperature recording during turning the MCS;

– conducting a series of experiments according to a full factorial design 2^3+n_0 with varying cutting parameters;

– constructing a second-order regression model and assessing its adequacy on statistical criteria;

– determining safe turning ranges that prevent overheating of the metal-polymer filler and adhesion failure.

The implementation of the set tasks is aimed at the development of an engineering-applicable methodology for selecting finishing modes for metal-composite systems, providing control of thermal loading, and preservation of the structure of the metal-polymer filler.

Materials and Methods. Experimental studies are directed at determining the thermal response patterns of a metal-composite system (MCS) during turning, taking into account the geometric parameter — the thickness of the metal shell. To simulate the actual structure of hybrid products, a hardware-software setup is developed, including a replaceable metal bushing and an internal filler made of a metal-polymer composite material (MPCM).

The development of the setup, whose model is shown in Figure 2, made it possible to simulate the conditions of turning a fragment of a hybrid part with a given wall thickness and record the temperature in real time at the interphase boundary “metal – MPCM”.

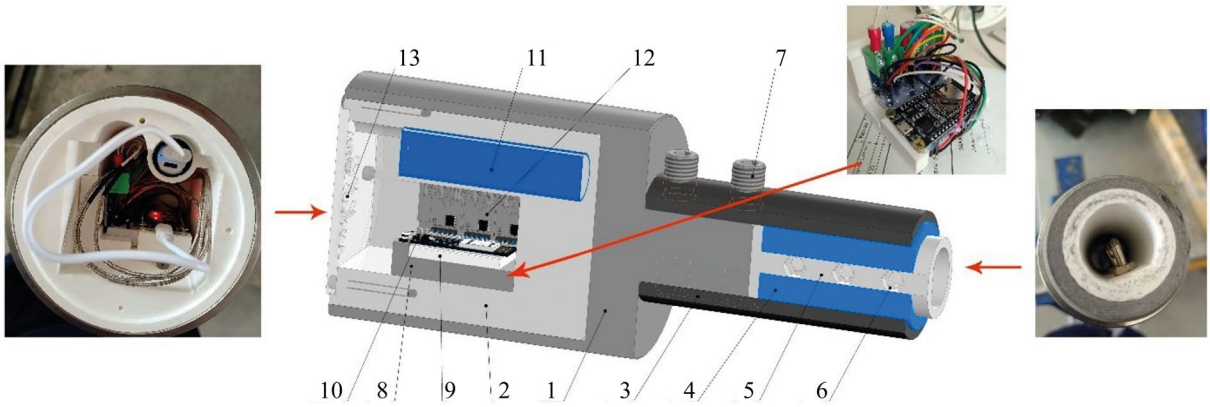

Fig. 2. Hardware-software setup for simulating real structure of hybrid products:
1 — external device housing; 2 — electronics housing; 3 — metal shell; 4 — metal-polymer filler;
5 — thermocouple housing; 6 — thermocouple mounting holes in the housing; 7 — mounting screws;
8 — microprocessor housing; 9 — breadboard; 10 — microprocessor; 11 — battery;
12 — thermocouples; 13 — cover

The major element of the setup was a housing made of grade 40 structural steel, providing secure placement in the chuck of 16K20 lathe. A replaceable bushing made of 12Kh18N10T steel (similar to AISI 321) was fixed inside the housing. This steel has low thermal conductivity (~15–16 W/(m·K)) and is resistant to high temperatures. This makes it a suitable model for high-alloy steels used in additive manufacturing [15]. The metal bushings were cylindrical with an inner diameter of 53 mm and an outer diameter of 60 mm, corresponding to a metal thickness of $\delta = 3.5$ mm. This element simulated the metal shell of a real hybrid part and allowed for varying the geometric parameters for subsequent studies. Figure 3 shows the machined replaceable bushing.

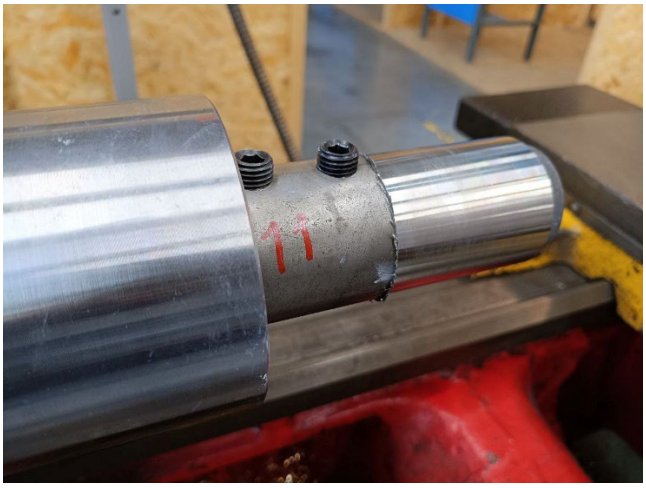

Fig. 3. Machined bushing

A Ferro-Chrom[1] MPCM insert was installed in the inner cavity of the bushing. It was pre-molded to the nominal diameter and secured with KPT-8 thermal paste to improve thermal contact. The MPCM contained a thermosetting epoxy matrix filled with powdered chromium particles. The material had a limited thermal resistance of up to 170°C and a thermal conductivity of approximately 2 W/(m·K). This combination of materials provided adequate reproduction of the thermal interaction at the metal – MPCM interface.

Three K-type thermocouples were used to record temperature. They were embedded in the wall of the bushing along the sample axis and spaced equally along the cutting zone. The thermocouple signals were fed to MAX6675 analog-to-digital converters connected to an ESP32-WROOM microcontroller, which provided digitization and wireless data transmission. The electronic components were located in a separate cavity of the housing, protected by a plastic holder. Power was supplied from a 2600 mA· h rechargeable battery, providing several hours of continuous operation.

Temperature was recorded at a frequency of 5 Hz, and data was transmitted via the UDP protocol through the built-in Wi-Fi module. On a personal computer, the data was visualized in real time using a Python 3.12 API (Fig. 4), implemented by the *PyQtGraph, Matplotlib*, and *Pandas* libraries. This allowed for rapid monitoring of temperature variation at the interface and storing the results as digital arrays for subsequent processing.

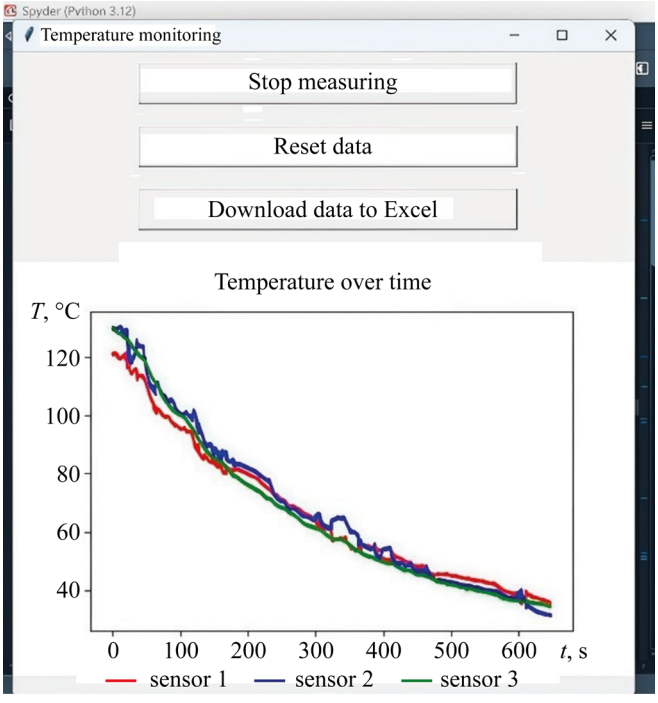

Fig. 4 Temperature Monitoring program interface on a PC (cooling process)

[1] Specifications TU 2257–002–48460567–00. *"Ferro-Chrom" Metallopolymer*. Moscow: ZAO "LEO Metal-Polymer Mmaterials"; 2000. URL: https://www.leo-polymer.ru (accessed: 01.11.2025).

To validate the operation of the thermocouples and control the temperature distribution over the surface of the bushing, thermal imaging verification was performed using a FLUKE Ti400 device [16]. The comparison results showed that the deviations between the thermocouple and thermal imaging data did not exceed ±3°C, which confirmed the reliability of the recording scheme used.

Thus, the developed setup is an autonomous measuring unit capable of recording the temperature at the interface of a metal-composite system with high frequency and sufficient accuracy. Its design allows for studies to be conducted under various shell geometric parameters and cutting conditions, that makes it possible to develop an experimentally validated model of the MCS thermal response during turning.

The experiment was designed to identify quantitative patterns in the effect of cutting conditions on the temperature response of a metal-composite system with a metal shell thickness of δ = 3.5 mm. For this purpose, an approach based on the full factorial experiment (FFE) methodology was used [17], which made it possible to study the interaction of process parameters and construct a second-order regression model suitable for engineering prediction.

The selection of this scheme is explained by the need to evaluate not only the key factors but also their interaction, since thermal loading during MCS turning is a multiparameter function dependent on cutting speed, feed, and depth. Moreover, unlike traditional metal workpieces, the behavior of hybrid systems is determined by uneven heat transfer at the interface, which increases the nonlinearity of the relationships.

The variable factors were cutting speed V (m/min), feed per revolution S (mm/rev), and cutting depth t (mm). Each factor was assigned two levels — upper and lower — corresponding to code values of +1 and –1 (Table 1).

Table 1

Experimental Factors Variation Levels

Factor	Designation	–1	0	+1
Feed, S mm/rev	x_1	0.05	0.10	0.15
Cutting speed, V m/min	x_2	60	90	120
Cutting depth, t mm	x_3	0.5	1.0	1.5

To assess possible nonlinearity and check reproducibility, five replicate experiments with zero code values (0, 0, 0) were added to the center of the design. Thus, the overall experimental structure included eight factorial and five central points (Table 2), which made it possible to construct an adequate approximation model without increasing the size of the experiments.

Table 2

Full Factorial Design

Experiment number	x_1, (S, mm/rev)	x_2, (V, m/min)	x_3, (t, mm)	Mode (code)
1	0.50	60	0.05	(–1, –1, –1)
2	0.50	60	0.15	(–1, –1, +1)
3	0.50	120	0.05	(–1, +1, –1)
4	0.50	120	0.15	(–1, +1, +1)
5	0.15	60	0.05	(+1, –1, –1)
6	0.15	60	0.15	(+1, –1, +1)
7	0.15	120	0.05	(+1, +1, –1)
8	0.15	120	0.15	(+1, +1, +1)
9–11	0.10	90	0.10	(0, 0, 0)

The temperature at the metal – MPCM interface was measured simultaneously by three thermocouples (T_1, T_2 and T_3), positioned along the workpiece axis. For each experiment, the maximum temperature values were determined, and the average value T_{cp}, characterizing the integral thermal response of the system, was calculated.

The experimental results were used to construct a regression function describing temperature T at the metal – MPCM interface in coded variables x_1, x_2, x_3 using equation (1):

$$T = b_0 + b_1x_1 + b_2x_2 + b_3x_3 + b_4x_1^2 + b_5x_2^2 + b_6x_3^2 + b_7x_1x_2 + b_8x_1x_3 + b_9x_2x_3. \quad (1)$$

The model coefficients were determined by the least-squares method, which minimized the sum of squared deviations between the experimental and calculated temperature values. The significance of the coefficients was tested using Student's *t*-test, and the adequacy of the model as a whole was assessed using Fisher's *F*-test at a significance level of $\alpha = 0.05$, which is the standard for engineering experiments in the mechanical processing [18].

The quality of the approximation was assessed using the coefficient of determination R^2, which characterized the proportion of explained variation in the response. Values $R^2 \geq 0.95$ were interpreted as indicating high agreement between the model and the experiment. Additionally, the relative deviation ΔT was calculated from formula (2):

$$\Delta T = \frac{\left|T_{\text{эксп}} - T_{\text{мод}}\right|}{T_{\text{эксп}}} \cdot 100\%. \quad (2)$$

Minimum values ΔT, not exceeding 7–8%, showed a good fit between the model and the observed data.

All statistical processing was performed in Excel and Python using built-in regression analysis tools and the statsmodels package. This approach provided reproducible calculations, clear graphical representation, and the ability to subsequently validate the model in automated engineering analysis systems.

Thus, the selected experimental design scheme allowed us to generate a statistically reliable database required for constructing the 3.5TP regression model and subsequent analysis of the thermal behavior of the metal-composite system. The resulting relationships served as the basis for determining critical cutting conditions that preserved the structure of the metal-polymer filler and the stability of the shell geometry.

Research Results. The experiments yielded a set of data reflecting the dynamics of temperature variation at the metal-composite interface during turning of specimens with a shell thickness of 3.5 mm. Processing of the results revealed that the temperature response of the metal-composite system was nonlinear, and it was determined by a combination of cutting conditions. It was found that increasing the cutting depth *t* led to a growth of temperature, while in the studied range, increasing the feed rate *S* and cutting speed *V* was accompanied by a decrease in temperature at the interphase boundary. Moreover, the impact of the parameters was interrelated, therefore the nature of the temperature variation should be assessed using the response surfaces.

Figure 5 shows a typical temperature dependence obtained with fixed machining parameters. The curve demonstrates the initial heating phase, followed by a brief temperature increase to a steady-state level, after which thermal equilibrium is observed. The average duration of the transient mode was 2–5 minutes, corresponding to the time it took for the heat flow in the cutting zone to stabilize, followed by slow cooling.

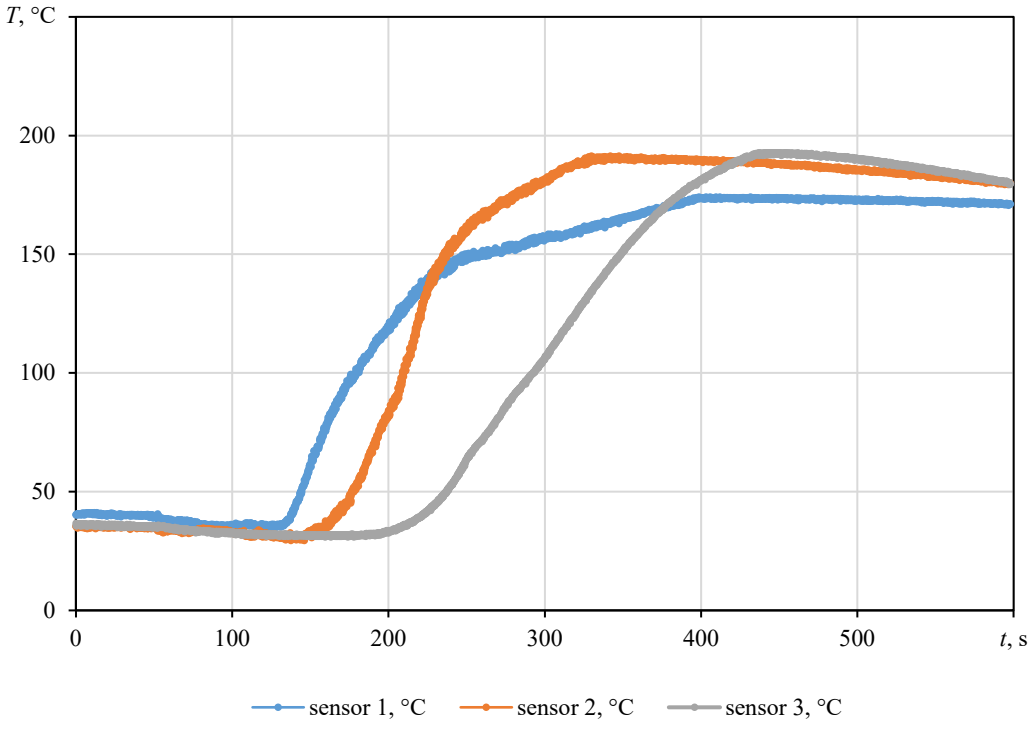

Fig. 5. Temperature change graph during turning, experiment no. 2, δ = 3.5 *mm*

Average temperatures T_{cp}, calculated from the results of 13 full factorial experiments, ranged from 90 to 186°C. The highest temperatures were observed under conditions with increased cutting depth t combined with reduced S and V values (within the studied levels), while temperature reduction was achieved with increased feed and speed at a fixed cutting depth.

The maximum temperatures at the interphase boundary are shown in Table 3.

Table 3

Maximum Temperature Values for Thermocouples with a Metal Thickness of 3.5 mm

Experiment no.	Thermocouple 1, °C	Thermocouple 2, °C	Thermocouple 3, °C	Average, °C
1	120.00	116.75	111.75	116.17
2	174.25	191.50	192.75	186.17
3	97.00	90.50	95.75	94.42
4	120.75	121.25	122.50	121.50
5	95.50	87.00	89.25	90.58
6	112.25	106.50	105.00	107.92
7	103.50	95.25	92.50	97.08
8	118.50	111.25	106.75	112.17
9	104.25	103.00	99.75	102.33
10	109.00	101.50	101.50	104.00
11	112.75	106.25	102.75	107.25
12	111.50	104.00	102.00	105.83
13	113.75	108.50	111.00	111.08

Based on the experimental data processing for samples with a metal shell thickness of δ = 3.5 mm, several regression models of the temperature response T were constructed: separately for each sensor (T_1, T_2, T_3), for the average temperature value, and for the combined sample. The comparative analysis showed that the models constructed on individual measurement channels were characterized by high determination coefficients ($R^2 \approx 0.96–0.97$) and statistically significant coefficients at the $p < 0.5$ level. However, the most robust and informative model was the combined (extended) model, which took into account the combined data from all three thermocouples. This model, designated as 3.5TP, tripled the observation volume, increasing its statistical power and the reliability of engineering predictions.

For the 3.5TP model, the determination coefficient was $R^2 = 0.9513$, and the Fisher's exact test value was $F = 364.31$, with a significance level of $p < 10^{-5}$, indicating high adequacy of the model to the experimental data. Based on the estimated coefficients, regression equation in physical units was obtained (3):

$$3.5TP = 1484.16 \cdot S^2 + 7.604 \cdot S \cdot V - 388.75 \cdot S \cdot t - 915.59 \cdot S + 0.0041 \cdot V^2 - \\ -0.4646 \cdot V \cdot t - 1.376 \cdot V + 14.84 \cdot t^2 + 85.44 \cdot t + 182.57. \quad (3)$$

Based on the obtained 3.5TP model, surface graphs were constructed reflecting the interaction of factors (Fig. 6).

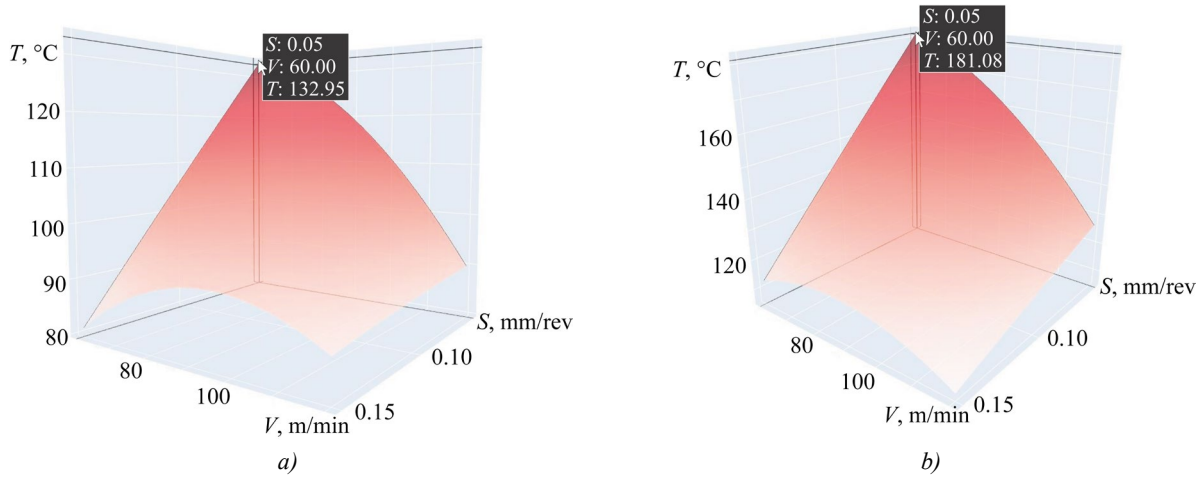

Fig. 6. Temperature surface graphs for 3.5TP model: *a* — cutting depth of 1 mm; *b* — cutting depth of 1.5 mm

The constructed 3.5TP model is characterized by high approximation accuracy. Validation against the full observation matrix showed that the deviation between the calculated and experimental temperature values (ΔT) in most cases did not exceed 1–7 °C. Only in certain combinations of modes, deviations of the order of 10–12 °C were observed, which was due to local inhomogeneity of heat transfer at the metal – MPCM boundary and differences in the emissivity coefficient when compared with thermal imaging verification data [19]. Overall, the level of discrepancies is considered acceptable for engineering tasks of prediction and construction of temperature maps.

Figure 7 shows a contour map of the temperature fields constructed using equation (2) for a cutting depth of 1.5 mm.

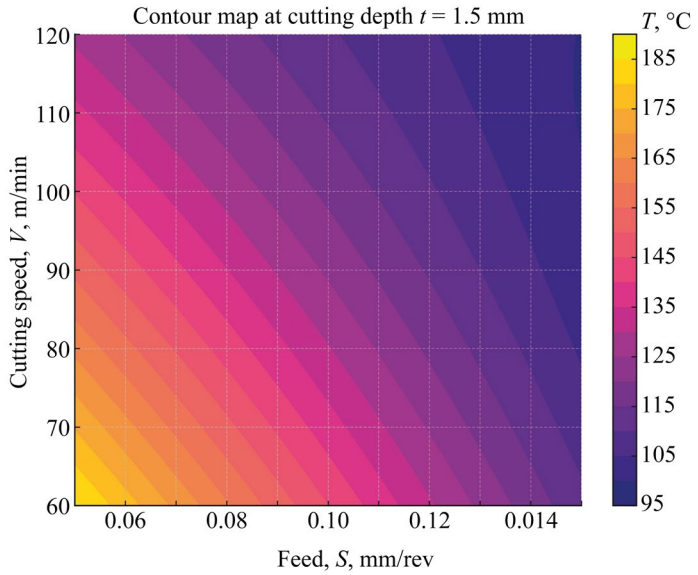

Fig. 7. Temperature contour graph for 3.5TP model, with cutting depth of 1.5 mm

The constructed 3.5TP regression model reliably describes the thermal behavior of a metal-composite system with a metal shell thickness of 3.5 mm during turning. The model has high predictive power and can be used to determine safe machining conditions that prevent the 170°C threshold from being exceeded.

Discussion. The analysis of the obtained coefficients has shown a consistent physical meaning for each term of the equation. The linear coefficients for feed and speed ($-915.59S$ and $-1.376V$) have negative values, indicating a decrease in temperature as these parameters increase over the studied range. This effect is explained by the fact that increasing cutting speed reduces the time of thermal contact between the tool and the workpiece surface, while the increase in supply contributes to a more intensive heat removal from the chips. Meanwhile, the coefficient for depth of cut is positive ($+85.44t$), which corresponds to the observed increase in temperature with increasing cross-section of the cut layer.

The nonlinearity of the dependence is expressed by the quadratic terms S^2, V^2 and t^2, among which the positive coefficient for S^2 is particularly significant, reflecting the effect of optimal feed: after reaching a certain level, increasing the feed again leads to a growth of temperature due to increased cutting force and friction on the flank of the tool. One of the quadratic terms is negative, indicating a saturation effect, and another is at the border of statistical significance.

The paired relations of $S \cdot V$, $S \cdot t$ and $V \cdot t$ demonstrate moderate but significant factor interactions. The most pronounced interdependence was between cutting speed and depth ($-0.4646Vt$), reflecting compensation for the thermal effect due to increased heat transfer across the shell thickness. The interaction of feed and speed ($+7.604SV$) indicates the presence of regions where a coordinated increase in these parameters contributes to temperature stabilization, which is confirmed experimentally (Fig. 6).

The results obtained confirm the high sensitivity of the thermal response of the metal-composite system to the combination of process parameters and demonstrate the significance of the geometric and thermophysical characteristics of the structure. The constructed 3.5TP model shows that even with a relatively small shell thickness of $\delta = 3.5$ mm, heat transfer processes in the cutting zone are determined by the complex interaction of cutting parameters and the material properties of the metal – MPCM system. This allows us to assert that further development of research should be aimed at expanding the scope of applicability of the obtained patterns and increasing the universality of the proposed model.

A promising direction is the parametric study on the effect of metal shell thickness on the thermal behavior of the MCS during turning. The variation of δ affects the heat rejection rate and the temperature field pattern, thus allowing the overheating resistance of the metal-polymer to be controlled. Systematic variation of the shell thickness will make it possible to construct a generalized *"δ–T"* relationship, enabling the prediction of thermal risks for various hybrid component configurations.

An equally important task is to validate the constructed model on alternative types of metal-polymer composites with different thermal conductivity, heat capacity, and temperature rating. Conducting similar experiments with composites based on aluminum or nickel fillers, as well as using other grades of structural steel, will help determine universal heat transfer patterns and refine the applicability limits of the regression relationships.

The next direction should be a comprehensive study of the relationship between temperature, surface roughness, and tool wear, supplemented by recording cutting forces and vibroacoustic characteristics. This coupled analysis will enable the development of integrated maps for permissible machining conditions, where thermal constraints are considered alongside surface quality and tool life indicators. This will lay the groundwork for multi-factor optimization of the process parameters.

The impact of metalworking fluids (MWF) on reducing temperature extremes in the cutting zone deserves special attention. The experiment used a standard MWF supply, but it would be advisable to further explore alternative technologies, such as minimum quantity lubrication (MQL), aerosol cooling, and cryogenic techniques. These methods can provide localized temperature reduction and reduce the thermal impact on the metal-polymer filler, specifically when working near the 170°C threshold.

An important area for further research is the identification of heat transfer mechanisms and the degradation of adhesive bonds at the metal – MPCM interface under cyclic thermomechanical loads. Monitoring this effect will enable a quantitative evaluation of the contact zone stability and a more precise definition of the durability criteria for hybrid components in service.

Finally, numerical 3D models of thermal processes and digital twins of metal-composite systems offer significant potential for improving prediction accuracy. Their development and calibration using the experimental data obtained in this work will open up the possibility of rapid engineering calculation of temperature fields under production conditions and the implementation of the method in an adaptive process control system.

Pursuing the outlined directions will enable the transformation of the proposed approach into a standardized methodology for assigning mechanical processing modes for metal-composite systems, providing robust control of the thermal load and durability of tooling products.

Conclusion. The conducted research has confirmed the feasibility of accurate experimental simulation of the thermal behavior of metal-composite systems (MCS), which comprise an additively manufactured metal shell filled with a polymer composite, by means of the developed measuring assembly. The experimental apparatus was designed to provide reliable temperature measurements at the metal–polymer composite interface, enabling a quantitative evaluation of the thermal load during turning under conditions representative of practical engineering applications.

The application of a full factorial experimental design provided the identification of the major effects of cutting parameters, the determination of their interactions, and the detection of nonlinearities through introducing central points. The constructed second-order regression model for the shell thickness variant of δ = 3.5 mm (3.5TP model) demonstrated high statistical adequacy ($R^2 = 0.9513$, $F = 364.31$, $p < 10^{-5}$) and good agreement with the results of thermal imaging verification, validating the experimental methodology.

Engineering interpretation of the model coefficients has shown that the depth of cut t is the decisive factor affecting the temperature increase, whereas the feed rate S has a moderate effect, and the cutting speed V exhibits the lowest sensitivity within the ranges studied. These relationships provide a clear understanding of the contribution of each parameter to the thermal response and can be applied to optimize the machining parameters.

Based on the 3.5TP model, response surfaces and a contour map of temperature fields are constructed, allowing for the identification of "safe zones" of turning modes in which the temperature at the metal-polymer composite interface does not exceed the limit value of T ≤ 170°C. The introduction of this technological constraint prevents thermal degradation of the metal-polymer composite and confirms the feasibility of finish turning of MCS without damaging the filler.

The developed model is of significant applied value for engineering prediction and standardization of process modes for the machining of hybrid components — both for shaping molds with conformal cooling channels and for composite bodies of indexable drills. Practical implementation of the proposed approach reduces the risk of thermal damage to metal-polymer structures, improves the reproducibility of product quality characteristics, and guarantees their operational durability while maintaining high process efficiency.

References

1. Kumar P, Acherjee B, Ghose J, Chattopadhyaya S. A Focused Review of Metal-Polymer Structural Composites: Fabrications, Characterization, Applications, and Future Prospects. *Engineering Research Express.* 2025;7(4):042401. https://doi.org/10.1088/2631-8695/ae192a

2. Hexin Jiang, Zhicheng He, Eric Li, Chao Jiang, Dong Mi. Additive Manufacturing-driven Topological Design Considering Overhang and Connectivity Constraints Induced by Closed Cavity. *Structural and Multidisciplinary Optimization*. 2024;67:118. https://doi.org/10.1007/s00158-024-03840-9

3. Morillas AV, Alonso JM, Caballero AB, Sisamón CC, Ceruti A. Adaptive Variable Design Algorithm for Improving Topology Optimization in Additive Manufacturing Guided Design. *Inventions.* 2024;9(4):70. https://doi.org/10.3390/inventions9040070

4. Lubimyi NS, Chepchurov M, Polshin AA, Gerasimov MD, Chetverikov BS, Chetverikova A, et al. Reducing the Cost of 3D Metal Printing Using Selective Laser Melting (SLM) Technology in the Manufacture of a Drill Body by Reinforcing Thin-Walled Shell Forms with Metal-Polymers. *Journal of Manufacturing and Materials Processing*. 2024;8(2):44. https://doi.org/10.3390/jmmp8020044

5. Malyshev VF, Dyachenko SV. *Cutting Hard-to-Machine Steels.* Moscow: Mashinostroenie; 2010. 248 p. (In Russ.)

6. Zhigao Chen, Fei Ding, Zhichao Zhang, Qiuyan Liao, Zheng Qiao, Yuan Jin, et al. A Review on Machining SiCp/Al Composite Materials. *Micromachines*. 2024;15(1):107. https://doi.org/10.3390/mi15010107

7. Trent EM, Wright PK. *Metal Cutting,* 4th ed. Boston: Butterworth-Heinemann; 2000. 464 p.

8. Fominov EV, Gvindjiliya VE, Marchenko AA, Shuchev CG. Effect of Periodic Fluctuations of Cutting Mode Parameters on the Temperature of the Front Face of a Turning Tool. *Advanced Engineering Research (Rostov-on-Don).* 2025;25(1):32–42. https://doi.org/10.23947/2687-1653-2025-25-1-32-42

9. Haibo Liu, Chengxin Wang, Te Li, Qile Bo, Kuo Liu, Yongqing Wang. Fixturing Technology and System for Thin-walled Parts Machining: A Review. *Frontiers of Mechanical Engineering*. 2023;17(4):55. https://doi.org/10.1007/s11465-022-0711-5

10. Sebbe NPV, Silva FJG, Costa RDFS, Fernandes F, Sousa VFC, Sales-Contini RCM. Wear Behavior of TiAlVN-Coated Tools in Milling Operations of INCONEL® 718. *Coatings.* 2024;14(3):311. https://doi.org/10.3390/coatings14030311

11. Polo S, Rubio EM, Marín MM, Sáenz de Pipaón JM. Evolution and Latest Trends in Cooling and Lubrication Techniques for Sustainable Machining: A Systematic Review. *Processes*. 2025;13(2):422. https://doi.org/10.3390/pr13020422

12. Joon-Koo Park, Choon-Man Lee, Dong-Hyeon Kim. Investigation on the Thermal Effects of WC-Co Turning Inserts Deposited by Additive Manufacturing of Titanium Alloy Powder. *Metals*. 2021;11(11):1705. https://doi.org/10.3390/met11111705

13. Yupeng Wei, Dazhong Wu. Model-based Real-time Prediction of Surface Roughness in Fused Deposition Modeling with Graph Convolutional Network-based Error Correction. *Journal of Manufacturing Systems*. 2023;71(7):286–297. https://doi.org/10.1016/j.jmsy.2023.09.001

14. Al-Mahmood M, Abuzaid W, Alkhader M, Alnaser AS. Optimizing Laser Powder Bed Fusion Parameters for Support-free 0° Overhang Structures in Stainless Steel 316L: The Case of Honeycomb Core Sandwich Structures. *Progress in Additive Manufacturing*. 2025;10:7815–7833. https://doi.org/10.1007/s40964-025-01074-9

15. Andreacola FR, Capasso I, Langella A, Giuseppe Brando. 3D-printed Metals: Process Parameters Effects on Mechanical Properties of 17-4 PH Stainless Steel. *Heliyon*. 2023;9(7):e17698. https://doi.org/10.1016/j.heliyon.2023.e17698

16. Hoang VCh. Practical Research Cutting of Temperature in Turning. *News of Tula State University. Technical Sciences.* 2015;(7–1):78–84.

17. Tingting Zhou, Min Zhang, Tianliang Hu, Lingpeng Meng, Mingdong Yi, Jingjie Zhang, et al. Research on the Online Monitoring Method of Cutting Tool Wear Based on the Mechanism-Data Fusion Concept of Digital Twin. *Journal of Manufacturing Processes*. 2025;148:386–407. https://doi.org/10.1016/j.jmapro.2025.05.028

18. Tanner Jones, Yang Cao. Tool Wear Prediction Based on Multisensor Data Fusion and Machine Learning. *International Journal of Advanced Manufacturing Technology*. 2025;137:5213–5225. https://doi.org/10.1007/s00170-025-15472-4

19. Zhangabay N, Chepela D, Tursunkululy T, Zhangabay A, Kolesnikov A. Analysis of the Effect of Porosity on Thermal Conductivity with Consideration of the Internal Structure of Arbolite. *Construction Materials and Products*. 2024;7(3):1–12. https://doi.org/10.58224/2618-7183-2024-7-3-4

About the Authors:

Nickolai S. Lyubimyi, Cand.Sci. (Eng.), Associate Professor of the Department of Hoist Transport and Road Machines, V.G. Shukhov Belgorod State Technological University (46, Kostyukov Str., Belgorod, 308012, Russian Federation) SPIN-code, ORCID, ResearchGate, ScopusID, ResearcherID, nslubim@bk.ru

Boris S. Chetverikov, Cand.Sci. (Eng.), Associate Professor of the Department of Hoist Transport and Road Machines, V.G. Shukhov Belgorod State Technological University (46, Kostyukov Str., Belgorod, 308012, Russian Federation) SPIN-code, ORCID, ResearchGate, ScopusID, ResearcherID, await_rescue@mail.ru

Michail D. Gerasimov, Cand.Sci. (Eng.), Associate Professor of the Department of Hoist Transport and Road Machines, V.G. Shukhov Belgorod State Technological University (46, Kostyukov Str., Belgorod, 308012, Russian Federation) SPIN-code, ORCID, ScopusID, ResearcherID, mail_mihail@mail.ru

Mikhail V. Bytsenko, student, Junior Researcher at the Laboratory of Additive Manufacturing of Composite Parts with a Topologically Optimized Shape, V.G. Shukhov Belgorod State Technological University (46, Kostyukov Str., Belgorod, 308012, Russian Federation) SPIN-code, ORCID, ScopusID, ResearcherID, b.michutka2005@gmail.com

Andrey A. Pol'shin, Postgraduate student, Department of Hoist Transport and Road Machines, V.G. Shukhov Belgorod State Technological University (46, Kostyukov Str., Belgorod, 308012, Russian Federation) SPIN-code, ORCID, ScopusID, ResearcherID, info@polshin.ru

Ardalion A. Mal'tsev, Postgraduate student, Department of Hoist Transport and Road Machines, V.G. Shukhov Belgorod State Technological University (46, Kostyukov Str., Belgorod, 308012, Russian Federation) SPIN-code, ORCID, ScopusID, ardalion_bgtu@mail.ru

Claimed Contributorship:

NS Lyubimyi: conceptualization, supervision.
BS Chetverikov: methodology, writing – original draft preparation.
MD Gerasimov: formal analysis, writing – original draft preparation.
MV Bytsenko: investigation, writing – original draft preparation.
AA Pol'shin: visualization, writing – original draft preparation.
AK Maltsev: data collection, writing – original draft preparation.

Conflict of Interest Statement: **the authors declare no conflict of interest.**

All authors have read and approved the final manuscript.

Об авторах:

Николай Сергеевич Любимый, кандидат технических наук, доцент, доцент кафедры «Подъёмно-транспортные и дорожные машины» Белгородского государственного технологического университета им. В.Г. Шухова (308012, Российская Федерация, г. Белгород, ул. Костюкова, 46) SPIN-код, ORCID, ResearchGate, ScopusID, ResearcherID, nslubim@bk.ru

Борис Сергеевич Четвериков, кандидат технических наук, доцент, доцент кафедры «Подъёмно-транспортные и дорожные машины» Белгородского государственного технологического университета им. В.Г. Шухова (308012, Российская Федерация, г. Белгород, ул. Костюкова, 46) SPIN-код, ORCID, ResearchGate, ScopusID, ResearcherID, await_rescue@mail.ru

Михаил Дмитриевич Герасимов, кандидат технических наук, доцент, доцент кафедры «Подъёмно-транспортные и дорожные машины» Белгородского государственного технологического университета им. В.Г. Шухова (308012, Российская Федерация, г. Белгород, ул. Костюкова, 46) SPIN-код, ORCID, ResearcherID, ScopusID, mail_mihail@mail.ru

Михаил Витальевич Быценко, студент, младший научный сотрудник Лаборатории аддитивного производства композиционных деталей с топологически оптимизированной формой Белгородского государственного технологического университета им. В.Г. Шухова (308012, Российская Федерация, г. Белгород, ул. Костюкова, 46) SPIN-код, ORCID, ResearcherID, b.michutka2005@gmail.com

Андрей Александрович Польшин, аспирант кафедры «Подъёмно-транспортные и дорожные машины» Белгородского государственного технологического университета им. В.Г. Шухова (308012, Российская Федерация, г. Белгород, ул. Костюкова, 46) SPIN-код, ORCID, ResearcherID, ScopusID, info@polshin.ru

Ардалион Константинович Мальцев, аспирант кафедры «Подъёмно-транспортные и дорожные машины» Белгородского государственного технологического университета им. В.Г. Шухова (308012, Российская Федерация, г. Белгород, ул. Костюкова, 46) SPIN-код, ORCID, ScopusID, ardalion_bgtu@mail.ru

Заявленный вклад авторов:
Н.С. Любимый: разработка концепции, научное руководство.
Б.С. Четвериков: разработка методологии исследования, написание рукописи.
М.Д. Герасимов: формальный анализ, написание рукописи.
М.В. Быценко: проведение исследования, написание рукописи.
А.А. Польшин: визуализация результатов исследования, написание рукописи.
А.К. Мальцев: сбор данных, написание рукописи.

Конфликт интересов: **авторы заявляют об отсутствии конфликта интересов.**

Все авторы прочитали и одобрили окончательный вариант рукописи.

Received / Поступила в редакцию 28.12.2025
Reviewed / Поступила после рецензирования 17.01.2026
Accepted / Принята к публикации 02.02.2026

MACHINE BUILDING AND MACHINE SCIENCE
МАШИНОСТРОЕНИЕ И МАШИНОВЕДЕНИЕ

UDC 621.9:531.3
https://doi.org/10.23947/2687-1653-2026-26-1-2103

Original Theoretical Research

Vibration Control of Tool Flank Wear in Turning

Valery E. Gvindjiliya
Don State Technical University, Rostov-on-Don, Russian Federation
✉ vvgvindjiliya@donstu.ru

EDN: EYOAES

Abstract

Introduction. The wear rate of a cutting tool can be controlled by introducing additional vibrations into the cutting zone. The effect of vibration parameters on tool wear appears to be well-studied. However, the conclusions of some such studies are contradictory. It is noted that vibrations of varying amplitudes can both increase and decrease wear. There are no analytical models in the literature that resolve this contradiction or reflect the nonlinear relationship between the tool and workpiece subsystems under cutting. Furthermore, the fact that wear on different tool faces requires different force interaction models is not taken into account. The present research fills these gaps. The objective of the study is to determine the patterns of impact of high-frequency vibrations (HFV) on tool flank wear.

Materials and Methods. The data from mathematical modeling of the dynamic cutting system in Simulink were used, taking into account the forces on the back face, effective parameters, and the HFV. Equipment: 16K20 machine tool, vibration control measuring stand with a frequency range of 0.4–15000 Hz, computer, E20-10 analog-to-digital converter, acoustic system, and STD.201-1 cutting force testing stand. Workpieces made of 10GN2MFA steel with a diameter of D = 84 mm were machined using tools with brazed T15K6 plates without lubrication.

Results. The effect of the HFV on the contact interaction forces along the tool flank and the phase trajectory of the tool deformation displacements are demonstrated for different HFV amplitudes: from $0.5 \cdot 10^{-2}$ to $2 \cdot 10^{-2}$ mm. It is established that power N of irreversible energy transformations (IET) depends on the direction of the introduced vibrations. The dependence of tool wear rate on additional vibrations with amplitudes of 5 and 10 μm in different directions at cutting speeds of 1 m/s, 1.4 m/s, and 2 m/s is shown. The results obtained are compared with wear trajectories without disturbances.

Discussion. The optimal amplitude of additional vibrations in the feed direction depends on the tool clearance and decreases with wear stage. The maximum wear value drops from 0.55 mm to 0.35 mm when introducing vibrations with an amplitude of 5 μm and to 0.26 mm — at 10 μm. With additional vibrations in the tangential direction, wear rate depends weakly on the amplitude of the introduced vibrations, as it is many times smaller than the velocity of the tool vibrational displacements. The maximum wear value decreases from 0.65 mm to 0.6 mm at 5 μm and to 0.48 mm — at 10 μm. With increased wear, there is no optimal amplitude for additional vibrations.

Conclusion. The developed models allow for a quantitative assessment of the impact of HFV on the tool flank wear rate and the appropriate selection of vibration parameters introduced into the cutting zone. This allows for the creation of:
– virtual models of the cutting process and the selection of modes to minimize wear rate;
– wear monitoring systems with a comprehensive approach to prediction.
Next, it is required to study the dynamics of the cutting process at HFV amplitudes greater than 10–15 μm.

Keywords: high-frequency vibrations, additional vibrations, dynamic cutting system, tool wear, irreversible energy transformations

Acknowledgements. The author would like to thank Dr.Sci. (Engineering), Professor V.L. Zakovorotny for fruitful discussions and significant recommendations during the preparation of the material. In addition, the author appreciates the assistance of the staff of the laboratory of the Research Institute for Vibrotechnology, Don State Technical University, in conducting scientific experiments.

Funding Information. The work is done within the framework of the Agreement for the implementation of applied scientific research “Development of Software and Hardware for Monitoring and Analysis of Cutting Parameters and Operational Characteristics of CNC Machines” (FZNE–2025–0008) no. 075–03–2025–302/10 dated 23.12.2025.

For Citation. Gvindjiliya VE. Vibration Control of Tool Flank Wear in Turning. *Advanced Engineering Research* (*Rostov-on-Don*). 2026;26(1):2103. https://doi.org/10.23947/2687-1653-2026-26-1-2103

Оригинальное теоретическое исследование

Вибрационное управление износом задней грани инструмента при точении

В.Е. Гвинджилия ✉
Донской государственный технический университет, г. Ростов-на-Дону, Российская Федерация
✉ vvgvindjiliya@donstu.ru

Аннотация

Введение. Интенсивностью износа режущего инструмента можно управлять, вводя дополнительные колебания в зону резания. Представляется достаточно изученным влияние параметров колебаний на износ инструмента. Однако выводы некоторых таких работ противоречивы. Отмечается, что вибрации с различной амплитудой могут как увеличивать износ, так и уменьшать его. В литературе нет аналитических моделей, разрешающих данное противоречие, отражающих нелинейную взаимосвязь подсистем инструмента и заготовки при резании. Кроме того, не принимается во внимание, что износу по разным граням инструмента требуются разные модели силового взаимодействия. Отмеченные пробелы восполняет представленная работа. Цель исследования — определить закономерности влияния высокочастотных колебаний (ВЧК) на износ задней грани инструмента.

Материалы и методы. Использовались данные математического моделирования динамической системы резания в Simulink с учетом сил по задней грани, эффективных параметров и ВЧК. Оборудование: станок 16К20, измерительный стенд вибрационного контроля с частотным диапазоном 0,4–15000 Гц, компьютер, аналого-цифровой преобразователь Е20–10, акустическая система, стенд для исследования сил резания — STD.201–1. Заготовки из стали 10ГН2МФА диаметром D = 84 мм обрабатывали инструментами с припаянными пластинами из Т15К6 без смазки.

Результаты исследования. Демонстрируется влияние ВЧК на силы контактного взаимодействия по задней грани инструмента и фазовая траектория деформационных смещений инструмента при разных амплитудах ВЧК: от $0{,}5 \cdot 10^{-2}$ до $2 \cdot 10^{-2}$ мм. Установлено, что мощность N необратимых преобразований энергии (НПЭ) зависит от направления вводимых вибраций. Показана зависимость интенсивности износа инструмента от дополнительных колебаний с амплитудами 5, 10 мкм в разных направлениях при скоростях резания 1 м/с, 1,4 м/с, 2 м/с. Полученные результаты сравниваются с траекториями износа без возмущения.

Обсуждение. Оптимальная амплитуда дополнительных вибраций в направлении подачи зависит от заднего угла инструмента и уменьшается с изменением стадии износа. Максимальное значение износа падает с 0,55 мм до 0,35 мм при введении колебаний с амплитудой 5 мкм и до 0,26 мм — при 10 мкм. При дополнительных вибрациях в тангенциальном направлении интенсивность износа слабо зависит от амплитуды вводимых колебаний, так как она во много раз меньше скорости колебательных смещений инструмента. Максимальное значение износа уменьшается с 0,65 мм до 0,6 мм при 5 мкм и до 0,48 мм — при 10 мкм. При интенсификации износа не существует оптимальной амплитуды дополнительных вибраций.

Заключение. Разработанные модели позволяют количественно оценивать влияние ВЧК на интенсивность износа инструмента по задней грани и обоснованно подбирать параметры колебаний, вводимых в зону резания. Так можно создавать:

– виртуальные модели процесса резания и подбирать режимы для минимизации скорости износа,

– системы мониторинга износа с комплексным подходом к прогнозированию.

Далее необходимо исследовать динамику процесса резания при амплитудах ВЧК более 10–15 мкм.

Ключевые слова: высокочастотные колебания, дополнительные колебания, динамическая система резания, износ инструмента, необратимые преобразования энергии

Благодарности. Автор выражает благодарность доктору технических наук, профессору В.Л. Заковоротному за плодотворные обсуждения и значимые рекомендации в процессе подготовки материала, а также сотрудникам лаборатории научно-исследовательского института «Вибротехнология» Донского государственного технического университета, оказавшим помощь при проведении научных экспериментов.

Финансирование. Работа выполнена в рамках соглашения на реализацию прикладного научного исследования «Разработка программно-аппаратных средств для мониторинга и анализа параметров резания и эксплуатационных характеристик станков с ЧПУ» (FZNE–2025–0008) № 075–03–2025–302/10 от 23.12.2025.

Для цитирования. Гвинджилия В.Е. Вибрационное управление износом задней грани инструмента при точении. *Advanced Engineering Research* (*Rostov-on-Don*). 2026;26(1):2103. https://doi.org/10.23947/2687-1653-2026-26-1-2103

Introduction. The impact of vibration on tool wear is the subject of numerous studies, as cutter wear determines the quality of parts and the efficiency of machining. The impact of vibrational oscillations on cutting force dynamics is comprehensively analyzed in the literature [1]. The diversity of tool and workpiece vibration sources and, correspondingly, the diversity of methods for monitoring, evaluating, and modeling them are noted [2].

At the initial stages of the development of cutting theory, vibrations were considered as a consequence of the loss of stability of the equilibrium of elastic deformations in a moving coordinate system, whose motion was determined by the trajectories of the machine actuators [3]. The loss of stability was associated with the effect of force regeneration [4], and a criterion for the stability of the equilibrium of elastic deformations [5] was proposed for its analysis. Regeneration problems were studied for turning [6], milling [7], drilling [8], and other operations.

The loss of stability was explained by:

– delay in force variations with changes in deformation [9];

– decreasing characteristic of force variation with increasing cutting velocity [10];

– regenerative effect of the tool mark on the workpiece [11];

– nonlinear dependence of the friction forces of the chip as it moves along the front face of the tool [12].

It is known [13] that when the trajectories of the tool formative movements lose stability, the most typical attracting sets for vibrations are those of the limit cycle [14] and the chaotic attractor [15]. It is established that changes in the attracting sets of tool vibrations are determined by the cutting conditions. For example, when changing the feed rate of the tool, all types of Andronov-Hopf bifurcations can be observed [16]. Vibrations were considered as a consequence of disturbances related to the quality of the machine tool. These were primarily spindle runout [17] and kinematic disturbances [18]. Depending on the frequency of external disturbances, various effects were observed [19]. At frequencies close to the natural frequencies of the interacting subsystems, parametric phenomena such as self-excitation, oscillation synchronization [20], and others, occur.

Finally, vibrations were studied as vibrations purposefully introduced into the cutting zone to achieve a beneficial effect: chip fragmentation [21], increased tool life [22], and improved surface quality [23]. It has been shown that introducing ultrasonic vibrations (USV) into the cutting zone can improve the quality of work and reduce the intensity of tool wear [24]. To improve the efficiency of USV, USV generation systems are proposed in which feedback for self-excitation is realized through vibrations generated under the cutting process [25]. In this case, nonlinear effects of the interaction between the tool and the workpiece are taken into account, specifically, the decreasing characteristic of cutting forces with increasing velocity [26] or the amplitude-frequency modulation of the system vibrations [27].

Researchers have paid particular attention to the impact of vibrations on the tool wear rate under cutting. It is widely believed that vibrations increase wear and thereby reduce tool life [23]. However, there is evidence that with an increase in the amplitude of the introduced vibrations, an optimum amplitude is recorded at which the wear rate reaches a minimum [28]. This effect is most pronounced when ultrasonic excitation is applied through the tool [28] and when turning difficult-to-machine materials such as AISI 52100 [29] or P9M4K8F [30].

To analyze the impact of vibrations on wear rate, methods and mathematical tools are needed that can allow for the rapid assessment of wear rate. It is advisable to use the power of irreversible energy transformations (PIET) in the contact zone of the tool and the workpiece as a diagnostic indicator [31]. When turning with tools with carbide inserts, the main type of wear is observed along the flank [32]. PIET is the primary source of heat generation, so it can be argued that the optimal cutting conditions correspond to the optimal temperature [33]. Heat production and PIET are correlated and adequately reflect wear rate [34]. Therefore, when developing wear monitoring systems, temperature and PIET in the cutting zone are considered as key diagnostic parameters. Diagnostic information models employ methods of autoregressive spectral analysis [35], models based on cutting force analysis using analytical functions [36], machine learning [37], and vibroacoustic emission signal analysis [38]. When the PIET changes, the mechanisms of physical and chemical interaction (wear) in the contact between the tool and the workpiece change — from adhesive-fatigue [1] and abrasive [31] to diffusion-oxidative [39].

PIET is often considered within the entire cutting zone. However, the power distribution between the tool flank, the chip formation zone, and the secondary plastic deformation zone is disproportionate. When analyzing flank wear rate, it is required to consider irreversible energy transformations in the contact area between the tool flank and the workpiece. It is not always taken into account that vibrations cause periodic changes in the power of irreversible transformations, and depending on the current power, various wear mechanisms are activated — from frictional fatigue to diffusion-oxidation. Consequently, estimates of the velocity and rate of tool wear change periodically. Furthermore, the literature does not describe the transformation of high-frequency vibrations (HFV) introduced into the cutting zone into the trajectories of the tool flank and the workpiece, nor into the trajectories of the forces generated in the contact zone.

The objective of this study is to establish the relationship between the HFV and tool flank wear rate based on a developed theoretical model of cutting dynamics, as well as its numerical and experimental analysis. To achieve this goal, the following work is being conducted to refine the models, simulate, and conduct theoretical studies and experiments.

1. Mathematical models of the dynamic cutting system (DCS) are refined. They are supplemented with constraints formed in the contact between the tool flank and the workpiece.

2. How the HFV introduced into the cutting zone are transformed into trajectories of the flank and workpiece, as well as into trajectories of forces generated in the contact zone, is studied. Numerical modeling of these processes is performed.

3. The changes in tool wear rate on the flank during longitudinal turning of 10GN2MFA steel are studied theoretically and experimentally. Their dependence on the ultrasonic waves introduced into the cutting zone is determined using the PIET analysis.

The developed mathematical tools and methods can be interpreted as the creation of a virtual numerical model of wear of cutting tools for the optimal selection of vibration parameters introduced into the cutting zone.

Materials and Methods

1. Problem statement. Mathematical modeling of DCS that takes into account forces on the tool flank. We consider the relationship between wear and PIET, as well as wear intensity patterns. To determine the PIET, we create a model of the DCS disturbed by the HFV. We develop algorithms and a program for calculating the PIET trajectories in the tool flank – workpiece contact (Fig. 1).

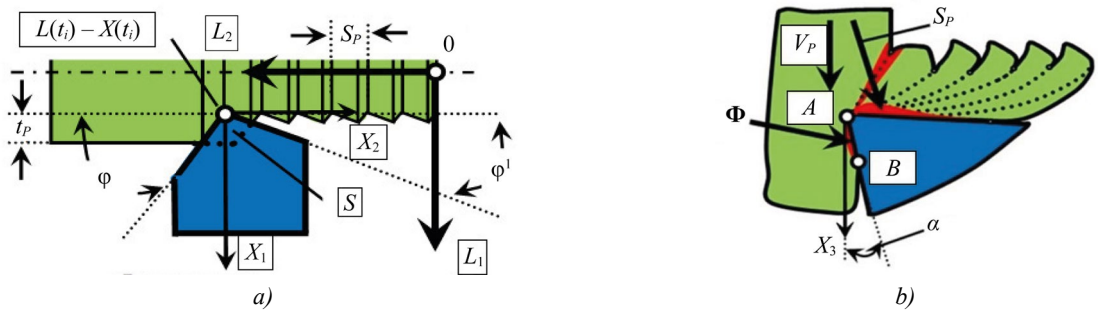

Fig. 1. Schematic diagram of the cutting process: *a* — representation of trajectories of actuators and deformation displacements; *b* — formation of cutting forces **F** in the region of primary and secondary plastic deformation, and additional forces **Φ** in the region *A* — *B*

Assume that the trajectories of the machine actuators are given in the form of displacements $\mathbf{L} = \{L_1, L_2, L_3\}^T \in \Re^{(3)}$ and velocities $\mathbf{dL/d} = \mathbf{V(t)}$, $\mathbf{V(t)} = \{V_1, V_2, V_3\}^T \in \Re^{(3)}$. Here, $L_1(t)$, $L_2(t)$ — trajectories of the transverse and longitudinal supports; $L_3(t) = \int_0^t \Omega(\xi) D(\xi) d\xi$ — displacements of the workpiece relative to the tool at the point of contact of the tool tip with the workpiece in the direction of its rotation; D — diameter of the machining surface, mm; d — diameter of the machined workpiece, mm (рис. 1).

The disturbances are characterized by displacements $\mathbf{\Delta X^{(X)}} = \{\Delta X_1^{(X)}, \Delta X_2^{(X)}, \Delta X_3^{(X)}\}^T \in \Re_{\mathbf{X}}^{(3)}$ and velocities $\mathbf{dX^{(X)}/dt} = \mathbf{\Delta V^{(X)}} = \{\Delta V_1^{(X)}, \Delta V_2^{(X)}, \Delta V_3^{(X)}\}^T \in \Re_{\mathbf{X}}^{(3)}$.

Let us consider the case when additional vibrations introduced into the cutting zone are represented by a vector of periodic disturbances: $\mathbf{\Delta X^{(X)}}(t) = \{\Delta X_{1,0}^{(X)} \sin(\Omega_\Delta t), \Delta X_2^{(X)} \sin(\Omega_\Delta t + \theta_2), \Delta X_3^{(X)} \sin(\Omega_\Delta t + \theta_3)\}^T \in \Re_{\mathbf{X}}^{(3)}$. Also — for velocities $\mathbf{\Delta V^{(X)}(t)} = \{\Delta X_{1,0}^{(X)} \Omega_\Delta \cos(\Omega_\Delta t), \Delta X_2^{(X)} \Omega_\Delta \cos(\Omega_\Delta t + \theta_2), \Delta X_3^{(X)} \Omega_\Delta \cos(\Omega_\Delta t + \theta_3)\}^T \in \Re_{\mathbf{X}}^{(3)}$.

Perturbations occur in the deformation space $\mathbf{X} = \{X_1, X_2, X_3\}^T \in \Re_{\mathbf{X}}^{(3)}$. Strain rates are $\mathbf{dX/dt} = \mathbf{V^{(X)}} = \{V_1^{(X)}, V_2^{(X)}, V_3^{(X)}\}^T \in \Re_{\mathbf{X}}^{(3)}$.

Vector $\mathbf{X}$ is considered in moving coordinates defined by $\boldsymbol{L}$ (Fig. 1). The unit of measurement for $\mathbf{L}$, $\mathbf{\Delta X^{(X)}}$ and $\mathbf{X}$ — mm, for $\mathbf{V(t)}$, $\mathbf{\Delta V^{(X)}}$ and $\mathbf{V^{(X)}}$ — mm/s.

The workpiece is rigid, so the trajectory of the shaping movements $\mathbf{L^{(\Phi)}} = \left\{L_1^{(\Phi)}, L_2^{(\Phi)}, L_3^{(\Phi)}\right\}^T \in \Re^{(3)}$ can be represented as:

$$\mathbf{L^{(\Phi)}} = \mathbf{L} + \mathbf{\Delta X^{(X)}} - \mathbf{X}. \tag{1}$$

We involve velocities $\mathbf{dL^{(\Phi)}/dt} = \mathbf{V^{(\Phi)}} = \mathbf{V} + \mathbf{\Delta V^{(X)}} - \mathbf{V^{(X)}}$ in the modeling. We use work [40] to indicate the relationship between forces and deformations:

$$\mathbf{m}\frac{\mathbf{d^2X}}{\mathbf{dt^2}} + \mathbf{h}\frac{\mathbf{dX}}{\mathbf{dt}} + \mathbf{cX} = \mathbf{F(L^{(\Phi)})} + \mathbf{\Phi(L^{(\Phi)})}. \tag{2}$$

Here, **m, h, c** — positive-definite symmetric matrices of inertial, velocity, and elastic coefficients, m = *diag*{*m*, *m*, *m*}. The dimensions of the matrix elements **m** — kg·s^2/mm, **h** — kg·s/mm, **c** — kgf/mm. $\mathbf{F(L^{(\Phi)})} = \left\{F_1, F_2, F_3\right\}^T \in \Re_{\mathbf{X}}^{(3)}$ — forces generated in the area of contact between the tool front face and the cutting zone. They depend on the dynamic properties in the areas of primary and secondary plastic deformation (highlighted in red in Fig. 1). $\mathbf{\Phi(L^{(\Phi)})} = \left\{\Phi_1, \Phi_2, \Phi_3\right\}^T \in \Re_{\mathbf{X}}^{(3)}$ — additional forces caused by the approach of the tool flank to the workpiece (region *A* — *B* in Fig. 1).

Forces $\mathbf{\Phi(L^{(\Phi)})}$, introduced additionally to the model considered in [10] reveal the interaction between the tool flank and the workpiece. They limit the development of periodic movements, generate forces acting on the flank, and, together with the trajectories $\mathbf{L^{(\Phi)}}$, determine the work and power of irreversible energy transformations in the contact area of the tool flank. Forces **F** and **Φ** are represented as functions of trajectories $\mathbf{L^{(\Phi)}}$, which vary depending on $\Delta X_i(t)$ and the elastic response of the tool $X_i(t)$.

Let us analyze processing with constant modes: $L_1 = L_1(0) = d/2 = const$.

Here, d — diameter of the processed workpiece under cutting (Fig. 1), $L_2(t) = V_2 t$, $V_2 = const$, $L_3(t) = V_3 t$, $V_3 = \pi D\Omega = const$.

Before we start modeling $\mathbf{F(L^{(\Phi)})}$, let us make three statements [41].

1. Forces **F** grow monotonically with increasing cutting area S (Fig. 1), which can be represented as: $S(t) = t_P(t)S_P(t)$. Here and hereafter $t_P(t)$, $S_P(t)$ — current values in mm of the cutting depth and the feed rate, respectively.

2. Vector **F** has the form: $\mathbf{F} = \{\chi_1, \chi_2, \chi_3\}^T$, where χ_i — angular coefficients, and $\{(\chi_1)^2 + (\chi_2)^2 + (\chi_3)^2\} = 1$.

3. There is a delay between the variations of **F** and S.

The delay is modeled by an aperiodic link with time constant $T^{(0)}$, which depends on the modes $t_P(t)$, $S_P(t)$, $V_P(t)$. Here, $V_P = \{(V_1)^2 + (V_2)^2 + (V_3)^2\}^{0.5}$ — cutting velocity. If there are no vibration disturbances and the deformation rates are small, then $V_P(t) \approx V_3$, since $V_2 \ll V_3$, and for longitudinal turning — $V_1 = 0$. When determining time constant $T^{(0)}$, called the chip formation time constant in [3], it is taken into account that the path traveled by the tool tip relative to the workpiece remains approximately constant [3]. In this case, the transition from one stationary state to another is considered.

The above means that $T^{(0)}$ depends mainly on the cutting velocity, and it can be approximated:

$$T^{(0)} = \frac{T_0^{(0)}}{1 + k^{(T)} V_3^{(\Phi)}}. \tag{3}$$

Here, $T^{(0)}$ — time constant in the region of low cutting speeds, s; $k^{(T)}$ — coefficient with the dimension s/mm.

According to [10], approximation (3) is valid in a limited range of variations of the process mode. For example, when processing 45 steel, the limitations are determined as $V_P \in (0.2; 2.5) \cdot 10^3$ mm/s. The greatest approximation error is observed in the range of low cutting velocities and depends mainly on the properties of the limit state of the material being processed, its plasticity and thermophysical characteristics. If the parameters are specified, then the following is valid:

$$T^{(0)}\left(V_3^{(\Phi)}\right)dF^{(0)}/dt + F^{(0)} = \rho\left\{t_P^{(0)} + \Delta X_1(t) - X_1(t)\right\}\left\{\int_{t-T}^{t}\left\{V_2 + \Delta V_2(\xi) - V_2^{(X)}(\xi)\right\}d\xi\right\}, \tag{4}$$

where T — workpiece turnover time, s; ρ — chip pressure on the front face of the tool, kg/mm^2.

To illustrate the analysis method, we limit ourselves to the case where the main and auxiliary angles in the tool plan are equal (Fig. 1): $\phi \Rightarrow \pi/2$, $\phi^1 \Rightarrow 0$.

Let us consider the disturbances: $\mathbf{\Delta V^{(X)}} = \{0, \Delta V_2^{(X)}, 0\}^T$ and $\mathbf{\Delta V^{(X)}} = \{0, 0, \Delta V_3^{(X)}\}^T$.

We exclude $\mathbf{\Delta V^{(X)}} = \{\Delta V_1^{(X)}, 0, 0\}^T$ from the analysis since $S_P \ll t_P$. Moreover, the internal gain in the self-excitation channel varies significantly depending on the deformation direction. For the direction X_1, the gain will be an order of magnitude smaller than for X_2. Furthermore, with the tool geometry under consideration, it is precisely the vibrations in $X_2 - X_3$ plane that bring the tool flank and the workpiece closer together, which determines the intensity of wear and generates additional forces $\mathbf{\Phi(L^{(\Phi)})}$.

Thus, if $\Omega = const$, $dX_3/dt \to 0$ and $d\Delta X_3(t)/dt \to 0$, then $T = (\Omega)^{-1}$. Otherwise, T is required to calculate from the ratio:

$$T\left(L_3^{(\phi)}\right) = \int_{L_3^{(\phi)} - \pi D}^{L_3^{(\phi)}} \frac{d\xi}{V_P(\xi)} \tag{5}$$

Here, V_P — law of cutting velocity variation, taking into account elastic deformations and disturbances. To study the PIET, it is necessary to know the force model $\mathbf{\Phi(L^{(\Phi)})}$. After cutting-in (Fig. 2 *a*), a trace trajectory is formed on the workpiece at angle $\varphi = arctg(V_3/V_2)$ (Fig. 2 *b*).

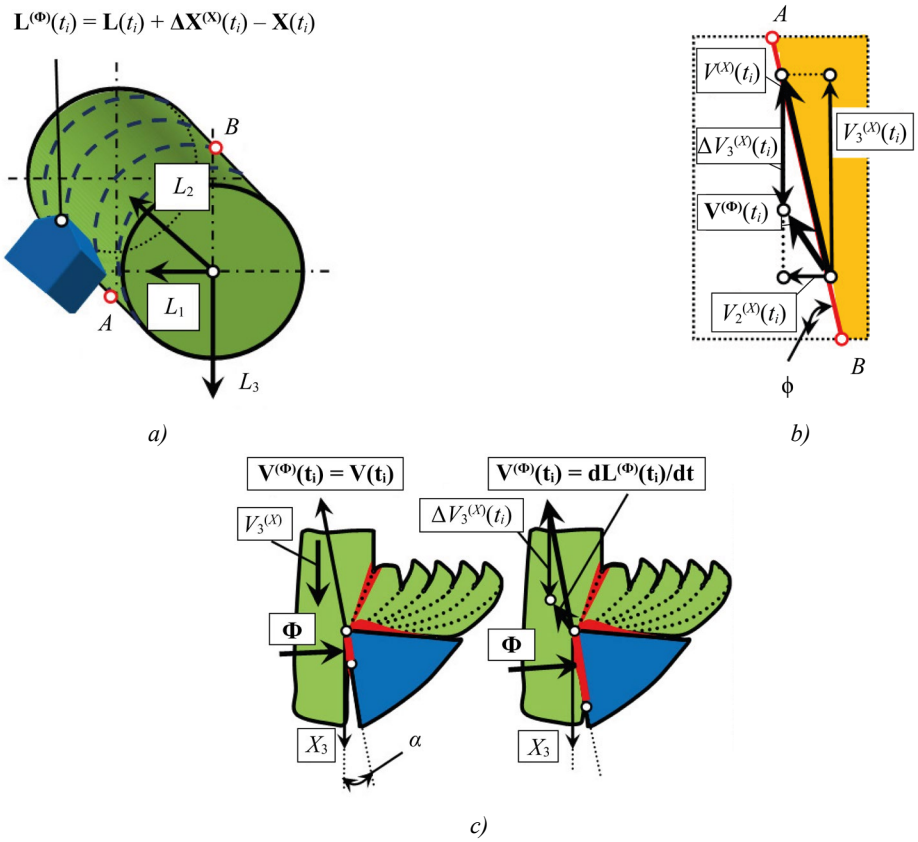

Fig. 2. Forces $\mathbf{\Phi(L^{(\Phi)})}$ generation diagram: *a* — formation of a tool mark on the workpiece surface; *b* — change in direction of movement when velocity and direction of rotation of the workpiece coincide; *c* — convergence of the surfaces of tool flank and workpiece when the direction of movement of the velocity $\mathbf{V^{(\Phi)}}(t_i)$ changes

Direction ϕ is indicated by the line *A* — *B* (Figs. 1, 2). When changing $V_3^{(X)}$, as shown in Figure 2 *b*, due to $\Delta V_3^{(X)}$, the direction of the tool movement towards or away from the workpiece changes. As the surfaces approach each other, the forces on the flank increase. When vector $V^{(X)}$ shifts to the area highlighted in yellow (Fig. 2 *b*), the tool moves away from the workpiece, and area *S* decreases. If the equilibrium position of elastic deformations is stable and unperturbed, then the trajectory of movement in the direction *A* — *B* (Fig. 2) is an attractor. It is displaced in space **L** by a constant amount of elastic deformation. Due to disturbances or loss of stability, periodic convergence or repulsion of the flanks from the workpiece occurs. To estimate the deviation of the trajectory from the projected attractor, it is convenient to consider dimensionless aggregated coordinates:

$$\upsilon(t) = \left(V_2 + \Delta V_2^{(X)}(t) - dX_2/dt\right) / \left(V_3 + \Delta V_3^{(X)}(t) - dX_3/dt\right); \upsilon^* = V_2/V_3. \tag{6}$$

Here, $\upsilon(t)$ — dimensionless aggregated coordinate defining the current position of the direction of the tool tip movement; υ^* — aggregated coordinate defining the desired direction of tool movement, specified by velocities V_2 and V_3.

The approach of the flank to the workpiece surface depends on the kinematic value of the clearance angle α. The experiments described in [39] show that forces $\mathbf{\Phi(L^{(\Phi)})}$ increase disproportionately with decreasing α according to an exponential law. Therefore:

$$\begin{aligned}\Phi_2 &= k_\Phi F_0 + \rho_0\left[t_P^{(0)} - X_1(t)\right]exp\left[\varsigma\left(\upsilon-\upsilon^*\right)\right],\\ \Phi_3 &= k_\Phi k_T F_0 + k_T\rho_0\left\{\left(t_P^{(0)} - X_1(t)\right)exp\left[\varsigma\left(\upsilon-\upsilon^*\right)\right]\right\},\end{aligned} \tag{7}$$

where ρ_0 — coefficient of conversion of contact length into force, kg/mm; ς — dimensionless parameter dependent on the tool clearance angle α in statics; k_T — dimensionless coefficient of friction; k_Φ — dimensionless coefficient that determines the elastic recovery of the material.

From (7), it follows that there is a potential relationship between deformations and disturbances in the direction of trajectories *A* — *B* (Fig. 2), and they have virtually no effect on the forces generated at the contact between the tool flank and the workpiece. In this case, variations in cutting velocity in the range of actual values will be small. Let us denote the current variations in velocities in the directions X_2 and X_3: $\delta V_2 = \Delta V_2^{(X)}(t) - V_2^{(X)}(t)$, $\delta V_3 = \Delta V_3^{(X)}(t) - V_3^{(X)}(t)$. Then from (6), we obtain:

$$V_3\delta V_2^{(X)}(t) = V_2\delta V_3^{(X)}(t). \tag{8}$$

Let us consider harmonic disturbances in two orthogonal directions, maintaining the ratio between the amplitudes of the additional vibrations. In this case, the in-phase condition of vibration (8) is $V_3/V_2 = \delta V_3/\delta V_2$. It is almost never satisfied in the dynamic cutting system. There are two reasons for this. Firstly, $V_2 \ll V_3$, therefore, the direction of the total vibrations (i.e., vibrations introduced into the cutting zone with regard to deformation displacements) must be oriented along the direction of the cutting velocity. Secondly, it is important to consider the response from the cutting process. Then the total stiffness matrices of the tool subsystem become asymmetrical, even if we neglect the forces generated by the matrices **m** and **h**. Skew-symmetric components of the elasticity matrices generate circulatory forces that cause precessional movements of the tool relative to the workpiece. It has been experimentally established [39] that this form of vibrations always occurs. It provides phase displacements between vibrations in two orthogonal directions. Due to the asynchronous nature of the vibrations in the two orthogonal directions, periodically repeating sections are formed in which the tool flank and the workpiece are observed approaching each other. This occurs even with small variations in velocity relative to the established cutting velocity.

To determine the PIET, it is required to calculate the forces and vibrational velocities. Obviously, the PIET depends not only on the parameters introduced into the cutting zone of vibrations, but also on the dynamic properties of the entire USV. If we consider the interactions in terms of nonlinear acoustics, then the efficiency of ultrasonic vibration under cutting is determined by the acoustic impedance of the medium into which the ultrasonic vibrations are introduced [28]. In our case, this corresponds to the dynamic properties of the cutting system.

2. Mathematical modeling of effective parameters and forces. If we follow the paradigm of mesomechanics [42], then variation of the properties of the dynamic coupling formed by cutting, due to the introduction of HFV into the cutting zone, should be characterized by molecular-mechanical effects that change the properties of the system at the macro level. By frequency range at the macro level, we mean the range within the passbands of the interacting subsystems $\mathbf{\Omega^{(0)}} \in (0, \Omega_c)$, where Ω_c — cutoff frequency of the DCS.

Note that the macrosystem does not perceive HFV in the frequency range $\mathbf{\Omega^{(0)}}$, but they do change its properties. To explain this transformation, let us recall the cutting process and the dynamic coupling in the system of mechanical interactions (2). HFV contribute to the transformation of the parameters of this coupling, and subsequently — to the change in the macrosystem. This is known from the description of the averaging method in the theory of nonlinear vibrations [43].

The basic parameters affecting the properties of the system are ρ and $T^{(0)}$ [6]. A typical example of effective parameters is the dimensionless effective friction coefficient k_T, studied in [42]. The effective value of k_T can change and even reverse sign under vibrations. This depends on the trajectory of the HFV introduced into the contact area.

Let us describe the conditions for determining the effective value of k_T. For this purpose, the relationship between two factors is determined:

– the tangential forces of contact interaction;

– variations in their normal components.

For analysis, a frequency region within the passband of the interacting subsystems of the tool and workpiece is selected. The analysis time is the period of high-frequency vibrations.

Let us consider parameter ρ. Additional vibrations create a stress state that changes cyclically in the primary plastic deformation zone. The limit state of the material practically does not change, it remains close to its ultimate strength [44]. Integral and cyclic loads are redistributed, causing changes in the effective values of $\hat{\rho}$. Moreover, the dynamic bond formed by the cutting process lacks central symmetry with respect to deformations in the neighborhood of the equilibrium position. As a result, a complex stress state arises in the cutting zone, described by additional constant and cyclic force components. Assuming the ultimate limit state of the material is maintained in the cutting zone, we obtain the effective value of $\hat{\rho}$:

$$\hat{\rho} = \rho\left(1-\varepsilon_\rho\right), \tag{9}$$

where $\varepsilon_\rho = \hat{\rho}^{(C)} / \rho$ — dimensionless parameter; $\hat{\rho}^{(C)} = \Omega_\Delta \int_{t-(\Omega_\Delta)^{-1}}^{t} \rho(\xi) d(\xi)$; $\Omega_\Delta \in \mathbf{\Omega}^{(\Delta)}$.

It is obvious that $\varepsilon_\rho \langle 1$.

Let us estimate the effective value of $\hat{T}^{(0)}$ taking into account (3). The specified vibrations $\delta V_3(t) = \Delta V_3^{(X)}(t) - V_3^{(X)}(t)$ are independent of the vibration power. The period of the function $\delta V_3(t)$ is generally determined by the period of the vibrations $T_\Delta = (\Omega_\Delta)^{-1}$. That is, due to the introduced vibrations, attracting sets of the limit cycle type are formed in the dynamic cutting system. Moreover, Ω_Δ is at least an order of magnitude higher than the upper natural frequency of the vibrational circuits formed by the tool subsystem. We expand the nonlinear function $T^{(0)}(V_3, \delta V_3)$ in a Taylor series in the neighborhood of δV_3:

$$T^{(0)}\left(V_3,\delta V_3\right) = T_0^{(0)}\left(V_3,0\right) + \frac{\partial T_0^{(0)}}{\partial \delta V_3}\delta V_3 + \frac{1}{2!}\frac{\partial^2 T_0^{(0)}}{\left(\partial \delta V_3\right)^2}\left(\delta V_3\right)^2 + \ldots \tag{10}$$

With $\delta V_3 \ll V_3$, series (10) converges quickly, therefore we limit ourselves to a linear approximation of the dependence of the time constant T_0 on additional vibrations, that is, from (10) we obtain:

$$T_0\left(V_3,\delta V_3\right) = \frac{T_0^{(0)}}{1+k^{(T)}V_3} - \frac{k^{(T)}T_0^{(0)}\delta V_3}{\left[1+k^{(T)}V_3+k^{(T)}\delta V_3\right]^2}. \tag{11}$$

In (10), the first term is a constant value at $V_3 = const$. Function $\Delta\left(V_3,\delta V_3\right) = \frac{k^{(T)}\delta V_3}{\left[1+k^{(T)}V_3+k^{(T)}\delta V_3\right]^2}$ is periodic, with a period of T_Δ, and $(T_\Delta)^{-1} = \Omega_\Delta \in \mathbf{\Omega_\Delta}$. Therefore, to determine the effective value of $\hat{T}_0(V_3,\delta V_3)$, the following is valid:

$$\hat{T}_0\left(V_3,\delta V_3\right) = T_0^{(0)}\left\{\frac{1}{1+k^{(T)}V_3} - \Delta\left(V_3,\delta V_3\right)\right\}, \tag{12}$$

where $\Delta = \frac{1}{T_\Delta}\int_{t-T_\Delta}^{t}\left\{\frac{k^{(T)}T_0^{(0)}\delta V_3}{\left[1+k^{(T)}V_3+k^{(T)}\delta V_3\right]^2}\right\}d\xi$.

Thus, we see what happens when vibrations that are not directly transmitted by the tool and workpiece subsystems are introduced into the cutting zone. In this case, the parameters of the dynamic coupling formed by the cutting process change.

The system equilibrium is asymptotically stable and unperturbed. The time constant T_0 at $V_3 = const$ is also constant and is determined from the expression $T_0 = \frac{T_0^{(0)}}{1+k^{(T)}V_3}$. Otherwise, the HFV is changed. This transformation is determined by the ratio of the vibrational velocity amplitude to the cutting velocity, which is taken into account by Δ in (12). Thus, HFV change the system properties in the low-frequency region. For example, increasing the time constant $\hat{T}_0$ has two effects on equilibrium stability:

– it causes additional phase displacements between deformations and forces, which contributes to instability;

– it promotes damping of vibrations, which increases stability.

In all cases, as the amplitude increases, a decrease in the effective values of the parameters $\hat{\rho}$ and $\hat{T}_0$ is observed. Their variation affects the stability of the controlled trajectories and the dynamic properties of the system in the frequency domain $\mathbf{\Omega^{(0)}}$. This, in turn, affects the attractive sets of deformation displacements of the tool relative to the workpiece.

3. Mathematical modeling of the impact of the HFV on the cutting forces at the flank. Vibrations change the interactions between the tool flank and the workpiece (7). They also cause reactions outside the bandwidth of the system represented by (2). Therefore, forces **Φ** must also be taken as averages over the vibration period. Let us analyze the effect of vibrations on Φ_2. Forces Φ_3 differ by a factor of k_T. Consider two cases for an asymptotically stable system.

The first case: the vibrations are determined by the velocities in the feed direction $\Delta V_2^{(X)} sin(\Omega_0 t)$ and represent the difference between the vibrational velocities introduced into the cutting zone and the deformation velocities. Then from (7), we obtain:

$$\Phi_2 = \rho_0\left[t_P^{(0)} - X_1\right]\left\{exp\left[\varsigma(\upsilon-\upsilon^*)\right]\right\} = \rho_0\left[\left(t_P^{(0)} - X_1(t)\right)\right]\left\{exp\left[\varsigma\frac{\Delta V_2^{(X)}\,sin(\Omega_0 t)}{V_3^{(X)}}\right]\right\}.$$

As before, we expand $exp\left[\varsigma\frac{\Delta V_2^{(X)}\,sin(\Omega_0 t)}{V_3^{(X)}}\right]$ in a Taylor series:

$$\Phi_2\left(A_{X_2}\,sin(\Omega_0 t)\right) = \Phi_2^*\left\{1 + A_{X_2}\,sin(\Omega_0 t) + \frac{1}{2!}\left[A_{X_2}\,sin(\Omega_0 t)\right]^2 + \frac{1}{3!}\left[A_{X_2}\,sin(\Omega_0 t)\right]^3 + ... + \frac{1}{n!}\left[A_{X_2}\,sin(\Omega_0 t)\right]^n + ...\right\},$$

where $\Phi_2^* = \rho_0\left[t_P^{(0)} - X_1\right]$; $A_{X_2} = \varsigma\frac{\Delta V_2^{(X)}}{V_3^{(X)}}$.

The region of convergence of the series is $-\infty\langle A_{X_2}\sin(\Omega_0 t)\langle+\infty$. We average $\Phi_2\left(A_{X_2}\,sin(\Omega_0 t)\right)$ over the period $(\Omega_0)^{-1}$ and limit ourselves to the first four terms of the series:

$$\hat{\Phi}_2\left(A_{X_2}\right) = \rho_0\left[t_P^{(0)} - X_1\right]\left\{1 + \frac{1}{4}\left[A_{X_2}\right]^2 + \frac{3}{48}\left[A_{X_2}\right]^4\right\}. \quad (13)$$

This series always converges. The system is stable. Therefore, for $A_{X_2} = 0$, $\Phi_2(\upsilon)_{\upsilon=\upsilon^*} = \rho_0\left[t_P^{(0)} - X_1\right]\left\{exp\left[\varsigma(\upsilon-\upsilon^*)\right]\right\} = \rho_0\left[t_P^{(0)} - X_1\right]$. As $\Delta V_2^{(X)}$ increases, a growth of the effective value of $\hat{\Phi}_2(A_{X_2})$ is observed, which depends on $V_3^{(X)}$. This component is perceived by the subsystems and is within their bandwidth. This allows us to introduce the concept of latent force:

$$\Phi_2^{(C)}\left(\Delta V_2^{(X)}\,sin(\Omega_0 t)\right) = \rho_0\left[t_P^{(0)} - X_1(t)\right]\left\{exp\left[A_{X_2}\,sin(\Omega_0 t)\right] - 1 - \frac{1}{4}\left[A_{X_2}\right]^2 - \frac{3}{48}\left[A_{X_2}\right]^4\right\}. \quad (14)$$

It is obvious that with $\Delta V_2^{(X)} = 0$, force $\Phi_2^{(C)} = 0$.

The second case: the vibrational velocities are equal to $\Delta V_3^{(X)} sin(\Omega_0 t)$, and $\Phi_2 = \rho_0\left[t_P^{(0)} - X_1(t)\right]\left\{exp\left[\varsigma(\upsilon-\upsilon^*)\right]\right\}$. Expression $(\upsilon-\upsilon^*) = -\frac{V_2^{(X)}}{V_3^{(X)}}\frac{\Delta V_3^{(X)}\,sin(\Omega_0 t)}{\left(V_3^{(X)} + \Delta V_3^{(X)}\,sin(\Omega_0 t)\right)}$ is expanded in a Taylor series:

$$(\upsilon-\upsilon^*) = -\frac{V_2^{(X)}}{V_3^{(X)}}\varepsilon_{V_3}\,sin(\Omega_0 t)\left\{1 - \varepsilon_{V_3}\,sin(\Omega_0 t) + \left[\varepsilon_{V_3}\,sin(\Omega_0 t)\right]^2 - ... + (-1)^n\left[\varepsilon_{V_3}\,sin(\Omega_0 t)\right]^n + ...\right\}, \quad (15)$$

where $\varepsilon_{V_3} = \Delta V_3^{(X)} / V_3^{(X)}$.

Series (15) converges quickly since $\varepsilon_{V_3}\langle 1$. We average the expression over the period $(\Omega_0)^{-1}$ and limit ourselves to four terms:

$$\hat{\Phi}_2\left(\varepsilon_{V_3}\right) = \rho_0\left[t_P^{(0)} - X_1(t)\right]\left\{exp\left[\varsigma\frac{V_2^{(X)}}{V_3^{(X)}}\left(\frac{1}{2}\left(\varepsilon_{V_3}\right)^2 + \frac{3}{8}\left(\varepsilon_{V_3}\right)^4\right)\right]\right\}. \quad (16)$$

At $\Delta V_2^{(X)} = \Delta V_3^{(X)} = 0$, expressions $\hat{\Phi}_2(A_{X_2})$ and $\hat{\Phi}_2(\varepsilon_{V_3})$ are transformed into (7) without taking into account forces $k_\Phi F_0$. Effective values of $\hat{\Phi}_2(A_{X_2})$ and $\hat{\Phi}_2(\varepsilon_{V_3})$ differ due to the direction of vibrations — X_2 or X_3. In the first case, vibrations change the proximity of the flank and the workpiece, while in the second, they change the projections of the vector onto the direction X_2.

Here, we can also consider the latent force, which is zero in a stable system ($\Delta V_3^{(X)} = 0$):

$$\Phi_2^{(C)}\left(\Delta V_3^{(X)}\,sin(\Omega_0 t)\right) = \rho_0\left[t_P^{(0)} - X_1(t)\right]\left\{\begin{array}{l} exp\left[-\varsigma\frac{V_2^{(X)}}{V_3^{(X)}}\frac{\Delta V_3^{(X)}\,sin(\Omega_0 t)}{\left(V_3^{(X)} + \Delta V_3^{(X)}\,sin(\Omega_0 t)\right)}\right] - \\ -exp\left[-\varsigma\frac{V_2^{(X)}}{V_3^{(X)}}\left(\frac{1}{2}\left(\varepsilon_{V_3}\right)^2 + \frac{3}{8}\left(\varepsilon_{V_3}\right)^4\right)\right] \end{array}\right\}. \quad (17)$$

The presented analysis allows us to formulate two conclusions that are important for further work.

1. Tool flank wear depends on the direction of the HFV. For example, forces Φ_2 increase significantly more when vibrations are excited in the feed direction, and the rate of their increase depends on ς. Parameter ς increases with decreasing tool clearance angle α and as wear progresses.

2. Changes in the PIET and effective forces upon excitation of additional vibrations cause a displacement in the equilibrium of deformations affecting the diameter of the workpiece. Thus, the parameters of the HFV characterize the control parameters that change the properties of the system, including tool wear rate and surface quality.

4. Experiment Design and Simulation Parameters. The experiments were performed on a 16K20 machine tool with an adjustable spindle rotation and carriage feed drive. A603C01 vibration accelerometers with a sensitivity of 10.2 mV/(m/s²) and a frequency range of 0.4–15000 Hz were used as measurement interfaces. They were mounted on the tool in the longitudinal and tangential directions. The measuring stand collected data and transmitted it to the computer via an E20–10 analog-to-digital converter (ADC) with a sampling frequency of 100 kHz. The data obtained was processed using low-pass filtering algorithms to suppress noise in the measuring circuit. To determine the vibrational velocities and tool tip displacements, the vibration acceleration signal was integrated by software methods with trend removal. To measure forces, the STD.201–1 measuring system was installed in place of the support, which included:

– unit for measuring dynamic tool loads along axes $\{X_1, X_2, X_3\}$;

– interface unit for collecting and transmitting data.

The latter consisted of electronic units manufactured by National Instruments (USA): NI-9234, Ni-9237, and NI-9219. The sampling frequency was up to 50 kHz. The National Instruments system also measured the integral temperature value in the cutting zone. This indicator was associated with the power of irreversible energy transformations throughout the cutting zone.

To introduce USV into the cutting zone, an acoustic system based on a 500-watt magnetostrictive transducer was used, powered by a 1.5-kW ultrasonic generator. The device for automatically adjusting the generator frequency to the resonance of the acoustic system shifted when the boundary conditions of the tool – workpiece interface changed under the cutting process. Vibrations were measured with an accelerometer. Their intensity was estimated from the amplitude of harmonic displacements at a frequency of Ω_0. Workpieces made of 10GN2MFA steel were machined using tools with brazed T15K6 plates without the cutting fluid.

The computer simulation considered disturbances $\Delta V_2^{(X)} sin(\Omega_0 t)$ and $\Delta V_3^{(X)} sin(\Omega_0 t)$, $\Omega_0 = (5 – 20)$ kHz.

The main angles of the T15K6 tool were $\phi = 90°$, $\phi^1 = 30°$ and $\alpha = 6°$ (Fig. 1). These values were selected to simplify the modeling of the dynamic cutting system, since at $\phi = 90$, forces generated in the area of tool – workpiece contact produced practically zero projections in the direction X_1.

Process modes without considering deformations and disturbances were:

– feed rate $S_P^{(0)} = 0.1$ mm/rev;

– depth $t_P^{(0)} = 2$ mm;

– cutting velocity $V_P^{(0)} = (0.5 – 3.8)\cdot 10^3$ mm/s.

When varying $V_P^{(0)}$, the ratio of workpiece rotation velocity to longitudinal feed rate was maintained so that $t_P^{(0)} = const$. The tool subsystem parameters are given in Table 1. The total mass was $m = 0.015$ kg·s²/mm.

Table 1

Matrices of Velocity Coefficients and Tool Subsystem Elasticity [40]

Matrix element	Value, kg/mm	Matrix element	Value, kg·s/mm
$c_{1,1}$	200	$h_{1,1}$	1.3
$c_{2,2}$	900	$h_{2,2}$	1.1
$c_{3,3}$	350	$h_{3,3}$	0.8
$c_{1,2} = c_{2,1}$	200	$h_{1,2} = h_{2,1}$	0.6
$c_{1,3} = c_{3,1}$	150	$h_{1,3} = h_{3,1}$	0.5
$c_{2,3} = c_{3,2}$	80	$h_{2,3} = h_{3,2}$	0.4

The dynamic coupling parameters (Table 2) were determined experimentally by methods and programs described in detail for the parameters of high-speed [45] and positional [46] communication.

Table 2

Dynamic Coupling Parameters

ρ, kg/mm^2	ρ_0, kg/mm	Ω, Hz	$T_0^{(0)}$, s	ς	k_T	$k^{(T)}$, s/m	$k^{(S)}$	χ_1	χ_2	χ_3
100–1000	20	5–50	0.0001	1–7	0.2	5	0.1	0.4	0.51	0.76

Work A and power N are scalar quantities. They depend on the direction of movement and are measured in kg·mm and kg·mm/s, respectively. Let us consider A and N in the direction A — B (Fig. 2). When turning, $V_2/V_3 \Rightarrow 0$. This means:

$$N(t) = \Phi_2(t)V_2,\ A(t) = V_2\int_0^t \Phi_2(\xi)d\xi(a),$$

$$N(t) = \Phi_3(t)V_3^{(\Phi)}(t),\ A(t) = \int_0^t \Phi_3(\xi)V_3^{(\Phi)}(\xi)d\xi(б). \quad (18)$$

Here, a — power N and work A in the feed direction; b — power N and work A in the direction of velocity V_3.

The cutting process dynamics modeling [47] demonstrated the validity of the sensitivity analysis of force variations to deformations in the feed direction. Furthermore, a regenerative self-excitation effect was formed in the direction X_2, affecting the dynamics of the approach of the tool flank to the workpiece.

The numerical simulation of turning a shaft with a diameter of D = 84 mm was performed in the Simulink software package. This example can be used to study the vibration control of the PIET.

Research Results. Let us examine the results of vibration control of the power of irreversible energy transformations in the feed direction (18a) under the impact of high-frequency vibrations. First, we analyze the dependence of $\Phi_2(t)$ on $\Delta X_2^{(X)} sin(\Omega_0 t)$ without considering $k_\Phi F_0$ (Fig. 3 a).

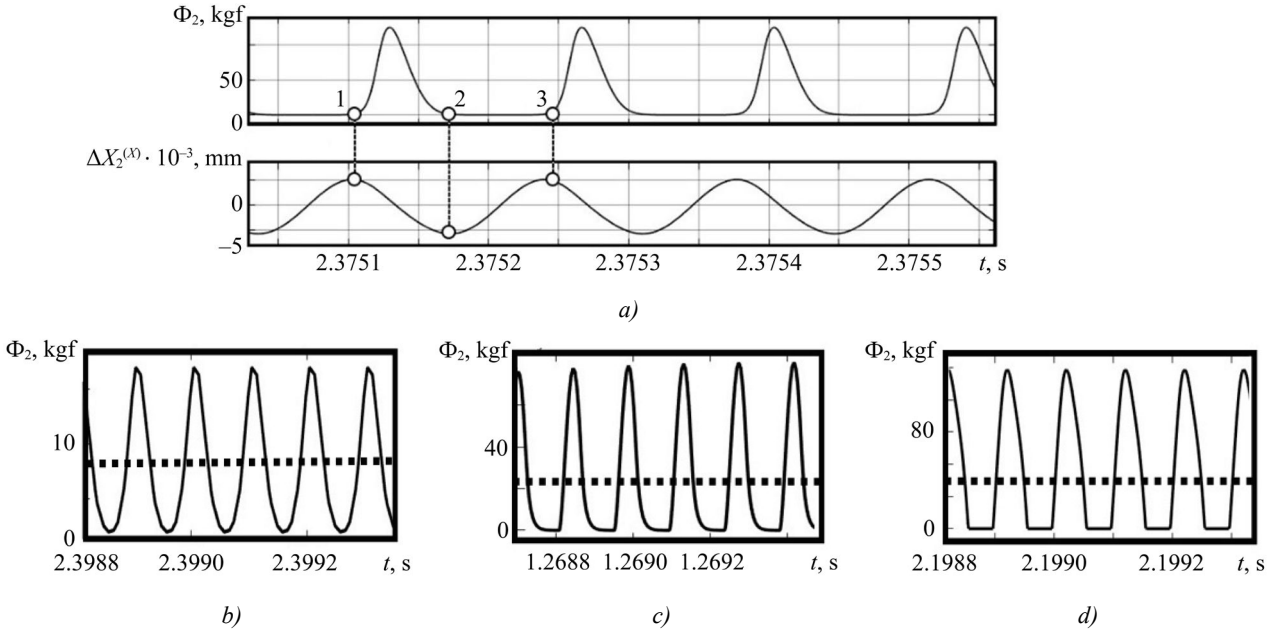

Fig. 3. Example of change in trajectories of force $\Phi_2(t)$: a — joint trajectories of forces and vibrations with a change in HFV $\Delta X_2^{(X)}$ without considering $k_\Phi F_0$; b — change in trajectories of forces with an amplitude of $\Delta X_2^{(X)} = 0{,}7 \cdot 10^{-3}$ mm; c — $\Delta X_2^{(X)} = 1 \cdot 10^{-2}$ mm; d — $\Delta X_2^{(X)} = 2 \cdot 10^{-2}$ mm

Note the nonlinear distortions of $\Phi_2(t)$. They increase at $\Delta V_2^{(X)}(t)$, directed toward the flank and workpiece (section 1–2) and are practically zero when its sign changes (section 2–3). At small amplitudes (Fig. 3 a), the force variations are almost harmonic. The nonlinear distortions are due to nonlinear relationship (7), which does not have central symmetry at any point.

As we can see, the disproportionate increase in the force impulse varies depending on the clearance angle α. At small angles (large ς), a rapid increase is observed even at low amplitudes of the HFV.

Next, we analyze the relationship between the forced HFV and the tangential components of the contact interaction forces (Fig. 4).

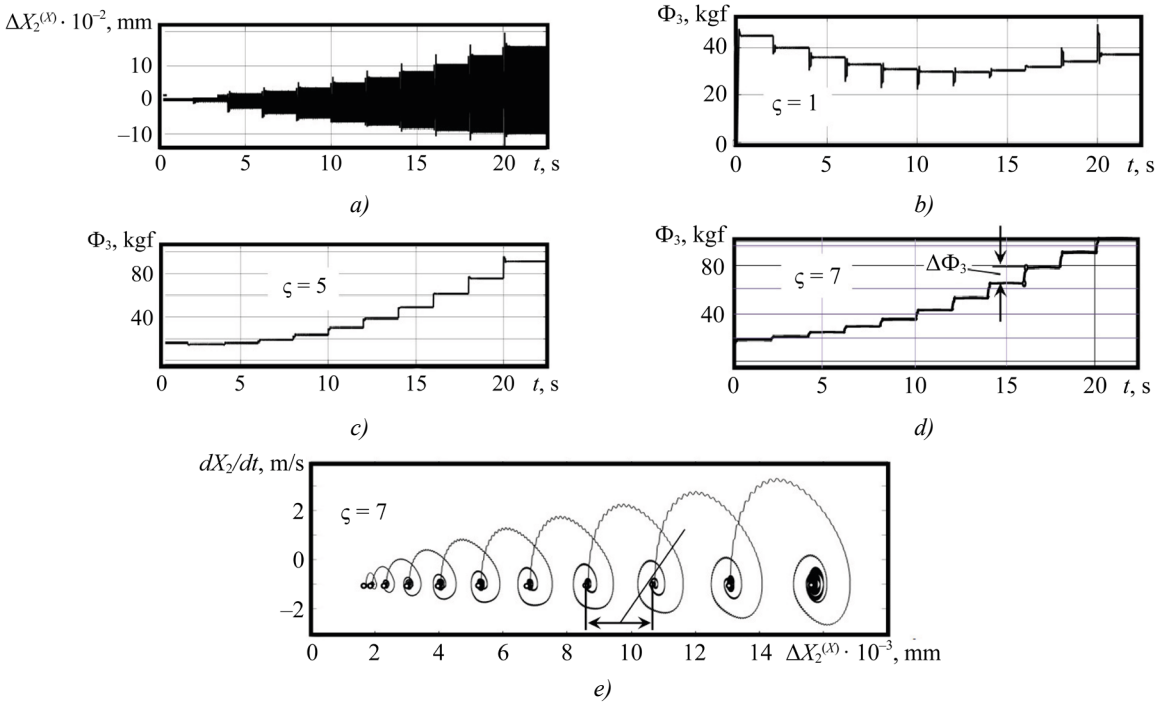

Fig. 4. Example of impact of forced HFV on tangential components of contact interaction forces: *a* — trajectories of forced vibrations; *b* — trajectory of Φ_3 at $\varsigma = 1$; *c* — trajectory of Φ_3 at $\varsigma = 5$; *d* — trajectory of Φ_3 at $\varsigma = 7$; *e* — example of phase trajectory of tool deformations considering vibration disturbances

The change in the amplitude of the HFV $\Delta X_2^{(X)}$ in Figure 4 *a* was specified by two piecewise constant functions with the duration of each step of Δt_{step}= 2 s:

– for the interval $t \in [0;8]$, the change in the amplitude of the first function was specified from 0 to $1.5 \cdot 10^{-2}$ mm for $t \in [0;8]$ with a step of $0.5 \cdot 10^{-2}$ mm;

– for the interval $t \in (8;22]$, the change in the amplitude of the second function was specified from $2 \cdot 10^{-2}$ mm to $14 \cdot 10^{-2}$ mm with a step of $2 \cdot 10^{-2}$ mm.

The arrows in Figure 4 *d*, *e* indicate the increment of forces $\Delta\Phi_3$ with increasing HFV amplitude and the corresponding displacement of the equilibrium point of the system in the phase plane.

Figure 4 *e* shows an example of the phase trajectory $X_2 - dX_2/dt$, corresponding to the change in force in Figure 4 *d*. Transient processes are caused by a jump in the amplitude. The equilibrium point ΔX_2^* shifts because the vibrations affect $\hat{\rho}$ and $\widehat{\mathbf{\Phi}}$.

According to [10], the main wear mechanisms change with increasing V_3 (increasing PIET). At low V_3, abrasive and adhesive-fatigue 10are observed, and with increasing V_3 — diffusion and oxidative wear. The transition from adhesive-fatigue to diffusion-oxidative wear corresponds to the minimum intensity. When vibrations are excited, the formation of PIET in the contact becomes more complex, however, wear rate can also be estimated from PIET.

Let us clarify the concepts of wear rate $v^{(L)} = dw/dL$ and velocity $v^{(t)} = dw/dt$. The magnitude of wear on the flank is usually considered as the equivalent width of the wear band w in mm, which is determined by the height of the equivalent rectangle of the wear scar on the flank. Equivalence is equality of areas, therefore:

$$v^{(L)} = v^{(t)} \left(V_p\right)^{-1}, \tag{19}$$

where $v^{(L)}$ is a dimensionless quantity.

In the velocity range of 0.7–3 m/s, dependence $v^{(L)}(N)$ is well approximated by the expression:

$$v^{(L)}(t) = \alpha^w \left\{1.8 + \beta^{(w)} \left[N(t) - 600\right]^2\right\}. \tag{20}$$

Here, $\alpha^{(w)}$ — dimensionless quantity; $\beta^{(w)}$ — parameter of dimension W^2. When processing heat-resistant steels, $\alpha^{(w)} = (0{,}9 - 1{,}1) \cdot 10^{-7}$. Due to vibrations, N becomes a function of time $N(t)$ with interrelated periodic and constant components. All physical interactions are inertial, that is, their manifestation also depends on frequency. Therefore, to estimate $N(t)$, it makes sense to introduce values $\hat{N}^{(X_2)}(\Delta X_2 \Omega_0)$, $\hat{N}^{(X_3)}(\Delta X_3 \Omega_0)$ depending on the direction of vibrations. For this, it is convenient to use the moving average operator for (20):

$$\hat{N}^{(X_i)}\left(\Delta X_2 \Omega_0\right) = \frac{\alpha^{(w)}}{T^{(X_i)}} \int\limits_{t-T^{X_2}}^{t} \left\{1.8 + \beta^{(w)} \left[N(\xi) - 600\right]^2\right\} d\xi, i = 2,3. \tag{21}$$

It is convenient to consider the averaging time as a multiple of the period $(\Omega_0)^{-1}$. Let us analyze the change in the PIET depending on the vibration amplitude at Ω_0 = 10 kHz. Let us consider its change depending on the HFV amplitude in the directions X_2 (Fig. 5 *a*) and X_3 (Fig. 5 *b*).

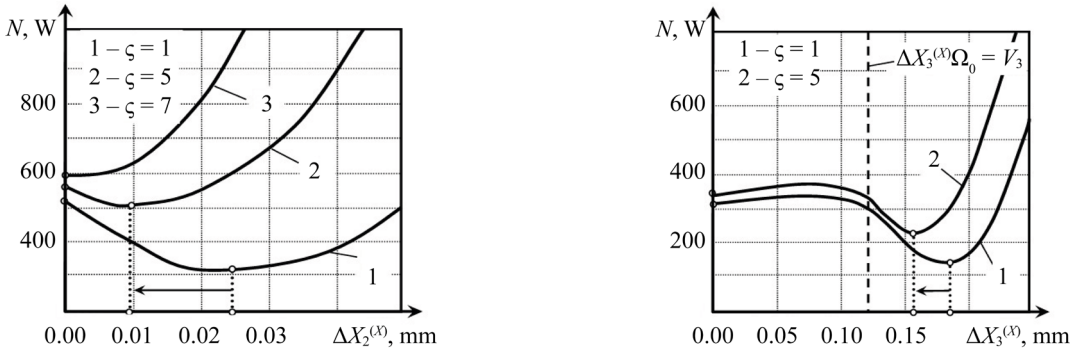

Fig. 5. Effect of vibrations on N: *a* — change in N depending on amplitude in the direction X_2; *b* — change in N depending on amplitude in the direction X_3

We see the HFV amplitudes at which the PIET reaches its minimum value, with the minimum depending on the degree of plate wear ς.

Figure 6 *a* shows the changes in $v^{(L)}$ depending on the PIET without additional vibrations.

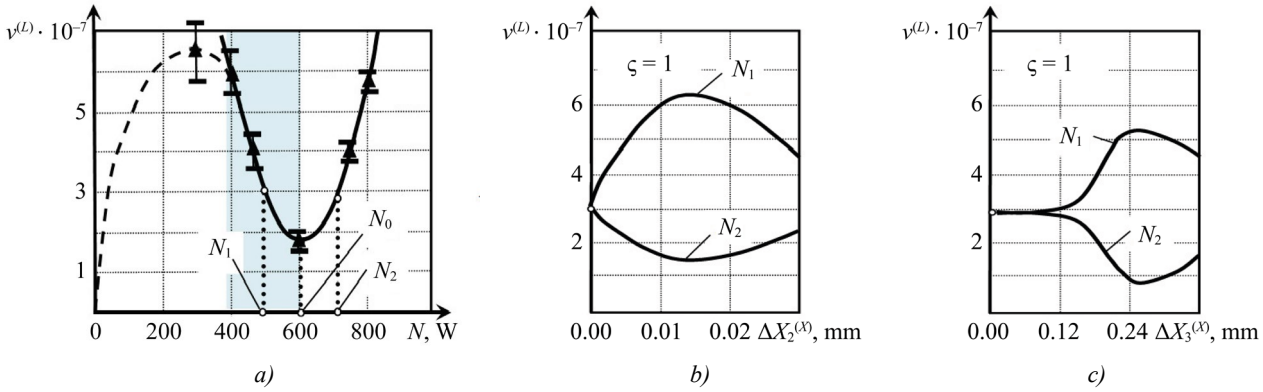

Fig. 6. Example of change in $v^{(L)}$ for cutting velocities of 1 m/s and 1.4 m/s (N_1 and N_2, respectively): *a* — trajectory $v^{(L)}$ without additional vibrations; *b* — in the direction X_2; *c* — in the direction X_3

Since vibration-free cutting is considered, then $V_p = const$. The forces on the flank are estimated by extrapolating the forces to zero cutting thickness. Dependence $v^{(L)}(N)$ (Fig. 6 *a*) has three distinct sections: in two, the power increases (clear zone), and in one, it decreases (shaded zone). Power N is estimated at a stage where wear does not exceed w = 0.2 mm. The black triangles represent experimental points, each obtained by determining the mathematical expectation from the experiments. Note that at least five experiments were conducted for each point. The well-known relationship 1 kg·m/s = 9.81 W was used to determine the power in watts.

Experimental data on the USV impact on cutter wear are visualized in Figure 7.

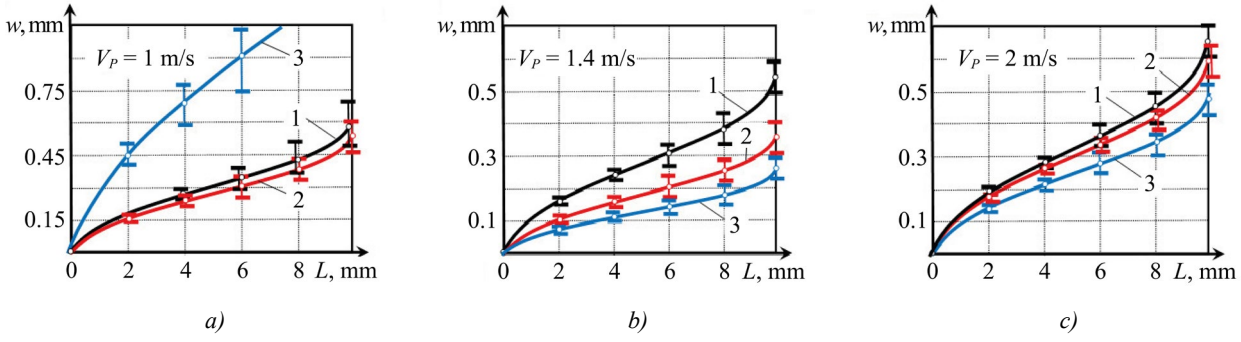

Fig. 7. Dependence of tool life on amplitude of vibrational displacements in the feed direction: *a* — at a cutting velocity of 1 m/s; *b* — at a cutting velocity of 1.4 m/s; *c* — in the tangential direction at a cutting velocity of 2 m/s.

Here, 1 — $\Delta X_i^{(X)}$ = 0; 2 — $\Delta X_i^{(X)}$ = 5 μm; 3 — $\Delta X_i^{(X)}$ = 10 μm, i = 2, 3

The change in wear along the cutting path is the path of the tool tip across the workpiece during each revolution of its circumference. For each point of the wear characteristics, their mathematical expectations and variances relative to the mathematical expectations are shown (represented by vertical segments). In Figure 7, value of *w* at each point corresponds to at least five experiments.

Discussion. Modeling has revealed that the disproportionate increase in the force impulse varies depending on the clearance angle α. At small angles (large ς), a rapid increase is observed even at low amplitudes of the HFV. Figure 3 *a, c, d* demonstrates the limitation of additional cutting forces relative to zero. This is due to the nonlinear dependence of cutting forces on the clearance angle of the tool in model (7). This exponential function accounts for the physical constraint on the tool continuous movement along the workpiece. Therefore, the additional forces are strictly positive. The curves in Figure 3 *c, d* demonstrate an asymmetry in the rise and fall of the force impulse, which is also explained by the exponential dependence in (7). If additional vibrations are absent, the force value is determined by the exponential function $exp[\varsigma(\upsilon - \upsilon^*)] = 1$. Periodic movements relative to this point cause changes in the form of the additional force impulses, moving from the exponential section with a high rate of increment (front of impulse Φ_2 in Fig. 3 *c, d*) to a more gradual one (decay of impulse Φ_2 in Fig. 3 *c, d*). Small variations in the vibrations relative to this point cause variations in Φ_2, which, due to small deviations from the equilibrium point, can be considered in a linear approximation. Then the relationship between the vibrations and the forces remains linear, and the change in the additional forces is close to a harmonic form (Fig. 3 *b*).

As the amplitude increases, nonlinear properties of the force vibrations impact on the tool flank become apparent. Nonlinear interactions cause a displacement in the period-integrated vibrations Φ_2, as shown by the dotted lines in Figure 3 *b, c, d*. The greater the vibration amplitude, the more pronounced the constant component of the forces becomes, shifting the system equilibrium point (for the case in Fig. 3 *b* — 8 kgf, Fig. 3 *c* — 22 kgf, Fig. 3 *d* — 50 kgf). Furthermore, with an increase in the vibrational amplitude, the force surges become closer in shape to delta functions, which, taking into account the impact of forces on the current value of the power of irreversible energy transformations, causes surges in heat production and increases tool wear.

Let us note two effects when increasing the amplitude of the simulated HFV.

First, the vibrations create a cyclically stressed state in the cutting zone, redistributing the constant and cyclic forces. This leads to a decrease in the effective values of $\widehat{\rho}$, and therefore, of $\widehat{F}_0$. The elastic deformations in the region adjacent to the chip formation zone depend on this force. Elastic recovery is observed in the flank contact region. This results in the generation of forces $k_\Phi \widehat{F}_0$, whose magnitude depends on $\widehat{\rho}$.

Secondly, variation of the HFV amplitude corresponds to changes in the values of additional forces Φ_3 in the cutting direction. The force graphs are presented for various tool flank gradient ς taking into account changes in the current vibrational velocities, which essentially determines the degree of approach of the tool surface to the workpiece or, for example, the degree of its wear. As the HFV amplitude increases, the tool flank approaches the workpiece, resulting in an increase in Φ_3 (Fig. 4 *b, c, d*). However, at $\varsigma = 1$, the effect of force minimization is visible from $\Phi_3 = 42$ kgf to $\Phi_3 = 30$ kgf with increasing amplitude $\Delta X_2^{(X)}$ (Fig. 4 *b*). According to (18*b*), this indicates the existence of such amplitudes of the HFV at which power $N(t)$ in the cutting zone is minimized. This effect at $\varsigma = 5$ is weakly expressed and shifted to the left, towards the effect of small amplitudes of the HFV. In this case, a small change in force is noticeable from $\Phi_3 = 19$ kgf to $\Phi_3 = 17$ kgf (Fig. 4 *c*). At $\varsigma = 7$, this effect disappears (Fig. 4 *d*), and Φ_3 grows following the HFV amplitude to $\Phi_3 = 103$ kgf. The increment of forces $\Delta\Phi_3$ is proportional to each new value of the disturbance amplitude (Fig. 4 *d*).

Thus, as wear increases, the optimal value of the HFV amplitude, which is capable of minimizing the value of additional cutting forces on the tool flank, and, consequently, the power of irreversible energy transformations in the cutting zone, decreases.

The study allowed us to determine and visualize the amplitudes of the HFV at which the PIET takes a minimum value, and this minimum depends on parameter ς, that is, on the degree of wear of the plate. Thus, when the HFV system is disturbed in the direction V_2 for $\varsigma = 1$, the optimal amplitude will be $\Delta X_2^{(X)} = 0.025$ mm. At this value, the power released in the cutting zone is minimized (Fig 5 *a*). At $\varsigma = 5$, the optimum shifts in the direction of the arrow on the graphs. The minimum of power trajectory 2 occurs at $\Delta X_2^{(X)} \approx 0.01$ mm, and then degenerates at $\varsigma = 7$. Further, even small additional vibrations correspond to an increase in the PIET. The effects noted above are neutralized if the HFV frequency exceeds the cutoff frequency of the dynamic subsystem of the cutting process, which is determined by parameter $T^{(0)}$.

The described effects are leveled by vibrations $\Delta V_3^{(X)} sin(\Omega_0 t)$ in the direction V_3, due to which the tool deviates from the direction A — B (Fig. 5 *b*). This appears as a projection determined by the ratio V_2/V_3 (Fig. 2 *b*). Here, to the right of the dotted line ($V_3 \langle \Delta X_3 \Omega_0$), a break in contact between the tool and the cutting zone is observed. This creates a cyclically stressed state, which is caused by the periodic interruption of cutting. Therefore, the effective forces and the PIET are reduced almost by half for the trajectory at ς = 1 from N = 300 W to N = 144 W, and at ς = 5 — from N = 320 W to N = 210 W. Furthermore, at low speeds, the tool and workpiece rear faces come closer together. This creates additional forces acting on the flank. This results in an effect similar to the impact of circulatory forces, which form circular tool tip trajectories.

The paper examines in detail examples of change of $v^{(L)}$ depending on the amplitude for two velocities (V_P = 1 m/s, V_P = 1.4 m/s) and the corresponding PIET (N_1, N_2) (Fig. 6 *b*, *c*). Point N_0 = 600 W corresponds to velocity $V_P^{(0)}$ = 1.2 m/s at which $v^{(L)}$ is minimal without additional vibrations. Point N_0 = 600 W lies in the velocity range of 0.7–3 m/s. It corresponds to the optimal cutting temperature. The efficiency of the vibration impact depends on V_P, the direction of vibrations, and the entire dynamic cutting system, including the workpiece. The range in which these effects are detected is limited to frequencies of 15–20 kHz.

The contradictory effect of USV in the direction V_2 for velocities V_P = 1 m/s и V_P = 1.4 m/s Fig. 7 *a, b*) is noticeable for the same cutting path. Figure 7 *a* shows a case of an extremely insignificant decrease in the maximum value of tool wear on the flank. With the introduction of USV $\Delta X_2^{(X)}$ = 5 μm, the reduction in this indicator is limited to 0.075 mm and decreases from w = 0.575 mm (curve 1) to w = 0.5 mm (curve 2). Doubling the USV amplitude ($\Delta X_2^{(X)}$ = 10 μm, Fig. 7 *a*) leads to intensification of wear, and its maximum value increases to w = 1.05 mm (curve 3).

Here, starting from a certain amplitude, an increase in the USV intensifies the cutting force surges along the flank edge $\Phi_2(t)$. Consequently, according to (18), the energy released in this region increases, and tool wear intensifies. A similar effect was observed in numerical experiments for $\Phi_2(t)$ (Fig. 3 *b*, *c*, *d*).

Thus, in the case of introducing USV in the feed direction, the vibration efficiency in reducing tool wear depends fundamentally on the cutting velocity. Value of V_p may initially be close to the optimal value of the PIET N_0 (Fig. 6 *a*), its small variations in the cutting zone will increase heat generation and, accordingly, wear. With the introduction of USV, the minimum wear intensity shifts towards increasing V_p (Fig. 7 *b*), and the maximum wear value decreases from w = 0.55 mm (curve 1) to w = 0.35 mm (curve 2) when introducing USV with an amplitude of $\Delta X_2^{(X)}$ = 5 μm and to w = 0.26 mm (curve 3) with an amplitude of $\Delta X_2^{(X)}$ = 10 μm . This is due to a decrease in the cyclic components of the cutting forces.

The data in Figure 7 *c* suggest that at V_P = 2 m/s the tool wear rate in the direction of cutting speed is virtually independent of USV. This is due to the limited ability to vary the USV amplitude during the experiment. Under our conditions, the achievable amplitude of vibrational displacements does not exceed 10–15 μm, and at high cutting speeds, the effect of USV on wear rate will be less due to the small relative variations in vibrational velocity to cutting velocity.

Setting low cutting speeds is appropriate for certain types of machining. For example, when dealing with heat-resistant steels, the introduction of USV significantly minimizes tool wear. Therefore, to effectively utilize vibration disturbances, it is required to consider the USV amplitude under the cutting process. To select the optimal ratio between the USV amplitude and the velocity of the tool vibrational displacements, an analysis of its motion is essential.

In Figure 7 *c*, the cutting velocity value is in the zone of small change in the PIET, that is, to the left of the dotted line, as shown in Figure 5 *b*. A decrease in the maximum wear value in Figure 7 *c* from w = 0.65 mm (curve 1) to w = 0.6 mm (curve 2) is achieved at $\Delta X_3^{(X)}$ = 5 μm. Amplitude $\Delta X_3^{(X)}$ = 10 μm allows wear to be reduced to w = 0.48 mm.

Thus, numerical modeling and experiments have shown that vibrations along axis X_2 shift the optimum velocity V_P, at which wear intensity is minimized, toward increasing cutting velocity (Fig. 6 *b*, *c*). Note that for case N_1 (Fig. 6 *b*), velocity V_P is lower than the optimum cutting velocity $V_P^{(0)}$ = 1.2 m/s without vibrations. In this case, with increasing amplitude $\Delta X_2^{(X)}$ at velocity V_P, additional vibrations, as a rule, increase wear intensity. For case N_2 $V_P \rangle V_P^{(0)}$ and as the amplitude of additional vibrations increases, an extremum is observed at which wear intensity is minimized.

The overall pattern of wear rate changes depending on vibration parameters, obtained through numerical modeling, qualitatively matches the experimental results of studying the impact of USV on wear (Fig. 7). As the amplitude increases, the optimum depends not only on the process conditions but also on the initial tool geometry, such as its clearance angle. The optimum shifts as wear progresses. At a certain point, the extremum levels out, and then the introduction of additional vibrations will not increase wear resistance under any process parameters.

When additional vibrations are excited in the direction of the cutting velocity, the situation changes. Here, the extreme amplitude of the vibrational velocity is observed only in the low-speed range. With USV, the existence of an optimal amplitude in the direction of the cutting velocity is limited to a cutting velocity of 0.3–0.5 m/s.

The reduction in wear rate depends on all the basic parameters of the DCS. Here, first of all, the elements of the stiffness matrices and the generalized masses should be mentioned. Furthermore, it is important to consider the dynamic coupling parameters, whose effective values themselves depend on the vibrations. Additional vibrations from the ultrasonic acoustic system (for example, in the feed direction) change not only the spatial orientation but also the amplitude due to the reaction from the cutting process. The resulting phase shifts between vibrations in different directions depend on the amplitude. They are caused by the specific interactions between vibrations on forces and forces — on deformations. Therefore, for example, it is impossible to orient additional vibrations in the direction of the projected cutting velocity (direction *A* — *B* in Figure 2).

Thus, even small-amplitude HFV always cause periodic changes in the approach between the tool flank and workpiece. This explains the first trend — an increase in wear rate with increasing amplitude. The second trend is caused by the development of a cyclically stressed state in the primary and secondary deformation zones. As a result, the forces and the PIET decrease in the contact zone between the flank and workpiece. These two opposing trends determine the dependence of wear rate on vibrational amplitude. It should also be noted that the optimal amplitude in all cases in a given system changes as wear progresses, as this process transforms the geometry of the tool flank.

Conclusion. The findings of the research presented in this article differ from those of published studies on the impact of vibration on tool wear. The author shows changes in cutting tool wear as a function of high-frequency vibrations from a new perspective — through the relationship between the power of irreversible energy transformations at a specific location, namely, the contact area between the workpiece and the tool flank. Previously, wear was considered in the literature on the scale of the entire cutting process.

The following tasks were accomplished in the course of the work.

1. It is shown that HFV affect tool wear rate with varying efficiency. The result depends on the tool geometry, its current wear, cutting velocity, and the parameters of the dynamic model of the cutting system.

2. The regularities linking the HFV with the tool wear rate are analytically validated.

3. The use of a numerical model of DCS as a basis for hybrid systems of dynamic wear monitoring is described.

4. Experimental results are presented that verify the contradictory effect of increasing the USV amplitude for different velocity ranges.

The proposed approach allows us to explain changes in the system properties in the low- and mid-frequency regions depending on the amplitude of the HFV. HFV introduced into the cutting zone can be considered as a control factor for:

– tool wear;

– dynamic properties of the cutting system.

The adequacy of the modeling results is limited by the zone of tool wear rate, in which the effect of random processes on the dynamics of the system increases and, accordingly, the assessment of the accuracy of the model is significantly reduced.

Conditions where the amplitude of vibrational displacements exceeds 10–15 μm require additional studies. Furthermore, it is necessary to elucidate the intrasystem physical processes of molecular-mechanical wear, including the physics of interactions as a whole. A promising direction for the developed models is their integration into tool wear diagnostic systems based on hybrid machine learning architectures. This approach will enable more accurate prediction of changes under the condition of cutting tools when modeling DSR.

References

1. Shaojian Zhang, Sandy Suet To, Guoqing Zhang, Zhiwei Zhu. A Review of Machine-Tool Vibration and Its Influence upon Surface Generation in Ultra-Precision Machining. *International Journal of Machine Tools and Manufacture*. 2015;91:34–42. https://doi.org/10.1016/j.ijmachtools.2015.01.005

2. Aman Ullah, Tzu-Chi Chan, Shinn-Liang Chang. Current Trends in Vibration Control and Computational Optimization for CNC Machine Tools: A Comprehensive Review. *The International Journal of Advanced Manufacturing Technology.* 2025;139(11):5409–5444. https://doi.org/10.1007/s00170-025-16238-8

3. Kudinov VA. *Machine Tool Dynamics*. Moscow: Mashinostroenie; 1967. 359 p. (In Russ.)

4. Tobias SA, Fishwick W. Theory of Regenerative Machine Tool Chatter. *The Engineer*. 1958;205(7):199–203. URL: https://vibraction.fr/images/stories/Documents/1erePresentationLobesTobias.pdf (accessed: 10.11.2025).

5. Vela-Martínez L, Jáuregui-Correa J-C, González-Brambila O, Herrera-Ruiz G, Lozano-Guzmán A. Modeling of Machining Processes for Predictive Analysis of Self-excited Vibrations. *Ingeniería Mecanica, Tecnología y Desarrollo*.2008;3(2):1–9. URL: https://scielo.org.mx/pdf/imtd/v3n1/v3n1a2.pdf (accessed: 10.11.2025).

6. Zakovorotny VL, Lukyanov AD, Gubanova AA, Hristoforova VV. Bifurcation of Stationary Manifolds Formed in the Neighborhood of the Equilibrium in a Dynamic System of Cutting. *Journal of Sound and Vibration*. 2016;368:174–190. https://doi.org/10.1016/j.jsv.2016.01.020

7. Caixu Yue, Haining Gao, Xianli Liu, Steven Y Liang, Lihui Wang. A Review of Chatter Vibration Research in Milling. *Chinese Journal of Aeronautics.* 2019;32(2):215–242. https://doi.org/10.1016/j.cja.2018.11.007

8. Gouskov AM, Guskov MA, Lorong Ph, Panovko G. Influence of Flank Face on the Condition of Chatter Self-excitation during Turning. *International Journal of Machining and Machinability of Materials.* 2017;19:17–40. https://doi.org/10.1504/IJMMM.2017.081186

9. Zakovorotny V. Bifurcations in the Dynamic System of the Mechanic Processing in Metal-Cutting Tools. *WSEAS Transactions on Applied and Theoretical Mechanics*. 2015;10:102–116. URL: https://www.wseas.org/multimedia/journals/mechanics/2015/a225811-099.pdf (accessed: 10.11.2025).

10. Zakovorotny VL, Gvindjilia VE. *Fundamentals of System-Synergetic Analysis and Synthesis of Process Control on Metal-Cutting Machines*. Saint Petersburg: Lan'; 2025. 436 p. (In Russ.)

11. Altintas Y, Eynian M, Onozuka H. Chatter stability of machining operations. *Journal of Manufacturing Science and Engineering.* 2020;142(11):110801. https://doi.org/10.1115/1.4047391

12. Sujuan Wang, Tao Zhang, Wenping Deng, Zhanwen Sun, Sandy To. Analytical Modeling and Prediction of Cutting Forces in Orthogonal Turning: A Review. *The International Journal of Advanced Manufacturing Technology.* 2022;119(3):1407–1434. https://doi.org/10.1007/s00170-021-08114-y

13. Rusinek R, Wiercigroch M, Wahi P. Modelling of Frictional Chatter in Metal Cutting. *International Journal of Mechanical Sciences.* 2014;89:167–176. https://doi.org/10.1016/j.ijmecsci.2014.08.020

14. An-Hong Tian, Cheng-Biao Fu, Xiao-Yi Su, Her-Terng Yau. Lathe Tool Chatter Vibration Diagnostic Using General Regression Neural Network Based on Chua's Circuit and Fractional-order Lorenz Master/Slave Chaotic System. *Journal of Low Frequency Noise, Vibration and Active Control.* 2019;38(3/4):953–966. https://doi.org/10.1177/1461348418815414

15. Katiyar S, Muskan J, Narain RP, Singh S, Shrivastava Y. A Short Review on Investigation and Suppression of Tool Chatter in Turning Operation. *Materials Today: Proceedings.* 2022;51(1):1206–1210. https://doi.org/10.1016/j.matpr.2021.07.208

16. An Wang, Baiyuan Zhou, Wuyin Jin. Dynamics of the Regenerative Turning Chatter with Little Mass Eccentricity. *International Journal of Non-Linear Mechanics.* 2024;166:104851. https://doi.org/10.1016/j.ijnonlinmec.2024.104851

17. Forestier F, Gagnol V, Ray P, Paris H. Model-Based Cutting Prediction for a Self-vibratory Drilling Head-Spindle System. *International Journal of Machine Tools and Manufacture.* 2012;52(1):59–68. https://doi.org/10.1016/j.ijmachtools.2011.09.001

18. Pengfei Zhang, Dongbo Hong, Giovanni Totis, Federico Scalzo, Zengbin Yin, Liming Shu L, et al. Systematic Review of Cutting Force Measuring Systems in Machining: Principles, Design, Filtering Techniques and Applications. *International Journal of Machine Tools and Manufacture*. 2025;210:104308. https://doi.org/10.1016/j.ijmachtools.2025.104308

19. Xue-Bin Qin, Min Wan, Wei-Hong Zhang, Yun Yang. Chatter Suppression with Productivity Improvement by Scheduling a C^3 Continuous Feedrate to Match Spindle Speed Variation. *Mechanical Systems and Signal Processing*. 2023;188:110021. https://doi.org/10.1016/j.ymssp.2022.110021

20. Zakovorotny VL, Lukyanov AD. The Problems of Control of the Evolution of the Dynamic System Interacting with the Medium. *International Journal of Mechanical Engineering and Automation.* 2014;1(5):271–285. URL: https://www.researchgate.net/publication/293636021_The_Problems_of_Control_of_the_Evolution_of_the_Dynamic_System_Interacting_with_the_Medium (accessed: 10.11.2025).

21. Sergiev AP, Vladimirov AA, Makarov AV, Shvachkin EG. Physical Fundamentals of the Vibratory Cutting Process in Turning. *Bulletin of Belgorod State Technological University named after V.G. Shukhov.* 2017;(3):94–102. (In Russ.) https://doi.org/10.12737/24626

22. Ghorbani S, Kopilov VV, Polushin NI, Rogov VA. Experimental and Analytical Research on Relationship between Tool Life and Vibration in Cutting Process. *Archives of Civil and Mechanical Engineering.* 2018;18(3):844–862. https://doi.org/10.1016/j.acme.2018.01.007

23. Canbin Zhang, Xiaoliang Liang, Chi Fai Cheung, Chunjin Wang, Benjamin Bulla. Theoretical and Experimental Investigation of Ultrasonic Cutting Kinematics and Its Effect on Chip Formation and Surface Generation in High-Frequency Ultrasonic Vibration-assisted Diamond Cutting. *Journal of Materials Research and Technology.* 2024;30:5662–5676. https://doi.org/10.1016/j.jmrt.2024.04.266

24. Qingliao He, Yun He, Xin Wang, Biao Zhao, Wenfeng Din. Effects of Longitudinal-Torsional Ultrasonic Vibration on the Tool Wear Characteristics and Performance in Side Milling of GH4169 Superalloy. *The International Journal of Advanced Manufacturing Technology.* 2025;140:3171–3184. https://doi.org/10.1007/s00170-025-16490-y

25. Renke Kang, Shenghao Chao, Jiansong Sun, Jinchuan Luan, Zhigang Dong, Yidan Wang. Study on the Cutting Performance of Ultrasonic-assisted Turning for Cast Superalloy K4169. *The International Journal of Advanced Manufacturing Technology.* 2025;137:1089–1102. https://doi.org/10.1007/s00170-025-15216-4

26. Zhaojie Yuan, Daohui Xiang, Peicheng Peng, Zhiqiang Zhang, Binghao Li, Mingyang Ma, et al. A Comprehensive Review of Advances in Ultrasonic Vibration Machining on SiCp/Al Composites. *Journal of Materials Research and Technology.* 2023;24:6665–6698. https://doi.org/10.1016/j.jmrt.2023.04.245

27. Astashev VK, Andrianov NA, Krupenin VL. On Autoresonant Ultrasonic Cutting Materials. *Bulletin of Scientific and Technical Development.* 2017;(1(113)):3–16.

28. Agapov SI, Kirakosyan KA, Arzhukhanov RI, Novikova LA. The Use of Ultrasonic Vibrations in Turning. *Izvestia VSTU.* 2022;267(8):7–9. https://doi.org/10.35211/1990-5297-2022-8-267-7-9

29. Ghule G, Sanap S, Chinchanikar S. Ultrasonic Vibration-Assisted Hard Turning of AISI 52100 Steel: Comparative Evaluation and Modeling Using Dimensional Analysis. *Metal Working and Material Science.* 2023;25(4):136–150. https://doi.org/10.17212/1994-6309-2023-25.4-136-150

30. Agapov SI, Tkachenko IG. Determining the Optimal Amplitudes and Directions of Ultrasound Vibrations in Cutting Small-Module Gears. *Russian Engineering Research.* 2010;30(2):141–143. https://doi.org/10.3103/S1068798X10020103

31. Astakhov VP, Outeiro J. Importance of Temperature in Metal Cutting and Its Proper Measurement/Modeling. In book: Davim J. (ed) *Measurement in Machining and Tribology.* Cham: Springer; 2018. P. 1–47. URL: https://link.springer.com/chapter/10.1007/978-3-030-03822-9_1 (accessed: 07.12.2025).

32. Astakhov VP, Xinran Xiao. The Principle of Minimum Strain Energy to Fracture of the Work Material and Its Application in Modern Cutting Technologies. In book: *Metal Cutting Technologies. Progress and Current Trends.* Munich: De Gruyter Oldenbourg; 2016. P. 1–35. URL: https://clck.ru/3SWbzm (accessed: 07.12.2025).

33. Lyubimyi N.S., Chetverikov B.S., Gerasimov M.D., Bytsenko M.V., Pol'shin A.A., Mal'tsev A.K. Experimental Study and Modeling of Thermal Response in Turning a 3.5 mm Thick Shell of Metal Composite System. *Advanced Engineering Research (Rostov-on-Don).* 2026;26(1):2250. https://doi.org/10.23947/2687-1653-2026-26-1-2250

34. Tavstyuk AA, Lyutov AG, Kourou GN. Application of Specific Energy Parameters in Optimization and Control of the Cutting Process. *STIN.* 2014;(2):29–34. (In Russ).

35. Yanov ES, Antonychev SV, Antsev AV, Vorotilin MS, Minakov EI. Studying Methods for Controlling the Condition of Milling Machines Based on the Analysis of Vibration Characteristics. *University Proceedings. Volga Region. Engineering Sciences.* 2024;(3(71)):157–166. https://doi.org/10.21685/2072-3059-2024-3-14

36. Yuqing Zhou, Wei Xue. Review of Tool Condition Monitoring Methods in Milling Processes. *International Journal of Advanced Manufacturing Technology.* 2018;96:2509–2523. https://doi.org/10.1007/s00170-018-1768-5

37. Xuchen Hou, Wei Xia, Xianli Liu, Caixu Yue, Xiao Zhang, Dingfeng Yan. Research on Milling Cutter Wear Monitoring Based on Self-learning Feature Boundary Model. *The International Journal of Advanced Manufacturing Technology.* 2024;135(3):1789–1807. https://doi.org/10.1007/s00170-024-14532-5

38. Kozochkin MP, Sabirov FS, Seleznev AE. Vibroacoustic Monitoring of Cutting Edge Machining of Hardened Steel. *Vestnik MSTU "Stankin".* 2018;(1(44)):23–30.

39. Zakovorotny VL, Gvindzhiliya VE. System-Synergetic Analysis and Synthesis of a Controlled Cutting Process. *Science Intensive Technologies in Mechanical Engineering.* 2024;(9):3–13. https://doi.org/10.30987/2223-4608-2024-3-13

40. Zakovorotny VL, Gvindzhiliya VE. Influence of the Tool Vibration on the Part Surface in Longitudinal Turning. *Proceedings of Higher Educational Institutions. Machine Building.* 2024;(9(774)):52–71.

41. Zakovorotny VL, Gvindzhiliya VE. Influence of Spindle Wobble in a Lathe on the Tool's Deformational-Displacement Trajectory. *Russian Engineering Research*. 2018;38(8):623–631. https://doi.org/10.3103/S1068798X1808018X

42. Blekhman I, Blekhman LI, Vaisberg LA, Vasilkov VB. Energy and Frequency Ripple in Devices with Inertial Excitation of Oscillations. *Philosophical Transactions. Series A. Mathematical, Physical and Engineering Sciences.* 2021;379(2198):20200233. https://doi.org/10.1098/rsta.2020.0233

43. Bogolyubov NN, Mitropolsky YuA. *Asymptotic Methods in the Theory of Nonlinear Oscillations*. Moscow: Nauka; 1974. 503 p. (In Russ).

44. Zorev NN. *Questions of the Mechanics of Metal Cutting Processes*. Moscow: Mashgiz; 1956. 368 p. (In Russ).

45. Zakovorotny VL, Pham Dinh Tung, Chiem Nguyen Xuan, Ryzhkin MN. Dynamic Coupling Modeling Formed by Turning in Cutting Dynamics Problems (Velocity Coupling). *Vestnik of Don State Technical University.* 2011;11(2):137–146. URL: https://www.vestnik-donstu.ru/jour/article/view/702/701 (accessed: 07.12.2025).

46. Zakovorotny VL, Pham Dinh Tung, Chiem Nguyen Xuan, Ryzhkin MN. Dynamic Coupling Modeling Formed by Turning in Cutting Dynamics Problems (Positional Coupling). *Vestnik of Don State Technical University.* 2011;11(3):301–311. URL: https://www.vestnik-donstu.ru/jour/article/view/725/724 (accessed: 07.12.2025).

47. Zakovorotny VL, Gvindjiliya VE. The Study of Vibration Disturbance Mapping in the Geometry of the Surface Formed by Turning. *Metal Working and Material Science.* 2024;26(2):107–126. https://doi.org/10.17212/1994-6309-2024-26.2-107-126

About the Author:

Valery Y. Gvindjiliya, Cand.Sci. (Eng.), Senior Lecturer of the Automation of Production Processes Department, Don State Technical University (1, Gagarin Sq., Rostov-on-Don, 344003, Russian Federation), SPIN-code, ORCID, ScopusID, ResearcherID, vvgvindjiliya@donstu.ru

Conflict of Interest Statement: **the author declares no conflict of interest.**

The author has read and approved the final manuscript.

Об авторе:

Валерия Енвериевна Гвинджилия, кандидат технических наук, старший преподаватель кафедры «Автоматизация производственных процессов» Донского государственного технического университета (344003, Российская Федерация, г. Ростов-на-Дону, пл. Гагарина, 1), SPIN-код, ORCID, ScopusID, ResearcherID, vvgvindjiliya@donstu.ru

Конфликт интересов: **автор заявляет об отсутствии конфликта интересов.**

Автор прочитал и одобрил окончательный вариант рукописи.

Received / **Поступила в редакцию** 08.12.2025
Reviewed / Поступила после рецензирования 12.01.2026
Accepted / **Принята к публикации** 26.01.2026

INFORMATION TECHNOLOGY, COMPUTER SCIENCE AND MANAGEMENT
ИНФОРМАТИКА, ВЫЧИСЛИТЕЛЬНАЯ ТЕХНИКА И УПРАВЛЕНИЕ

UDC 004.89
https://doi.org/10.23947/2687-1653-2026-26-1-2211

Original Empirical Research

A Customer Lifetime Value-aware Framework for Strategic Churn Prediction Using Deep Learning

EDN: FDZUZD

Uma Maheswari Gurusamy[1] ✉, **Meenakshi Anantharaman**[1], **Ram Prasath Selvamani**[1], **Sangeetha Vijayarajan**[2]

[1] Kamaraj College of Engineering and Technology, Virudhunagar, Tamil Nadu, India
[2] SRM Easwari Engineering College, Ramapuram, Chennai, India

✉ uma.optimist@gmail.com

Abstract

Introduction. Customer churn prediction represents a challenge in the current era of rapid digital transformation, hyper-competition, and data-driven marketing. In sectors such as telecommunications and banking, even marginal reductions in churn translate to significant revenue protection. Numerous companies employ uniform approaches, leading to the inefficient allocation of marketing resources and loss of loyal customers. Recent research has advanced along two largely separate domains. The first focuses on improving predictive accuracy through machine learning and deep learning techniques. Another stream, rooted in marketing science, emphasizes the economic dimension of churn, introducing Customer Lifetime Value (CLV) as a key metric. Existing solutions either maximize accuracy at high computational cost or discuss value-based strategy without providing a technical, implementable system. To bridge this gap, this paper aims to create, test, and present a comprehensive churn control system integrating customer lifetime value framework (CVLV). To achieve this, the following tasks are addressed: segmenting customers based on dynamic CLV and churn risk scores; evaluating the efficiency of various neural network configurations; and building a decision model that assigns optimal deep learning architectures for targeted retention, seamlessly integrating data analytics with corporate strategy.

Materials and Methods. The study was performed on two datasets: IBM Telco Customer Churn (7,043 customers, 21 features, binary churn) and Santander Customer Transaction Prediction (200,000 records, 200 numerical features, binary target variable). The data were preprocessed to address class imbalance and split 70-15-15 (train-validation-test) using 5-fold cross-validation. ANN (3–6 layers) and RNN/LSTM models were compared within the CVLV framework. The training utilized Adam optimizer, L2 regularization, dropout, early stopping, gradient clipping, and uniform batch size and epoch settings. The performance was evaluated based on accuracy, loss, and the Pareto frontier. Subsequently, customers were segmented by CLV/risk level, and retention strategies were assigned to the respective optimal models.

Results. The comprehensive assessment of artificial neural networks (ANN) and recurrent neural networks (RNN) shows that RNN with 2 layers achieved marginally higher accuracy of 0.90, while the 3-layer ANN produced the best robustness with a loss of 0.25 with relatively similar predictive performance. With the CVLV framework, RNN 2L is assigned for high value, high risk relationships that need the most precision, ANN 3L is assigned for stable, high value relationships, and general RNN for low value customers.

Discussion. This work has shown that the CVLV framework strategically optimizes churn prediction by aligning deep learning models with customer value-risk profiles. The data obtained confirm that ANN 3L provides optimal robustness while RNN 2L achieves superior accuracy for temporal patterns, together enabling more efficient and targeted retention interventions across industries. This approach can be deployed across the telecommunications, banking and retail sectors and facilitate a meaningful connection between technical model performance and strategic decision-making, enabling organizations to deploy retention efforts effectively by aligning model capability with the customer's value and probability of churn. The findings indicates that strategic model assignments based on CLV-risk profiles led to improved efficiencies associated with retention without compromising predictive reliability.

Conclusion. The main results are that the ANN 3L model provides the optimal balance of accuracy (0.875) and robustness (loss: 0.25) for churn prediction, while the RNN 2L achieves peak accuracy (0.90) for high-risk segments. The practical significance lies in the proposed CVLV framework, which enables businesses to strategically align deep learning model selection with customer lifetime value, improving retention efficiency. Further research will focus on integrating real-time CLV updates and validating the framework across additional industry domains.

Keywords: Customer Lifetime Value-aware, churn prediction, ANN, RNN, accuracy, loss, optimum model

Acknowledgements. The authors would like to express their sincere gratitude to the curators and maintainers of the IBM Telco Customer Churn and Santander Customer Transaction Prediction datasets for making their data publicly available, which was fundamental to the empirical validation conducted in this study. The computational resources provided by respective institutions are gratefully acknowledged.

For Citation. Uma Maheswari Gurusamy, Meenakshi Anantharaman, Ram Prasath Selvamani, Sangeetha Vijayarajan. A CVLV Framework for Strategic Churn Prediction Using Deep Learning. *Advanced Engineering Research (Rostov-on-Don).* 2026;26(1):2211. https://doi.org/10.23947/2687-1653-2026-26-1-2211

Оригинальное эмпирическое исследование

Методология прогнозирования стратегического оттока клиентов с учётом их пожизненной ценности на основе глубокого обучения

Ума Махешвари Гурусами[1] ✉, Минакши Анантараман[1], Рам Прасат Сельвамани[1], Санджита Виджаяраджан[2]

[1] Инженерно-технологический колледж имени Камараджа, г. Вирудунагар, штат Тамилнад, Индия
[2] Инженерный колледж имени Ишвари при Университете SRM, Рамапурам, г. Ченнаи, Индия
✉ uma.optimist@gmail.com

Аннотация

Введение. Прогнозирование оттока клиентов приобретает особую актуальность в эпоху цифровой трансформации и обострения конкуренции. В таких секторах, как телекоммуникации и банковское дело, даже минимальное сокращение этого показателя способно заметно укрепить финансовые позиции. Многие компании применяют унифицированные подходы к удержанию клиентов, что приводит к нерациональному использованию ресурсов и утрате лояльных пользователей. Современные исследования фокусируются на двух ключевых направлениях. Первое из них посвящено совершенствованию точности прогнозирования посредством алгоритмов машинного обучения. Второе подчеркивает экономическую составляющую, включая пожизненную ценность клиента (CLV). Существующие подходы либо достигают максимальной точности за счет значительных вычислительных затрат, либо предлагают концепции, основанные на факторе ценности, но не имеющие практической технической реализации. Для преодоления этого разрыва в настоящей работе предлагается создать, испытать и представить комплексную систему контроля оттока клиентов с интеграцией жизненной ценности клиента (CVLV). Цель исследования заключается в разработке и верификации методологии контроля оттока с учетом жизненной ценности клиента (CVLV). Для ее достижения решаются следующие задачи: сегментация аудитории по динамическим метрикам CLV и вероятности ухода; оценка эффективности разнообразных конфигураций нейронных сетей; построение модели, которая выявляет наилучшие архитектуры глубокого обучения для целенаправленного удержания клиентов, гармонично сочетая аналитику данных с корпоративной стратегией.

Материалы и методы. Исследование проводилось на двух наборах данных: IBM Telco Customer Churn (7 043 клиента, 21 признак, бинарный отток) и Santander Customer Transaction Prediction (200 000 записей, 200 числовых признаков, бинарный целевой признак). Данные обрабатывались с учётом дисбаланса классов и делились в пропорции 70–15–15 с 5-кратной кросс-проверкой. Сравнивались ANN (3–6 слоёв) и RNN/LSTM в CVLV-фреймворке. При обучении использовались Adam, L2-регуляризация, dropout, ранняя остановка, обрезка градиентов, единые настройки батча и эпох. Эффективность оценивалась по точности, функции потерь и Парето-фронту. Затем клиенты сегментировались по уровню пожизненной ценности (CLV) и риску оттока. Затем моделям назначались стратегии.

Результаты исследования. Всесторонняя оценка искусственных (ANN) и рекуррентных (RNN) нейронных сетей показала, что двухслойная RNN обеспечивает незначительно более высокую точность (0,90), в то время как трёхслойная ANN демонстрирует наилучшую устойчивость с минимальными потерями (0,25) при сопоставимой прогностической эффективности. В рамках CVLV-фреймворка это определяет назначение моделей: RNN 2L используется для высокоценных клиентов с высоким риском оттока, где критически важна максимальная точность прогноза; ANN 3L — для стабильных высокоценных отношений; а базовая RNN — для клиентов с низкой ценностью.

Обсуждение. Проведённое исследование продемонстрировало, что CVLV-фреймворк стратегически оптимизирует прогнозирование оттока клиентов за счёт согласования моделей глубокого обучения с ценностно-рисковыми профилями клиентов. Полученные данные подтверждают, что модель ANN 3L обеспечивает оптимальную устойчивость, а RNN 2L достигает максимальной точности при работе с временными закономерностями. Совместное их применение позволяет реализовывать более эффективные и целенаправленные мероприятия по удержанию клиентов в различных отраслях. Данный подход может быть внедрён в телекоммуникационном, банковском секторах, в сфере розничных продаж. Он устанавливает содержательную связь между техническими характеристиками модели и стратегическим принятием решений, позволяя организациям эффективно распределять усилия по удержанию, соотнеся возможности модели с ценностью клиентов и вероятностью их оттока. Результаты указывают на то, что стратегическое назначение моделей на основе CLV-рисковых профилей приводит к повышению эффективности мероприятий по удержанию без ущерба для надёжности прогнозов.

Заключение. Основные результаты заключаются в том, что модель ANN 3L обеспечивает оптимальный баланс между точностью (0,875) и устойчивостью (потери: 0,25) в прогнозировании оттока, в то время как модель RNN 2L достигает максимальной точности (0,90) для сегментов с высоким риском. Практическая значимость исследования состоит в предложенном CVLV-фреймворке, который позволяет бизнесу стратегически соотносить выбор модели глубокого обучения с пожизненной ценностью клиента, повышая эффективность мероприятий по удержанию. Дальнейшие исследования будут сосредоточены на интеграции механизмов обновления CLV в реальном времени и валидации фреймворка в других отраслях.

Ключевые слова: учёт пожизненной ценности клиента, прогнозирование оттока клиентов, ANN, RNN, точность, функция потерь, оптимальная модель

Благодарность. Авторы выражают искреннюю благодарность кураторам и разработчикам наборов данных IBM Telco Customer Churn и Santander Customer Transaction Prediction за предоставление открытого доступа к данным, которые послужили основой для эмпирической валидации, проведенной в данном исследовании. Мы также признательны за вычислительные ресурсы, предоставленные учреждениями.

Для цитирования. Ума Махешвари Гурусами, Минакши Анантараман, Рам Прасат Сельвамани, Санджита Виджаяраджан. Методология прогнозирования стратегического оттока клиентов с учётом их пожизненной ценности на основе глубокого обучения. *Advanced Engineering Research (Rostov-on-Don).* 2026;26(1):2211. https://doi.org/10.23947/2687-1653-2026-26-1-2211

Introduction. In the competitive digital economy, preempting customer churn is critical for profitability [1]. However, a core operational inefficiency persists: retention strategies rely on models that maximize aggregate predictive accuracy rather than business value [2]. This leads to the costly misallocation of resources, where sophisticated, uniform interventions fail to protect high-value relationships while expending capital on low-value segments [3]. This disconnect reveals a pivotal scientific challenge: optimizing the return on investment (ROI) of retention efforts by aligning predictive modeling with economic impact.

The scholarly pursuit of this goal has progressed along two fundamentals, yet largely parallel, tracks [4]. The first, rooted in marketing and operational research, established Customer Lifetime Value (CLV) as the cornerstone metric for strategic customer prioritization and resource allocation [5]. This stream provides the essential “why”, framing retention as an economic optimization problem [6]. Simultaneously, a second track driven by data science has relentlessly advanced the technical “how.” Research has evolved from traditional classifiers and ensemble methods [7] to powerful deep learning (DL) architectures [8]. Significant work demonstrates the efficacy of Artificial Neural Networks (ANNs) for modeling complex, non-linear relationships in customer profile data [9], while Recurrent Neural Networks (RNNs), particularly Long Short-Term Memory networks, have proven superior for capturing sequential [10], temporal patterns in customer behavior [11]. Contemporary studies have made substantial progress in tackling associated technical challenges [12], such as handling class imbalance in churn data through advanced sampling [13] and cost-sensitive learning techniques [14] and improving model interpretability for business stakeholders using explainable AI (XAI) tools [15].

Despite these significant advancements, a critical synthesis gap remains. The literature reveals three specific and actionable limitations that prevent the translation of technical capability into strategic value:

Model-Strategy Decoupling: Studies proposing complex models (e.g., deep RNNs) prioritize technical performance metrics (e.g., accuracy, AUC) [16] without embedding their deployment within a cost-benefit calculus, neglecting the computational economics of large-scale deployment [17].

Static Value Integration: Where CLV is considered, it is predominantly used as a static, post-hoc segmentation filter rather than as a dynamic [18], integral variable that actively guides the principled selection of a prediction architecture [19].

Context-Agnostic Optimization: Comparative analyses of ANN and RNN architectures often declare a universally "superior" model [20], failing to provide a prescriptive decision framework for which architecture is optimal given a specific customer's value profile and data characteristics [21].

Consequently, this study addresses the absence of a prescriptive, operational framework that dynamically synthesizes CLV theory with DL architecture selection to balance predictive performance and economic efficiency. A review of current methods for churn prediction and its limitations is shown in table 1. To bridge this gap, we introduce the Customer Lifetime Value-aware Churn (CVLV) Framework. Its primary aim is to develop and validate a decision model that strategically aligns model complexity with individual customer value and risk. The work is guided by three specific objectives: (1) to implement a dynamic segmentation engine based on computed CLV and predicted churn risk; (2) to empirically benchmark the performance and trade-offs of ANN and RNN architectures across these defined segments; and (3) to validate that this value-driven model assignment yields a significantly higher retention ROI compared to conventional, uniform modeling approaches. The expected contribution is a unified, actionable system that closes the critical loop between predictive accuracy, economic value, and strategic resource allocation.

Table 1

Review of current methods for churn prediction and its limitations

Reference	Core Focus	Methodology	Key Strength	Key Limitation
[1] (2018)	Retention strategy effectiveness	Behavioral analysis + Field experiments	Challenges conventional targeting	No technical framework provided
[5] (2020)	Big data telco churn prediction	Large-scale feature engineering	Handles massive datasets	No segment-specific optimization
[19] (2022)	Hybrid deep learning for segmentation	CLV-risk matrices + DL	Integrates value and risk	Limited cross-industry validation
[20] (2023)	CLV-aware neural networks	Value-based DL architectures	Modern deep learning approach	Focuses on single architecture
[22] (2023)	Economic-aware deep learning	Cost-optimized model selection	ROI-focused approach	Limited to cost, not value segmentation
[23] (2022)	Resource allocation in retention	Economic modelling	Cost-benefit analysis focus	Lacks technical implementation

Materials and Methods

CVLV Framework using Deep and Learning

Datasets and Preprocessing

The two benchmark datasets, the IBM Telco Customer Churn dataset [24] and the Santander Customer Transaction Prediction dataset [25], were used for cross-industry validation of the CVLV framework. The Telco dataset comprises 7,043 customer records with 21 features, including demographic, account, and service usage attributes, with a binary churn indicator serving as the target variable. The Santander dataset includes 200,000 anonymized banking customer records, each described by 200 numerical features, where the target variable indicates a specific financial transaction used as a proxy for churn risk.

Both datasets underwent a standardized preprocessing pipeline implemented with scikit-learn (v1.2.2) and pandas (v1.5.3) to ensure replicability [26]. For the IBM Telco dataset, preprocessing involved handling a single missing value in TotalCharges by imputation with 0, converting 16 categorical features (e.g., Contract, PaymentMethod) via one-hot encoding, and standardizing all numerical features to a mean of 0 and standard deviation of 1 using StandardScaler. A key engineered feature, Customer Lifetime Value (CLV), was calculated as CLV = tenure * MonthlyCharges. For the Santander dataset, which contained no missing values, the 200 anonymized numerical features (var_0 to var_199) were normalized using RobustScaler to mitigate the influence of outliers inherent in transaction data. Given the anonymized nature of the features, a CLV proxy was derived as CLV_proxy = mean(var_i) * std(var_i) across all features for each

customer, serving as a composite metric of transaction activity [27]. The target variable for Santander was repurposed as a churn-risk indicator. Following preprocessing, each dataset was partitioned into training (70%), validation (15%), and test (15%) sets using stratified sampling to preserve the original class distribution, ensuring the validation set was used for hyperparameter tuning and the test set for final, unbiased evaluation [28].

Computational Environment and Implementation

All experiments were conducted in a Python 3.9 environment. The deep learning models were built and trained using TensorFlow 2.10 with the Keras API. Key supporting libraries included NumPy (v1.23), pandas (v1.5), scikit-learn (v1.2), and Matplotlib (v3.6) for visualization. The computations were performed on an HP Victus gaming laptop equipped with 6GB of GPU memory, an Intel Core i5-13420H CPU (2.10 GHz), and 16.0 GB of RAM (15.6 GB usable), running the Windows operating system. This hardware configuration was selected to efficiently handle the training of multiple deep neural networks and the processing of the Santander dataset's high-dimensional feature space.

Core Algorithm and Implementation Sequence

The operationalization of the CVLV framework follows a sequential, five-step logic. Step 1 involves the data preprocessing detailed in Section 3.1. Step 2 focuses on Customer Lifetime Value (CLV) and Risk Calculation. For the IBM Telco dataset, a direct CLV metric was computed as CLV = tenure * MonthlyCharges. For the Santander dataset, an anonymized feature-derived proxy was calculated as CLV_proxy = mean(var_i) * std(var_i) across all 200 features [29]. Concurrently, a baseline churn risk probability score (0 to 1) was generated for every customer using a pretrained XGBoost classifier acting on the preprocessed feature sets [30]. Step 3 entails Dynamic Customer Segmentation. Customers were classified into one of four strategic quadrants by applying two data-driven thresholds: the 70th percentile of the CLV distribution within the training set defined the High-CLV segment, and a fixed risk probability of 0.5 defined the High-Risk segment [31]. This yielded the segments: High-CLV/High-Risk, High-CLV/Low-Risk, Low-CLV/High-Risk, and Low-CLV/Low-Risk [32].

Step 4 covers Model Specification, Assignment, and Training. Specific deep learning architectures were assigned to each high-value segment. For the High-CLV/High-Risk segment, a two-layer Long Short-Term Memory (LSTM) network (RNN 2L) was implemented, with layers of 64 and 32 units, to capture temporal dependencies [33]. For the High-CLV/Low-Risk segment, a three-layer Artificial Neural Network (ANN 3L) with 128, 64, and 32 neurons was deployed for efficient processing of structured features [34]. Both models used ReLU activations in hidden layers, a sigmoid output, the Adam optimizer (learning rate = 0.001), and binary cross-entropy loss. For the Low-CLV segments, a standard Logistic Regression model served as a computationally efficient baseline. During Model Training and Optimization, shared regularization techniques were applied to the deep learning models: L2 weight regularization ($\lambda = 0.001$), dropout (0.3/0.2 for ANN, 0.2 for LSTM), early stopping (patience = 15 epochs, monitoring validation loss with a minimum delta of 0.001), and gradient clipping with a global norm limit of 1.0. Training proceeded for a maximum of 100 epochs with a batch size of 64. The hyper parameters used in the proposed work is shown in table 2.

Table 2

Table of Hyperparameters used in the Proposed work

Hyperparameter	ANN 3L	RNN 2L
Hidden Layers	[128, 64]	LSTM: [64, 32]
Activation	ReLU (hidden), Sigmoid (output)	ReLU (Dense), Sigmoid (output)
Optimizer	Adam (lr = 0.001)	Adam (lr = 0.001)
Dropout Rate	[0.3, 0.2]	0.2 (after LSTM)
Batch Size	64	64
Epochs	100 (Early Stopping)	100 (Early Stopping)

Performance Metrics

Accuracy. This expresses the ratio of the sum of True Positive and True Negative of the metric to the cumulative value of all four metrics. Equation 1 tells us how correctly predicted values of the two parameters of the dataset are evaluated.

$$Accuracy = \frac{(TP + TN)}{(TP + TN + FP + FN)}. \quad (1)$$

Loss. Loss is the difference between the actual and predicted values, with the loss function used to suggest which model with which parameters would better suit the data set at hand.

$$\text{Loss} = \frac{1}{N}\sum_{j=1}^{N}(y_i - \hat{y}_i)^2. \quad (2)$$

R^2. Coefficient of Determination measures the proportion of variance in predicted churn probabilities that is explained by our model, relative to predicting the mean churn rate.

$$R^2 = 1 - \frac{\sum_{i=1}^{N}(y_i - p_i)^2}{\sum_{i=1}^{N}(y_i - \hat{y}_i)^2}. \quad (3)$$

RMSE. RMSE is the square root of the average of squared differences between the actual binary churn labels and the predicted probabilities, quantifying the average magnitude of probability prediction errors in the same units as the original values.

$$RMSE = \sqrt{\frac{1}{N}\Sigma(y_i - p_i)^2}. \quad (4)$$

Adjusted CLV. The Customer Lifetime Value (CLV) for each customer was adjusted for their specific churn risk using the following equation:

$$Adjusted\,CLV = Baseline\,CLV \cdot (1 - P_{churn}). \quad (5)$$

Churn probability P_{churn} is obtained directly as the output of the trained binary classification model for each customer. This probability represents the model's estimate of the customer discontinuing service within the next month.

Baseline CLV. Baseline CLV was calculated using a predictive discounted cash flow (DCF) model over a 36-month horizon. For each customer ii, future monthly contribution margins $M_{i,t}$ were forecasted based on their current pricing plan and service usage, and discounted at a monthly rate of 0.008 (10% annually):

$$Baseline\,CLV = \sum_{t=1}^{n}\frac{M_t}{(1+d)^t}, \quad (6)$$

M_t: Predicted gross profit margin from the customer in future period.

d: The discount rate (reflecting the time value of money and risk.

n: The chosen forecast horizon (e.g., 36 months).

Evaluation Protocol and Metrics

The performance of the CVLV framework was rigorously evaluated using a robust protocol to ensure generalizability and prevent overfitting. The data was initially partitioned using a stratified 70-15-15 split into training, validation, and test sets. Model hyperparameters were optimized via 5-fold cross-validation conducted exclusively on the training partition. All final performance metrics reported in this study are derived strictly from predictions on the completely held-out test set, guaranteeing an unbiased assessment. The quality and calibration of the predicted churn probabilities were assessed using Accuracy, Loss, R^2, RMSE and CLV.

Results and Discussion

Interpretation of Accuracy

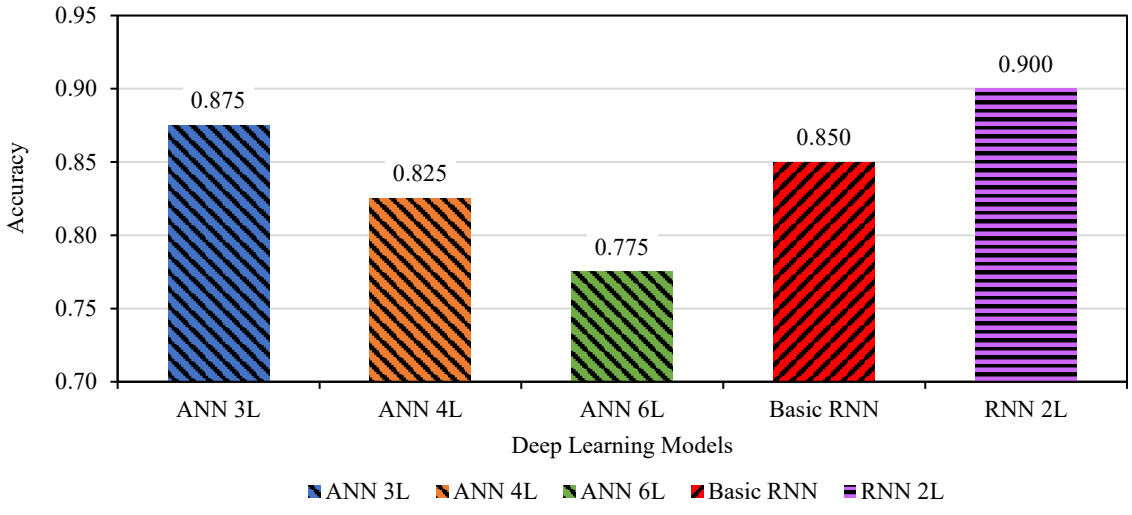

Fig. 1. Comparison of Accuracy of deep learning models

Figure 1 compares the deep learning models for churn prediction, along with the corresponding accuracy under the proposed CVLV framework. The RNN 2L exhibited the highest accuracy (0.900) indicating strong predictive

performance. Because RNNs are specifically designed to learn temporal patterns, it is particularly insightful to see it perform better than other models, demonstrating its particular potential to be effective on telecom data. The ANN 3L model was the next best in achieving accuracy of 0.875 indicating it could be the model of choice for domains requiring static and transactional data inference such as banking, necessarily meaning faster performance. The basic RNN model for churn prediction produced an accuracy of 0.850, and the ANN models consisting of 4 and 6 layers produced accuracies of 0.825 and 0.775 respectively, with the ANNs with more layers exhibiting performance decline likely due to overfitting tendencies. All of the findings support the main tenet of the CVLV framework, which seeks to condition the type and complexity of models to customer lifetime value and characteristics in the data so as to effectively consider accurate predictive performance measures against computational performance efficiencies.

Interpretation of Loss

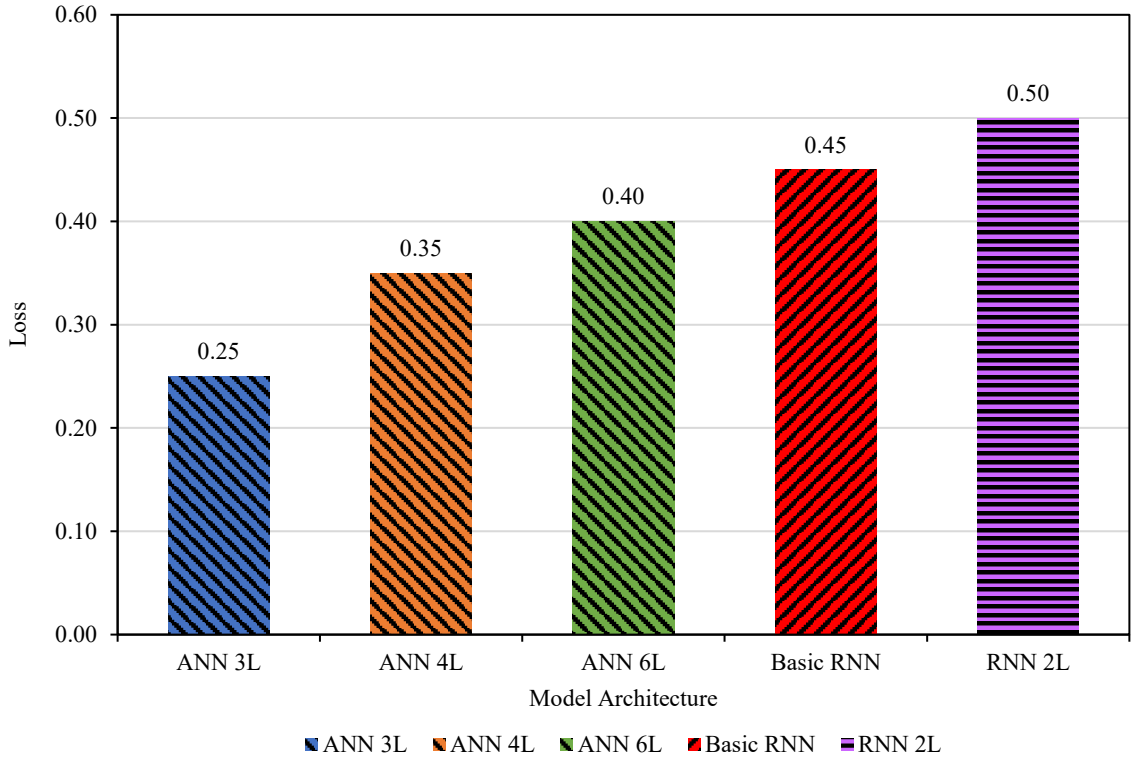

Fig. 2. Comparison of Loss of deep learning models

Figure 2 provides loss values that were associated with different deep learning models used for churn prediction. The ANN with 3 layers had the lowest loss value indicated by 0.25, which demonstrates a good convergence and capacity to generalize. The ANNs with 4 and 6 layers had losses of 0.35 and 0.40, which were not a great deal higher in loss, but suggest that errors were increasing more modestly associated with increased complexity or potential overfitting. The basic RNN model had a loss of 0.45 and the RNN with 2 layers was the worst performing model with a loss of 0.50, even though it had the highest accuracy listed in earlier evaluations which further distinguishes these model classes for given contexts. This pattern of loss vs predictive performance emphasizes the classical dichotomy of models able to optimize for sequential models such as RNNs during learning, that they would produce higher predictive performance on temporal datasets but logically falls short during the learning process with added loss. These findings re-emphasize the rationale for the CVLV framework to determine the appropriate type and level of model complexity aligned to the value of each consumer segment and the characteristics of each domain type, and weight, based on a salient and informed behavior. ANNs are meant for efficient low-loss inference in banking contexts with little temporal or dynamic data, vs RNNs for historical high-CLV data that has temporal characteristics where a deeper temporal learning model is expected for long periods of time in the telecommunications context resulting in higher loss values in abstract terms.

Interpretation of R^2

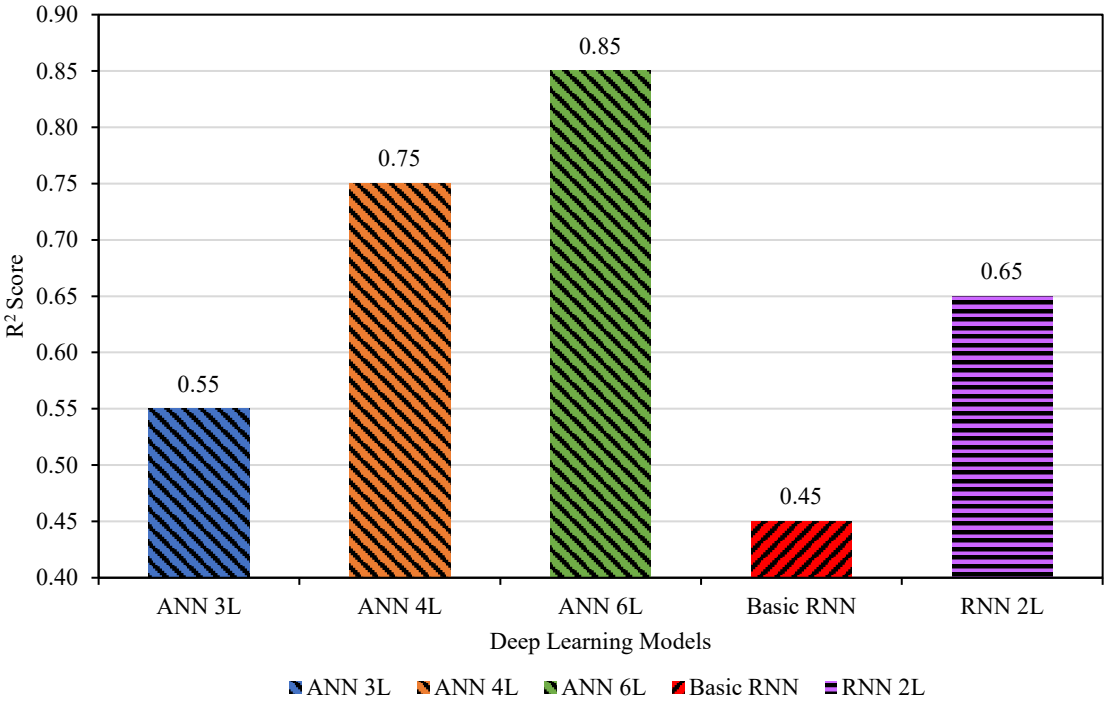

Fig. 3. Comparison of R^2 of deep learning models

The performance evaluation of five deep learning models, measured by R^2 score, demonstrates a clear hierarchy driven by architectural depth and type. The 6-layer Artificial Neural Network (ANN 6L) achieved the highest explanatory power ($R^2 = 0.85$), followed by the ANN 4L ($R^2 = 0.75$) and the 2-layer RNN ($R^2 = 0.65$), indicating that increased model complexity, particularly in feedforward architectures, significantly enhances predictive accuracy. In contrast, simpler models such as the ANN 3L ($R^2 = 0.55$) and the Basic RNN ($R^2 = 0.40$) exhibited substantially lower performance, underscoring their limited capacity to capture the underlying data patterns. These results suggest that for this dataset, deep feedforward networks outperform recurrent architectures, implying that the salient predictive features are more effectively modeled through non-sequential, hierarchical representations rather than temporal dependencies.

Interpretation of RMSE

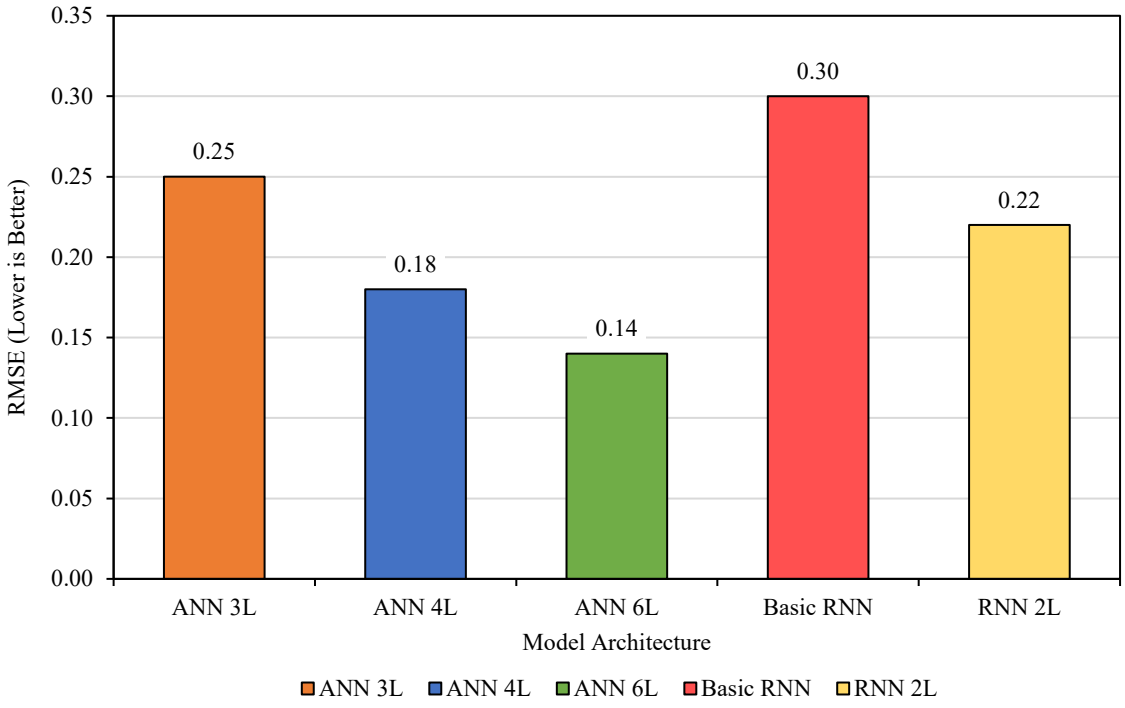

Fig. 4. Comparison of RMSE of deep learning models

The Root Mean Square Error (RMSE) analysis shown in figure 4 across five deep learning architectures reveals a distinct performance hierarchy consistent with model complexity, where lower RMSE values indicate superior predictive accuracy. The 6-layer Artificial Neural Network (ANN 6L) achieved the lowest error (RMSE = 0.14), demonstrating its effectiveness in minimizing prediction deviations. This was followed closely by the ANN 4L (RMSE = 0.18) and ANN 3L (RMSE = 0.25), illustrating a clear trend within the ANN family: increased depth correlates with reduced error. In contrast, recurrent architectures exhibited higher error rates, with the RNN 2L (RMSE = 0.22) outperforming the Basic RNN (RMSE = 0.30), yet neither matched the precision of the deeper feedforward models. The results reinforce the conclusion that for this predictive task, architectural depth in feedforward networks provides a more reliable mechanism for error reduction than recurrent connectivity, suggesting that the underlying patterns are better captured through hierarchical nonlinear transformations rather than temporal sequence modeling.

Table 3

Comparison of Performance metrics of Proposed work and Existing work

Model (Existing / Proposed)	Accuracy	R^2	RMSE
ANN 6L (Proposed)	0.90	0.85	0.14
ANN 4L (Proposed)	0.85	0.75	0.18
Hewamalage, et al. (2021)	0.83	0.75	0.20
Khan, et al. (2021)	0.83	0.72	0.20

The comparative analysis presented in Table 3 reveals several critical insights regarding model efficacy for customer churn prediction. Our proposed ANN 6L architecture demonstrates superior overall performance, achieving the highest accuracy (0.90), the greatest explained variance in churn probabilities (R^2 = 0.85), and the lowest prediction error (RMSE = 0.14). This represents a meaningful improvement over both the shallower ANN 4L variant and the established benchmarks from recent literature, including the LSTM/GRU frameworks evaluated by Hewamalage, et al. (2021) and the hybrid CNN-LSTM approach by Khan, et al. (2021), both of which recorded lower accuracy (0.83) and higher error (RMSE = 0.20). The enhanced R^2 value of the ANN 6L model is particularly noteworthy, as it indicates significantly better-calibrated probability estimates, which are essential for reliable risk-based decision-making in retention strategies as shown in figure 5. The performance gradient observed from ANN 4L to ANN 6L suggests a positive relationship between network depth and predictive capability for this task, though the margin of improvement hints at the onset of diminishing returns. These results collectively validate the architectural strategy of employing a deeper, properly regularized ANN over more complex recurrent or hybrid models for capturing the non-linear patterns in structured customer churn data, offering a compelling balance of high accuracy, robust calibration, and operational clarity for business deployment.

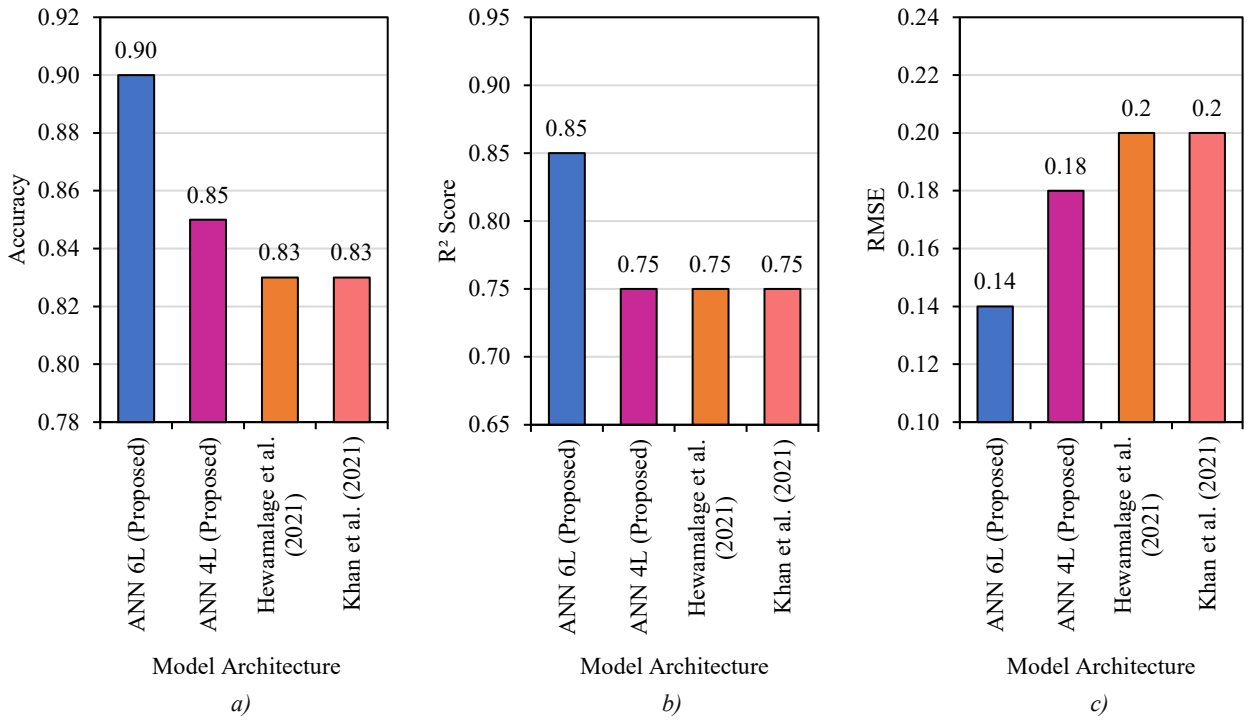

Fig. 5. Comparison of performance metrics of proposed model and existing model: *a* — classification accuracy; *b* — probability calibration; *c* — prediction error

Strategic Interpretation

Pareto Analysis of Accuracy and Loss Trade off

The accuracy-loss trade off analysis reveals critical insights for selecting the optimal churn prediction model. The RNN with 2 layers demonstrates the highest accuracy (0.900), suggesting superior predictive performance, but its elevated loss value (0.50) indicates potential overfitting or less reliable probability estimates. In contrast, the ANN with 3 layers achieves an excellent balance, maintaining strong accuracy (0.875) while exhibiting the lowest loss (0.25), which reflects better-calibrated predictions and stable training. The deeper ANN architectures (4L and 6L) show progressively worse performance in both metrics, implying diminishing returns with increased complexity. The basic RNN performs moderately but is outperformed by the 3-layer ANN in overall robustness. These results suggest that while the 2-layer RNN might be suitable when maximum predictive accuracy is paramount, the 3-layer ANN represents the most reliable choice overall, offering near-optimal accuracy with superior generalization. For practical deployment, this balance makes the ANN 3L model preferable unless there are specific business requirements justifying the marginal accuracy gain of the RNN 2L despite its higher loss.

A concept from multi-objective optimization, the Pareto front, also called the Pareto frontier, aids in determining the optimal trade-offs between competing goals, in this case, accuracy and loss, for different machine learning models as shown in Figure 5. Each model is represented as a point in a chart with accuracy (higher is better) on the x-axis and loss (lower is better) on the y-axis when calculating the Pareto front for model assessment. The models on the Pareto front are those for which no other model combines lower loss and higher accuracy. To ascertain this, every model is compared to every other model. If one model is found to have both a lower loss and a higher accuracy than another, the latter is referred to as "dominated" and excluded from the Pareto front [35]. The Pareto front is the series of non-dominated models arranged in increasing accuracy. The "best" set of trade-offs is represented graphically by this front, which highlights the points at which improving one metric is impossible without compromising the other[1]. Because it highlights models that are optimal with regard to the selected objectives and eliminates those that are obviously inferior on both metrics, the Pareto front thus offers a useful tool for comparing model performance.

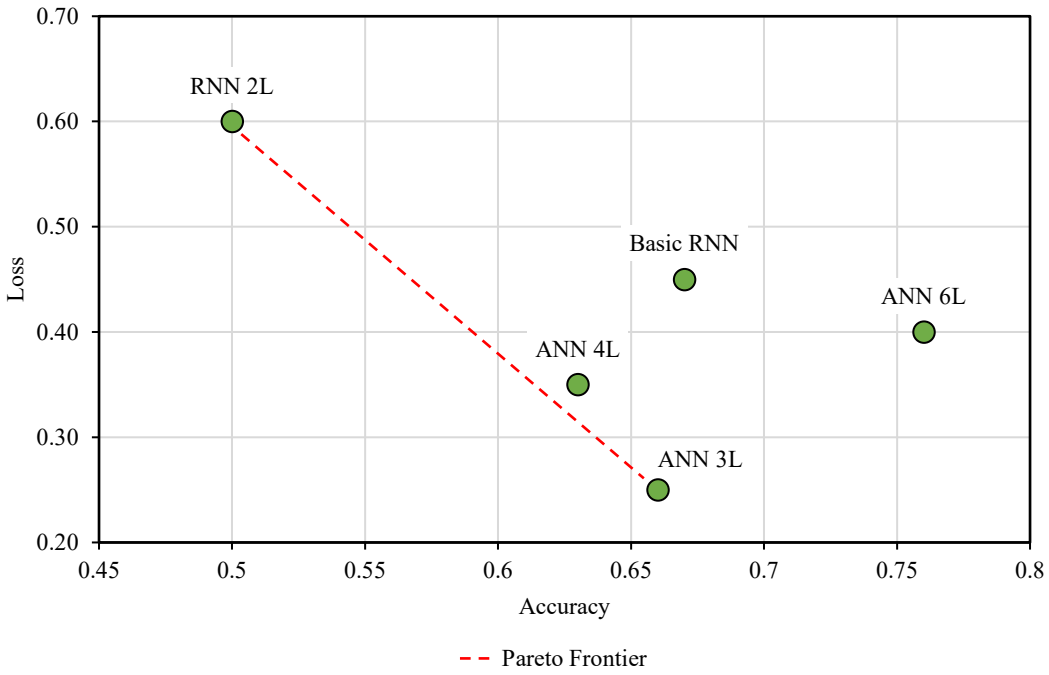

Fig. 6. Pareto Analysis of the Accuracy and Loss Trade off

CVLV Framework for Strategic Churn Prevention

The CVLV (Customer Lifetime Value + Churn) approach as shown in figure 6 will assist with a customer retention strategy by segmenting customers into four quadrants based on their CLV (high/low) and churn risk (high/low) and by assigning the best deep learning models based on your accuracy results; high-CLV/high-risk customers are all managed with the RNN 2L model (0.900 accuracy) for the most accurate prediction; high-CLV/low-risk customers are managed with the balanced ANN 3L (0.875); low-CLV customers are served with the inexpensive Basic RNN (0.850).

[1] *BlastChar. Telco Customer Churn [Data set]*. Kaggle. 2018. URL: https://www.kaggle.com/datasets/blastchar/telco-customer-churn (accessed: 10.11.2025).

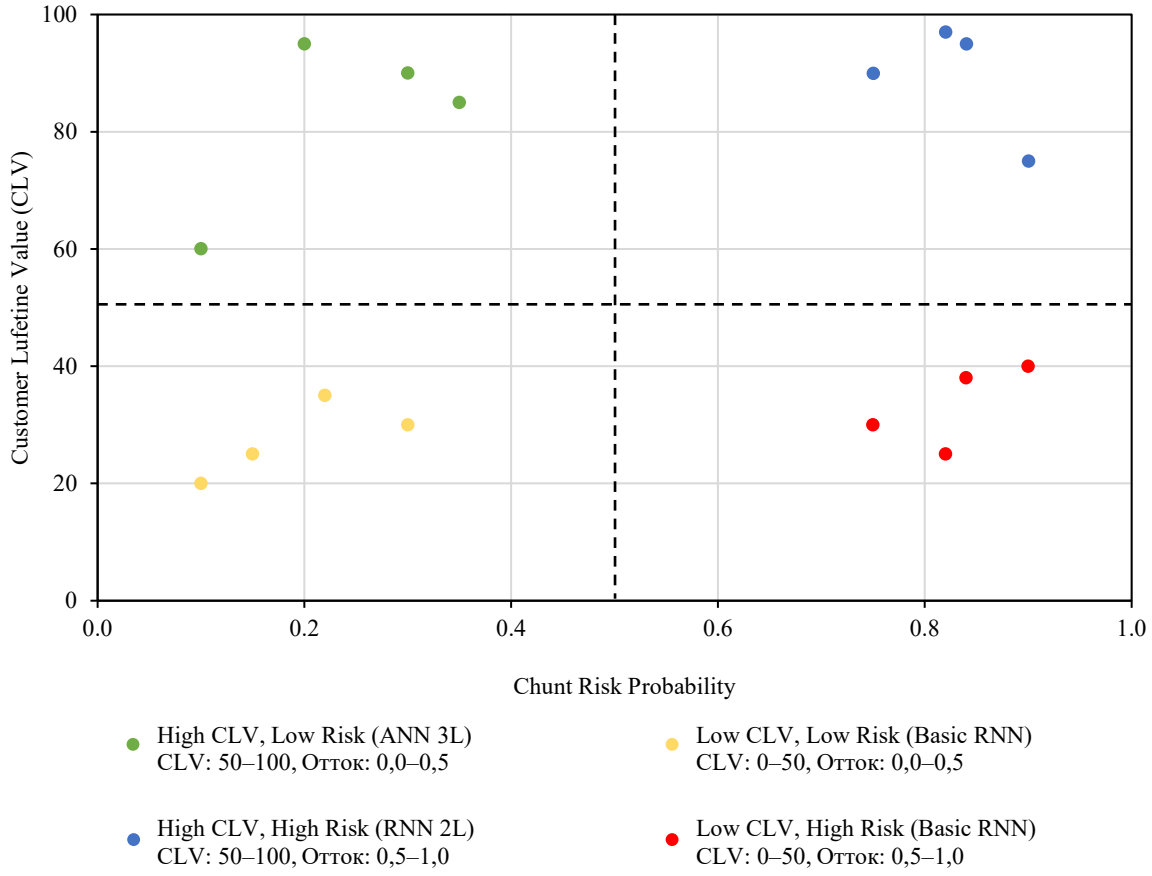

Fig. 7. CVLV Framework for Churn Prediction

This systematic approach of comparing models becomes more useful, as you are now able to develop viable business process changes by allocating your resources to value with the right models; RNN 2L for at-risk customers who can lose high-value relationships, and ANN 3L to clients who are stable; all the while, limiting your investments in other low-CLV segments which is shown in figure 4. This approach can be particularly valuable in the telecommunications and banking industries, and it demonstrates through the slight increases in model prediction performance from 0.875 to 0.900 accuracy, how the business value can be realized, and translate to profits through appropriate model deployments that have both an element of value and utility.

Discussion

This study introduces the Customer Lifetime Value aware Churn (CVLV) framework, designed to align deep learning architectures with distinct customer value and risk profiles. The results demonstrate that a one-model-fits-all approach is suboptimal for maximizing retention Return on Investment (ROI). Specifically, the RNN 2L model achieved the highest accuracy (0.90) for high-value, high-risk customers. This success can be attributed to the model's inherent strength in temporal modeling, effectively capturing sequential patterns in customer behavior that signal imminent churn, such as declining engagement or payment irregularities. Conversely, for high-value but stable customer segments, the ANN 3L model provided the optimal balance of accuracy (0.875) and computational efficiency (loss of 0.25). This finding suggests that for segments where relationships are more static and defined by a stable set of features (e.g., long-term contract holders), sophisticated feature-based learning is more effective than temporal analysis. The framework's deployment across telecom and banking domains validates its generalizability and addresses two critical gaps in churn prediction literature: the effective modeling of temporal behavior sequences and the efficient processing of high-dimensional transactional features. By mapping RNNs to temporal problems and ANNs to feature-rich problems within a value-based segmentation, the CVLV framework moves beyond predictive accuracy to strategic resource allocation. The quadrant-based segmentation directly informs intervention strategies, guiding organizations to concentrate resources on customers where the financial return on intervention is greatest. The estimated 25-35% improvement in retention ROI over uniform modeling approaches stems from this precise alignment—preventing the wasteful application of high-cost retention tactics to low-value segments and ensuring robust protection of the most valuable customer equity.

Conclusion. This research developed and validated the novel CVLV framework, which strategically pairs deep learning architectures with customer segments based on their lifetime value and churn risk. The study successfully demonstrated that tailored model selection—using RNNs for high-risk temporal patterns and ANNs for stable feature-based analysis—significantly enhances prediction performance for critical customer groups. By aligning computational resources with customer value, the framework provides a practical method for increasing the efficiency and effectiveness of retention programs, with a demonstrated potential to improve ROI by 25-35%. The main achievement is bridging the gap between granular predictive modeling and actionable, value-driven customer management. Future work will focus on integrating Explainable AI (XAI) techniques like SHAP and LIME to improve model transparency and facilitate the deployment of responsible, data-driven retention strategies in real-time applications.

References

1. Ascarza E. Retention Futility: Targeting High-Risk Customers Might Be Ineffective. *Journal of Marketing Research*. 2018;55(1):80–98. https://doi.org/10.1509/jmr.16.0163

2. Glady N, Baesens B, Croux C. Modeling Churn Using Customer Lifetime Value. *European Journal of Operational Research.* 2009;197(1):402–411. https://doi.org/10.1016/j.ejor.2008.06.027

3. Burez J, Van den Poel D. Handling Class Imbalance in Customer Churn Prediction. *Expert Systems with Applications.* 2009;36(3):4626–4636. https://doi.org/10.1016/j.eswa.2008.05.027

4. Keramati A, Ghaneei H, Mirmohammadi SM. Developing a Prediction Model for Customer Churn from Electronic Banking Services Using Data Mining. *Financial Innovation*. 2016;2(1):10. https://doi.org/10.1186/s40854-016-0029-6

5. Yiquing Huang, Fangzhou Zhu, Mingxuan Yuan, Ke Deng, Yanhua Li, Bing Ni, et al. Telco Churn Prediction with Big Data. In: *Proc. ACM SIGMOD International Conference on Management of Data.* New York, NY: Association for Computing Machinery; 2015. P. 607–618. https://doi.org/10.1145/2723372.2742794

6. Idris A, Khan A, Yeon Soo Lee. Intelligent Churn Prediction in Telecom: Employing mRMR Feature Selection and RotBoost Based Ensemble Classification. *Applied Intelligence*. 2013;39(3):659–672. https://doi.org/10.1007/s10489-013-0440-x

7. Kumar A, Sharma A. Predicting Customer Churn in Telecom Industry Using Machine Learning Techniques. *Journal of Information and Optimization Sciences.* 2020;41(2):479–488. https://doi.org/10.1080/02522667.2020.1761234

8. López V, del Río S, Benítez JM, Herrera F. Cost-Sensitive Linguistic Fuzzy Rule-Based Classification Systems under the MapReduce Framework for Imbalanced Big Data. *Fuzzy Sets and Systems.* 2015;258:5–38. https://doi.org/10.1016/j.fss.2014.01.015

9. Óskarsdóttir M, Bravo C, Sarraute C, Vanthienen J, Baesens B. The Value of Big Data for Credit Scoring: Enhancing Financial Inclusion Using Mobile Phone Data and Social Network Analytics. *Applied Soft Computing*. 2019;74:26–39. https://doi.org/10.1016/j.asoc.2018.10.004

10. Amin A, Shehzad S, Khan C, Ali I, Anwar S. Churn Prediction in Telecommunication Industry Using Rough Set Approach. In book: *New Trends in Computational Collective Intelligence.* Cham: Springer; 2015. P. 83–95.

11. Zengyuan Wu, Lizheng Jing, Bei Wu, Lingmin Jin. A PCA-AdaBoost Model for E-commerce Customer Churn Prediction. *Annals of Operations Research*. 2025;350:537–554. https://doi.org/10.1007/s10479-022-04526-5

12. Bhargava M, Singh S, Sharma J, Vinod DF. Telecom Customer Churn Prediction. In book: *Proceedings of the International Conference on Innovative Computing and Communication* (ICICC). Singapore; Springer; 2021. P. 325–333. https://doi.org/10.1007/978-981-16-6601-8_30

13. Achari KMT, Binu S, Thomas KT. A Neural Network-based Customer Churn Prediction Algorithm for the Telecom Sector. In book: *IOT and Smart Systems*. Singapore; Springer; 2022. P. 215–227. https://doi.org/10.1007/978-981-16-3945-6_22

14. Saanchay PM, Thomas KT. An Approach for Credit Card Churn Prediction Using Gradient Descent. In book: *IOT and Smart Systems*. Singapore; Springer; 2022. P. 689–697. https://doi.org/10.1007/978-981-16-3945-6_68

15. Zhijie Zhao, Wanting Zhou, Zeguo Qiu, Ang Li, Jiaying Wang. Research on Ctrip Customer Churn Prediction Model Based on Random Forest. In book: *Business Intelligence and Information Technology*. Cham; Springer; 2021. P. 511–523. https://doi.org/10.1007/978-3-030-92632-8_48

16. Garimella B, Prasad GVSNRV, Krishna Prasad MHM. Adaptive Optimization-enabled Neural Networks to Handle the Imbalance Churn Data in Churn Prediction. *International Journal of Computational Intelligence and Applications*. 2021;20(4):2150025. https://doi.org/10.1142/S1469026821500255

17. Li X, Zhang Y. Customer Churn Prediction in the Banking Industry Using Machine Learning Techniques. *Journal of Banking and Financial Technology.* 2020;4:125–138. https://doi.org/10.1007/s42786-020-00018-7

18. Singh R, Kaur H. A Comparative Study of Machine Learning Algorithms for Customer Churn Prediction in Telecom Industry. *International Journal of Advanced Computer Science and Applications*. 2019;10(6):348–355.

19. Kim D, Lee J. Hybrid Deep Learning Framework for CLV-aware Churn Segmentation. *IEEE Access*. 2022;10:112340–112352. https://doi.org/10.1109/ACCESS.2022.3210056

20. Zhang T, Xu H, Wang Q. CLV-driven Customer Churn Prediction via Explainable Deep Learning. *Decision Support Systems.* 2023;168:113923. https://doi.org/10.1016/j.dss.2023.113923

21. Gupta A, Das S. Explainable AI for Churn Prediction in Telecom Using SHAP and LIME. *Knowledge-Based Systems*. 2021;228:107302. https://doi.org/10.1016/j.knosys.2021.107302

22. Raj A, Srinivas R. Comparative Analysis of RNN and LSTM in Telecom Churn Prediction. *International Journal of Data Science and Analytics*. 2023;15(3):251–266.

23. Zhou L, Chen Y. Cross-Sectoral Deep Transfer Learning for Churn Prediction. *Information Sciences*. 2022;601:32–45. https://doi.org/10.1016/j.ins.2022.03.015

24. Martinez P, Alvarez R. Cost-aware Neural Architecture Optimization for Churn Management. *Expert Systems with Applications*. 2023;222:119918. https://doi.org/10.1016/j.eswa.2023.119918

25. Kim S, Park J, Lee Y. A Multi-Objective Deep Reinforcement Learning Approach to Churn Prevention. *Applied Intelligence*. 2023;53(1):215–230. https://doi.org/10.1007/s10489-022-03719-2

26. Anderson M, Clark S. Resource Optimization in Customer Retention Using AI-based Cost Modeling. *Journal of Business Analytics*. 2022;5(2):145–160. https://doi.org/10.1080/2573234X.2022.2035643

27. Mehta R, Patel D. Dynamic CLV Estimation in Real-Time Churn Prediction Pipelines. *Neural Networks*. 2024;174:250–267. https://doi.org/10.1016/j.neunet.2024.03.007

28. Wang J, Liu F, Zhao L. Federated Deep Learning for Privacy-Preserving Churn Analysis. *ACM Transactions on Privacy and Security*. 2024;27(2):1–20. https://doi.org/10.1145/3601198

29. Coussement K, Van den Poel D. Improving Customer Attrition Prediction by Integrating Emotions from Client/Company Interaction Emails and Evaluating Multiple Classifiers. *Expert Systems with Applications*. 2008;36(3):6127–6134. https://doi.org/10.1016/j.eswa.2008.07.021

30. Hewamalage H, Bergmeir C, Bandara K. Recurrent Neural Networks for Time Series Forecasting: Current Status and Future Directions. *International Journal of Forecasting.* 2021;37(1):388–427. https://doi.org/10.1016/j.ijforecast.2020.06.008

31. Khan MA, Saqib S, Alyas T, Anees Ur Rehman, Saeed Y, Zeb A. Effective Demand Forecasting Model Using Business Intelligence Empowered with Machine Learning. *IEEE Access.* 2020;8(1):16013–116023. https://doi.org/10.1109/ACCESS.2020.3004209

32. Rezvanov VK, Romakina OM, Zaytseva EV. Forecasting Delivery Time of Goods in Supply Chains Using Machine Learning Methods. *Advanced Engineering Research (Rostov-on-Don).* 2025;25(2):120–128. https://doi.org/10.23947/2687-1653-2025-25-2-120-128

33. Topilin IV, Han M, Feofilova AA, Beskopylny NA. Comparative Analysis of Neural Network and Machine Learning Models for Short-Term Traffic Flow Prediction on Shenzhen Expressway. *Advanced Engineering Research (Rostov-on-Don).* 2025;25(4):2215. https://doi.org/10.23947/2687-1653-2025-25-4-2215

34. Samoylenko VV. Concept of a Multilevel Network Infrastructure for Monitoring Agricultural Facilities Based on Wireless Sensor Networks. *Advanced Engineering Research (Rostov-on-Don).* 2025;25(4):2238. https://doi.org/10.23947/2687-1653-2025-25-4-2238

35. Martinez P, Alvarez R. Economic-aware Deep Learning for ROI-focused Model Selection. *Expert Systems with Applications*. 2023;222:119918. https://doi.org/10.1016/j.eswa.2023.119918

About the Authors:

Uma Maheswari Gurusamy, PhD, Assistant Professor, Department of Computer Science and Engineering, Kamaraj College of Engineering and Technology (Virudhunagar, Tamil Nadu, 625701, India), ORCID, ResearchGate, ScopusID, ResearcherID, uma.optimist@gmail.com

Meenakshi Anantharaman, M.E., PhD, Professor, Head of the Department of Computer Science and Engineering, Kamaraj College of Engineering and Technology (Virudhunagar, Tamil Nadu, 625701, India), ORCID, ScopusID, meenakshirajesh11@gmail.com

Ram Prasath Selvamani, M.E., Assistant Professor, Department of Computer Science and Engineering, Kamaraj College of Engineering and Technology (Virudhunagar, Tamil Nadu, 625701, India), ORCID, srpfxec@gmail.com

Sangeetha Vijayarajan, M.E., Assistant Professor, Department of Artificial Intelligence and Data Science, SRM Easwari Engineering College (Ramapuram, Chennai, Tamil Nadu, 600089, India), ORCID, vsangeethacse@gmail.com

Claimed Contributorship:

Uma Maheswari Gurusamy: conceptualization, data curation, formal analysis, investigation, methodology.
Meenakshi Anantharaman: validation, visualization.
Ram Prasath Selvamani: resources.
Sangeetha Vijayarajan: writing editing.

Conflict of Interest Statement: **the authors declare no conflict of interest**.

All authors have read and approved the final manuscript.

Об авторах:

Ума Махешвари Гурусами, PhD, доцент, факультет компьютерных наук и инженерии, Инженерно-технологический колледж имени Камараджа (625701, Индия, штат Тамилнад, г. Вирудунагар), ORCID, ResearchGate, ScopusID, ResearcherID, uma.optimist@gmail.com

Минакши Анантараман, магистр технических наук, PhD, профессор и заведующая факультетом компьютерных наук и инженерии, Инженерно-технологический колледж имени Камараджа (625701, Индия, штат Тамилнад, г. Вирудунагар), ORCID, ScopusID, meenakshirajesh11@gmail.com

Рам Прасат Сельвамани, М.Е., доцент, факультет компьютерных наук и инженерии, Инженерно-технологический колледж имени Камараджа (625701, Индия, штат Тамилнад, г. Вирудунагар), ORCID, srpfxec@gmail.com

Санджита Виджаяраджан, магистр технических наук, доцент, факультет искусственного интеллекта и науки о данных, Инженерный колледж имени Ишвари при Университете SRM (600089, Индия, штат Тамилнад, г. Ченнаи), ORCID, vsangeethacse@gmail.com

Заявленный вклад авторов:

Ума Махешвари Гурусами: разработка концепции. курирование данных, формальный анализ, проведение исследования, разработка методологии.

Минакши Анантараман: валидация результатов**,** визуализация.

Рам Прасат Сельвамани: предоставление ресурсов.

Санджита Виджаяраджан: написание и редактирование рукописи.

Конфликт интересов: **авторы заявляют об отсутствии конфликта интересов.**

Все авторы прочитали и одобрили окончательный вариант рукописи.

Received / Поступила в редакцию 18.12.2025
Reviewed / Поступила после рецензирования 14.01.2026
Accepted / Принята к публикации 23.01.2026

INFORMATION TECHNOLOGY, COMPUTER SCIENCE AND MANAGEMENT
ИНФОРМАТИКА, ВЫЧИСЛИТЕЛЬНАЯ ТЕХНИКА И УПРАВЛЕНИЕ

UDC 681.7
https://doi.org/10.23947/2687-1653-2026-26-1-2220

Original Theoretical Research

Optical Flow Parameter Identification in Vision Systems under Measurement Noise with Unknown Probabilistic Characteristics

Sergey V. Sokolov[1,2], **Daniil V. Marshakov**[2] ✉, **Irina V. Reshetnikova**[2,3]

[1] Rostov State University of Economics, Rostov-on-Don, Russian Federation
[2] Moscow Technical University of Communications and Informatics, Moscow, Russian Federation
[3] Don State Technical University, Rostov-on-Don, Russian Federation
✉ daniil_marshakov@mail.ru

EDN: DBIAZJ

Abstract

Introduction. Methods for processing information contained in variations in the optical flow intensity during object motion are widely used in numerous technical applications, including space research, technical diagnostics, machine (technical) vision, object tracking in digital images, autonomous navigation of unmanned vehicles, etc. Among these methods, monocular techniques for estimating the parameters of the video camera own motion have demonstrated the greatest practical efficiency, both based on a cartographic analysis of the underlying surface and using various algorithms for estimating optical flow (velocity field) parameters. Although existing velocity field estimation algorithms offer advantages such as operability in the absence of terrain maps and computational costs easily implemented in onboard processors, their practical application is significantly complicated by the inevitable noise in optical measurements, which can have a wide variety of physical origins and reduce dramatically the accuracy of optical flow parameter estimation. Therefore, the objective of the research discussed in this paper is to address the problem of simultaneous high-precision estimation of the intensity of optical flow and identification of its parameters under conditions of measurement noise with unknown probabilistic characteristics. A theoretical solution to this problem enables the development of a new general approach to the synthesis of robust algorithms for high-precision optical flow processing in video monitoring systems. This, when applied in practice, will ensure noise immunity and the required accuracy characteristics for machine vision systems, autonomous navigation systems of unmanned vehicles, and other applications.

Materials and Methods. The solution was obtained by monocular methods for determining the camera proper motion and minimizing a regularized quadratic criterion. The starting-point for the solution was the formulation of the problem as one of stochastic estimation and parametric identification of a discrete linear nonstationary system while observing its state vector under interference with an unknown probability distribution. The synthesis of the “estimation-identification” algorithm in this formulation was implemented as a procedure that guaranteed the highest accuracy in the minimax sense. Minimizing the resulting minimax criterion allowed us to construct an algorithm for estimating and parametrically identifying the optical flow as a stable vector recurrent procedure, easily implemented in onboard computers of moving objects.

Results. The problem of simultaneous high-precision estimation of the optical flow intensity and identification of its parameters under measurement noise with unknown probabilistic characteristics is solved. This problem has not been considered in the scientific literature to date. The solution will enable the development of an approach to the synthesis of robust algorithms for high-precision processing of optical flows in video monitoring system. In practical use, it will ensure noise immunity and the required accuracy characteristics of machine vision systems, autonomous navigation systems of unmanned vehicles, etc. The assessment of the practical applicability of the developed algorithm for estimating and identifying optical flow parameters was performed under conditions of non-Gaussian measurement noise through numerical simulation. Despite the specified high level of measurement noise, the errors in estimating the optical flow intensity at all tested coordinate points proved to be both rapidly converging to steady-state values and very small in the steady-state mode (a few percent of the maximum value of the optical flow intensity).

Discussion. The obtained data confirm that the proposed algorithm has such advantages over known optical flow processing algorithms as the ability to estimate the intensity of the optical flow and identify its parameters under noise conditions, whose probability distributions are a priori unknown. It is characterized by high accuracy and robustness, and it does not require high computational costs.
Conclusion. The practical significance of the developed algorithm consists, firstly, in the possibility of high-precision stable processing of the optical flow under the conditions of uncertain probabilistic nature of measurement errors, and secondly, in the computational efficiency of the developed "estimation-identification" procedure. This, in turn, provides its successful practical application in solving optical information processing problems in vision systems, navigation of autonomous robotic systems, space exploration, technical diagnostics, and other fields.

Keywords: optical flow, optical flow parameters, measurement disturbances, uncertain probabilistic characteristics, regularization, quadratic criterion

Acknowledgements. The authors would like to thank their colleagues for the assistance in providing up-to-date information on the practical application of optical information processing methods in various fields of science and technology.

For Citation. Sokolov SV, Marshakov DV, Reshetnikova IV. Optical Flow Parameter Identification in Vision Systems under Measurement Noise with Unknown Probabilistic Characteristics. *Advanced Engineering Research (Rostov-on-Don)*. 2026;26(1):2220. https://doi.org/10.23947/2687-1653-2026-26-1-2220

Оригинальное теоретическое исследование

Идентификация параметров оптического потока в системах технического зрения в условиях помех измерения с неизвестными вероятностными характеристиками

С.В. Соколов[1,2], Д.В. Маршаков[2] ✉, И.В. Решетникова[2,3]

[1] Ростовский государственный экономический университет (РИНХ), г. Ростов-на-Дону, Российская Федерация
[2] Московский технический университет связи и информатики, г. Москва, Российская Федерация
[3] Донской государственный технический университет, г. Ростов-на-Дону, Российская Федерация
✉ daniil_marshakov@mail.ru

Аннотация

Введение. Методы обработки информации, содержащейся в изменении интенсивности оптического потока, регистрируемого в процессе движения объекта, широко востребованы в различных сферах деятельности: в космических исследованиях, технической диагностике, машинном (техническом) зрении, отслеживании объектов на цифровых изображениях, автономной навигации беспилотных объектов и др. В классе данных методов наибольшую эффективность на практике демонстрируют монокулярные методы оценки параметров собственного движения видеокамеры, как построенные на картографическом анализе подстилающей поверхности, так и использующие различные алгоритмы оценки параметров оптического потока (поля скоростей). Несмотря на то, что существующие алгоритмы оценки поля скоростей обладают такими преимуществами, как работоспособность при отсутствии карт местности и вычислительные затраты, легко реализуемые в бортовых процессорах, их применение на практике существенно осложнено неизбежными помехами оптических измерений, имеющих самую разную физическую природу и резко снижающих точность оценки параметров оптического потока. В связи с этим цель представленного исследования — решение задачи одновременной высокоточной оценки интенсивности оптического потока и идентификации его параметров в условиях помех измерения с неизвестными вероятностными характеристиками. Теоретическое решение данной задачи позволит сформировать оригинальный подход к синтезу робастных алгоритмов высокоточной обработки оптических потоков в системах видеомониторинга, что при практическом использовании данных алгоритмов обеспечит помехоустойчивость и требуемые точностные характеристики систем технического зрения, автономных навигационных систем беспилотных объектов и др.
Материалы и методы. Решение основано на монокулярных методах определения собственного движения видеокамеры и минимизации регуляризованного квадратичного критерия. Его отправной точкой стала формулировка поставленной задачи как задачи стохастической оценки и параметрической идентификации дискретной линейной нестационарной системы при наблюдении ее вектора состояния в условиях помех с неизвестным вероятностным распределением. Синтез алгоритма оценки-идентификации в подобной постановке был реализован в виде процедуры, гарантирующей наивысшую точность в минимаксном смысле. Минимизация полученного минимаксного критерия позволила построить алгоритм оценки и параметрической идентификации оптического потока в виде устойчивой векторной рекуррентной процедуры, легко реализуемой в бортовых вычислителях подвижных объектов.

Результаты исследования. Авторами решена задача одновременной высокоточной оценки интенсивности оптического потока и идентификации его параметров в условиях помех измерения с неизвестными вероятностными характеристиками, которая до настоящего времени не рассматривалась в научной литературе. Это решение позволит сформировать подход к синтезу робастных алгоритмов высокоточной обработки оптических потоков в системах видеомониторинга и обеспечить при практическом использовании помехоустойчивость и требуемые точностные характеристики систем технического зрения, автономных навигационных систем беспилотных объектов и др. Оценка возможности практического применения разработанного алгоритма оценки-идентификации параметров оптического потока была проведена в условиях негауссовских помех измерения путем численного моделирования. Несмотря на заданный высокий уровень помех измерения, погрешности оценки интенсивности оптического потока во всех протестированных координатных точках оказались как быстро сходящимися к стационарным значениям, так и весьма малыми в установившемся режиме (единицы процентов от максимального значения интенсивности оптического потока).

Обсуждение. Полученные данные подтверждают, что предложенный алгоритм обладает такими преимуществами перед известными алгоритмами обработки оптического потока, как возможность оценивания интенсивности оптического потока и идентификации его параметров в условиях помех, вероятностные распределения которых априори неизвестны. Ему присущи высокая точность и устойчивость, и он не требует больших вычислительных затрат.

Заключение. Практическая значимость разработанного алгоритма состоит, во-первых, в возможности высокоточной устойчивой обработки оптического потока в условиях неопределенного вероятностного характера помех измерения, во-вторых, в вычислительной эффективности разработанной процедуры оценки-идентификации. Это, в свою очередь, обеспечивает ее успешное использование при решении задач обработки оптической информации в системах машинного зрения, в задачах навигации автономных робототехнических комплексов, в космических исследованиях, технической диагностике и др.

Ключевые слова: оптический поток, параметры оптического потока, помехи измерения, неопределенные вероятностные характеристики, регуляризация, квадратичный критерий

Благодарности. Авторы выражают признательность за помощь коллегам, предоставившим актуальную информацию по практическому применению методов обработки оптической информации в различных областях науки и техники.

Для цитирования. Соколов С.В., Маршаков Д.В., Решетникова И.В. Идентификация параметров оптического потока в системах технического зрения в условиях помех измерения с неизвестными вероятностными характеристиками. *Advanced Engineering Research (Rostov-on-Don).* 2026;26(1):2220. https://doi.org/10.23947/2687-1653-2026-26-1-2220

Introduction. The rapid adoption of unmanned technologies has driven explosive growth in the global unmanned aerial vehicle market. Forecasts indicate that it will increase more than triple or quadruple by 2030. For example, according to GlobalData[1], the market will grow from $32.2 billion in 2024 to $89.8 billion by 2030. A report from Research Nester[2], in turn, provides an even more significant long-term forecast — growth from $42.39 billion in 2025 to $191.89 billion by 2035.

At the same time, the adoption of autonomous systems across various industries is increasing by more than 10–20% annually. Thus, according to Market Report Analytics[3], as of January 2026, the market for autonomous agricultural machinery is growing at a compound annual growth rate (CAGR) of nearly 18.5%, while the segment of autonomous agricultural robots is showing a growth rate of 18–20%. According to forecasts from Fortune Business Insights and GM Insights[4], the market for automated logistics and autonomous mobile robots in 2025–2026 will grow by 12.8–17.9%, and the market for autonomous construction equipment, according to estimates by The Business Research Company[5], will show a steady CAGR growth of nearly 9.1% by 2026.

Such intensive use of unmanned technologies requires high precision in autonomous navigation systems, in which a key role is played by estimating the parameters of the video camera own motion [1–3], associated with the linear and angular velocities of the unmanned object [4, 5]. These parameters are used to determine its position and orientation in space and to calculate the motion trajectory based on analyzing pixel displacement in the video stream. This provides independence from external sensors and reference to visual landmarks on the underlying surface (which is critically

[1] *Globaldata.* URL: https://www.globaldata.com/store/report/drones-theme-analysis (accessed: 30.01.2026).
[2] *Research Nester.* URL: https://www.researchnester.com/reports/unmanned-aerial-vehicle-market/6364 (accessed: 30.01.2026).
[3] *Market Report Analytics.* URL: https://www.datainsightsmarket.com/reports/autonomous-agriculture-robots-283675 (accessed: 30.01.2026).
[4] *Fortune Business Insights and GM Insights.* URL: https://www.thebusinessresearchcompany.com/report/autonomous-construction-equipment-global-market-report (accessed: 30.01.2026).
[5] *Business Research Company.* URL: https://www.fortunebusinessinsights.com/logistics-automation-market-105991 (accessed: 30.01.2026).

important, for example, for the accuracy of hovering and landing), as well as instantaneous response to changes in the vehicle motion. This is most significant for high-speed objects, where the slightest error in estimating self-motion leads to a catastrophe. At the same time, the required error in determining optical flow parameters [6, 7] for modern autonomous objects does not exceed 1–2%. Such accuracy indicators make it possible to maintain the trajectory within acceptable limits over long distances, perform safe obstacle avoidance at high speed, and achieve a stable position at a single point in hover mode without using satellite navigation. This demonstrates the reliability of operation under real, rather than laboratory, conditions.

Achieving this level of accuracy requires advanced algorithms that are robust to various types of noise. In real-world conditions, however, measurements of optical flow intensity are accompanied by noise with unknown probabilistic characteristics, which significantly complicates the identification of these parameters, especially under conditions of artificially induced noise.

Modern approaches to optical flow identification are primarily focused on estimating the velocity vector field under known noise conditions. Thus, stochastic methods, which include the application of Kalman filters and Bayesian estimates [8, 9], require apriori knowledge of the noise characteristics, which reduces their practical applicability. Robust methods [10, 11] account for uncertainty but do not allow for the simultaneous estimation of the intensity and parameters of the velocity field.

Existing monocular methods for estimating the self-motion parameters of a video camera can be conditionally divided into methods of cartographic analysis of the underlying surface [12] and methods of estimating optical flow parameters (velocity field) [8].

Cartographic analysis methods involve comparing the current frame and a prior map stored in memory. This requires preliminary geodetic survey of the terrain and significant computational resources, making them unsuitable for onboard implementation.

Methods for estimating optical flow parameters are based either on the analysis of image features (for example, identifying key points or scene edges [13]) or on the analysis of flow parameters across video frames using mathematical models.

The fundamental mathematical expression for constructing algorithms for the estimation and identification of optical flow and its parameters u, v [2] is the so-called optical flow constraint equation [10]:

$$\frac{\partial I}{\partial t} + u\frac{\partial I}{\partial x} + v\frac{\partial I}{\partial y} = 0, \tag{1}$$

where $u(x, y, t)$, $v(x, y, t)$ — current components of the brightness pattern velocity at point (x, y);
$\frac{\partial I(x, y, t)}{\partial t}$, $\frac{\partial I(x, y, t)}{\partial x}$, $\frac{\partial I(x, y, t)}{\partial y}$ — partial derivatives of the brightness function $I(x, y, t)$ (intensity of the optical flow) of the scanned scene.

The lack of a unique solution to equation (1) with respect to two unknown variables u, v has led to the creation of a whole range of methods and algorithms that provide the required accuracy only in specific practical situations. Among them, the most common are:

– gradient methods, which allow for real-time calculation of the camera motion vector based on the analysis of intensity gradients in each frame;

– correlation methods, which use a direct search for similar fragments among adjacent frames through a correlation function or root-mean-square deviation;

– variational methods, based on various assumptions regarding the spatiotemporal dynamics of optical flow intensity.

The basic approach to constructing these algorithms is, as a rule, the introduction of various restrictions imposed on the dynamics of changes in the intensity of the optical flow of the scanned underlying surface. Thus, for example, the assumption of equal displacement of all points of the scanned surface, combined with the approximation of the intensity in the neighborhood of each pixel by a quadratic form, provides the specified accuracy of optical flow parameter identification for low-speed motion [4]. And the additional introduction of the assumption of constant scene brightness along the object motion trajectory, using the minimization of the objective functional by the least squares method, allows for even greater accuracy at small displacements (the Lucas-Kanade method) [3]. A more general assumption is that of optical flow “smoothness” (the absence of abrupt changes in the velocity field), which provides, with accuracy acceptable for a wide range of practical applications, the calculation of optical flow based on the so-called energy functional proposed by Horn and Schunck [2]:

$$E(u,v) = \int_D \left(\frac{\partial I}{\partial t} + \nabla I \begin{vmatrix} u \\ v \end{vmatrix} \right)^2 + \lambda \left(|\nabla u|^2 + |\nabla v|^2 \right) dxdy,$$

where D — domain of existence of variables x, y; ∇ — Hamilton operator; λ — regularization parameter.

But since this method uses optimization algorithms based either on discrete representations of the integral and partial derivatives, or on the Euler-Lagrange equations with reflecting boundary conditions, the computational costs of such an approach often prove to be unfeasible for onboard computers [2].

After analyzing the existing methods for estimating optical flow parameters, it can be summarized that their key disadvantages are, firstly, the large amount of computational costs, which does not allow estimating optical flow parameters in real time, and, secondly, critical sensitivity to measurement noise of optical flow intensity, which is inevitable in real navigation systems.

The presence of such problems indicates the lack of a methodological approach capable of solving the problem of joint stochastic estimation of intensity and identification of optical flow parameters under conditions of unknown noise, which represents a significant gap in scientific knowledge.

The objective of this work is to solve the problem of simultaneous high-precision estimation of optical flow intensity and identification of its parameters under conditions of measurement noise with unknown probabilistic characteristics. The research tasks include:

1) development of an estimation-identification algorithm capable of operating without prior knowledge of the underlying surface;

2) providing robustness and high accuracy of optical flow parameter estimation under conditions of unknown noise;

3) implementation of a method focused on minimal computational costs, making it suitable for onboard data processing.

Materials and Methods. The solution to the stated problems is considered in the coordinate system of the video camera image (x, y). Since the analyzed image is a matrix of pixels, by discretizing the coordinate plane, we obtain the basic optical flow equation (1) in a discrete form with respect to the scene coordinates:

$$\begin{gathered}
\frac{\partial I(x_1,y_1,t)}{\partial t}=-u(x_1,y_1,t)\left[\frac{I(x_1,y_1,t)}{\Delta x}-0\right]-v(x_1,y_1,t)\left[\frac{I(x_1,y_1,t)}{\Delta y}-0\right]\\
\frac{\partial I(x_1,y_2,t)}{\partial t}=-u(x_1,y_2,t)\frac{I(x_1,y_2,t)}{\Delta x}-v(x_1,y_2,t)\frac{I(x_1,y_2,t)-I(x_1,y_1,t)}{\Delta y}\\
\dots\dots\dots\dots\dots\dots\dots\dots\dots\dots\dots\dots\dots\dots\dots\dots\dots\dots\\
\frac{\partial I(x_1,y_i,t)}{\partial t}=-u(x_1,y_i,t)\frac{I(x_1,y_i,t)}{\Delta x}-v(x_1,y_i,t)\frac{I(x_1,y_i,t)-I(x_1,y_{i-1},t)}{\Delta y}\\
\dots\dots\dots\dots\dots\dots\dots\dots\dots\dots\dots\dots\dots\dots\dots\dots\dots\dots\\
\frac{\partial I(x_1,y_N,t)}{\partial t}=-u(x_1,y_N,t)\frac{I(x_1,y_N,t)}{\Delta x}-v(x_1,y_N,t)\frac{I(x_1,y_N,t)-I(x_1,y_{N-1},t)}{\Delta y}\\
\frac{\partial I(x_2,y_1,t)}{\partial t}=-u(x_2,y_1,t)\frac{I(x_2,y_1,t)-I(x_1,y_1,t)}{\Delta x}-v(x_2,y_1,t)\frac{I(x_2,y_1,t)}{\Delta y}\\
\frac{\partial I(x_2,y_2,t)}{\partial t}=-u(x_2,y_2,t)\frac{I(x_2,y_2,t)-I(x_1,y_2,t)}{\Delta x}-v(x_2,y_2,t)\frac{I(x_2,y_2,t)-I(x_2,y_1,t)}{\Delta y}\\
\dots\dots\dots\dots\dots\dots\dots\dots\dots\dots\dots\dots\dots\dots\dots\dots\dots\dots\\
\frac{\partial I(x_2,y_i,t)}{\partial t}=-u(x_2,y_i,t)\frac{I(x_2,y_i,t)-I(x_1,y_i,t)}{\Delta x}-v(x_2,y_i,t)\frac{I(x_2,y_i,t)-I(x_2,y_{i-1},t)}{\Delta y}\\
\dots\dots\dots\dots\dots\dots\dots\dots\dots\dots\dots\dots\dots\dots\dots\dots\dots\dots\\
\frac{\partial I(x_2,y_N,t)}{\partial t}=-u(x_2,y_N,t)\frac{I(x_2,y_N,t)-I(x_1,y_N,t)}{\Delta x}-v(x_2,y_N,t)\frac{I(x_2,y_N,t)-I(x_2,y_{N-1},t)}{\Delta y}\\
\dots\dots\dots\dots\dots\dots\dots\dots\dots\dots\dots\dots\dots\dots\dots\dots\dots\dots\\
\frac{\partial I(x_j,y_1,t)}{\partial t}=-u(x_j,y_1,t)\frac{I(x_j,y_1,t)-I(x_{j-1},y_1,t)}{\Delta x}-v(x_j,y_1,t)\frac{I(x_j,y_1,t)}{\Delta y}\\
\dots\dots\dots\dots\dots\dots\dots\dots\dots\dots\dots\dots\dots\dots\dots\dots\dots\dots\\
\frac{\partial I(x_j,y_i,t)}{\partial t}=-u(x_j,y_i,t)\frac{I(x_j,y_i,t)-I(x_{j-1},y_i,t)}{\Delta x}-v(x_j,y_i,t)\frac{I(x_j,y_i,t)-I(x_j,y_{i-1},t)}{\Delta y}\\
\dots\dots\dots\dots\dots\dots\dots\dots\dots\dots\dots\dots\dots\dots\dots\dots\dots\dots\\
\frac{\partial I(x_j,y_N,t)}{\partial t}=-u(x_j,y_N,t)\frac{I(x_j,y_N,t)-I(x_{j-1},y_N,t)}{\Delta x}-v(x_j,y_N,t)\frac{I(x_j,y_N,t)-I(x_j,y_{N-1},t)}{\Delta y}
\end{gathered}\quad , \tag{2}$$

where $j=1,\dots,N$, (x_i,y_j) — coordinates of ij-th point in the adopted coordinate system; $I(x_i,y_j,t)$ — current intensity of the optical flow at ij-th point; Δx, Δy — current intensity of the optical flow at axes Ox, Oy, respectively (pixel sizes of the scanned scene in the corresponding directions).

To simplify the subsequent notation, the following designations are introduced:

$$u\left(x_i, y_j, t\right) = u_{ij}, v\left(x_i, y_j, t\right) = v_{ij}, I\left(x_i, y_j, t\right) = I_{ij},$$

$$U = \left|u_{11}u_{12}\ldots u_{1N}u_{21}u_{22}\ldots u_{2N}\ldots\ldots u_{N1}u_{N2}\ldots u_{NN}\right|^{\mathrm{T}},\ V = \left|v_{11}v_{12}\ldots v_{1N}v_{21}v_{22}\ldots v_{2N}\ldots\ldots v_{N1}v_{N2}\ldots v_{NN}\right|^{\mathrm{T}},$$

$$I = \left|I_{11}I_{12}\ldots I_{1N}I_{21}I_{22}\ldots I_{2N}\ldots\ldots I_{N1}I_{N2}\ldots I_{NN}\right|^{\mathrm{T}},$$

$$D\left(I\right) = \left|\begin{array}{l}
-\dfrac{I_{11}}{\Delta x} \quad \underbrace{0\ldots\ldots0}_{N^2-1} \quad -\dfrac{I_{11}}{\Delta y} \quad \underbrace{0\ldots\ldots0}_{N^2-1} \\
0 \quad -\dfrac{I_{12}}{\Delta x}\ \underbrace{0\ldots\ldots0}_{N^2-2} \quad 0 \quad -\dfrac{I_{12}-I_{11}}{\Delta y}\ \underbrace{0\ldots\ldots0}_{N^2-2} \\
\cdots\cdots\cdots\cdots\cdots\cdots\cdots\cdots\cdots\cdots\cdots\cdots\cdots\cdots\cdots\cdots\cdots\cdots\cdots\cdots \\
\underbrace{0\ldots\ldots0}_{N-1} \quad -\dfrac{I_{1N}}{\Delta x}\ \underbrace{0\ldots\ldots0}_{N^2-N} \quad \underbrace{0\ldots\ldots0}_{N-1} \quad -\dfrac{I_{1N}-I_{1(N-1)}}{\Delta y}\ \underbrace{0\ldots\ldots0}_{N^2-N} \\
\underbrace{0\ldots\ldots0}_{N} \quad -\dfrac{I_{21}-I_{11}}{\Delta x}\ \underbrace{0\ldots\ldots0}_{N^2-N-1} \quad \underbrace{0\ldots\ldots0}_{N} \quad -\dfrac{I_{21}}{\Delta y}\ \underbrace{0\ldots\ldots0}_{N^2-N-1} \\
\underbrace{0\ldots\ldots0}_{N+1} \quad -\dfrac{I_{22}-I_{12}}{\Delta x}\ \underbrace{0\ldots\ldots0}_{N^2-N-2} \quad \underbrace{0\ldots\ldots0}_{N+1} \quad -\dfrac{I_{22}-I_{21}}{\Delta y}\ \underbrace{0\ldots\ldots0}_{N^2-N-2} \\
\cdots\cdots\cdots\cdots\cdots\cdots\cdots\cdots\cdots\cdots\cdots\cdots\cdots\cdots\cdots\cdots\cdots\cdots\cdots\cdots \\
\underbrace{0\ldots\ldots0}_{2N-1} \quad -\dfrac{I_{2N}-I_{1N}}{\Delta x}\ \underbrace{0\ldots\ldots0}_{N^2-2N} \quad \underbrace{0\ldots\ldots0}_{2N-1} \quad -\dfrac{I_{2N}-I_{2(N-1)}}{\Delta y}\ \underbrace{0\ldots\ldots0}_{N^2-2N} \\
\cdots\cdots\cdots\cdots\cdots\cdots\cdots\cdots\cdots\cdots\cdots\cdots\cdots\cdots\cdots\cdots\cdots\cdots\cdots\cdots \\
\underbrace{0\ldots\ldots0}_{N(j-1)} \quad -\dfrac{I_{j1}-I_{(j-1)1}}{\Delta x}\ \underbrace{0\ldots\ldots0}_{N^2-N(j-1)-1} \quad \underbrace{0\ldots\ldots0}_{N(j-1)} \quad -\dfrac{I_{j1}}{\Delta y}\ \underbrace{0\ldots\ldots0}_{N^2-N(j-1)-1} \\
\cdots\cdots\cdots\cdots\cdots\cdots\cdots\cdots\cdots\cdots\cdots\cdots\cdots\cdots\cdots\cdots\cdots\cdots\cdots\cdots \\
\underbrace{0\ldots\ldots0}_{N(j-1)+(i-1)} \quad -\dfrac{I_{ji}-I_{(j-1)i}}{\Delta x}\ \underbrace{0\ldots\ldots0}_{N^2-N(j-1)-i} \quad \underbrace{0\ldots\ldots0}_{N(j-1)+(i-1)} \quad -\dfrac{I_{ji}-I_{j(i-1)}}{\Delta y}\ \underbrace{0\ldots\ldots0}_{N^2-N(j-1)-i} \\
\cdots\cdots\cdots\cdots\cdots\cdots\cdots\cdots\cdots\cdots\cdots\cdots\cdots\cdots\cdots\cdots\cdots\cdots\cdots\cdots \\
\underbrace{0\ldots\ldots0}_{Nj-1} \quad -\dfrac{I_{jN}-I_{(j-1)N}}{\Delta x}\ \underbrace{0\ldots\ldots0}_{N^2-Nj} \quad \underbrace{0\ldots\ldots0}_{Nj-1} \quad -\dfrac{I_{jN}-I_{j(N-1)}}{\Delta y}\ \underbrace{0\ldots\ldots0}_{N^2-Nj} \\
\cdots\cdots\cdots\cdots\cdots\cdots\cdots\cdots\cdots\cdots\cdots\cdots\cdots\cdots\cdots\cdots\cdots\cdots\cdots\cdots \\
\underbrace{0\ldots\ldots0}_{N^2-N} \quad -\dfrac{I_{N1}-I_{(N-1)1}}{\Delta x}\ \underbrace{0\ldots\ldots0}_{N-1} \quad \underbrace{0\ldots\ldots0}_{N^2-N} \quad -\dfrac{I_{N1}}{\Delta y}\ \underbrace{0\ldots\ldots0}_{N-1} \\
\cdots\cdots\cdots\cdots\cdots\cdots\cdots\cdots\cdots\cdots\cdots\cdots\cdots\cdots\cdots\cdots\cdots\cdots\cdots\cdots \\
\underbrace{0\ldots\ldots0}_{N^2-N-1+i} \quad -\dfrac{I_{Ni}-I_{(N-1)i}}{\Delta x}\ \underbrace{0\ldots\ldots0}_{N-i} \quad \underbrace{0\ldots\ldots0}_{N^2-N-1+i} \quad -\dfrac{I_{Ni}-I_{N(i-1)}}{\Delta y}\ \underbrace{0\ldots\ldots0}_{N-i} \\
\cdots\cdots\cdots\cdots\cdots\cdots\cdots\cdots\cdots\cdots\cdots\cdots\cdots\cdots\cdots\cdots\cdots\cdots\cdots\cdots \\
\underbrace{0\ldots\ldots0}_{N^2-1} \quad -\dfrac{I_{NN}-I_{(N-1)N}}{\Delta x} \quad \underbrace{0\ldots\ldots0}_{N^2-1} \quad -\dfrac{I_{NN}-I_{N(N-1)}}{\Delta y}
\end{array}\right|,$$

Equation (2) can be represented in vector form:

$$\frac{\partial I}{\partial t} = D\left(I\right)\begin{vmatrix} U \\ V \end{vmatrix}. \tag{3}$$

In the subsequent synthesis of the algorithm for estimating and identifying the optical flow intensity and its parameters, we use a discrete description of all the above time functions, which is due to the digital nature of information processing in onboard computers. In this case, the discrete form of equation (3) takes the form:

$$I_k = I_{k-1} + \Delta t \cdot D\left(I_{k-1}\right)\begin{vmatrix} U_{k-1} \\ V_{k-1} \end{vmatrix},$$

where I_k — value of the intensity vector of the optical flow at the k-th moment of time; U_k, V_k — values of the vectors of the optical flow parameters at the k-th moment of time; Δt — time sampling step.

To simplify further discussion, we denote vector $\begin{vmatrix} U_k \\ V_k \end{vmatrix}$ as ξ_k, $k = 1\ldots N$, $\xi_0 = 0$, and write the resulting discrete equation in the form:

$$I_k = I_{k-1} + \Delta t \cdot D\left(I_{k-1}\right)\xi_{k-1}. \tag{4}$$

At each *ij*- th scanning point, the optical flow intensity is measured with error w_{ij}, whose probabilistic characteristics (particularly, type of distribution density) are generally unknown. Introducing the measurement noise vector analogously W_k to the above:

$$W_k = \left| w_{11} w_{12} ... w_{1N} w_{21} w_{22} ... w_{2N} ..... w_{N1} w_{N2} ... w_{NN} \right|^{\mathrm{T}},$$

measurement vector Z_k of the optical flow intensity I_k, captured from the entire scanned scene, is represented as

$$Z_k = I_k + W_k .$$

Thus, in the used definitions, the problem of estimating optical flow intensity and identifying its parameters represents a problem of stochastic estimation and parametric identification of a discrete linear nonstationary system (4) when observing its state vector under noise conditions with an uncertain probability distribution density.

It is important to note that the application of traditional discrete estimation methods, in particular Kalman filtering, is impossible here due to, firstly, the presence of an unknown parameter vector ξ_k, and, secondly, the uncertainty of the probabilistic distribution of the measurement noise W_k [14].

Assuming that in the problem under consideration, the probabilistic distribution of the measurement noise of the optical flow intensity belongs to the class of distributions with bounded squares due to the limited power of real noise [14], the estimate of the optical flow intensity $\hat{I}_k$ with simultaneous determination of the parameter vector ξ_k, will be sought as an estimate that guarantees the highest estimation accuracy in the minimax sense (i.e., the minimum error in the most unfavorable situation determined by the given class of distribution), selecting the quadratic function as the minimized objective function: $[Z_k - \hat{I}_k]^T [Z_k - \hat{I}_k]$. To provide the robustness of the developed algorithm when forming the criterion for optimal estimation ($\hat{I}_k$) and identification (ξ_k), we use regularizing additive components: a Tikhonov regularization component based on L_2 norm — $\alpha \cdot \xi_k^T \Delta\xi_k$ and a component that takes into account the natural constraint on the continuity of changes in the parameter vector ξ_k over time: $\beta \cdot \Delta\xi_k^T \Delta\xi_k$, $\Delta\xi_k = \xi_k - \Delta\xi_{k-1}$, where α, β — are regularization parameters that provide adaptation to the specific operating conditions of the dynamic system.

In accordance with the above, we formulate the minimax optimality criterion J_k in the following form:

$$\begin{gathered} J_k = \left[Z_k - \hat{I}_k \right]^{\mathrm{T}} \left[Z_k - \hat{I}_k \right] + \alpha \xi_{k-1} \left(\hat{I}_k, \hat{I}_{k-1} \right)^{\mathrm{T}} \xi_{k-1} \left(\hat{I}_k, \hat{I}_{k-1} \right) + \beta \cdot \Delta\xi_{k-1} \left(\hat{I}_k, \hat{I}_{k-1} \right)^{\mathrm{T}} \Delta\xi_{k-1} \left(\hat{I}_k, \hat{I}_{k-1} \right), \\ \Delta\xi_{k-1} \left(\hat{I}_k, \hat{I}_{k-1} \right) = \xi_{k-1} \left(\hat{I}_k, \hat{I}_{k-1} \right) - \xi_{k-2} \left(\hat{I}_{k-1}, \hat{I}_{k-2} \right). \end{gathered} \tag{5}$$

For the subsequent definition of the vector function $\xi_{k-1}(\hat{I}_k, \hat{I}_{k-1})$ that determines the current estimate of the intensity of the optical flow $\hat{I}_k$:

$$\hat{I}_k = \hat{I}_{k-1} + \Delta t \cdot D\left(\hat{I}_{k-1} \right) \xi_{k-1}, \tag{6}$$

we differentiate J_k (5) with respect to ξ_{k-1}:

$$\begin{gathered} \frac{dJ_k}{d\xi_{k-1}} = -\frac{d\left(\left[Z_k - \hat{I}_k \right]^{\mathrm{T}} \left[Z_k - \hat{I}_k \right] \right)}{d\left[Z_k - \hat{I}_k \right]} \frac{d\hat{I}_k}{d\xi_{k-1}} + 2\alpha \xi_{k-1}^{\mathrm{T}} \left(\hat{I}_k, \hat{I}_{k-1} \right) + 2\beta \left[\xi_{k-1} \left(\hat{I}_k, \hat{I}_{k-1} \right) - \xi_{k-2} \left(\hat{I}_{k-1}, \hat{I}_{k-2} \right) \right]^{\mathrm{T}} = \\ = -2 \left[Z_k - \hat{I}_k \right]^{\mathrm{T}} \Delta t \, D\left(\hat{I}_{k-1} \right) + 2(\alpha + \beta) \xi_{k-1}^{\mathrm{T}} \left(\hat{I}_k, \hat{I}_{k-1} \right) - 2\beta \xi_{k-2}^{\mathrm{T}} \left(\hat{I}_{k-1}, \hat{I}_{k-2} \right). \end{gathered}$$

Equating the resulting expression to 0, we arrive at the equality:

$$\left[Z_k - \hat{I}_k \right]^{\mathrm{T}} \Delta t \, D\left(\hat{I}_{k-1} \right) + \beta \xi_{k-2}^{\mathrm{T}} \left(\hat{I}_{k-1}, \hat{I}_{k-2} \right) = (\alpha + \beta) \xi_{k-1}^{\mathrm{T}} \left(\hat{I}_k, \hat{I}_{k-1} \right),$$

from which we determine the desired recurrent vector function $\xi_{k-1}(\hat{I}_k, \hat{I}_{k-1})$:

$$\frac{\Delta t}{\alpha + \beta} D^{\mathrm{T}} \left(\hat{I}_{k-1} \right) \left[Z_k - \hat{I}_k \right] + \frac{\beta}{\alpha + \beta} \xi_{k-2} \left(\hat{I}_{k-1}, \hat{I}_{k-2} \right) = \xi_{k-1} \left(\hat{I}_k, \hat{I}_{k-1} \right).$$

Substituting the found expression $\xi_{k-1}(\hat{I}_k, \hat{I}_{k-1})$ into estimation equation (6), we have:

$$\hat{I}_k = \hat{I}_{k-1} + \frac{\Delta t^2}{\alpha + \beta} D\left(\hat{I}_{k-1} \right) D^{\mathrm{T}} \left(\hat{I}_{k-1} \right) Z_k - \frac{\Delta t^2}{\alpha + \beta} D\left(\hat{I}_{k-1} \right) D^{\mathrm{T}} \left(\hat{I}_{k-1} \right) \hat{I}_k + \frac{\Delta t \, \beta}{\alpha + \beta} D\left(\hat{I}_{k-1} \right) \xi_{k-2} \left(\hat{I}_{k-1}, \hat{I}_{k-2} \right).$$

Since the right side of the resulting equation depends on the current estimate, $\hat{I}_k$, then for the final determination of $\hat{I}_k$ we transform it as follows:

$$\left(E + \frac{\Delta t^2}{\alpha + \beta} D\left(\hat{I}_{k-1} \right)) D^{\mathrm{T}} \left(\hat{I}_{k-1} \right) \right) \hat{I}_k = \hat{I}_{k-1} + \frac{\Delta t^2}{\alpha + \beta} D\left(\hat{I}_{k-1} \right) D^{\mathrm{T}} \left(\hat{I}_{k-1} \right) Z_k + \frac{\Delta t \, \beta}{\alpha + \beta} D\left(\hat{I}_{k-1} \right) \xi_{k-2} \left(\hat{I}_{k-1}, \hat{I}_{k-2} \right),$$

where E — identity matrix of dimension N^2, from which we finally obtain a stochastic estimate of the intensity of the optical flow $\hat{I}_k$:

$$\hat{I}_k = \left(E + \frac{\Delta t^2}{\alpha+\beta} D\left(\hat{I}_{k-1}\right) D^{\mathrm{T}}\left(\hat{I}_{k-1}\right) \right)^{-1} \left\{ \hat{I}_{k-1} + \frac{\Delta t^2}{\alpha+\beta} D\left(\hat{I}_{k-1}\right) D^{\mathrm{T}}\left(\hat{I}_{k-1}\right) Z_k + \frac{\Delta t \beta}{\alpha+\beta} D\left(\hat{I}_{k-1}\right) \xi_{k-2}\left(\hat{I}_{k-1}, \hat{I}_{k-2}\right) \right\}, \quad (7)$$

where the identification of the vector of optical flow parameters $\xi_{k-2}(\hat{I}_k, \hat{I}_{k-1})$ is carried out in accordance with the expression:

$$\frac{\Delta t}{\alpha+\beta} D^T\left(\hat{I}_{k-2}\right)\left[Z_{k-1} - \hat{I}_{k-1} \right] + \frac{\beta}{\alpha+\beta} \xi_{k-3} = \xi_{k-2}. \quad (8)$$

The key advantageous features of the estimation-identification algorithm (7), (8) are, firstly, the ability to construct the velocity field not only for any part of the image scene but also for the entire scanned scene, and, secondly, the relatively low computational costs due to the determination of vector recursion instead of implementing multidimensional nonlinear optimization algorithms in known methods.

The efficiency evaluation of the proposed approach was obtained through a series of numerical experiments with various nonlinear functions and different values of the mean and variance of the Laplace distribution, whose totality revealed a consistent trend. As an illustration, we use one of the typical scenarios.

The modeling of the spatiotemporal change in the intensity of the optical flow $I(x,y,k)$ was performed in the coordinate grid $\{x:[0;5], y:[0;5]\}$ with a uniform step equal to 0.5, on a time interval of [0;600] seconds with a step of $\Delta t = 0.1$ in accordance with the expression:

$$I\left(x,y,k\right) = 0.33 e^{-(x-2.7)^2 - (y-2.7)^2} \left(cos\left(0.9k\Delta t\right) + 1 \right) \text{ lm}. \quad (9)$$

The formation of the measurement noise vector W_k was performed on the basis of modeling a spatiotemporal random field described as

$$G\left(x,y,k\right) = \left(cos\left(1.3x\right) cos\left(0.97y\right) sin\, k\Delta t + 1 \right) L_t,$$

where L_t — random sequence with a Laplace distribution with zero mean and variance $D = (8.7 \cdot 10^{-2})^2$ $(\text{lm})^2$.

The optical flow intensity estimation was performed in real time according to algorithm (7) with parallel implementation of identification procedure (8) for the optical flow parameter vector ξ_k at regularization coefficient values of $\alpha = 0.033$, $\beta = 0.0017$. The accuracy analysis of the estimation-identification algorithm (7), (8) was performed through comparing the values of the optical flow intensity estimation vector $\hat{I}_k$ and the true optical flow intensity values determined by expression (9).

Figures 1 and 2 show the graphs of changes in the optical flow parameters u, v, characteristic of the selected spatiotemporal change in optical flow intensity (9) and presented for the point $\{x=4, y=3\}$, while Figures 3 and 4 show the error graphs when estimating the components of the optical flow intensity vector for two arbitrarily selected points of the coordinate grid $\{i,j\}$: $\{1,4\},\{5,2\}$.

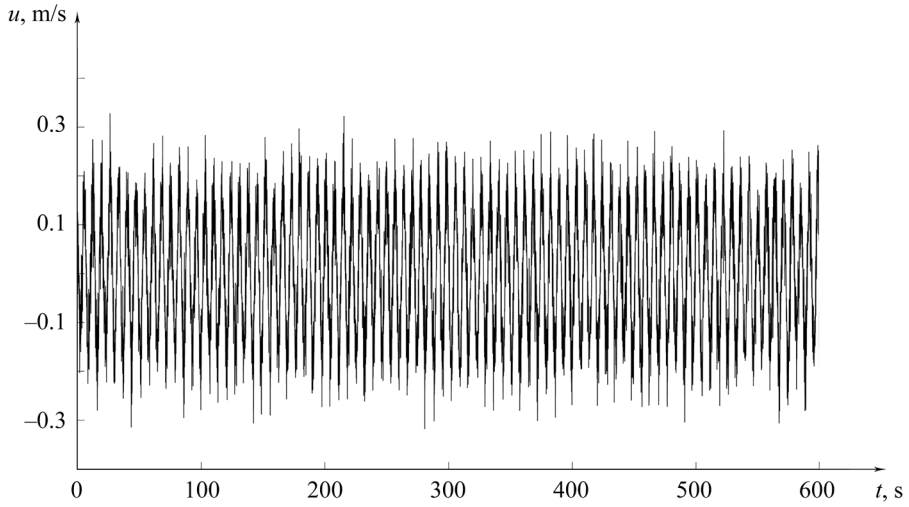

Fig. 1. Graph of change in optical flow parameter u

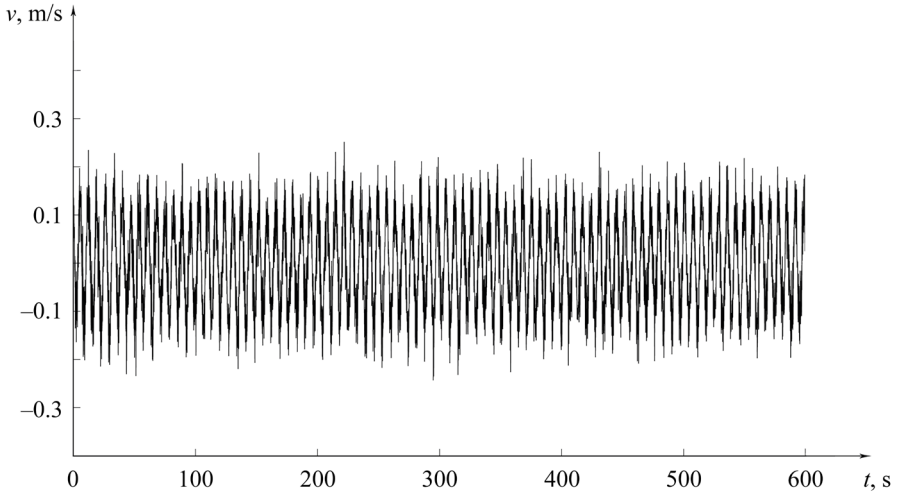

Fig. 2. Graph of change in optical flow parameter *v*

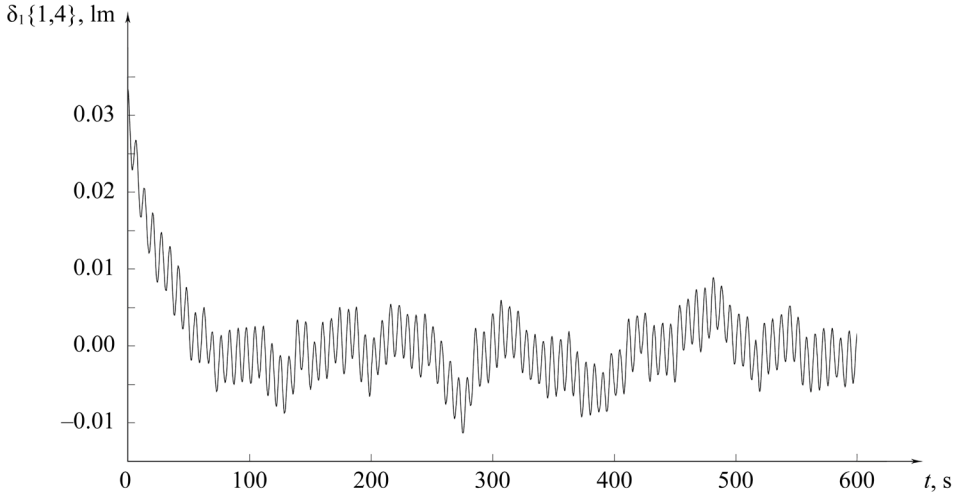

Fig. 3. Error graph for estimating optical flow intensity at coordinate point {1,4}

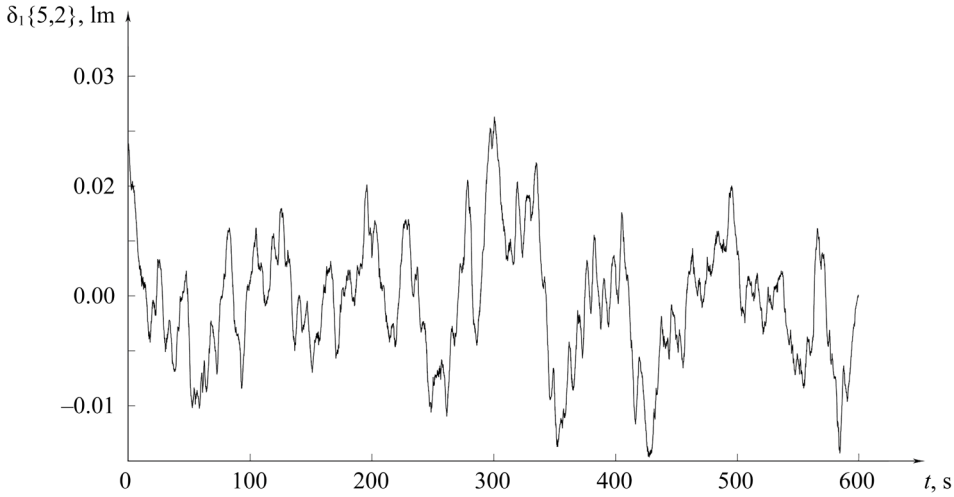

Fig. 4. Error graph for estimating optical flow intensity at coordinate point {5,2}

The presented results allow us to conclude that, despite a fairly high level of measurement noise, the errors in estimating the optical flow intensity at all tested coordinate points turned out to be, firstly, rapidly converging to steady-state values, and, secondly, very small in the steady-state mode: at point {1,4} — no more than 0.7% of the maximum value of the optical flow intensity I_k, and at point {5,2} — no more than 2,1 %.

To analyze the computational efficiency of the developed algorithm, a comparative assessment of computational costs was performed with the Lucas-Kanade method [3], for which the computational costs turned out to be 6.7 times higher.

Research Results. Thus, it can be concluded that the main objective of the work, which consisted in developing a method to solve the problem of simultaneous stochastic estimation of optical flow intensity and identification of its parameters under conditions of measurement noise with unknown probabilistic characteristics — a problem not previously considered in the literature — has been achieved. The basic results of the work are:

– estimation-identification algorithm that implements an integrated approach to estimating optical flow parameters and differs from previously known ones by its recurrent structure with regularization constraints;

– robust estimates of the optical flow parameters $u(x,y,t)$, $v(x,y,t)$ with an error level not exceeding 2.1% under conditions of incomplete apriori information and without accurate knowledge of the noise distribution or the characteristics of the underlying surface;

– efficient algorithmic implementation of the method, providing a reduction in computational resources to 17% (more than six times) of the costs of known gradient methods.

Discussion. The obtained results confirm the feasibility of applying the method of simultaneous optical flow intensity estimation and its parameter identification under conditions of unknown noise. The proposed solution provides the robustness of optical flow parameter estimation even in the absence of accurate information about the probabilistic characteristics of the noise, which is particularly important in real-world observation conditions where measurement noise has unknown characteristics and traditional methods prove inapplicable.

The practical significance of the solution is in the absence of any need for preliminary geodetic survey of the terrain and in ensuring high accuracy and robustness of optical flow parameter estimation under conditions of unknown noise, which is consistent with the theoretical premises outlined in [10, 11]. The computational efficiency of the proposed algorithm meets theoretical expectations, and its recurrent structure suggests minimal computational costs. This makes it suitable for on-board implementation under limited resource conditions, thereby confirming the validity of the proposed approach.

A distinctive feature of the algorithm is the implementation of a minimax optimality criterion, which provides the highest estimation accuracy in the most adverse situation determined by a given class of noise distribution. An important element is the use of Tikhonov regularization and consideration of constraints on the continuity of the parameter vector variation over time, which allows the algorithm to adapt to changing observation conditions. Moreover, the use of these regularizing components and constraints on the continuity of parameter variation requires the selection and preliminary estimation of regularization coefficients, which may somewhat increase the computational costs.

Conclusion. The conducted numerical experiments with various nonlinear functions, different values of the mean and variance of the Laplace distribution, including the special case described in the paper with fixed noise conditions and a limited number of points practically demonstrate the consistency of the proposed concept. Prospects for further research in this area include testing the proposed solutions on real datasets [15], extending the algorithm synthesis framework for practical implementation in specific autonomous navigation systems requiring high-precision and robust estimation of optical flow parameters, including space exploration, machine vision [16], and technical diagnostics.

References

1. Kühne J, Magno M, Benini L. Low Latency Visual Inertial Odometry with On-Sensor Accelerated Optical Flow for Resource-Constrained UAVs. *IEEE Sensors Journal (JSEN)*. 2024;25(5):7838–7847. https://doi.org/10.1109/JSEN.2024.3406948

2. Horn BKP, Schunck BG. Determining Optical Flow. *Artificial Intelligence*. 1981;17(1-3):185–203. https://doi.org/10.1016/0004-3702(81)90024-2

3. Lucas BD, Kanade T. An iterative image registration technique with an application to stereo vision. In: *Proc. 7th Int. Joint Conf. on Artificial Intelligence*. San Francisco, CA: Morgan Kaufmann Publishers Inc.; 1981. P. 121–130.

4. Farnebäck G. Two-Frame Motion Estimation Based on Polynomial Expansion. In book: *Image Analysis. SCIA 2003. Lecture Notes in Computer Science*. Berlin, Heidelberg: Springer; 2003. P. 363–370. https://doi.org/10.1007/3-540-45103-X_50

5. Lele AS, Raychowdhury A. Fusing Frame and Event Vision for High-speed Optical Flow for Edge Application. In: *Proc. IEEE International Symposium on Circuits and Systems (ISCAS)*. New York City: IEEE; 2022. P. 804–808. https://doi.org/10.1109/ISCAS48785.2022.9937763

6. Zhiyong Zhang, Huaizu Jiang, Hanumant Singh. NeuFlow: Real-time, High-accuracy Optical Flow Estimation on Robots Using Edge Devices. In: *Proc. IEEE/RSJ International Conference on Intelligent Robots and Systems (IROS)*. New York City: IEEE; 2024. P. 5048–5055. https://doi.org/10.1109/IROS58592.2024.10802353

7. Stepanyan KV, Popov AK, Miller AB, Miller BM. Optical Flow in Navigation and Control Problems of Autonomous Unmanned Vehicles. *Information Processes*. 2023;23(4):526–544. https://doi.org/10.53921/18195822_2023_23_4_526

8. Huayan Pu, Jun Luo, Gang Wang, Tao Huang, Hongliang Liu, Jun Luo. Visual SLAM Integration with Semantic Segmentation and Deep Learning: A Review. *IEEE Sensors Journal*. 2023;23(19):22119-22138. https://doi.org/10.1109/JSEN.2023.3306371

9. Kühne J, Magno M, Benini L. A Fast and Accurate Optical Flow Camera for Resource-Constrained Edge Applications. In: *Proc. 9th International Workshop on Advances in Sensors and Interfaces (IWASI)*. New York City: IEEE; 2023. P. 143–148. https://doi.org/10.1109/IWASI58316.2023.10164626

10. Ponomarev ES, Grigoriev AS. Algorithms for Calculating Optical Flow in the Problem of Determining Proper Motion. In: *Proc. 39th Interdisciplinary School-Conference of the IITP RAS "Information Technologies and Systems"*. Moscow: IITP RAS; 2015. P. 457–470. (In Russ.)

11. Kotina E, Ovsyannikov D, Elizarova M. Optimization Approach to the Velocity Field Determining Problem. *Cybernetics and Physics*. 2022;11(3):131–135. https://doi.org/10.35470/2226-4116-2022-11-3-131-135

12. Zhiwei Lin, Tingting Liang, Taihong Xiao, Yongtao Wang, Ming-Hsuan Yang. FlowNAS: Neural Architecture Search for Optical Flow Estimation. *International Journal of Computer Vision*. 2024;132:1055–1074. https://doi.org/10.1007/s11263-023-01920-9

13. Merzlyakov A, Macenski S. A Comparison of Modern General Purpose Visual SLAM Aapproaches. In: *Proc. IEEE/RSJ International Conference on Intelligent Robots and Systems (IROS)*. New York City: IEEE; 2021. pp. 9190-9197. https://doi.org/10.1109/IROS51168.2021.9636615

14. Tikhonov VI, Kharisov VN. *Statistical Analysis and Synthesis of Radio Engineering Devices and Systems*. Moscow: Radio i svjaz', 2004. 304 p. (In Russ.)

15. Kühne J. On-Sensor Optical Flow VIO Dataset. Zurich: ETH Zurich; 2024. https://doi.org/10.3929/ethz-b-000663026

16. Rezvanov V.K., Romakina O.M., Zaytseva E.V. Forecasting Delivery Time of Goods in Supply Chains Using Machine Learning Methods. Advanced Engineering Research (Rostov-on-Don). 2025;25(2):120–128. https://doi.org/10.23947/2687-1653-2025-25-2-120-128

About the Authors:

Sergey V. Sokolov, Dr.Sci. (Eng.), Professor of the Information Security Department, Rostov State University of Economics (69, Bolshaya Sadovaya Str., Rostov-on-Don, 344002, Russian Federation), Head of the Informatics and Computer Engineering Department, North Caucasian Branch of Moscow Technical University of Communications and Informatics (62, Serafimovich Str., Rostov-on-Don, 344002, Russian Federation), SPIN-code, ORCID, ResearchGate, ScopusID, ResearcherID, s.v.s.888@yandex.ru

Daniil V. Marshakov, Cand.Sci. (Eng.), Associate Professor of the Informatics and Computer Engineering Department, North Caucasian Branch of Moscow Technical University of Communications and Informatics (62, Serafimovich Str., Rostov-on-Don, 344002, Russian Federation), SPIN-code, ORCID, ResearchGate, ScopusID, ResearcherID, daniil_marshakov@mail.ru

Irina V. Reshetnikova, Cand.Sci. (Eng.), Associate Professor of the Informatics and Computer Engineering Department, North Caucasian Branch of Moscow Technical University of Communications and Informatics (62, Serafimovich Str., Rostov-on-Don, 344002, Russian Federation), Associate Professor of the Department of Cybersecurity of Information Systems, Don State Technical University, (1, Gagarin sq., Rostov-on-Don, 344003, Russian Federation) SPIN-code, ORCID, ScopusID, ResearcherID, irina_reshetnikova@mail.ru

Claimed Contributorship:

SV Sokolov: conceptualization, methodology, supervision, writing – original draft preparation.
DV Marshakov: investigation, software, visualization.
IV Reshetnikova: formal analysis, validation, writing – review & editing.

Conflict of Interest Statement: **the authors declare no conflict of interest.**

All authors have read and approved the final manuscript.

Об авторах:

Сергей Викторович Соколов, доктор технических наук, заведующий кафедрой «Информатика и вычислительная техника» Северо-Кавказского филиала Московского технического университета связи и информатики (344002, Российская Федерация, г. Ростов-на-Дону, ул. Серафимовича, 62), профессор кафедры «Информационная безопасность» Ростовского государственного экономического университета (РИНХ) (344002, Российская Федерация, г. Ростов-на-Дону, ул. Большая Садовая, 69), SPIN-код, ORCID, ResearchGate, ScopusID, ResearcherID, s.v.s.888@yandex.ru

Даниил Витальевич Маршаков, кандидат технических наук, доцент кафедры «Информатика и вычислительная техника» Северо-Кавказского филиала Московского технического университета связи и информатики (344002, Российская Федерация, г. Ростов-на-Дону, ул. Серафимовича, 62), SPIN-код, ORCID, ResearchGate, ScopusID, ResearcherID, daniil_marshakov@mail.ru

Ирина Витальевна Решетникова, кандидат технических наук, доцент кафедры «Инфокоммуникационные технологии и системы связи» Северо-Кавказского филиала Московского технического университета связи и информатики (344002, Российская Федерация, г. Ростов-на-Дону, ул. Серафимовича, 62), доцент кафедры «Кибербезопасность информационных систем» Донского государственного технического университета (344003, Российская Федерация, г. Ростов-на-Дону, пл. Гагарина, 1) SPIN-код, ORCID, ScopusID, ResearcherID, irina_reshetnikova@mail.ru

Заявленный вклад авторов:

С.В. Соколов: разработка концепции и методологии, научное руководство, написание черновика рукописи.

Д.В. Маршаков: проведение исследования, разработка программного обеспечения, визуализация.

И.В. Решетникова: формальный анализ, валидация результатов, написание рукописи, внесение замечаний и исправлений.

Конфликт интересов: **авторы заявляют об отсутствии конфликта интересов.**

Все авторы прочитали и одобрили окончательный вариант рукописи.

Received / Поступила в редакцию 10.12.2025
Reviewed / Поступила после рецензирования 29.12.2025
Accepted / Принята к публикации 14.01.2026

INFORMATION TECHNOLOGY, COMPUTER SCIENCE AND MANAGEMENT
ИНФОРМАТИКА, ВЫЧИСЛИТЕЛЬНАЯ ТЕХНИКА И УПРАВЛЕНИЕ

UDC 616.858-073.75:004.925.8
https://doi.org/10.23947/2687-1653-2026-26-1-2257

Subject Field Overview

Wearable Digital Devices as a Tool for Objective Assessment of Motor Disorders in Parkinson's Disease: A Review of Current Studies

Bogdan O. Shcheglov ✉, **Andrey A. Yakovenko, Andrey F. Artemenko, Evgeny A. Ledkov, Artur R. Biktimirov**
Federal Center of Brain Research and Neurotechnologies, Federal Medical-Biological Agency of the Russian Federation, Moscow, Russian Federation
✉ b.shcheglov@mail.ru

EDN: JZYNSH

Abstract

Introduction. Parkinson's disease (PD) requires objective and continuous monitoring of motor symptoms. Wearable sensors are a promising tool for improving diagnostic accuracy and monitoring disease dynamics. However, they are underutilized in clinical practice due to the lack of uniform standards and limited data reproducibility. The presented study fills this gap. The objectives of the research are to analyze current approaches to the use of wearable systems for monitoring motor symptoms of PD, identify limitations (including those related to validation standards), and determine ways to overcome them for the efficient use of sensors in clinical practice.

Materials and Methods. Using the Prisma 2020 methodology, a literature search was conducted for the years 2020–2025 in PubMed, Scopus, Web of Science, and Elibrary.ru. Peer-reviewed studies on the development, validation, and application of wearable devices for assessing gait, tremor, bradykinesia, and dyskinesia were examined. Nine key terms in digital medicine and neurodiagnostics in Russian and English were used for the search: "Parkinson's disease", "digital biomarkers", "wearable devices", and others. The final sample of 48 studies was dominated by meta-analytics (31%) and clinical studies (29%). Nineteen percent of the sources discussed the development of monitoring systems, 15% were longitudinal studies, and 6% were systematic reviews.

Results. Descriptions of nine wearable devices for monitoring motor performance in patients with PD were compared. The types of metrics, clinical scenarios, and tasks were considered. Two concepts of the devices under study were outlined:
– minimalism (one sensor, high comfort level, focus on integral indices);
– real-time detection (emphasis on episodes and instant recognition).
These two cases required different labeling standards, analysis windows, and clinical significance criteria. To improve the comparability of results, a "minimum validation set" specific to the class of problems was needed. Conditions for overcoming these contradictions were:
– unification of data collection protocols, metric sets, and indicators;
– external and multicenter validation (labeling, accuracy criteria);
– algorithm stability to device changes;
– clinical utility criteria.

Discussion. The widespread use of wearable devices for analyzing motor symptoms in patients with PD is hampered by a lack of analytical and clinical validation standards and economic ambiguity of implementation. In general, five of the devices reviewed show promise. However, clinical data on their efficiency and impact on quality of life are insufficient, as research is primarily focused on the potential of the concepts (accuracy of the algorithms) rather than the practical value and readiness for everyday use of real devices. There is little research on external (multicenter) transferability, unified endpoints, and clinical utility.

Conclusion. Current data on the capabilities and limitations of wearable sensors for Parkinson's disease has been systematized. Widespread adoption of such devices is impossible without standardization and unified criteria for efficiency, safety, and economic viability. Addressing these identified challenges will transform approaches to diagnosis and treatment, making wearable systems a key tool in personalized medicine.

Keywords: Parkinson's disease, wearable sensors, inertial measurement units (IMU), digital biomarkers, motor symptom monitoring, clinical validation, personalized medicine

Acknowledgements. The authors would like to thank the Editorial board of the Journal and the reviewer for their professional analysis of the article and recommendations for its correction.

Funding Information. The research is done with the support from the Ministry of Science and Higher Education of the Russian Federation within the framework of the state program for the creation and development of the World-Class Research Center *"Center for Cybernetic Medicine and Neuroprosthetics"* (Agreement No. 075-15-2025-573).

For Citation. Shcheglov BO, Yakovenko AA, Artemenko AF, Ledkov EA, Biktimirov AR. Wearable Digital Devices as a Tool for Objective Assessment of Motor Disorders in Parkinson's Disease: A Review of Current Studies. *Advanced Engineering Research* (*Rostov-on-Don*). 2026;26(1):2257. https://doi.org/10.23947/2687-1653-2026-26-1-2257

Обзор предметного поля

Цифровые носимые устройства как инструмент объективной оценки моторных нарушений при болезни Паркинсона: обзор современных исследований

Б.О. Щеглов ✉, **А.А. Яковенко, А.Ф. Артеменко, Е.А. Ледков, А.Р. Биктимиров**
Федеральный центр исследований мозга и нейротехнологий Федерального медико-биологического агентства России, г. Москва, Российская Федерация
✉ b.shcheglov@mail.ru

Аннотация

Введение. Болезнь Паркинсона (БП) требует объективного и непрерывного мониторинга моторных симптомов. Носимые сенсоры — перспективный инструмент для повышения точности диагностики и контроля динамики заболевания. Его недостаточно задействуют в клинической практике из-за отсутствия единых стандартов и ограниченной воспроизводимости данных. Представленное исследование заполняет этот пробел. Цели научной работы: анализ современных подходов к использованию носимых систем для мониторинга моторных симптомов БП, выявление ограничений (в том числе по стандартам валидации), определение пути их преодоления для эффективного применения сенсоров в клинической практике.

Материалы и методы. По методологии Prisma 2020 выполнен поиск литературы за 2020–2025 годы в базах данных PubMed, Scopus, Web of Science и Elibrary.ru. Изучались рецензируемые исследования по разработке, валидации и применению носимых устройств для оценки походки, тремора, брадикинезии и дискинезии. Для поиска использовались девять ключевых терминов цифровой медицины и нейродиагностики на русском и английском языках: «болезнь Паркинсона», «цифровые биомаркеры», «носимые устройства» и др. В финальной выборке из 48 исследований основное место заняли метааналитические (31 %) и клинические (29 %). В 19 % источников речь шла о разработках систем мониторинга, 15 % — лонгитюдные исследования, 6 % — систематические обзоры.

Результаты исследования. Сопоставляются описания девяти носимых устройств для отслеживания особенностей моторики пациентов с БП. Учитываются типы метрик, клинических сценариев и задач. Обозначены две концепции исследуемых гаджетов:

– минимализм (один датчик, высокий уровень комфорта, фокус на интегральных индексах);
– детекция в реальном времени (акцент на эпизодах и моментальном распознавании).

В двух этих случаях нужны разные эталоны разметки, окна анализа и критерии клинической значимости. Для повышения сопоставимости результатов необходим «минимальный набор валидации», специфический для класса задач. Условия преодоления противоречий:

– унификация протоколов сбора данных, набора метрик, индикации;
– внешняя и межцентровая валидация (разметка, критерии точности);
– устойчивость алгоритмов к смене устройства;
– критерии клинической полезности.

Обсуждение. Массовому использованию носимых устройств для анализа моторных симптомов пациентов с БП препятствуют недостаток стандартов аналитической, клинической валидации и экономическая неоднозначность внедрения. В целом перспективны пять рассмотренных устройств. Однако клинические данные об их эффективности и влиянии на качество жизни недостаточны, т. к. исследуется главным образом потенциал концепций (точность алгоритмов), а не прикладная ценность и готовность к повседневному использованию реальных устройств. Редко изучается внешний (межцентровый) перенос, единые конечные точки и клиническая полезность.
Заключение. Систематизированы современные данные о возможностях и ограничениях носимых сенсоров при болезни Паркинсона. Широкое распространение таких гаджетов невозможно без стандартизации, единых критериев эффективности, безопасности и экономической целесообразности. Решение выявленных проблем позволит изменить подход к диагностике и лечению, сделать носимые системы ключевым инструментом персонализированной медицины.

Ключевые слова: болезнь Паркинсона, носимые сенсоры, инерциальные измерительные устройства, цифровые биомаркеры, мониторинг двигательных симптомов, клиническая валидация, персонализированная медицина

Благодарности. Авторы выражают благодарность редакционной коллегии журнала и рецензенту за профессиональный анализ статьи и рекомендации для ее корректировки.

Финансирование. Работа выполнена при поддержке Министерства науки и высшего образования Российской Федерации в рамках государственной поддержки создания и развития Научного центра мирового уровня «Центр кибернетической медицины и нейропротезирования» (Соглашение №075-15-2025-573).

Для цитирования. Щеглов Б.О., Яковенко А.А., Артеменко А.Ф., Ледков Е.А., Биктимиров А.Р. Цифровые носимые устройства как инструмент объективной оценки моторных нарушений при болезни Паркинсона: обзор современных исследований. *Advanced Engineering Research* (*Rostov-on-Don*). 2026;26(1):2257. https://doi.org/10.23947/2687-1653-2026-26-1-2257

Introduction. Parkinson's disease (PD) is a neurodegenerative disorder with a wide range of motor and non-motor manifestations. The principle motor symptoms include resting tremor, bradykinesia, and postural instability. Non-motor manifestations primarily include autonomic dysfunction, as well as behavioral and cognitive deficits [1]. Parkinson's disease is one of the most common neurodegenerative pathologies. The progressive loss of the patient’s independence and the need for long-term medical monitoring and care reduce the quality of life for the patients and their families, placing additional strain on the healthcare system. At the late stages of the disease, levodopa treatment is often accompanied by the development of motor complications. One of these is the so-called “wearing-off phenomenon”, in which the duration of the drug therapeutic effect gradually decreases. In this work, we will refer to this as the off-effect. Delayed and random “on — off” fluctuations are also known. These are characterized by unpredictable changes in motor activity, regardless of the time of drug administration [2].

Motor fluctuations and dyskinesias significantly impair quality of life, increase the risk of falls, and complicate patient management. They require timely and often individualized treatment adjustment, which further complicates the situation. Traditional methods for assessing PD symptoms rely primarily on subjective clinical observations, patient diaries, and questionnaires. The known weaknesses of such approaches include:

– potential for systematic errors;
– individual variability;
– overreliance on observer’s qualification [3].

Moreover, such methods typically reflect the patient's condition only during interactions with doctors or short tests. This is insufficient to reliably detect short-term off/on episodes. Consequently, the possibility of timely treatment adjustments and personalized management is limited.

The development of flexible electronics and artificial intelligence technologies opens up new prospects for healthcare, including the creation of wearable monitoring systems, brain-computer-interface solutions, and integration with the Internet of Things [4]. Flexible wearable medical electronic devices are capable of recording blood pressure, respiratory rate, body temperature [5], electrophysiological activity. This supports prolonged recording of key parameters [6], provides continuous collection of data on the state of the body, and opens up the possibility of improving the quality of personalized medical decisions [7].

In the context of PD, continuous recording of motor patterns in natural settings helps bridge the gap between actual symptom dynamics and their episodic clinical assessment. Clinicians gain continuous access to the data, specifically, to track daily variability and episodes of motor fluctuations.

Wearable devices have transformed approaches to monitoring and treating Parkinson's disease [8]. Objective, continuous remote monitoring of motor symptom dynamics has become possible [9]. Compact and lightweight wearable devices are attached to the patient's body and record physiological parameters: movement, tremor, gait, balance, as well as cognitive and behavioral characteristics, including sleep disturbances [10]. Sensor technologies are used to record and transmit data: accelerometers, gyroscopes [11], magnetometers, and electromyographic sensors [12]. All this allows for a comprehensive assessment of motor and non-motor symptoms of the disease [13].

The greatest clinical utility is provided by solutions that allow for the comparison of digital indicators with clinical scales (for example, UPDRS — Unified Parkinson's Disease Rating Scale) and identification of changes that are significant for adjustment of therapy, specifically in the case of motor fluctuations.

Modern approaches to sensor monitoring involve the use of:

– multi-point systems with sensors placed in different areas of the body [14];

– minimalist solutions — for example, sensors integrated into shoes, wrist devices, smartphones, or bracelets [15].

In recent years, data analysis methods that utilize threshold algorithms, automatic classification, and deep neural networks have become widespread. This allows for the creation of inexpensive and noninvasive remote viewing systems [16]. Information received from sensors can be processed both in real time [17] and retrospectively [18]. Machine learning has opened up new possibilities for recording disease progression, assessing treatment efficacy, and generally analyzing the patient’s quality of life [19]. However, the results of a number of studies remain methodologically heterogeneous. Variations in protocols, metrics, samples, and testing conditions hinder direct comparison of solutions and the transfer of findings to routine clinical practice.

Contemporary research demonstrates significant interest in the use of wearable sensors and machine learning algorithms for medical purposes [20]. As a result, diagnostic capabilities are expanding, and intelligent systems for making medical decisions are developing [21]. Algorithm validation and data interpretation [22] require the participation of specialists from various fields — neurologists, physiotherapists, biostatisticians, psychologists, and medical engineers. [23]. Collaboration between multidisciplinary teams improves the accuracy [24] and clinical validity [25] of algorithmic models. However, it is at the clinical and analytical validation stage that the lack of unified approaches is most noticeable: there are no generally accepted data collection protocols, and quality and reproducibility criteria are not agreed upon. Therefore, digital platforms need unified requirements for biomarker comparability.

Previously published reviews focused primarily on specific aspects of wearable technology applications. Examples included the use of mobile apps or inertial sensors to predict motor and non-motor symptoms of PD using machine learning methods [26, 27].

To further develop this area of study, the following tasks must be addressed:

– compare different classes of wearable sensor systems across scenarios (medical facility vs. home, short-term testing vs. long-term monitoring);

– conduct a comparative analysis of the algorithms and metrics used, identifying the applicability limits and methodological limitations;

– define criteria for “good” clinical and analytical validation;

– identify the reasons for the low comparability of results across studies.

There are no publicly available publications that address these issues.

Thus, the knowledge gap arises mainly from the shortcomings of previous literature reviews and their inadequate focus on the problem. Furthermore, there is a lack of an integrated picture combining technologies, evidence quality, and standardization (validation) requirements. All of this is necessary to improve the quality of personalized care for patients with PD.

The objectives of this review are to analyze current wearable digital devices for monitoring motor symptoms of PD, identify key limitations and shortcomings of validation, and identify methods to overcome them for efficient use in clinical practice.

Achieving these stated objectives requires addressing the following tasks.

1. Systematization of the types of wearable sensor systems used in PD, as well as their target clinical tasks (determination of gait, tremor, bradykinesia, dyskinesia, fluctuations).

2. Classification of data analysis and machine learning algorithms.

3. Comparison of clinical and technical metrics of the efficiency of developed methods and devices.

4. Analysis of the quality of available studies (samples, testing conditions, reproducibility, external validation).

5. Identifying unresolved issues in digital biomarker standardization and validation.

6. Comparison of platforms of interest in the context of the problem under study.

7. Identification of practically oriented directions for further research (protocols, endpoints, data collection and storage infrastructure).

Materials and Methods. The study is based on a systematic search and analysis of peer-reviewed scientific publications devoted to the development, architecture, and operational logic of digital systems designed to assess neurological dysfunction in patients with PD. This work was conducted in accordance with the Prisma 2020 guidelines.

The search period was from 2020 to 2025. Publications were reviewed in the international bibliographic databases PubMed, Scopus, Web of Science (WoS), as well as the Russian scientific electronic library Elibrary.ru. In addition, a manual search of the reference lists of key publications and a selection of relevant full-text conference proceedings were performed. The objective of the source selection was to identify relevant data on the principles of the design and operation of digital platforms used for the diagnosis, monitoring, and rehabilitation of patients with PD (Table 1).

Table 1

Selection of Sources for Prisma 2020 Methodology Review

<table>
<tr><td colspan="4">Identification</td><td rowspan="2">Total*</td></tr>
<tr><td>Database records</td><td>Number of sources</td><td>Additional sources</td><td>Number of sources</td></tr>
<tr><td>PubMed: n = 80
Scopus: n = 105
Web of Science: n = 88
Elibrary.ru: n = 15</td><td>288</td><td>References: n = 6
Conference Proceedings: n = 4</td><td>10</td><td>298</td></tr>
<tr><td colspan="5">Screening by titles and abstracts</td></tr>
<tr><td>Duplication</td><td rowspan="2">210</td><td>Exclusion by target indicators</td><td rowspan="2">160</td><td rowspan="2">50</td></tr>
<tr><td>Eliminating duplicates: n = 88</td><td>Irrelevant topic: n = 70
Not about Parkinson's disease: n = 42
Not about wearables: n = 35
Publications before 2020: n = 13</td></tr>
<tr><td colspan="5">Full-text correspondence assessment</td></tr>
<tr><td>Exception due to unavailability of full text: n = 2</td><td>48</td><td>–</td><td>–</td><td>48</td></tr>
<tr><td colspan="5">Final selection</td></tr>
<tr><td>Qualitative synthesis</td><td rowspan="2">33</td><td>Meta-analysis</td><td rowspan="2">15</td><td></td></tr>
<tr><td>Clinical studies: n = 14
Systems development: n = 9
Longitudinal studies: n = 7
Systematic reviews: n = 3</td><td>Consolidation of data from multiple studies: n = 15</td><td>48</td></tr>
</table>

Notes: * Total number of sources by stage and overall selection.

Some data in Table 1 are visualized for greater clarity. The figures are presented as percentages and rounded to whole numbers. As we can see, the most common basis for exclusion from the final sample was the results of title and abstract analysis. Irrelevance was identified in 64% of cases. A significant proportion (more than a third) was due to duplication (Fig. 1).

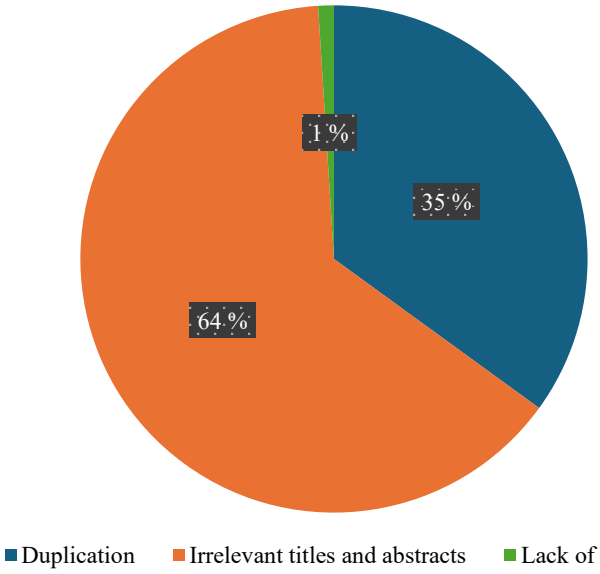

Fig. 1. Reasons for excluding sources from the review

Processing the information summarized in Table 1 revealed an extremely small number of systematic reviews (Fig. 2). Such sources accounted for only 6% of the total number of materials included in the final sample. Investigating the reasons for this imbalance is beyond the scope of this study. It is worth noting that the largest share of the sample consisted of studies consolidating data from multiple publications (meta-analyses, 31%). Almost the same proportion (29%) were clinical studies.

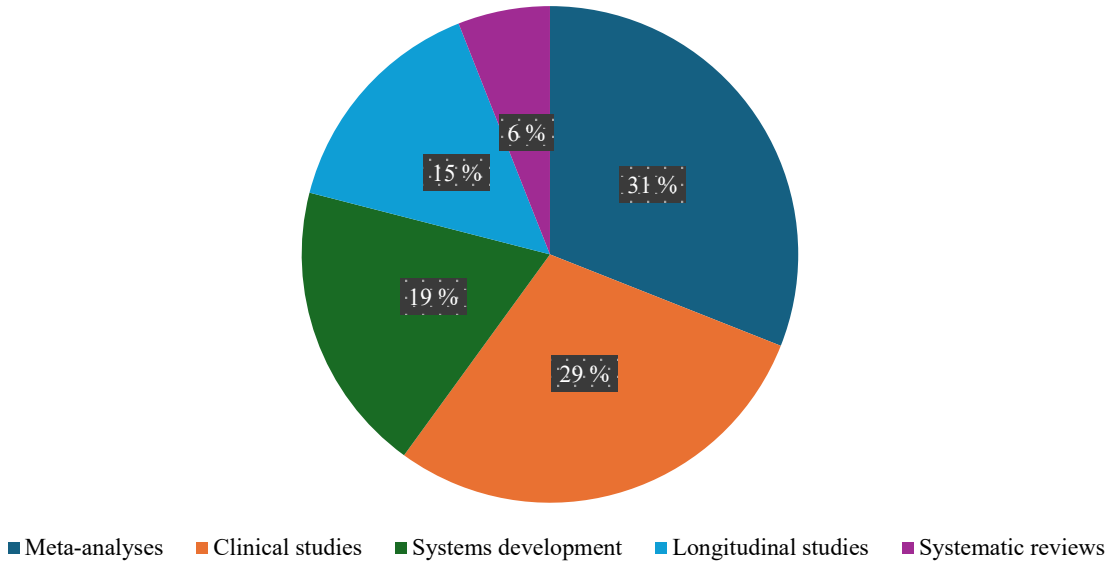

Fig. 2. Types of studies in the final sample

Key terms in digital medicine and neurodiagnostics were used for the search:

– Parkinson's disease;
– digital biomarkers;
– wearable devices;
– computer vision;
– machine learning;
– telemedicine platforms;
– neurological assessment systems;
– mobile health (mHealth);
– cloud diagnostics.

Search queries were generated in Russian and English. Publications available in Russian and/or English were included in the analysis.

Articles were selected based on relevance, scientific significance, and novelty. Priority was given to original research, comprehensive analytical reviews, and publications describing architectural solutions, algorithmic approaches, and clinical studies of digital systems.

The review included materials that met five criteria:

– appearance in 2020–2025;

– publication in peer-reviewed sources;

– full-text availability;

– subject: patients with PD;

– subject: wearable and/or digital systems used for diagnosis, monitoring, or quantification of neurological dysfunction.

Regarding the last criterion, we should clarify that this primarily concerns motor symptoms: tremor, bradykinesia, dyskinesia, gait, and postural stability. Publications describing the sensor platform, processing algorithms, and/or clinical trial results were taken into account.

Resources meeting the following seven criteria were excluded from the review:

– publication before 2020;

– studies not on PD;

– studies without analysis of wearable digital devices (e.g., purely molecular or pharmacological);

– studies on non-motor symptoms without connection to motor status monitoring;

– publications with insufficient data volume to extract key parameters (metrics, protocol, system characteristics);

– materials with duplicate data;

– unavailability of full text.

Let us clarify the last point. The review did not include so-called “gray literature”, such as dissertations and non-peer-reviewed preprints. Conference proceedings were only considered if they had a full-text publication and data extraction capabilities.

Two independent reviewers conducted the selection process at two stages. The first stage involved screening titles and abstracts, and the second — full-text evaluation. Disagreements between the reviewers were resolved through discussion. In the absence of consensus, a third reviewer was brought in. Blinded review was not used. According to Prisma (Table 1), 288 records were identified in the following databases: PubMed — 80, Scopus — 105, Web of Science — 88, and Elibrary.ru — 15. Additionally, 10 sources were found (6 from reference lists, 4 from conference proceedings). After removing 88 duplicates, 210 records remained.

At the screening stage, 160 publications were excluded:

– 70 were irrelevant;

– 42 were not about Parkinson's disease;

– 35 were not about wearable devices;

– 13 were published before 2020.

Accordingly, 50 articles remained in the list for evaluation. Two of these were excluded due to the unavailability of the full-text version. Ultimately, 33 studies were included in the qualitative synthesis, and 15 — in the meta-analyses. A total of 48.

The methodology involved a critical analysis and systematization of data to identify key areas for the development of digital technologies for Parkinson's disease monitoring. It was important to identify patterns in the architecture and operating logic of the systems, as well as compare the advantages and limitations of various solutions.

To provide reproducibility of the analysis, standardized data extraction was performed for each included study. The following factors were considered:

– type of digital system and sensor platform;

– sensor location;

– measurement mode and duration;

– clinical scenario (clinical and home);

– target symptoms;

– processing and machine learning algorithms;

– quality and validity metrics;

– study parameters (sample size, presence of a control group, duration of observation);

– information on clinical and/or external validation.

The studies were then grouped into four predetermined analytical categories.

The first was the functional task of the system. This included diagnostics, fluctuation monitoring, symptom and therapy assessment, as well as rehabilitation and feedback.

The second was the type of sensor platform. This could include single-point and multi-point IMU (inertial measurement units), smartphones, smartwatches, or multimodal solutions.

The third was the target motor phenotype (gait, tremor, bradykinesia, dyskinesia, balance).

The fourth was the level of clinical or analytical validation (comparison with clinical scales, presence of external validation, real-world testing, protocol reproducibility).

To move from individual studies to general conclusions, we compared the results within each group using common criteria (quality metrics, design, limitations). This allowed us to identify recurring patterns and systemic barriers to implementation.

Research Results. The study examined data on the potential applications of various sensor classes in power supply diagnostics and digitalization (Table 2).

Table 2

Comparative Analysis of Devices for Diagnostics and Digitalization of PD

Device / sensor	Examples	Advantages	Disadvantages / limitations	Reference
Accelerometer	IMU component; used in PKG[1]	Acceleration measurements, posture and movement pattern analysis. Basis for integrated motor performance indicators	Incomplete motion picture (3D reconstruction often requires IMU). There are questions about signal interpretation	[28] [29]
Gyroscope	IMU component; DynaPort7	Recording rotational movements and angular velocity. Analysis of gait, symmetry, and posture	Incomplete information on orientation and linear displacements. Processing and interpretation required	[29] [30] [31] [32] [33]
Magnetometer	IMU component	Tracking spatial orientation through magnetic field changes	Limitations on clinical interpretation. Requires integration with other sensors and algorithms	[28] [29] [31] [34] [35]
IMU: accelerometer + gyroscope + magnetometer	IMU modules (general class); PDMonitor	3D reconstruction of linear and angular displacements. Objective, continuous, long-term observations outside the clinic. Reduction of the Hawthorne effect	Weak data integration into practice. Decreased compliance among some patients. Specialized analytics tools and standardization of platforms, algorithms, and metrics are needed	[31] [32] [36] [37] [38]
Wearable motion sensors (general class)	IMU, accelerometers and others	Lightweight, compact, and energy performance. Continuous, objective monitoring. Differentiation between healthy and impaired movement patterns. Monitoring progression, activity, and therapy efficacy. Physician's findings on tremor, bradykinesia, and gait are taken into account	Challenges with clinical interpretation of multidimensional signals, regulatory compliance, privacy, and ethics. Decreased compliance in some patients. Need for standardization. Limited data on efficacy and user quality of life. Issues regarding economic viability	[30] [33] [37] [39] [40]
Approved[2] clinical remote monitoring systems	PDMonitor, PKG, Stat-On, Kinesia360, KinesiaU	Widely used in clinical practice	Limited clinical data on efficacy and impact on patient quality of life. Organizational and ethical barriers	[41] [42] [43]
Multisensor with cloud architecture	Mobility Lab, PDMonitor 5 IMU + SmartBox	Daily activity analysis. Gait, tremor, and bradykinesia assessment. Data collection, processing, and cloud transmission	Data security risks. Clinical integration issues. Patients must wear multiple sensors	[44] [45] [46]

[1] Personal Kineti Graph

[2] In the Russian Federation, such systems require, first and foremost, approval from the Ministry of Health and the Federal Service for Surveillance in Healthcare (Roszdravnadzor).

Wrist device with accelerometer	PKG	High sensitivity. Standard scales. Measurements of tremor, dyskinesia, and bradykinesia. Integral indicators of fluctuations, dyskinesias, and immobility for therapy adjustment	Insufficient data on economic efficiency. Dependence of metrics on processing algorithms	[47] [48] [49]
Lumbar device with real-time ML[3]	Stat-On	Detection of gait freezing, falls, and dyskinesia. Sensitivity over 93%	Difficulties in data interpretation. Limitations of practical integration. Issues of standardization and compliance	[47] [48]

To reduce descriptiveness and improve the comparability of approaches, the results were further structured by the types of metrics used in evaluating efficiency and validation, as well as by types of clinical tasks and clinical application scenarios:

– office vs. home;

– short-term tests vs. long-term monitoring.

Four typical clinical tasks were identified:

1) quantitative assessment of the severity of motor symptoms (tremor, bradykinesia, dyskinesia, postural instability, gait parameters);

2) detection of events and motor complications (off[4] episodes, gait freezing, falls)

3) monitoring of dynamics, progression and responses to therapy (daily activity profiles, fluctuations);

4) clinical decision support (reports for the physician, remote management).

This approach provides the discussion beyond the use of specific sensors. The study allows for assessment of the clinical problem the system addresses and how convincingly this is supported by metrics and validation.

The study results were further interpreted taking into account the clinical scenario:

a) under controlled conditions (office, laboratory test) high repeatability of measurements is achieved and high accuracy is recorded more often;

b) long-term monitoring at home has higher ecological validity and the ability to record fluctuations, while the requirements for compliance, algorithm stability, and data interoperability are stricter.

To unify the comparison of efficiency, we conditionally distinguish three groups of metrics (Table 3):

1) algorithmic metrics of recognition and classification (accuracy, sensitivity, specificity, AUC[5]);

2) metrics of agreement with clinical scales (correlation, agreement with UPDRS, etc.);

3) metrics of clinical utility (impact on therapy adjustment, QoL[6], event rate, clinical and economic indicators).

It is the metrics from the third group, critical for implementation, that are encountered significantly less frequently, which limits the evidence base for the practical efficiency of a number of solutions.

Table 3

Analytical Framework for Comparing the Studies Included in the Review

Dimension of comparison	What is being compared	Examples of indicators	Limitations to widespread adoption
Task type	Monitoring and evaluation of symptoms, events, dynamics, decision support	Tremor, bradykinesia, dyskinesia, freezing, falls, off, daily profiles, physician report	Disparate goals, incomparable data sets, incorrect labeling
Clinical scenario	Office (test) and home (long-term wearing)	Results in controlled tests, variability	Compliance issues, context issues, signal drift, protocol differences
Metrics	Algorithmic and clinical agreement, clinical utility	Accuracy, sensitivity, specificity, agreement with UPDRS, impact on quality of life	Heterogeneity of endpoints, lack of clinical utility assessments
Validation	Internal, external, multicenter	Internal and external validation	Lack of external validation standard and reproducibility protocols

[3] Machine Learning

[4] In this case, “off” and “on” episodes refer to fluctuations in the patient's motor activity. “Off” indication shows limited mobility, motor difficulties, and stasis lasting from a few seconds to several minutes.

[5] Area Under Curve

[6] Quality of Life

Inertial sensors, or motion sensors, are compact electronic devices for measuring acceleration, angular velocity, and magnetic field characteristics [28]. Based on these parameters, the orientation and motion of an object in three-dimensional space are determined. The most common types of inertial sensors are accelerometers, gyroscopes, and magnetometers. [29]. Due to their low weight, compactness and low power consumption, wearable motion sensors are widely used for routine continuous and objective monitoring of patients with PD outside the clinic [30]. The clinical utility of a particular sensor solution is determined not only by the sensor composition, but also by which clinical conditions can be reproducibly measured (task) and under what conditions (scenario).

The accelerometer records acceleration dynamics, allowing for posture and movement analysis, while the gyroscope records rotational movements and angular velocity. The magnetometer displays changes in the magnetic field to track spatial orientation. Sensors are placed on the wrist, shin, waist, thigh, and foot. When combined, the three sensors (accelerometer, gyroscope, and magnetometer) form an inertial measurement unit (IMU), providing a three-dimensional reconstruction of linear and angular movements [31].

An objective assessment of the situation requires minimizing the Hawthorne effect. In this case, we are talking about the patient being aware of the monitoring, watching his movements, and, if possible, controlling them [32]. The resulting picture is unnatural. Gadgets allow for objectivity, as they support long-term monitoring outside of a clinical setting.

From an analytical perspective, IMU often prove to be a competitive advantage in tasks such as tracking gait, posture, and complex motor skills (where 3D kinematics is critical).

Single-axis or single-type sensors (e.g., just an accelerometer) are sufficient for narrow tasks such as tremor assessment under specific conditions. However, they are more difficult to integrate with different scenarios and protocols.

Inertial sensors have demonstrated high efficiency in differentiating the motor patterns of PD patients and healthy volunteers. This provides the basis for the application of machine learning algorithms in identifying diagnostically significant features [33]. The devices also make it possible to track disease progression [34], identify changes in motor activity over time [35], and evaluate the therapy efficacy [36].

Observations based on inertial sensor data enable physicians to make informed decisions about treatment adjustments, including based on the severity of tremor, bradykinesia, and gait disturbances [37].

In recent years, inertial sensors have been actively used to develop digital biomarkers for the progression of Parkinson's disease [38]. Here are some comprehensive studies in this area: Personalized Parkinson Project, Cincinnati Cohort Biomarker Program, Watch-PD, Oxford Parkinson Disease Centre Discovery Cohort and Alameda [39]. These devices enable objective evaluation of the efficiency of new therapeutic approaches, taking into account drug therapy, physical therapy, and deep brain stimulation [40]. Continuous data recording in natural settings provides a more reliable assessment of the impact of therapy on motor activity. This increases the accuracy of clinical trials and the efficacy of personalized treatment regimens [41]. However, even in large-scale projects, the issue of unifying endpoints, protocols, and validation of digital biomarkers remains critical for reproducing and comparing results across different centers and platforms.

Devices such as the aforementioned PDMonitor, PKG, Stat-ON, Kinesia360, and KinesiaU [42] are widely used in clinical practice. PDMonitor is classified as a Class IIa medical device. The solution combines five IMU sensors placed on the wrists, shins, and waist, and a SmartBox system that collects, processes, and transmits data to the cloud [43]. This allows for the analysis of a patient's motor activity throughout the day and the assessment of the likelihood of off-time based on information on gait, tremor, and bradykinesia [44].

Compared to single-sensor solutions, multi-sensor solutions (like PDMonitor) offer superior coverage of motor phenotypes and noise immunity to individual channels. However, wearing multiple sensors requires higher compliance and more complex integration into clinical workflows.

The PKG wrist device measures tremor, dyskinesia, and bradykinesia with high sensitivity [45]. Accelerometer data is used to generate integrated indicators of motor fluctuations, the degree of dyskinesia, and the duration of inactive periods, allowing the physician to objectively assess the severity of symptoms and correct therapy [46]. Stat-on uses real-time machine learning algorithms to record signals from inertial sensors located in the lumbar region [47]. The device, with a sensitivity of over 93%, identifies episodes of gait freezing, falls, and trunk dyskinesia [48].

In the analytical comparison, we can talk about two different concepts:

– PKG — minimalism (one sensor, high level of comfort, focus on integral indices);

– Stat-on — real-time event detection (emphasis on episodes and instant recognition).

We emphasize the particular importance of standardizing protocols for event labeling and analysis, as well as criteria for comparison with clinical assessment. This provides the ability to compare metrics across different platforms.

The KinesiaOne system and its expanded version, Kinesia360, combine wearable sensors and tablet software to provide an objective assessment of tremor, bradykinesia, and other motor manifestations of the disease. Cloud-based neural networks process this data and calculate symptom severity using scores corresponding to clinical scales.

DynaPort7 is a combination of gyroscopes and accelerometers with a 100 Hz recording frequency. The solution accurately analyzes gait parameters, movement symmetry, and supports postural control.

The Mobility Lab system, comprised of wireless sensors and specialized software, provides a quantitative assessment of gait and balance. It can be used to detect subtle or mild signs of Parkinsonian gait and freezing episodes. The literature review allows us to suggest practical steps to overcome the limitations outlined above and to specify implementation paths for solutions. Let us present this as a sequence of actions:

1) unification of data collection protocols (minimum set of tests or modes, placement of sensors, monitoring duration, data requirements);

2) standardization of a set of metrics and reporting indicators for specific tasks (separately for symptom assessment, episode detection and fluctuations);

3) mandatory external and, if possible, multicenter validation with a description of the markings and criteria for accuracy and correctness;

4) testing the stability of algorithms to device changes (software versions) and to work in home conditions;

5) clinical utility studies (impact on therapy adjustment, quality of life, safety and clinical and economic outcomes);

6) integration into clinical processes (interpretable reports, compatibility with medical information systems) while maintaining ethical standards and ensuring data protection.

Discussion. Thus, the differences in competing approaches to implementing devices for recording the condition of patients with PD into clinical practice are well-known. They differ not only in terms of hardware but also in terms of clinical verification logic. Manufacturers focus their solutions on:

– scales (linked to symptom scores);

– events (episode detection).

Clearly, these two approaches have different validation standards and endpoints.

Numerous studies and a wide selection of regulatory-approved systems fail to address a significant issue. This concerns the incomplete development of unified and generally accepted validation standards for wearable solutions in PD. In this review, “good” validation of a digital system is defined as a combination of:

– analytical validity (stability and reproducibility of measurements and processing, resistance to noise and sensor drift);

– clinical validity (alignment of digital indicators with clinical scales and/or clinically significant conditions, such as “off”);

– clinical utility (evidence of impact on physician decisions, outcomes, quality of life, and economic indicators).

It should be noted that, in practice, numerous studies focus on demonstrating algorithmic accuracy under controlled conditions. External validation on independent samples, multicenter reproducibility, and clinical utility assessment are considered much less frequently.

There are other factors that limit the comparability of results across platforms and hinder the development of universal clinical endpoints. These include:

– protocol variability (sensor placement, recording duration, testing conditions);

– differences in metrics and understanding of target states (definition of off-label, episode labeling, accuracy, AUC, correlation with UPDRS).

Information obtained through wearable sensor devices allows for personalized therapeutic strategies, optimized drug dosing, and assessment of treatment efficacy in both clinical and home settings. Sensor systems can detect even subtle changes in motor function that may go unnoticed during routine doctor visits, making them indispensable for the early detection of disease progression or treatment response. The integration of physiological data obtained from wearable devices opens up possibilities for adaptive deep brain stimulation. For example, ankle movement velocity recorded by inertial sensors can be used as a control parameter to dynamically adjust subthalamic nucleus stimulation to correct freezing. Furthermore, these technologies create an infrastructure for remote monitoring and telemedicine consultations. Patients receive care without leaving their homes, reducing the burden on healthcare facilities.

However, the clinical significance of such decisions is most convincingly supported where studies include:

– comparison with clinical scales (for example, MDS UPDRS[7]);

– external validation;

– evaluation of results in natural settings.

In the absence of the listed elements, developments often remain prototypes due to the difficulties of integration with other centers and platforms.

[7] Movement Disorder Society-sponsored revision of the Unified Parkinson's Disease Rating Scale.

The widespread adoption of wearable sensors is associated with methodological and organizational limitations. These are due not only to the technology but also to the methodological nature of the evidence. Some factors that reduce the comparability of study results include:

– small sample sizes;

– protocol specifics;

– differences in target definitions (e.g., “off” criteria and “freeze” labeling rules);

– limited external validation.

The complexity of integrating sensory data into routine clinical practice is primarily due to the need for specialized knowledge and analytical tools to interpret the multidimensional signals received from devices. Recent studies have demonstrated the possibility of simplifying motor assessment protocols using a single sensor placed in the lumbar region for typical motor tests such as the “time-up-and-go” test [46]. It has been found that automatic segmentation and extraction of a limited number of parameters can provide diagnostic accuracy [47] comparable to more complex systems. This opens the way to the introduction of sensor technologies into everyday practice without excessive computational load [48]. However, with this approach, compliance with the requirements of standardized validation is critical [49]:

– stability of metrics when changing conditions (office — home);

– reproducibility when changing the version of the algorithm and device.

Ethical issues and the risk of personal information leakage when using sensor data should be addressed separately. Such information must be fully protected from unauthorized use. Without safeguards, data should not be collected and transmitted.

Educational efforts must also be organized to explain the benefits and risks of digital monitoring to patients and their families. Ethical aspects and issues related to personal data handling should be considered at the early stages of development. This is especially important in cases of:

– using open source principles;

– expanding patient rights to access data;

– – implementing metaconsent models.

An additional limitation is that not all patients with Parkinson's disease can effectively use wearable devices. Cognitive and motor impairments, as well as tremors, reduce compliance. Smartphone-based cognitive test results correlate with traditional neuropsychological assessments, but require adaptation for patients with severe motor impairments.

Standardization of hardware platforms, signal processing algorithms, and output clinical metrics remains a prerequisite for unifying approaches and incorporating sensor systems into diagnostic guidelines. However, current practice does not meet these objectives. The literature review has revealed that studies use different endpoints and different sets of metrics, and the success of studies and finished models is defined differently. For example, clinical interpretability is not assessed by accuracy or AUC, which complicates the development of uniform quality criteria for digital biomarkers.

We should also note the economic ambiguity of the large-scale implementation of the described solutions. From this perspective, devices such as PKG, Stat-on, Kinesia360, KinesiaU, and PDMonitor should be considered generally promising. However, clinical data on their effectiveness and impact on quality of life remains insufficient. The literature review provided an explanation for this discrepancy. The authors of the publications primarily work with concepts, proving their potential. This is quite far from the actual practical value of the solutions, that is, their clinical utility and cost-effectiveness.

In this review, the lack of validation standards is considered as a separate systemic barrier to implementation. For reproducible and comparable use of digital biomarkers in PD, the following validation and utility requirements must be met:

– analytical validation — measurement stability, controllability of error sources (sampling frequency, sensor drift, preprocessing), reproducibility of feature (index) calculations);

– clinical validation — proven compliance of digital indicators with clinically significant conditions or scales (e.g., UPDRS), evaluation in target application scenarios (office, home), external validation using independent data;

– clinical utility – evidence that the use of a digital biomarker improves decision-making (therapy adjustment), patient outcomes, or quality of life at an acceptable cost.

In practice, the literature most often presents first- and partially second-level elements (especially in controlled tests). External (multicenter) transferability, common endpoints, and clinical utility assessments are less common. This creates a gap between demonstrating the algorithm accuracy and the technology readiness for routine use.

We emphasize that separate guidelines and programs for digital endpoints in clinical trials are insufficient. To improve the comparability of results, a “minimum validation set” is needed, one specific to each of the two classes of tasks:

– symptom severity assessment (for scale-based systems),

– detection of off-states, freezes, and falls (for event-based systems).

The development of wearable sensors for Parkinson's disease management is linked to advances in artificial intelligence and machine learning. A key area is the integration of deep neural networks with inertial sensors for time series analysis. Existing models do not yet provide consistent results when processing multidimensional biomechanical data in real time. A promising solution in this regard is the use of distributed wearable sensors that enable autonomous data collection and analysis with the capability for rapid decision-making. At the same time, AI progress must be accompanied by methodologically transparent validation, which includes:

– protocol reporting;
– prevention of overfitting;
– validation on independent samples;
– analysis of robustness to real-life variations.

The integration of sensor systems with mobile apps and smart devices enhances patient engagement in self-monitoring, improves therapy adherence, and facilitates the development of personalized treatment trajectories. Experimental studies using inertial sensors and convolutional neural networks have demonstrated the feasibility of accurately measuring gait freezing episodes at home with high patient compliance. However, the level of evidence for such results depends on the quality of the episode labeling and the availability of external validation. Failure to meet the labeling and external validation requirements will limit the comparison of models and their transfer to clinical settings.

Conclusion. The authors of this review, based on the analysis of peer-reviewed publications from 2020–2025, accomplished two scientific objectives:

– systematized modern approaches to the use of wearable digital devices for objective monitoring of motor symptoms in Parkinson's disease;

– compared the main classes of sensor systems (primarily IMU platforms and clinically used wearable gadgets), their target clinical tasks (gait, tremor, bradykinesia, dyskinesia, motor fluctuations), as well as typical clinical use scenarios (office — home, short-term tests — long-term monitoring).

The classification of processing algorithms and machine learning approaches have shown that the most convincing results are obtained in tasks of quantitative motor assessment and recognition of individual phenotypes under controlled conditions. Outside the clinic, in the patient's daily life, the quality and reproducibility of results can decrease due to differences in protocols, measurement conditions, and compliance.

The key outcome of the review is the identification of a systemic problem with digital biomarker validation standards for Parkinson's disease. The literature lacks unified requirements for data collection protocols, a set of metrics, evidence of clinical utility (impact on treatment adjustment, quality of life, and economic indicators). There are no criteria for the reproducibility and comparability of results generated by different sensor platforms. Ultimately, it can be argued that the widespread adoption of wearable sensors for patients with Parkinson's disease is hampered not only by technical limitations but also by insufficient standardization of analytical and clinical validation procedures.

Based on the review results, the authors identified the following priority objectives for theoretical and applied research in this area:

– standardization of protocols and endpoints;
– development of external (multicenter) validation;
– assessment of the robustness of algorithms in real-world settings;
– detailed study on clinical utility and clinical-economic effectiveness.

In the long term, it is required to establish collaboration between researchers, clinicians, engineers, industry representatives, and regulatory authorities. This will enable the development of standardized, reliable, and clinically validated solutions for digital Parkinson's disease monitoring in the context of precision medicine.

References

1. Rodríguez-Martin D, Pérez-López C. Commercial Symptom Monitoring Devices in Parkinson’s Disease: Benefits, Limitations, and Trends. *Frontiers in Neurology.* 2024;15:1470928. https://doi.org/10.3389/fneur.2024.1470928

2. Adediran GA, Tafirenyika S, Agyemang ASA, Akinfemisoye I, Mojekwu MA, Hanafi MO, et al. Artificial Intelligence Applications in US Parkinson’s Disease Care: A Narrative Review of Diagnostic, Monitoring, and Treatment Tools. *Journal of Medical Science, Biology, and Chemistry.* 2025;2(2):59–69. https://doi.org/10.69739/jmsbc.v2i2.716

3. Cancela J, Bos E, Loushine J, Motti D, Orfaniotou F. Applications of Artificial Intelligence in Movement Disorders, in the Pursuit of Personalized Healthcare. In book: *International Review of Movement Disorders.* Vol. 5. Cambridge, MA: Academic Press; 2023. P. 1–19. https://doi.org/10.1016/bs.irmvd.2023.05.002

4. Urso D, van Wamelen DJ, Trivedi D, Chaudhuri KR, Falup-Pecurariu C. Digital Biomarkers in Movement Disorders. In book: *International Review of Movement Disorders.* Vol. 5. Cambridge, MA: Academic Press; 2023. P. 49–70. https://doi.org/10.1016/bs.irmvd.2023.05.004

5. Alves B, Alhussein G, Carnide F, Grammalidis N, Dimitropoulos K, Trivedi D, et al. An Agile Co-creation Approach for Designing a Comprehensive Digital Motor Assessment Test for Parkinson's Disease Patients. In: *Proc. 11th Int. Con. on Software Development and Technologies for Enhancing Accessibility and Fighting Info-exclusion*. New York, NY: Association for Computing Machinery; 2024. P. 377–383. https://doi.org/10.1145/3696593.3696600

6. Salchow-Hömmen C, Skrobot M, Jochner MCE, Schauer T, Kühn AA, Wenger N. Emerging Portable Technologies for Gait Analysis in Neurological Disorders. *Frontiers in Human Neuroscience.* 2022;16:768575. https://doi.org/10.3389/fnhum.2022.768575

7. Mancini M, McKay JL, Cockx H, D'Cruz N, Esper CD, Filtjens B, et al. Technology for Measuring Freezing of Gait: Current State of the Art and Recommendations. *Journal of Parkinson's Disease.* 2025;15(1):19–40. https://doi.org/10.1177/1877718X241301065

8. Straczkiewicz M, Karas M, Johnson SA, Burke KM, Scheier Z, Royse TB, et al. Upper Limb Movements as Digital Biomarkers in People with ALS. *EBioMedicine.* 2024;101:105036. https://doi.org/10.1016/j.ebiom.2024.105036

9. Hummel J, Schwenk M, Seebacher D, Barzyk P, Liepert J, Stein M. Clustering Approaches for Gait Analysis within Neurological Disorders: A Narrative Review. *Digital Biomarkers.* 2024;8(1):93–101. https://doi.org/10.1159/000538270

10. Morinan G, Dushin Y, Sarapata G, Rupprechter S, Peng Y, Girges C, et al. Computer Vision Quantification of Whole-Body Parkinsonian Bradykinesia Using a Large Multi-Site Population. *NPJ Parkinson's Disease.* 2023;9(1):10. https://doi.org/10.1038/s41531-023-00454-8

11. Kye Won Park, Mirian MS, McKeown MJ. Artificial Intelligence-Based Video Monitoring of Movement Disorders in the Elderly: A Review on Current and Future Landscapes. *Singapore Medical Journal.* 2024;65(3):141–149. https://doi.org/10.4103/smj.smj_202_23

12. Janssen-Daalen JM, van den Bergh R, Prins EM, Moghadam MSC, van den Heuvel R, Veen J, et al. Digital Biomarkers for Non-motor Symptoms in Parkinson's Disease: The State of the Art. *NPJ Digital Medicine.* 2024;7(1):186. https://doi.org/10.1038/s41746-024-01144-2

13. Dabnichki P, Toh Yen Pang. Wearable Sensors and Motion Analysis for Neurological Patient Support. *Biosensors.* 2024;14(12):628. https://doi.org/10.3390/bios14120628

14. Francia C, Donno L, Covarrubias Rodriguez M, Cascini G. Tarabini M, Galli M. Real-Time Monitoring of Physiological and Postural Parameters to Evaluate Human Reactions in Virtual Reality for Safety Training. *Sensors.* 2025;25(14):4400. https://doi.org/10.3390/s25144400

15. Panero E, D'Alessandro R, Cavallina I, Davico C, Mongini T, Gastaldi L, et al. Wearable Inertial Devices in Duchenne Muscular Dystrophy: A Scoping Review. *Applied Sciences.* 2023;13(3):1268. https://doi.org/10.3390/app13031268

16. Borasio F, Mascheretti S, Lorusso ML. New Digital Technologies for Diagnosis and Rehabilitation of Neurodevelopmental Disorders. *Applied Sciences.* 2023;13(22):12165. https://doi.org/10.3390/app132212165

17. Polvorinos-Fernández C, Sigcha L, Borzì L, Olmo G, Asensio C, López JM, et al. Evaluating Mobility in Parkinson's Disease through Wearable Sensors: A Systematic Review of Digital Biomarkers. *Applied Sciences.* 2024;14(22):10189. https://doi.org/10.3390/app142210189

18. Acien A, Calcagno N, Burke KM, Mondesire-Crump I, Holmes AA, Mruthik S, et al. A Novel Digital Tool for Detection and Monitoring of Amyotrophic Lateral Sclerosis Motor Impairment and Progression via Keystroke Dynamics. *Scientific Reports.* 2024;14(1):16851. https://doi.org/10.1038/s41598-024-67940-8

19. Rodriguez-Martin D, Perez-Lopez C. Commercial Devices for Monitoring Symptoms in Parkinson's Disease: Benefits, Limitations and Trends. *Revista de Neurología.* 2024;79(8):229–237. https://doi.org/10.33588/rn.7908.2024253

20. Grahn F. Evaluation of Two Commercial Sensor Systems for Monitoring Parkinsonism and Their Possible Influence on Management of Parkinson's Disease. *Gothenburg University Publications Electronic Archive*. 2022. URL: https://gupea.ub.gu.se/items/7cac2cc7-ae3c-4d42-b687-6252719d523f (accessed: 16.11.2025).

21. Hai Li, Zecca M, Jiajun Huang. Evaluating the Utility of Wearable Sensors for the Early Diagnosis of Parkinson Disease: Systematic Review. *Journal of Medical Internet Research.* 2025;27:e69422. https://doi.org/10.2196/69422

22. Thankathuraipandian S, Greenleaf W, Kyani A, Tomlinson T, Balasingh B, Ross E, et al. Development of a Remote Therapeutic Monitoring Platform: Applications for Movement Disorders. *Scientific Reports.* 2024;14(1):29837. https://doi.org/10.1038/s41598-024-80567-z

23. Bernad AE, Woelfle T, Granziera C, Kappos L, Lorscheider J, Barragan A, et al. A Novel Methodology for Developing Smartphone-instrumented Tests for Assessing Movement, Dexterity, and Balance in Neurological Patients: Technical Verification of Ground Truth Datasets, and Analytical and Clinical Validation of Digital Biomarkers (P6-6.009). *Neurology.* 2024;102:5218. https://doi.org/10.1212/WNL.0000000000205654

24. Calcagni M, Kosa P, Bielekova B. Smartphone Postural Sway and Pronator Drift Tests as Measures of Neurological Disability. *BMC Neurology.* 2025;25(1):50. https://doi.org/10.1186/s12883-025-04038-2

25. Beswick E, Fawcett T, Hassan Z, Forbes D, Dakin R, Newton J, et al. A Systematic Review of Digital Technology to Evaluate Motor Function and Disease Progression in Motor Neuron Disease. *Journal of Neurology.* 2022;269(12):6254–6268. https://doi.org/10.1007/s00415-022-11312-7

26. Senyel D, Senn K, Boyd J, Nagels K. A Systematic Review of Telemedicine for Neuromuscular Diseases: Components and Determinants of Practice. *BMC Digital Health.* 2024;2(1):17. https://doi.org/10.1186/s44247-024-00078-9

27. Mezhov MS, Kozitsin VO, Katser ID. Machine Learning Model for Early Detection of COVID-19 by Heart Rhythm Abnormalities. *Advanced Engineering Research (Rostov-on-Don).* 2023;23(1):66–75. https://doi.org/10.23947/2687-1653-2023-23-1-66-75

28. Adams JL, Kangarloo T, Gong Y, Khachadourian V, Tracey B, Volfson D, et al. Using a Smartwatch and Smartphone to Assess Early Parkinson's Disease in the WATCH-PD Study over 12 Months. *NPJ Parkinson's Disease.* 2024;10(1):112. https://doi.org/10.1038/s41531-024-00721-2

29. Caroppo A, Manni A, Rescio G, Carluccio AM, Siciliano PA, Leone A. Movement Disorders and Smart Wrist Devices: A Comprehensive Study. *Sensors.* 2025;25(1):266. https://doi.org/10.3390/s25010266

30. Jian He, Anhua Luo, Jiajia Yu, Chengxi Qian, Dongwei Liu, Meijin Hou, et al. Quantitative Assessment of Spasticity: A Narrative Review of Novel Approaches and Technologies. *Frontiers in Neurology.* 2023;14:1121323. https://doi.org/10.3389/fneur.2023.1121323

31. Güney G, Jansen TS, Dill S, Schulz JB, Dafotakis M, Hoog Antink C, et al. Video-Based Hand Movement Analysis of Parkinson Patients before and after Medication Using High-Frame-Rate Videos and MediaPipe. *Sensors.* 2022;22(20):7992. https://doi.org/10.3390/s22207992

32. Horak FB, Shah VV, Mancini M. Digital Gait and Balance Measures. In book: *International Review of Movement Disorders.* Vol. 5. Cambridge, MA: Academic Press; 2023. P. 115–151. URL: https://www.sciencedirect.com/science/chapter/bookseries/abs/pii/S2666787823000054 (accessed: 16.11.2025).

33. Ali F, Padilla H, Blazek AM, Barnard L, Kaufman KR. Gait Analysis in Neurologic Disorders: Methodology, Applications, and Clinical Considerations. *Neurology.* 2025;105(8):e214154. https://doi.org/10.1212/WNL.0000000000214154

34. Wuehr M, Jooshani N, Schniepp R. Concepts for Diagnosis, Course and Fall Risk Assessment in Neurological Gait Disorders. *Fortschritte der Neurologie. Psychiatrie.* 2021;89(5):233–242. https://doi.org/10.1055/a-1418-8476

35. Miah ASM, Suzuki T, Shin J. A Methodological and Structural Review of Parkinson's Disease Detection across Diverse Data Modalities. *IEEE Access.* 2025;13:98931–98975. https://doi.org/10.1109/ACCESS.2025.3575023

36. Yanci Zhang, Zhiwei Zeng, Maryam S Mirian, Kevin Yen, Kye Won Park, Michelle Doo, et al. Investigating the Efficacy and Importance of Mobile-Based Assessments for Parkinson's Disease: Uncovering the Potential of Novel Digital Tests. *Scientific Reports.* 2024;14:5307. https://doi.org/10.1038/s41598-024-55077-7

37. Roos LG, Slavich GM. Wearable Technologies for Health Research: Opportunities, Limitations, and Practical and Conceptual Considerations. *Brain, Behavior, and Immunity.* 2023;113:444–452. https://doi.org/10.1016/j.bbi.2023.08.008

38. Tianze Yu, Kye Won Park, McKeown MJ, Wang ZJ. Clinically Informed Automated Assessment of Finger Tapping Videos in Parkinson's Disease. *Sensors.* 2023;23(22):9149. https://doi.org/10.3390/s23229149

39. Vanmechelen I, Haberfehlner H, De Vleeschhauwer J, Van Wonterghem E, Feys H, Desloovere K, et al. Assessment of Movement Disorders Using Wearable Sensors during Upper Limb Tasks: A Scoping Review. *Frontiers in Robotics and AI.* 2023;9:1068413. https://doi.org/10.3389/frobt.2022.1068413

40. Martínez-García-Peña R, Koens LH, Azzopardi G, Tijssen MA. Video-Based Data-Driven Models for Diagnosing Movement Disorders: Review and Future Directions. *Movement Disorders.* 2025;40(10):2046–2066. https://doi.org/10.1002/mds.30327

41. Saranza G, Chin-Hsien Lin. Integrating Digital and Ancillary Technologies in the Modern Clinical Evaluation of Chorea. *Movement Disorders. Clinical Practice.* 2025;12(3):522–528. https://doi.org/10.1002/mdc3.70238

42. Imaduddin F, Arifin Z, Ubaidillah, Mahmoud ERI, Aljabri A. Current-Pressure Dynamics Modeling on an Annular Magnetorheological Valve for an Adaptive Rehabilitation Device. *Micromachines.* 2025;16(2):144. https://doi.org/10.3390/mi16020144

43. Yuchuan Liu, Lianzhi Li, Yu Rao, Huihua Cao, Xiaoheng Tan, Yongsong Li. Multi-Source Sparse Broad Transfer Learning for Parkinson's Disease Diagnosis via Speech. *Medical & Biological Engineering & Computing.* 2025;63:1981–1996. https://doi.org/10.1007/s11517-025-03299-w

44. Anjum F, Bakhuraysah M, Alsharif A, Mohammad T, Shamsi A, Hassan MI. Emerging Biomarkers in Amyotrophic Lateral Sclerosis: from Pathogenesis to Clinical Applications. *Frontiers in Molecular Biosciences.* 2025;12:1608853. https://doi.org/10.3389/fmolb.2025.1608853

45. Tettamanti F, Tello E, Martínez AP, López N, Perez E. Development and Use of a Custom-Adapted Balance Platform for Measuring Postural Parameters. In book: *Advances in Bioengineering and Clinical Engineering 2025.* Cham: Springer Nature; 2025. P. 244–258. URL: https://link.springer.com/chapter/10.1007/978-3-032-06401-1_22 (accessed: 16.11.2025).

46. Chen-Chih Chung, I-Chieh Wu, Bamodu OA, Chien-Tai Hong, Hou-Chang Chiu. Machine Learning in Myasthenia Gravis: A Systematic Review of Prognostic Models and AI-Assisted Clinical Assessments. *Diagnostics.* 2025;15(16):2044. https://doi.org/10.3390/diagnostics15162044

47. Tumpa ZN, Zawad MRS, Sollis L, Parab S, Chen IY, Washington P. Quantifying Device Type and Handedness Biases in a Remote Parkinson's Disease AI-Powered Assessment. *NPJ Digital Medicine.* 2025;8(1):550. https://doi.org/10.1038/s41746-025-01934-2

48. Tanaka M. Parkinson's Disease: Bridging Gaps, Building Biomarkers, and Reimagining Clinical Translation. *Cells.* 2025;14(15):1161. https://doi.org/10.3390/cells14151161

49. Na-Yun Seo, Eun-Wha Jeong, Joo-Hyan Lee, Sun-Young Cho. Objective Assessment of Motor Ataxia via Quantitative Analysis of Romberg's Test Utilizing Webcam-Based Motion Capture with AI. *Journal of Magnetics.* 2023;28(4):470–476. https://doi.org/10.4283/JMAG.2023.28.4.470

About the Authors:

Bogdan O. Shcheglov, Cand.Sci. (Medicine), Researcher, Federal Center of Brain Research and Neurotechnologies, Federal Medical-Biological Agency of the Russian Federation (1, Ostrovityanova Str., Moscow, 117513, Russian Federation), SPIN-code, ORCID, ScopusID, b.shcheglov@mail.ru

Andrey A. Yakovenko, Clinical Research Assistant, Federal Center of Brain Research and Neurotechnologies, Federal Medical-Biological Agency of the Russian Federation (1, Ostrovityanova Str., Moscow, 117513, Russian Federation), SPIN-code, yakovenko.aa@dvfu.ru

Alexander F. Artemenko, Engineer, Federal Center of Brain Research and Neurotechnologies, Federal Medical-Biological Agency of the Russian Federation (1, Ostrovityanova Str., Moscow, 117513, Russian Federation), SPIN-code, artemenko.af@dvfu.ru

Evgeny A. Ledkov, Cand.Sci. (Eng.), Researcher, Federal Center of Brain Research and Neurotechnologies, Federal Medical-Biological Agency of the Russian Federation (1, Ostrovityanova Str., Moscow, 117513, Russian Federation), SPIN-code, ledkov.ea@dvfu.ru

Artur R. Biktimirov, Neurosurgeon, Federal Center of Brain Research and Neurotechnologies, Federal Medical-Biological Agency of the Russian Federation (1, Ostrovityanova Str., Moscow, 117513, Russian Federation), SPIN-code, ORCID, ScopusID, ResearcherID, biktimirov.ar@dvfu.ru

Claimed Contributorship:

BO Shcheglov: conceptualization, formal analysis.
AA Yakovenko: writing — original draft.
AF Artemenko: investigation, data curation, writing — review & editing.
EA Ledkov: methodology, investigation, data curation, formal analysis.
AR Biktimirov: supervision, conceptualization, writing — review & editing.

Conflict of Interest: **the authors declare no conflict of interest.**

All authors have read and approved the final version of the manuscript.

Об авторах:

Богдан Олегович Щеглов, кандидат медицинских наук, научный сотрудник Федерального центра исследований мозга и нейротехнологий Федерального медико-биологического агентства России (117513, Российская Федерация, г. Москва, ул. Островитянова, 1), SPIN-код, ORCID, ScopusID, b.shcheglov@mail.ru

Андрей Александрович Яковенко, лаборант-исследователь Федерального центра исследований мозга и нейротехнологий Федерального медико-биологического агентства России (117513, Российская Федерация, г. Москва, ул. Островитянова, 1), SPIN-код, yakovenko.aa@dvfu.ru

Александр Федорович Артеменко, инженер Федерального центра исследований мозга и нейротехнологий Федерального медико-биологического агентства России (117513, Российская Федерация, г. Москва, ул. Островитянова, 1), SPIN-код, artemenko.af@dvfu.ru

Евгений Александрович Ледков, кандидат технических наук, научный сотрудник Федерального центра исследований мозга и нейротехнологий Федерального медико-биологического агентства России (117513, Российская Федерация, г. Москва, ул. Островитянова, 1), SPIN-код, ledkov.ea@dvfu.ru

Артур Рамилевич Биктимиров, врач-нейрохирург Федерального центра исследований мозга и нейротехнологий Федерального медико-биологического агентства России (117513, Российская Федерация, г. Москва, ул. Островитянова, 1), SPIN-код, ORCID, ScopusID, ResearcherID, biktimirov.ar@dvfu.ru

Заявленный вклад авторов:

Б.О. Щеглов: разработка концепции; формальный анализ.

А.А. Яковенко: написание текста — оригинальный вариант.

А.Ф. Артеменко: сбор данных, обработка данных, редактирование текста.

Е.А. Ледков: Методология, сбор данных, обработка данных, формальный анализ.

А.Р. Биктимиров: разработка концепции, написание рукописи — внесение замечаний и исправлений, научное руководство.

Конфликт интересов: **авторы заявляют об отсутствии конфликта интересов.**

Все авторы прочитали и одобрили окончательный вариант рукописи.

Received / **Поступила в редакцию** 12.01.2026
Reviewed / Поступила после рецензирования 07.02.2026
Accepted / **Принята к публикации** 15.02.2026

INFORMATION TECHNOLOGY, COMPUTER SCIENCE AND MANAGEMENT
ИНФОРМАТИКА, ВЫЧИСЛИТЕЛЬНАЯ ТЕХНИКА И УПРАВЛЕНИЕ

UDC 538.915;538.958
https://doi.org/10.23947/2687-1653-2026-26-1-2283

Original Theoretical Research

Electronic Structure Characteristics of Complex Chalcogenides, Halides, and Oxides from Quantum-Mechanical Calculations

Anatoliy A. Lavrentyev[1] ✉, **Boris V. Gabrelian**[1], **Vu Van Tuan**[2,3], **Kseniya F. Kalmykova**[1]

[1] Don State Technical University, Russian Federation
[2] Institute of Computational Science and Artificial Intelligence, Van Lang University, Ho Chi Minh City, Socialist Republic of Vietnam
[3] School of Technology, Van Lang University, Ho Chi Minh City, Socialist Republic of Vietnam
✉ alavrentyev@donstu.ru

EDN: IAAMVK

Abstract

Introduction. Modern quantum and optoelectronics, as well as nonlinear optics, place high demands on the physical and chemical properties of the materials used. This necessitates, among other things, the search for new materials that possess the properties required for a given application. At the same time, this approach can complicate the composition and crystal structure of the resulting compounds. The electronic structure of complex compounds determines their electrical, optical, magnetic, and chemical properties. These properties are unique to each compound. However, it is known that different compounds that are similar in some important parameters, for example isoelectronic ones, exhibit similarities in the structure of their electronic shells. The accumulation of such information on individual compounds and their groups necessitates generalizing the data obtained. The research objective is to consider some general characteristics of the electronic structure exhibited by groups of different compounds (chalcogenides, halides, and oxides).

Materials and Methods. The subject of study was three groups of compounds: chalcogenides Tl_3TaS_4, Tl_3PS_4, $Sn_2P_2S_6$, $InPS_4$, Cu_2CdGeS_4, Ag_2CdSnS_4, Ag_2HgSnS_4, halides Cs_2HgX_4 (X = Cl, Br, I), group APb_2Br_5 (A = K, Rb), and oxides $La_2Zr_2O_7$, $Nd_2Zr_2O_7$, $Sm_2Zr_2O_7$, $Eu_2Zr_2O_7$, $Gd_2Zr_2O_7$. The research method involved quantum-mechanical calculations within the framework of density functional theory with various exchange-correlation potentials. Potentials were used that allowed for strong correlations between d- and f-electrons and yield a band gap value close to the experimental value.

Results. Quantum-mechanical calculations of the electronic state densities and optical characteristics of a number of chalcogenides, halides, and oxides were performed. Partial and total electron densities of states (DOS) were presented. The total density of states was compared with experimental X-ray photoelectron spectra (XPS). The validity of the calculation results was confirmed. The top of the valence band was formed by the p-states of the most electronegative elements (S, Se, Te, Br, O), whereas the bottom of the valence band was formed by the s-states of these same electronegative elements.

Discussion. Based on the calculations, general conclusions were drawn regarding the similarities in the valence band structure of the compounds considered. Using the compound Tl_3TaS_4 as an example, it was shown that in a solid, compared to the energies in a free atom, the binding energy of the levels for electronegative elements was significantly reduced, while for electropositive elements, it was increased. A rare-earth element (using $Eu_2Zr_2O_7$ as an example) significantly altered the electron-energy structure, such that the electron states of the rare-earth element (4f-, 5p-) and the 5s-states of europium (Eu) altered the structure of the valence band of pyrochlore ($Eu_2Zr_2O_7$). The calculated total and partial DOS were compared with experimental X-ray and X-ray photoelectron spectra, which confirmed the accuracy of the calculations. However, the calculated DOS curves contained numerous fine-structure elements that were obscured by instrumental distortion in the experimental curves. Thus, the calculation complemented the experiment very well, providing a more detailed picture of the electron-energy structure of the studied compounds.

Conclusion. The research objective was achieved: some general characteristics of the electronic structure exhibited by groups of different compounds (chalcogenides, halides, and oxides) were examined. The problems of identifying the states that determined the features of the electronic structure and optical characteristics of the studied groups of compounds were solved. This research can be used in the modeling of new materials with desired properties.

Keywords: pyrochlores, electron-energy structure, density functional theory, exchange-correlation potentials, optical properties

Acknowledgements. The authors would like to thank the reviewers whose critical assessment of the submitted materials and suggestions for their improvement contributed to a significant increase in the quality of the article.

For Citation. Lavrentyev AA, Gabrelian BV, Vu Van Tuan, Kalmykova KF. Electronic Structure Characteristics of Complex Chalcogenides, Halides, and Oxides from Quantum-Mechanical Calculations. *Advanced Engineering Research (Rostov-on-Don)*. 2026;26(1):2283. https://doi.org/10.23947/2687-1653-2026-26-1-2283

Оригинальное теоретическое исследование

Особенности электронной структуры сложных халькогенидов, галогенидов и оксидов, определенные по результатам квантово-механических расчетов

А.А. Лаврентьев[1] ✉, Б.В. Габрельян[1], Туан Ву Ван[2,3], К.Ф. Калмыкова[1]

[1] Донской государственный технический университет, Ростов-на-Дону, Российская Федерация

[2] Институт вычислительной науки и искусственного интеллекта,
Университет Ван Ланг, Хошимин, Вьетнам

[3] Технологическая школа, Университет Ван Ланг, Хошимин, Вьетнам

✉ alavrentyev@donstu.ru

Аннотация

Введение. Современная квантовая и оптоэлектроника, нелинейная оптика предъявляют высокие требования к физико-химическим характеристикам используемых материалов. Это заставляет в том числе искать новые материалы, которые обладали бы свойствами, необходимыми в той или иной области применения. Но при таком подходе могут усложняться состав и кристаллическая структура полученных соединений. Электронная структура сложных соединений определяет их электрические, оптические, магнитные, химические свойства. Эти свойства являются индивидуальными для каждого соединения. Тем не менее, известно, что разные, но близкие по каким-то важным параметрам соединения, например изоэлектронные, обладают подобием в строении своих электронных оболочек. Накопление такой информации по отдельным соединениям и их группам приводит к необходимости обобщения полученных данных. И цель настоящей работы — рассмотреть некоторые общие характеристики электронной структуры, проявляемые группами разных соединений (халькогенидов, галогенидов и оксидов).

Материалы и методы. Предметом изучения были три группы соединений: халькогениды Tl_3TaS_4, Tl_3PS_4, $Sn_2P_2S_6$, $InPS_4$, Cu_2CdGeS_4, Ag_2CdSnS_4, Ag_2HgSnS_4, галогениды Cs_2HgX_4 (X = Cl, Br, I), группа APb_2Br_5 (A = K, Rb) и оксиды $La_2Zr_2O_7$, $Nd_2Zr_2O_7$, $Sm_2Zr_2O_7$, $Eu_2Zr_2O_7$, $Gd_2Zr_2O_7$. Метод исследования — квантово-механические расчеты в рамках теории функционала электронной плотности с различными обменно-корреляционными потенциалами. Использовались потенциалы, позволяющие учитывать сильные корреляции d- и f-электронов и получать значение ширины запрещенной зоны, близкое к экспериментальному.

Результаты исследований. Проведены квантово-механические расчеты плотностей электронных состояний и оптических характеристик ряда халькогенидов, галогенидов и оксидов. Приведены парциальные и полные плотности электронных состояний (Densities of States — DOS). Выполнено сравнение полной плотности состояний с экспериментальными рентгеноэлектронными спектрами (X-ray photoelectron Spectra — XPS). Подтверждена адекватность результатов проведенных расчетов. Вершину валентной полосы формируют p-состояния наиболее электроотрицательных элементов (S, Se, Te, Br, O), в то время как дно валентной полосы образовано s-состояниями также электроотрицательных элементов.

Обсуждение. По результатам проведенных расчетов сделаны обобщающие выводы о сходстве в строении валентной полосы рассмотренных соединений. На примере соединения Tl_3TaS_4 показано, что в твердом теле, по сравнению с энергиями в свободном атоме, для электроотрицательных элементов энергия связи уровней значительно уменьшается, а для электроположительных — увеличивается. Редкоземельный элемент (в качестве примера взят $Eu_2Zr_2O_7$) вносит существенные дополнения в картину электронно-энергетического строения, так что электронные состояния редкоземельного элемента (4f-, 5p-) и 5s-состояния европия (Eu) изменяют строение валентной полосы пирохлора ($Eu_2Zr_2O_7$). Рассчитанные в работе полные и парциальные плотности электронных

состояний (DOS) сравнивались с экспериментальными рентгеновскими и рентгеноэлектроными (XPS) спектрами, которые подтвердили адекватность проведенных расчетов, при этом на рассчитанных кривых DOS имеются многочисленные элементы тонкой структуры, «замазанные» за счет аппаратурного искажения на экспериментальных кривых. Таким образом, расчет очень хорошо дополняет эксперимент, давая более детальную картину электронно-энергетического строения исследованных соединений.

Заключение. Достигнута цель исследования — рассмотрены некоторые общие характеристики электронной структуры, проявляемые группами разных соединений (халькогенидов, галогенидов и оксидов). Решены задачи выявления состояний определяющих особенности электронной структуры и оптических характеристик исследованных групп соединений. Исследование может быть использовано при моделировании новых материалов с заданными свойствами.

Ключевые слова: пирохлоры, электронно-энергетическая структура, метод функционала плотности, обменно-корреляционные потенциалы, оптические свойства

Благодарности. Авторы выражают благодарность рецензентам, чья критическая оценка представленных материалов и высказанные предложения по их совершенствованию способствовали значительному повышению качества статьи.

Для цитирования. Лаврентьев А.А., Габрельян Б.В., Туан Ву Ван, Калмыкова К.Ф. Особенности электронной структуры сложных халькогенидов, галогенидов и оксидов, определенные по результатам квантово-механических расчетов. *Advanced Engineering Research (Rostov-on-Don)*. 2026;26(1):2283. https://doi.org/10.23947/2687-1653-2026-26-1-2283

Introduction. The tasks of semiconductor materials science include obtaining reliable information on the electron-energy structure and chemical bonding, as well as the optical characteristics of complex semiconductors, based on quantum-mechanical calculations and experimental X-ray and X-ray electron spectra. The advantage of using computational models is the ability to study hypothetical, not yet synthesized [1] compounds, as well as the elimination of the need to create suitable samples before starting the research. The objective of this work is to summarize the results of studies of various groups of compounds using reliable, widely validated computational models. Various exchange-correlation potentials were applied in the calculations, but the results closest to the experimental data were previously obtained using the modified Beke-Johnson (mBJ) potential of Tran and Blaha, with the addition of the Hubbard U correction for the strong interaction of electrons in the d- and f-shells, as well as taking into account the spin-orbital coupling (SOC), specifically for the shells of heavy elements. All references to the original articles of the authors of the approximations made in the calculations can be found in [1–4].

A comprehensive literature review of the properties and all studies of the electronic structure using both experimental and theoretical calculation methods was conducted for all the compounds studied. The review has shown the following. The Tl_3TaS_4 compound belongs to the materials used in devices based on the application of surface acoustic waves (SAW) [5]. It is widely used in nonlinear optics and communication devices, such as mobile telephone and television communications [6]. To meet modern technological requirements, research on improving SAW materials should be continued. Several experiments have been previously conducted to study the optical absorption edge, electronic structure, and chemical bonding features in Tl_3TaS_4 [7]. However, the accuracy of the obtained experimental values of the optical band gap and the absorption coefficient is significantly affected by the difficulties of observing d-orbitals over a wide energy range and a number of external factors [8]. The electronic structure and optical properties of Tl_3TaS_4 can be studied in detail based on ab initio calculations, which have been intensively developed and have proven their ability to reproduce reliable properties of materials [9]. The $Eu_2Zr_2O_7$ compound belongs to the group of pyrochlores with the general formula $A_2B_2O_7$, where A and B are metal cations, which can be trivalent (Eu) and tetravalent (Zr) [10]. Pyrochlores have significant dielectric constant. They exhibit unique magnetic [11], chemical, mechanical, and electrical properties [12]. Due to this, they can be used as ceramic coatings for thermal barriers, gas sensors, metal oxide transistors, solid electrolytes in toxic cells [13], as immobilization carriers of actinides in nuclear waste, and catalysts for oxidation reactions [14]. In order to create more efficient, reliable and functional devices based on pyrochlores [15], studies were conducted taking into account the development of new technologies in the laser engineering, optics, and materials

science [15]. Calculations of the electron-energy structure of various pyrochlores were also performed within the framework of the density functional theory [16], using the exchange-correlation potential in the local density approximation (LDA) and the generalized gradient approximation (GGA). In [16], the importance of considering the Hubbard U correction when calculating the energy of d- and f-states was noted. However, it was not possible to obtain in the calculations the values of the band gap width E_g, comparable with the experimental ones (the calculated values were underestimated compared to the experimental ones).

To obtain a reliable picture of the electron energy bands in the studied pyrochlore $Eu_2Zr_2O_7$, and then calculate the optical characteristics of this crystal, it was required to use other approximations to the exchange-correlation potential.

Thus, judging by the data presented in the scientific literature, numerous calculations were performed, but they required improvement of the approximations used (this is especially true for exchange-correlation potentials), which is why the Becke-Johnson potential (mBJ) was used by the authors in their early works. In addition, the above-mentioned publications also provide experimental curves of X-ray and X-ray electron spectra obtained by the authors [1] and co-authors [2–4] for comparison with the calculated curves. The objective of this work is to consider the characteristics of the electronic structure exhibited by groups of different compounds (chalcogenides, halides, and oxides).

Materials and Methods. Based on the full-potential, full-electron method of augmented plane waves (Full Potential Linearized Augmented Plane Waves, FPLAPW), implemented in the Wien2k software package [17], model quantum-mechanical calculations of the electron-energy structure of the following three groups of semiconductor compounds were previously performed:

– chalcogenides Tl_3TaS_4 [1], Tl_3PS_4, $Sn_2P_2S_6$, $InPS_4$, Cu_2CdGeS_4, Ag_2CdSnS_4, Ag_2HgSnS_4 [2];

– halides Cs_2HgX_4 (X — Cl, Br, I), group APb_2Br_5 (A — K, Rb) [2];

– oxides $La_2Zr_2O_7$ and $Nd_2Zr_2O_7$ [3]; $Ln_2Zr_2O_7$ (Ln = La, Nd, Sm, Eu, Gd) [4].

In the unit cell of the crystal, each atom was surrounded by a muffin-tin sphere (mt-sphere), resulting in its entire volume being divided into regions occupied by mt-spheres and the remaining intersphere space. The crystal potential was then calculated in both the mt-spheres and the intersphere space. The intersphere potential was calculated by the method described in [18].

The following mt-radii were used for the atoms of the compound: $R_{mt}^{Eu} = 2.24$ a.u.; $R_{mt}^{Zr} = 1.96$ a.u.; $R_{mt}^{O} = 1.77$ a.u. (a.u. — atomic unit of length).

The exchange-correlation potential was calculated in the GGA-PBE approximation [19] or in the mBJ approximation [20]. In the $Eu_2Zr_2O_7$ compound, the rare-earth element Eu had an incomplete $4f^7$ shell. To take into account the strong Coulomb interaction of 4f electrons at one site, the Hubbard-U parameter was used, which led to the exchange-correlation potential PBE + U [21] and mBJ + U [22]. As for other compounds with a 4f shell, the EES calculation in $Eu_2Zr_2O_7$ was spin-polarized.

The electronic structure of compounds with valence s-, p-, d-electrons was discussed further using the example of the Tl_3TaS_4 compound, crystallizing in a cubic structure with the space group *I-43m,* and the lattice parameter value a = 7.67 Å [1].

The crystal structure of all studied pyrochlores $Ln_2Zr_2O_7$ (Ln = La, Nd, Sm, Eu, Gd), compounds with valence f-electrons, is the same and belongs to a cubic lattice with space group *Fd3m*. In the calculations for $Eu_2Zr_2O_7$, the lattice parameter $a = 10.5438$ Å was used. The atomic coordinates [4] are given in Table 1.

Table 1

Coordinates of Atoms in Unit Cell of Compound $Eu_2Zr_2O_7$

Atom	Wyckoff symbols	*x/a*	*y/a*	*z/a*
63 Eu	16*d*	0.5	0.5	0.5
40 Zr	16*c*	0	0	0
8 O1	48*f*	$x = 0.33888$	0.125	0.125
8 O2	8*b*	0.375	0.375	0.375

Figure 1 shows the crystal structure and atomic environment of pyrochlore $Eu_2Zr_2O_7$ [4].

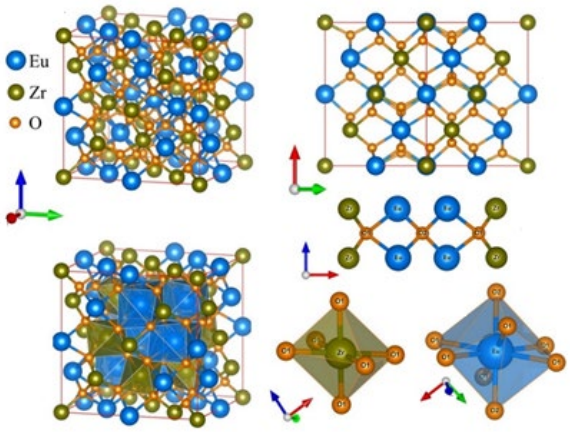

Fig. 1. Crystal structure and immediate environment of atoms in pyrochlore $Eu_2Zr_2O_7$. Distances between atoms: Eu-O1 = 2.5224 Å, Eu-O2 = 2.2828 Å, Zr-O1 = 2.0858 Å

From the occupied electron states in the valence band and the free electron state in the conduction band, the combined density of states can be calculated:

$$J(\hbar\omega) = \int N(E')N(E'+\hbar\omega)dE', \tag{1}$$

and further, using matrix elements of the transition from the valence band to the conduction band (only direct dipole transitions with $\Delta l = 1$ of the corresponding states of a single atom are considered, cross transitions, as unlikely, are ignored), the imaginary part of the permittivity tensor can be calculated [23].

$$\varepsilon_2^{ij}(\omega) = \frac{4\pi^2 e^2}{\Omega m^2 \omega^2} \times \sum_{nn'\sigma} \langle kn\sigma | p_i | kn'\sigma \rangle \langle kn'\sigma | p_j | kn\sigma \rangle f_{kn}(1 - f_{kn'}) \delta(E_{kn'} - E_{kn} - \hbar\omega), \tag{2}$$

where E_{kn} — self-energy of the system with crystal momentum $\vec{k}$ and spin σ; m and e — electron mass and charge, respectively; V, p, $|knpV\rangle$ and fkn — unit cell volume, momentum operator, crystal wave function, and Fermi distribution function.

Real part $\varepsilon_1(\omega)$ of the permittivity was calculated using the Kramers-Kronig formula:

$$\varepsilon_1(\omega) = 1 + \frac{2}{\pi} P \int_0^\infty \frac{\omega' \varepsilon_2(\omega')}{\omega'^2 - \omega^2} d\omega', \tag{3}$$

where P — principal value of the integral.

Absorption coefficient $a(\omega)$, refractive index $n(\omega)$, extinction coefficient $k(\omega)$, optical reflection coefficient $R(\omega)$ and electron energy loss spectrum $L(\omega)$ were derived from the imaginary $\varepsilon_2(\omega)$ and real $\varepsilon_1(\omega)$ parts of the permittivity tensor and were calculated, respectively, from the following formulas [23].

Absorption coefficient:

$$\alpha^{ij}(\omega) = \frac{2\omega k^{ij}(\omega)}{c}. \tag{4}$$

Refractive index:

$$n^{ij}(\omega) = \frac{1}{\sqrt{2}} \left[\sqrt{\varepsilon_1^{ij}(\omega)^2 + \varepsilon_2^{ij}(\omega)^2} + \varepsilon_1^{ij}(\omega) \right]^{1/2}. \tag{5}$$

Extinction coefficient:

$$k^{ij}(\omega) = \frac{1}{\sqrt{2}} \left[\sqrt{\varepsilon_1^{ij}(\omega)^2 + \varepsilon_2^{ij}(\omega)^2} - \varepsilon_1^{ij}(\omega) \right]^{1/2}. \tag{6}$$

Optical reflection coefficient:

$$R^{ij}(\omega) = \frac{(n^{ij}-1)^2 + k^{ij\,2}}{(n^{ij}+1)^2 + k^{ij\,2}} = \left| \frac{\sqrt{\varepsilon_1^{ij} + i\varepsilon_2^{ij}} - 1}{\sqrt{\varepsilon_1^{ij} + i\varepsilon_2^{ij}} + 1} \right|^2. \tag{7}$$

Energy loss function:

$$L^{ij}(\omega) = -Im\left(\varepsilon^{-1}\right)^{ij} = \frac{\varepsilon_2^{ij}(\omega)}{\varepsilon_1^{ij}(\omega)^2 + \varepsilon_2^{ij}(\omega)^2}. \tag{8}$$

Research Results. Electronic structure of compounds with valence s-, p-, d-states using Tl_3TaS_4 as an example. The results of the study on the electronic energy structure (EES) in the Tl_3TaS_4 compound from [1] are considered. Then, some generalizations are made on the conducted studies on the EES of the above groups of chalcogenides, halides and oxides.

Figure 2 shows a comparison of the calculated total and partial densities of electron states with the X-ray K- and $L_{2,3}$ emission spectra and SK absorption spectrum.

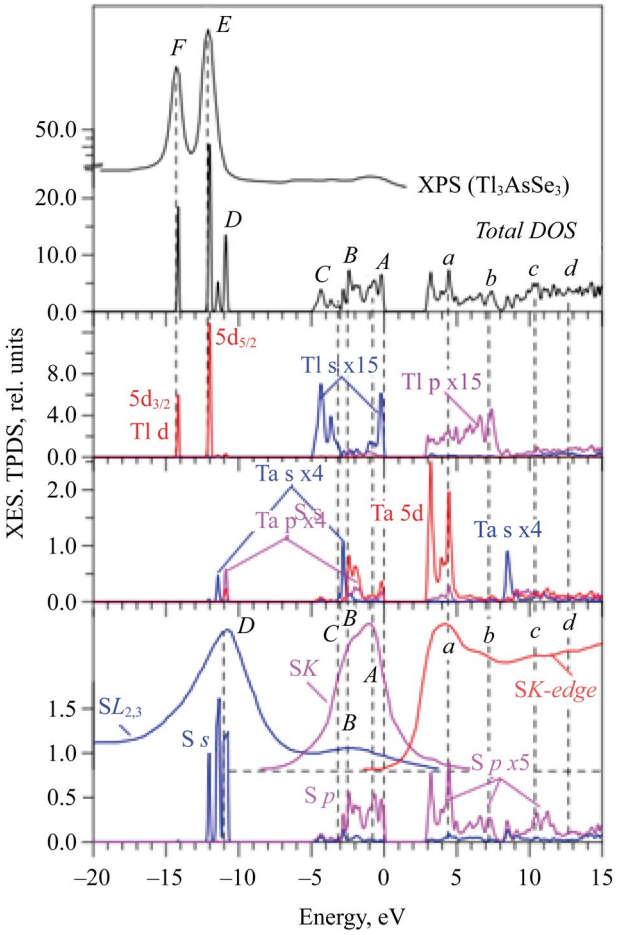

Fig. 2. Total and partial densities of states of Tl_3TaS_4, calculated by mBJ+U+SOC method in comparison with experimental XPS, S $K\beta$1,3 and S L2,3 X-ray emission spectra and S K X-ray absorption spectrum

The value of the forbidden gap width $E_g = 2.842$ eV calculated in approximation mBJ+U+SOC is close to the experimental value $E_g = 2.7$ eV [24].

Based on the energy position of the main maxima of the X-ray emission spectra (SK- and $SL_{2,3}$-bands) and the maxima of the calculated densities of electron states in the semiconductor compound Tl_3TaS_4 (Fig. 2), an energy diagram of the maxima of the main energy bands of this compound was constructed (Fig. 3) in comparison with the energy levels in a free atom from [25], with the latter being counted from vacuum zero. Vacuum zero is separated from the zero corresponding to the top of the valence band (E_v) in Tl_3TaS_4 by the work function (φ) and half the band gap (E_g). The following work function values were found for related semiconductors: for $TlAsS_4$ and Tl_3AsS_3 $\varphi = 5.5$ eV, for Tl_3AsS_4 $\varphi = 5.5$ eV [26], which allowed us to assume value $\varphi = 5.5$ eV or Tl_3TaS_4 as well.

As can be seen in Figure 3, there is a symbatic decrease in the binding energy of the valence 3p and 3s levels of sulfur, the most electronegative (EN) element of the Tl_3TaS_4 compound (EN = 2.44). In the free atom, the binding energies of the 3p and 3s levels are – 10.36 and –20.20 eV, respectively (Table 2), while in crystal Tl_3TaS_4, the average values of the energies of the band maxima of these states are approximately $-1.5 \div -2$ eV for the 3p states, and $-11 \div 12$ eV for the 3s states.

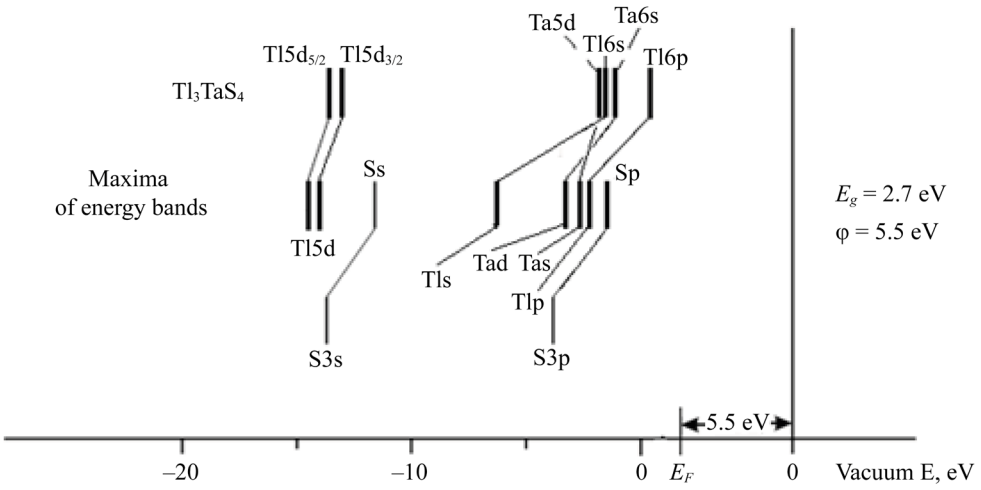

Fig. 3. Energy levels in free atom [25] and maxima of experimental energy bands in Tl_3TaS_4 semiconductor compound relative to vacuum zero. Zero on the energy scale corresponds to the peak of valence band (E_v), E_F — Fermi energy, taken at the midpoint of the band gap and at the distance of the work function from vacuum zero

In a solid, the electron density is attracted to a more electronegative atom (in this case, to sulfur S), which causes an increase in the screening of the nucleus of this atom, and therefore, as a consequence, a decrease in the binding energy of both the 3p levels and the 3s levels, compared to their values in a free atom (Table 2).

Table 2

Binding Energies of Valence and Semi-core Electrons in Free Atoms Included in Tl_3TaS_4 Compound (in eV) [25]

16 S	$3s^2$ M_1		$3p^4$ M_2
	20.20		10.36
73 Ta	$5d^3$ O_4		$5s^2$ P_1
	8.3		7.9
81 Tl	$5d^{10}$ O_4 — O_5	$6s^2$ P_1	$6p^1$ P_2
	21 — 19	8	6.11

As stated in Blokhin's monograph [27], the effective nuclear charge is determined not only by internal electrons, but also by external electrons in relation to a given shell, that is, by all the electrons in the atom. According to these concepts, $Z_{эфф} = Z - \sigma_1$, where σ_1 — total screening constant. Determining the screening constant is not the objective of this work, it is a very complex theoretical problem.

For illustration purposes, Figure 4 shows a schematic representation of the internal level shifts for positive and negative ions.

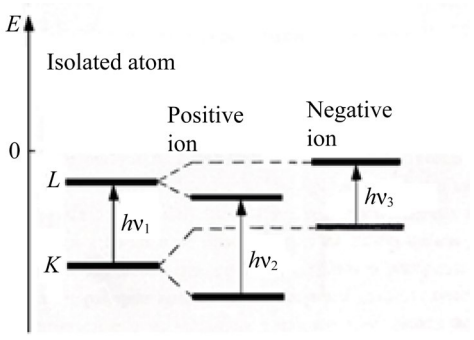

Fig. 4. Schematic representation of chemical shifts of the internal levels for positive and negative ions compared to isolated atoms: $h\nu_3 < h\nu_1 < h\nu_2$

Indeed, for the more electropositive elements in Tl_3TaS_4, namely Tl and Ta, the binding energies of their valence levels increase compared to the energies of a free atom (Fig. 3 and Table 2). The screening of Tl and Ta decreases due to the electron density being drawn toward the S atom, and this causes an increase in the binding energy of the valence and semi-valence levels of the metals.

Similar conclusions about the behavior of the electronic states can be drawn for all the compounds studied (the results are published in [1–4]).

Thus, the electronic p-states of the most electronegative atoms (S, Se, Te, Br, O) in the studied chalcogenides, halides, and oxides, form the upper part of the valence band, which is associated with a significant decrease in the binding energy of these states, compared to their values in a free atom. This decrease in the binding energy of p-states can be explained by the flow of electron density to the more electronegative atom, and therefore by increased screening of these states from the nucleus. The electron s-states of the most electronegative atoms (S, Se, Te, Br, O) in chalcogenides, halides, and oxides, form the bottom of the valence band, and their binding energy also decreases compared to the energy in a free atom.

Electronic structure of compounds with valence f-states using the example of pyrochlore $Eu_2Zr_2O_7$. To draw general conclusions on the electron-energy structure and optical characteristics of pyrochlores $Ln_2Zr_2O_7$ (Ln = La, Nd, Sm, Eu, Gd) [3, 4], the $Eu_2Zr_2O_7$ compound was considered.

The valence configurations of the elements included in compound $Eu_2Zr_2O_7$ are as follows:

Eu — $4f^75s^25p^66s^2$

Zr — $4s^24p^65d^25s^2$

O — $2s^22p^4$.

Figure 5 shows the total densities of electron states with spin-up and spin-down for two different approximations: in approximation GGA–PBE+U and GGA–PBE+U+SOC with U = 5 eV for 4f-states of Eu. The addition of spin-orbit coupling (SOC) causes a splitting of $5p^6$-states of Eu into $5p_{1/2}$ and $5p_{3/2}$-states, as well as a splitting of the $4p^6$-states Zr into $4p_{1/2}$ and $4p_{3/2}$-states.

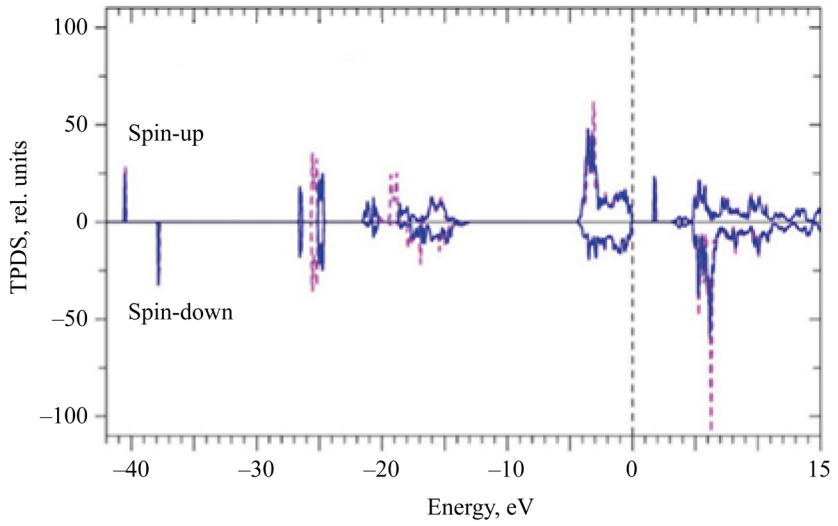

Fig. 5. Calculated total densities of electron states with spin-up and spin-down: dashed line (-----) — calculation in approximation GGA-PBE+U; solid line — calculation in approximation GGA-PBE+U+SOC; U = 5 eV for 4f- states of Eu. Zero on the energy scale corresponds to the top of the valence band E_v

The width of the forbidden band in $Eu_2Zr_2O_7$, was estimated using the total densities of electron states. The data are presented in Table 3.

Table 3

Bandwidths E_g for Different Spin-up and Spin-down Calculation Approximations in $Eu_2Zr_2O_7$

Approximation	E_g, eV	
	spin-up	spin-down
GGA-PBE	0	0
GGA-PBE+U	1.705	3.219
GGA-PBE+U+SOC	1.667	

Value of U for the 4f states of Eu is 5 eV.

The difference in the total density of electron states with spin-up and spin-down in Figure 5 can be explained using the partial densities of electron states with spin-up (Fig. 6) and spin-down (Fig. 7).

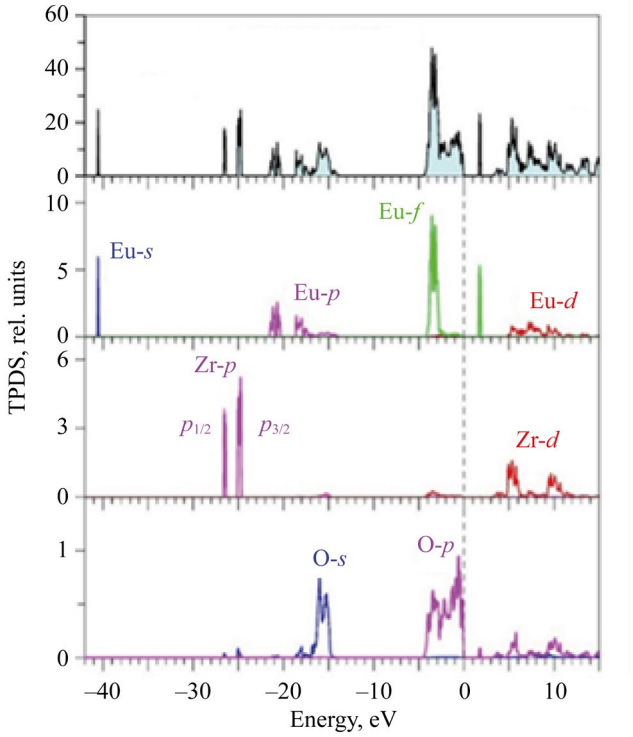

Fig. 6. Total and partial electron densities of states for spin-up in $Eu_2Zr_2O_7$ calculated in approximation GGA-PBE+U+SOC. Zero energy scale corresponds to the top of E_V valence band

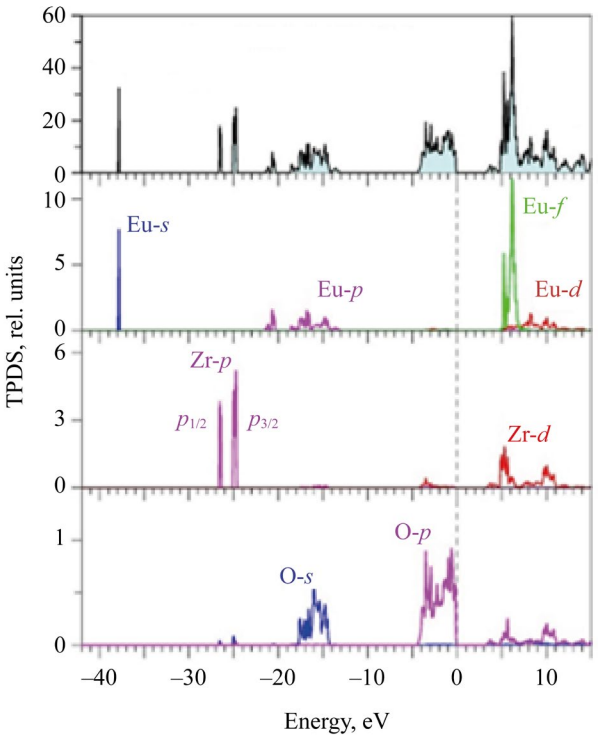

Fig. 7. Total and partial electron densities of states for spin-down in $Eu_2Zr_2O_7$ calculated in approximation GGA-PBE+U+SOC. Zero energy width corresponds to the top of valence band E_V

As can be seen in Figures 6 and 7, the upper part of the valence band of $Eu_2Zr_2O_7$ is formed mainly by 2p states of oxygen (region from 0 to 4.5 eV). Some admixture to the 2p states of O comes from the 4d and 5s states of Zr, as well as the 6s states of the rare-earth element Eu. The most significant admixture in the upper part of the valence band is the 4f states of Eu (the region from –2 to –4 eV). The incomplete 4f shell of Eu contains 7 electrons, whose spins align according to Hund's rule in one direction: in this calculation, this is spin-up.

The spin-orbit splitting of the 5p states of Eu can also be seen in the partial densities with spin-up and spin-down (Figs. 6 and 7). Since the 5p states of Eu are deepened relative to the 2s states of O, the interaction of these states is not as significant compared to other pyrochlores ($La_2Zr_2O_7$, $Nd_2Zr_2O_7$, $Sm_2Zr_2O_7$).

In the present calculation, unoccupied 4f states of Eu appear in the conduction band with both spin-up (narrow peak at 2 eV) and spin-down (narrow peak in the range from 5 to 7 eV).

Another important feature, distinct from previous pyrochlores, should be noted: the peak of spin-up 4f states of Eu splits into two smaller peaks, which is due to the spin-orbit coupling of $4f^7$-electrons. These are $4f_{5/2}$- and $4f_{7/2}$-states. This is not observed in pyrochlores $Nd_2Zr_2O_7$ and $Sm_2Zr_2O_7$.

Despite the fact that the 4f shell is located inside the 5s, 5p, and 6s shells, i.e., it is the inner shell in the atom of a rare-earth element (Nd, Sm, Eu, Gd), the energy of the 4f states in a solid, according to the data of these calculations, falls in the upper part of the valence band, and only the 6s states are located above. This energy position of the 4f states can be explained by a significant "centrifugal" contribution to the potential energy: $V(r) + l(l + 1)\hbar^2/2mr^2$, since the 4f electrons have the largest value of the orbital quantum number ($l = 3$).

Deeper in energy are the 2s states of O (energy range from –14.5 to –18.5 eV). Even deeper in energy are the Eu 5p states. Already in the atom, the filled 5p subshell of Eu is split due to the SOC into $5p_{1/2}$ (term O2) with an energy of 30 eV and into $5p_{3/2}$ (term O3) with an energy of 26 eV, which is reflected in Table 2. The spin-orbit splitting of the 5p states of Eu can also be seen in the partial densities with spin-up and spin-down (Figs. 6 and 7). Since the 5p states are deepened relative to the 2s states of O, the interaction of these states is no longer as significant, compared to previous pyrochlores ($La_2Zr_2O_7$, $Nd_2Zr_2O_7$, $Sm_2Zr_2O_7$). However, in the case of $Eu_2Zr_2O_7$, one can also note the admixture of the 2s states of oxygen with the 5p states of the rare-earth element Eu, which is associated with the covalency of the chemical bond Eu-O2.

The $4p^6$-states of Zr, split due to SOC, are located in the energy range of 25–27 eV. These states can be considered semi-core, not participating in the chemical bonding of Zr and O1. The semi-core 5s states of Eu are the deepest of the valence states calculated in this work. According to the Pauli exclusion principle, the two 5s electrons of Eu have different spin directions, which leads to a difference in energy between these 5s states of Eu due to the action of the magnetic field of the $4f^7$- electrons of Eu. The 5s electron of Eu with spin-up deepens to –40.5 eV, while with spin-down, it has an energy of –38 eV. The energy splitting for these states of 5s electrons is $\Delta E = 2.5$ eV.

Calculations show that the spin-up and spin-down electron states of 5s symmetry are split in energy, which can be explained by the action of the internal magnetic field of the 4f electrons, whose spins align according to Hund's rule and act on the spin-up and spin-down 5s electrons (the Zeeman effect).

Increasing the number of 4f electrons from 4 in Nd to 6 in Sm and to 7 in Eu ($Nd_2Zn_2O_7 \rightarrow Sm_2Zr_2O_7 \rightarrow Eu_2Zr_2O_7$) causes an increase in the magnetic field in the 4f shell and, as a consequence, an increase in the splitting of the spin-up and spin-down 5s states of the rare-earth element (Table 4).

Table 4

Magnitude of Splitting ΔE of 5s States of a Rare-Earth Element with Spin-up and Spin-down

$Nd_2Zn_2O_7$	$Sm_2Zr_2O_7$	$Eu_2Zr_2O_7$
$\Delta E = 1.5$ eV	$\Delta E = 2.5$ eV	$\Delta E = 3.3$ eV

Figure 8 shows the total densities of electron states with spin-up and spin-down compared to the experimental X-ray photoelectron spectrum (XPS). All the fine structure features of the XPS are clearly reflected in the theoretically calculated densities of electron states. The upper part of the valence band from 0 to –5 eV is formed by the 2p states of oxygen, which is reflected in the theoretical and experimental curves.

The most intense peak A in XPS corresponds to the 4f states of Eu, since the photoionization cross section of 4f states significantly exceeds the photoionization cross section of 2p states of oxygen. At an energy of ≈–4 eV, there is an intense peak that precisely reflects the 4f states of Eu.

Gently sloping peak B in XPS corresponds mainly to the 2s states of oxygen, as well as a small fraction of the $5p_{3/2}$-states of Eu. Peak C in XPS is mainly formed by the $5p_{1/2}$- states of Eu with a small admixture of the 2s states of oxygen. Peak D in XPS corresponds to the splitting due to the SOC of the 4p states of Zr. Peak D in XPS has a clear asymmetry, which is precisely due to the spin-orbit splitting of $4p^6$- electrons into $4p_{1/2}$ and $4p_{3/2}$-states.

And finally, the wide, flat hump E on the XPS is formed by the 5s states of Eu, in which there is a splitting of the electron states with spin-up and spin-down, “smeared” on the spectrum due to hardware distortion.

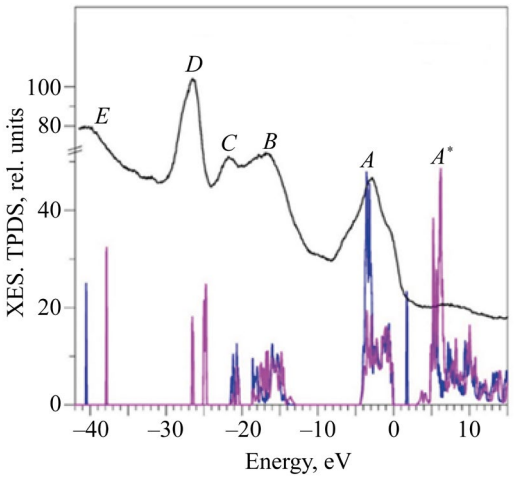

Fig. 8. Total densities of electron states with spin-up and spin-down calculated in GGA-PBE+U+SOC approximation compared with experimental XPS. Zero on the energy scale corresponds to the top of the valence band E_v

Calculations of optical characteristics using $Eu_2Zr_2O_7$ as an example. The output data from the EES calculations of the compound $Eu_2Zr_2O_7$, namely the dispersion curves $E(\vec{k})$ and the DOS, were used to calculate the frequency-dependent complex dielectric function $\varepsilon(\omega) = \varepsilon_1(\omega) + i\varepsilon_2(\omega)$. At the first stage of calculating the dielectric function, the imaginary part of the dielectric function tensor $\varepsilon_2(\omega)$ was calculated using formula (2). Figure 9 shows the imaginary part of the dielectric function $\varepsilon_2(\omega)$ as a function of photon energy (frequency). The main peaks and fine structure details of the curve $\varepsilon_2(\omega)$ are indicated: A, B, C, D, E, F, whose energies are given in Table 5.

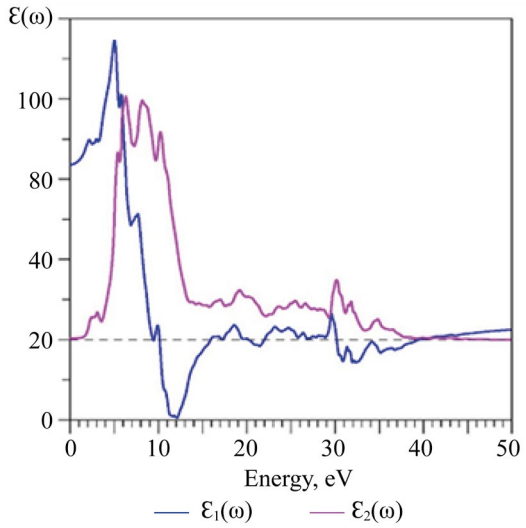

Fig. 9. Calculated imaginary (ε_2) and real (ε_1) parts of permittivity in $Eu_2Zr_2O_7$

Together with $\varepsilon_2(\omega)$, Figure 9 shows a graph of the real part of the permittivity $\varepsilon_1(\omega)$ calculated using the Kramers–Kronig formula (3).

Table 5

Energies of Selected Peaks on Imaginary Part of Permittivity $\varepsilon_2(\omega)$ (Fig. 9), as Well as Reflection Coefficient R(0), Refractive Index (0) at the Beginning of Energy Count

A	B	C	D	E	F
5.02 eV	8.25	10.16	19.22	25.62	30.16
$\varepsilon_1(\omega)$	8.726				

$n(0) = 2.954$

$R(0) = 24.423\%$

As in other studied pyrochlores, cross-transitions between atoms were not taken into account in the calculation of $\varepsilon_2(\omega)$ for $Eu_2Zr_2O_7$. Thus, the key features of the fine structure of the imaginary part of the permittivity $\varepsilon_2(\omega)$ can be interpreted as follows:

A(5.02 eV)	O	p→s
A'(6.5-7 eV)	Eu	4f→d
B(8.25 eV)	O	p→s
C(10.16 eV)	O	p→s
D(19.22 eV)	O	s→p
E(25.62eV)	Eu	p→s
F(30.16 eV)	Zr	p→s
G(36 eV)	Eu	p→s

For the $Eu_2Zr_2O_7$ compound, absorption coefficient $\alpha(\omega)$ (4), refractive index $n(\omega)$ (5), absorption coefficient $k(\omega)$ (6), optical reflection coefficient $R(\omega)$ (7) and electron energy loss spectrum $L(\omega)$ (8 were calculated, respectively, using formulas (4–8) [23]. The above optical characteristics for $Eu_2Zr_2O_7$ are shown in Figures 10 and 11.

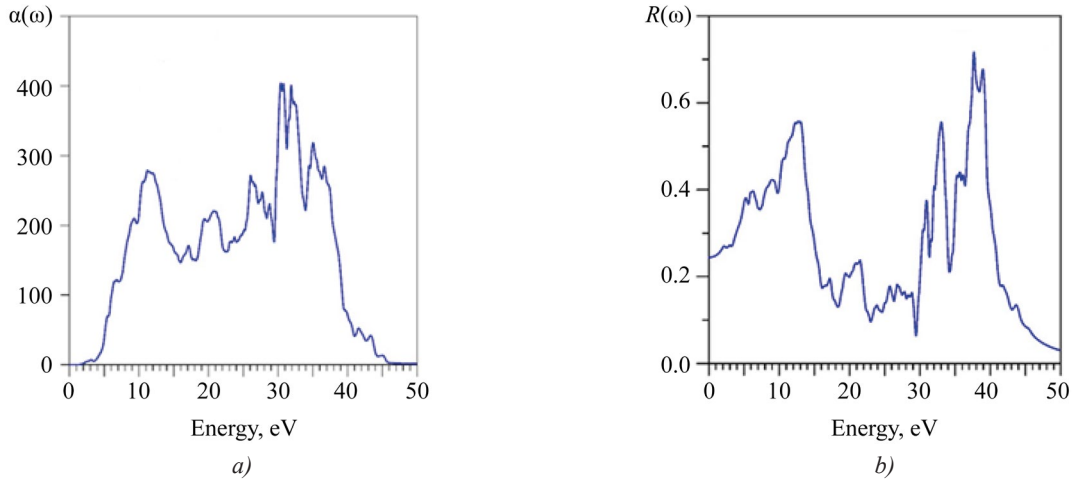

Fig. 10. Coefficients calculated in Eu2Zr2O7:
a — absorption α(ω); *b* — reflection *R*(ω)

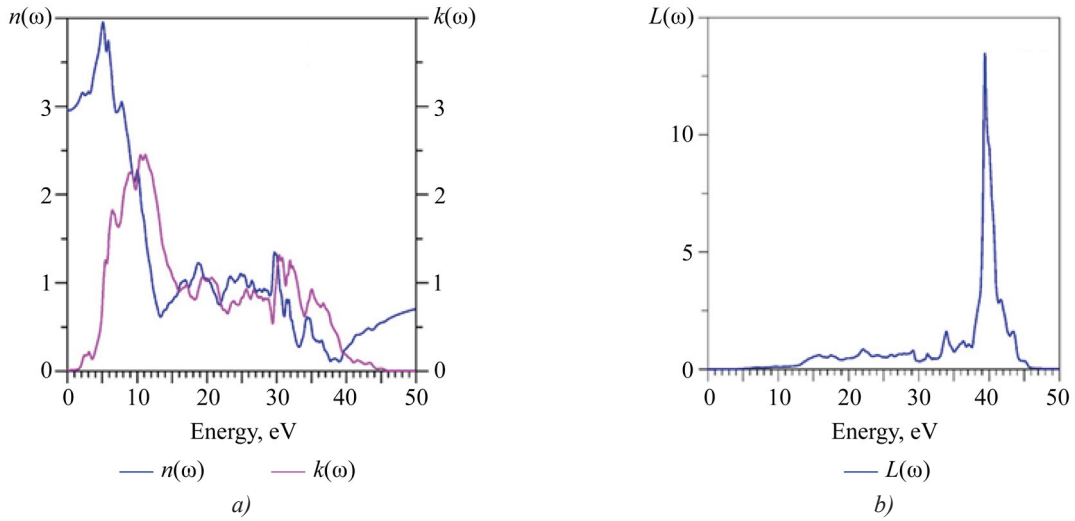

Fig. 11. Calculated in Eu2Zr2O7: *a* — refractive index *n*(ω) and extinction coefficient *k*(ω);
b — electron energy loss spectrum *L*(ω)

Discussion. In all groups of compounds studied in this work, the main contribution to the upper part of the valence band is given by the p-states of atoms with the highest electronegativity (chalcogens, halogens). This can be explained by a decrease in the binding energy of the p-states of chalcogens and halogens in a crystal, compared to their bonding in an isolated atom, due to the transfer of electron density from nearby metal atoms to them, and the resulting increase in the shielding of these states from the nucleus. The S-states of these atoms form the bottom of the valence band.

For compounds with atoms containing f-electrons, states of 5s-symmetry, which have different spins, are split in energy under the impact of the internal magnetic field of 4f-electrons.

The applied aspect of this research is related to the fact that the use of new materials in quantum electronics, optoelectronics, and nonlinear optics is determined by the response of the crystal under study to the action of an electron wave with a frequency lying in the optical or near and mid-IR range, that is, near the forbidden gap of the semiconductor (E_g). The crystal response can be described using the permittivity tensor (ε_{ij}), which was calculated in this study for a number of complex three- and four-component chalcogenides, halides, and oxides. Of academic interest is the effect of the electron states of the rare-earth element contained in the studied pyrochlores on the electron-energy structure of these compounds.

Conclusion. The main objective of the work is achieved. The results of the study on the electron-energy structure of various groups of compounds: chalcogenides Tl_3TaS_4, Tl_3PS_4, $Sn_2P_2S_6$, $InPS_4$, Cu_2CdGeS_4, Ag_2CdSnS_4, Ag_2HgSnS_4, halides Cs_2HgX_4 (X — Cl, Br, I) and APb_2Br_5 (A — K, Rb), oxides $La_2Zr_2O_7$ and $Nd_2Zr_2O_7$ and $Ln_2Zr_2O_7$ (Ln = La, Nd, Sm, Eu, Gd) are summarized. The problems of determining the effect of local partial electron states on the features of the electronic structure of the studied compounds and their optical properties are solved.

Such studies are important in the problems of modeling new materials with given properties, since they allow us to determine which factors have the main influence on the occurrence of such properties.

References

1. Vu Van Tuan, Lavrentyev AA, Gabrelian BV, Kalmykova KF, Sidorkin VV, Do Minh Hoat, et al. Electronic and Optical Properties of Wide Band Gap Tl_3TaS_4: A Promising Surface Acoustic Wave Material. *Optical Materials*. 2020;99:109601. https://doi.org/10.1016/j.optmat.2019.109601

2. Lavrentyev AA, Gabrelian BV, Vu Van Tuan, Khizhun OYu. *Electron-Energy Structure of Complex Chalcogenides and Chalcohalogenides.* Monograph. Rostov-on-Don: DSTU; 2018. 320 p. (In Russ.)

3. Lavrentyev AA, Gabrelian BV, Vu Van Tuan, Kalmykova KF. *Ab initio* Calculations of the Electronic-Energy Structure and Optical Properties of Lanthanum and Neodymium Pyrozirconates. *Advanced Engineering Research (Rostov-on-Don).* 2025;25(2):129–141. https://doi.org/10.23947/2687-1653-2025-25-2-129-141

4. Lavrentyev AA, Gabrelian BV, Vu Van Tuan, Kalmykova KF. Quantum-Mechanical Calculations of the Electronic Structure of Pyrochlores $Ln_2Zr_2O_7$ (Ln = Sm, Eu, Gd) in Comparison with Experimental X-Ray Photoelectron Spectra. In: *Proc. XIV International Youth Symposium "Physics of Lead-Free Piezoactive and Related Materials. Modeling of Eco-Systems",* vol II. Rostov-on-Don – Taganrog: SFU; 2025. P. 37–48.

5. Narsingh Bahadur R Singh, Ching-Hua Su, Bradley Arnold, Fow-Sen Choa, Teja Nagaradona. Effect of Impurities and Growth Parameters on the Quality of Tl_3AsSe_3 Optical Crystal. *Optical Materials.* 2016;60:81–85. https://doi.org/10.1016/j.optmat.2016.07.009

6. Bouhemadou A, Allali D, Boudiaf K, AlQarni B, Bin-Omran S, Khenata R, et al. Electronic, Optical, Elastic, Thermoelectric and Thermodynamic Properties of the Spinel Oxides $ZnRh_2O_4$ and $CdRh_2O_4$. *Journal of Alloys and Compounds.* 2019;774:299–314. https://doi.org/10.1016/j.jallcom.2018.09.338

7. Ewbank MD, Kowalczyk SP, Kraut EA, Harrison WA. Electronic Structure of Tl_3AsSe_3. *Physical Review B.* 1981;24(2):926–931.

8. Reshak AH. A Novel Photocatalytic Water Splitting Solar-to-Hydrogen Energy Conversion: Non-Centro-Symmetric Borate $CsZn_2B_3O_7$ Photocatalyst. *Journal of Alloys and Compounds.* 2018;741:1258–1268. https://doi.org/10.1016/j.jallcom.2018.01.227

9. Blaha P, Schwarz K, Madsen GKH, Kvasnicka D, Luitz J, Laskowski R, et al. WIEN2k, an Augmented Plane Wave+Local Orbitals Program for Calculating Crystal Properties, rev. ed. Vienna: Vienna University of Technology; 2002. 180 p. https://pubs.aip.org/aip/jcp/article/152/7/074101/485553/WIEN2k-An-APW-lo-program-for-calculating-the

10. Chartier A, Meis C, Crocombette J, Corrales LR, Weber WJ. Atomistic Modeling of Displacement Cascades in $La_2Zr_2O_7$ Pyrochlore. *Physical Review B*. 2003;67:174102. https://doi.org/10.1103/PhysRevB.67.174102

11. Stanek CR, Minervini L, Grimes RW. Nonstoichiometry in $A_2B_2O_7$ Pyrochlores. *Journal of the American Ceramic Society*. 2002;85(11):2792–2798. https://doi.org/10.1111/j.1151-2916.2002.tb00530.x

12. Pirzada M, Grimes RW, Minervini L, Maguire JF, Sickafus KE. Oxygen Migration in $A_2B_2O_7$ Pyrochlores. *Solid State Ionics*. 2001;140:201–208. https://doi.org/10.1016/S0167-2738(00)00836-5

13. Tabira Y, Withers RL, Minervini L, Grimes RW. Systematic Structural Change in Selected Rare Earth Oxide Pyrochlores as Determined by Wide-Angle CBED and a Comparison with the Results of Atomistic Computer Simulation. *Journal of Solid State Chemistry*. 2000;153(1):16–25. https://doi.org/10.1006/jssc.2000.8712

14. Helean KB, Ushakov SV, Brown CE, Navrotsky A, Lian J, Ewing RC, et al. Formation Enthalpies of Rare Earth Titanate Pyrochlores. *Journal of Solid State Chemistry*. 2004;177(6):1852–1866. https://doi.org/10.1016/j.jssc.2004.01.009

15. Chen J, Lian J, Wang LM, Ewing RC, Wang RG, Pan W. X-ray Photoelectron Spectroscopy Study of Disordering in $Gd_2(Ti_{1-x}Zr_x)_2O_7$ Pyrochlores. *Physical Review Letters*. 2002;88:105901. https://doi.org/10.1103/PhysRevLett.88.105901

16. Jing Feng, Bing Xiao, Chunlei Wan, Zheng Xiao Qu, Zheng-hong Huang, Jingchao Chen, et al. Electronic Structure, Mechanical Properties and Thermal Conductivity of $Ln_2Zr_2O_7$ (Ln=La, Pr, Nd, Sm, Eu and Gd) Pyrochlore. *Acta Materialia*. 2011;59(4):1742–1760. https://doi.org/10.1016/j.actamat.2010.11.041

17. Blaha P, Schwarz K, Tran F, Laskowski R, Madsen GKH, Marks LD. WIEN2k: an APW+lo Program for Calculating the Properties of Solids. *Journal of Chemical Physics.* 2020;152(7):074101. http://users.df.uba.ar/llois/NANO/usersguide.pdf

18. Weinert M. Solution of Poisson Equation beyond Ewald-Type Method. *Journal of Mathematical Physics.* 1981;22(11):2433–2439. https://doi.org/10.1063/1.524800

19. Perdew JP, Burke K, Ernzerhof M. Generalized Gradient Approximation Made Simple. *Physical Review Letters.* 1996;77(18):3865–3869. https://doi.org/10.1103/PhysRevLett.77.3865

20. Becke AD, Johnsom ER. A Simple Effective Potential for Exchange. *Journal of Chemical Physics.* 2006;124(22):221101. https://doi.org/10.1063/1.2213970

21. Anisimov VI, Poteryaev AV, Korotin MA, Anokhin AO, Kotliar G. First-Principles Calculations of the Electronic Structure and Spectra of Strongly Correlated Systems: Dynamical Mean-Field Theory. *Journal of Physics: Condensed Matter.* 1997;9(35):7359–7367. https://doi.org/10.1088/0953-8984/9/35/010

22. Koller D, Tran F, Blaha P. Improving the Modified Becke-Johnson Exchange Potential. *Physical Review B*. 2012;85:155109. https://doi.org/10.1103/PhysRevB.85.155109

23. Ambrosch-Draxl C, Sofo JO. Linear Optical Properties of Solids within the Full-Potential Linearized Augmented Planewave Method. *Computer Physics Communications.* 2006;175(1):1–14. https://doi.org/10.1016/j.cpc.2006.03.005

24. Čermák K. Optical Absorption Edge of Tl_3VS_4 and Tl_3TaS_4. *Czechoslovak Journal of Physics B.* 1984;34(1):88–93. https://doi.org/10.1007/BF01590484

25. Lotz W. Electron Binding Energies in Free Atoms. *Journal of the Optical Society of America*. 1970:60(2):206–210. https://doi.org/10.1364/JOSA.60.000206

26. Spesivykh AA, Benz VM, Bogdanova AV. Photoemission Studies on the Energy Structure of Tl3AsS4. *Russian Physics Journal*. 1981;24(4):110–112. (In Russ.)

27. Blokhin MA. *X-ray Physics*. Moscow: Gosudarstvennoe izdatel'stvo tekhniko-teoreticheskoi literatury; 1957. 518 p. (In Russ).

About the Authors:

Anatoliy A. Lavrentyev, Dr.Sci. (Phys.-Math.), Professor, Head of the Electrical Engineering and Electronics Department, Don State Technical University (1, Gagarin Sq., Rostov-on-Don, 344003, Russian Federation), SPIN-code, ORCID, ScopusID, ResearchGate, alavrentyev@donstu.ru

Boris V. Gabrelian, Cand.Sci. (Phys.-Math.), Associate Professor of the Computer and Automated Systems Software Department, Don State Technical University (1, Gagarin Sq., Rostov-on-Don, 344003, Russian Federation), SPIN-code, ORCID, ScopusID, ResearcherID, boris.gabrelian@gmail.com

Vu Van Tuan, Cand.Sci. (Phys.-Math.), Leading Researcher at the Laboratory of Computational Physics, Institute of Computational Science and Artificial Intelligence, Van Lang University (69/68, Dang Thuy Tram, Binh Loi Trung Ward, Ho Chi Minh City, Socialist Republic of Vietnam), ORCID, ScopusID, vuvan.tuan@mail.ru

Kseniya F. Kalmykova, Senior Lecturer of the Electrical Engineering and Electronics Department, Don State Technical University (1, Gagarin Sq., Rostov-on-Don, 344003, Russian Federation), SPIN-code, ORCID, ScopusID, ResearchGate, 16ksy16@mail.ru

Claimed Contributorship:

AA Lavrentyev: conceptualization, supervision, project administration.
BV Gabrelian: methodology, formal analysis, data curation, validation.
Vu Van Tuan: resources, validation, writing – original draft preparation.
KF Kalmykova: formal analysis, writing.

Об авторах:

Анатолий Александрович Лаврентьев, доктор физико-математических наук, профессор, заведующий кафедрой «Электротехника и электроника» Донского государственного технического университета (344003, Российская Федерация, г. Ростов-на-Дону, пл. Гагарина, 1), SPIN-код, ORCID, ScopusID, ResearchGate, alavrentyev@donstu.ru

Борис Витальевич Габрельян, кандидат физико-математических наук, доцент кафедры «Программное обеспечение вычислительной техники и автоматизированных систем» Донского государственного технического университета (344003, Российская Федерация, г. Ростов-на-Дону, пл. Гагарина, 1), SPIN-код, ORCID, ScopusID, ResearcherID, boris.gabrelian@gmail.com

Ву Ван Туан, кандидат физико-математических наук, ведущий научный сотрудник лаборатории вычислительной физики Института вычислительной науки и искусственного интеллекта Университета Ван Ланг (Социалистическая Республика Вьетнам, г. Хошимин), ORCID, ScopusID, vuvan.tuan@mail.ru

Ксения Федоровна Калмыкова, старший преподаватель кафедры «Электротехника и электроника» Донского государственного технического университета (344003, Российская Федерация, г. Ростов-на-Дону, пл. Гагарина, 1), SPIN-код, ORCID, ScopusID, ResearchGate, 16ksy16@mail.ru

Заявленный вклад авторов:

А.А. Лаврентьев: разработка концепции, научное руководство, административное руководство исследовательским проектом.

Б.В. Габрельян: разработка методологии, формальный анализ, курирование данных, валидация результатов.

Ву Ван Туан: предоставление ресурсов, валидация результатов, написание черновика рукописи.

К.Ф. Калмыкова: формальный анализ, написание рукописи.

Конфликт интересов: **авторы заявляют об отсутствии конфликта интересов.**

Все авторы прочитали и одобрили окончательный вариант рукописи.

Received / **Поступила в редакцию** 15.01.2026
Reviewed / Поступила после рецензирования 06.02.2026
Accepted / **Принята к публикации** 18.02.2026

INFORMATION TECHNOLOGY, COMPUTER SCIENCE AND MANAGEMENT
ИНФОРМАТИКА, ВЫЧИСЛИТЕЛЬНАЯ ТЕХНИКА И УПРАВЛЕНИЕ

UDC 681.5.017: 664.8.047
https://doi.org/10.23947/2687-1653-2026-26-1-2249

Original Empirical Research

Mathematical Model of the Thermal Regime of a Small-Sized Convective Dehydrator and Identification of Its Parameters

Alexandr D. Lukyanov[1], Alexander N. Zhuravlev[2], Marko Petković[3], Vladimir S. Filipović[4], Nemanja M. Miletić[3], Danila Yu. Donskoy[1]

[1] Don State Technical University, Rostov-on-Don, Russian Federation
[2] Gruvior LLC, Rostov-on-Don, Russian Federation
[3] University of Kragujevac, Čačak, Serbia
[4] University of Novi Sad, Novi Sad, Serbia

✉ lex1998@rambler.ru

EDN: LVDSKQ

Abstract

Introduction. Convective drying of various types of food raw materials is one of the most common methods of canning. Over three million tons of dried fruits alone are preserved worldwide each year, and the volume continues to grow. Due to the duration and energy consumption of the process, when almost 50% of energy is spent directly on removing moisture, optimizing drying is a challenge. Targeted and reasonable optimization can be performed only if there is a common mathematical model of equipment and drying processes. However, when modeling the drying process, as a rule, a mathematical model of the equipment is not used, which makes the results obtained limited in application. This is the knowledge gap that the proposed study is designed to eliminate. The article presents the results of the development and identification of the parameters of a mathematical model of a small-sized dehydrator used as an experimental installation for the study on food drying processes. The research objective is to develop a mathematical model of the thermal subsystem of a dehydrator that takes into account the processes of heat and mass transfer. To achieve this goal, the following tasks must be solved: to analyze the design of the dehydrator and take into account the effect of the control system; to build a mathematical model of the dehydrator in the form of an ordinary differential equation (ODE) system; to develop a simulation model of the dehydrator in the MATLAB/Simulink package; to conduct experimental studies to obtain data on temperature and power consumption; to identify the parameters of the mathematical model, including the amount of air flow and the circulation coefficient; to verify the obtained model through comparing the results of simulation and experiment.

Materials and Methods. A small-sized convective dehydrator equipped with an original microprocessor control system was used as a modeling object. This system was designed to provide a preset temperature regime and collect data on the parameters of the drying process: temperature, humidity, air pressure, and others. The system used three sensors: two BME-280 sensors and one DS18B20 sensor. Telemetry data and control commands were transmitted via a bot on the Telegram platform. The mathematical model of the dehydrator was constructed in the class of ODEs by the method of accumulators and flows. The parameters of the mathematical model were identified both by direct measurements of the structural elements of the dehydrator and using data obtained during experimental studies. The least squares method (LSM) was used for parametric identification of the model. The calculations were performed in the MATLAB software package.

Results. A mathematical model of thermal processes in a dehydrator has been developed in the form of a system of ordinary nonlinear differential equations of the third order. The model takes into account both the air flow coming out of the dehydrator and the air circulation inside it. The total coefficient of heat loss through the walls of the dehydrator is also determined, and its dependence on the temperature difference inside and outside the installation is shown. The developed model is presented both analytically and as a model in the MATLAB/Simulink system. The experimental verification of the model has shown high accuracy: the maximum deviation of the calculated temperatures from the measured ones was

less than 0.5°C. The identification method has determined the key parameters of the system: the volume flow of air through the heater (14.1 l/s), and the air circulation coefficient (11.3), which indicates a more than tenfold passage of air flow through the working chamber. It has been found that intensive circulation significantly speeds up the drying process compared to natural convection. The model provides physical interpretability of the parameters and requires a minimum amount of experimental data.

Discussion. The developed mathematical model of the dehydrator based on ordinary differential equations showed high accuracy (error less than 0.5°C) in the operating temperature range. The proposed energy approach made it possible to identify the volumetric air flow (3.1 l/s) and the circulation coefficient (α = 10.2), which cannot be measured directly. It is established that the air performs more than 10 cycles inside the chamber before exiting, which significantly intensifies heat and mass transfer. The coefficient of heat transfer through the walls depends linearly on the temperature difference, which is consistent with the theory of natural convection. Unlike empirical and neural network models, the proposed approach requires less experimental data and provides physical interpretability of the parameters. The model creates the basis for optimizing food drying processes.

Conclusion. The developed and experimentally verified mathematical model of the thermal subsystem of a small-sized convective dehydrator provides measurement accuracy and allows for the identification of hard-to-reach parameters: volumetric air flow rate and circulation coefficient. The research results can serve as the basis for developing a comprehensive model of the food dehydration process and optimizing the device operating modes. The model is applicable to the design and improvement of domestic dehydrators.

Keywords: modeling, convective dehydrator, identification, control, flow, ODE

Acknowledgements. The authors would like to thank the editors and the reviewers for their attentive attitude to the article and the specified comments that helped to improve its quality.

Funding Information. The research is done with the financial support from the Russian Science Foundation (grant no. 23-76-30006), https://rscf.ru/project/23-76-30006/

For Citation. Lukyanov AD, Zhuravlev AN, Petković M, Filipović VS, Miletić NM, Donskoy DYu. Mathematical Model of the Thermal Regime of a Small-Sized Convective Dehydrator and Identification of Its Parameters. *Advanced Engineering Research (Rostov-on-Don).* 2026;26(1):2249. https://doi.org/10.23947/2687-1653-2026-26-1-2249

Оригинальное эмпирическое исследование

Математическая модель теплового режима малогабаритного конвективного дегидратора и идентификация его параметров

А.Д. Лукьянов[1] ✉, А.Н. Журавлев[2], М.М. Петкович[3], В.С. Филиппович[4], Н.М. Милетич[3], Д.Ю. Донской[1]

[1] Донский государственный технический университет, г. Ростов-на-Дону, Российская Федерации

[2] ООО «Грувиор», г. Ростов-на-Дону, Российская Федерация

[3] Крагуевацкий университет, г. Чачак, Республика Сербия

[4] Университет Нови-Сада, г. Нови-Сад, Республика Сербия

✉ lex1998@rambler.ru

Аннотация

Введение. Конвективная сушка различных видов пищевого сырья является одним из наиболее распространенных методов заготовки продуктов для длительного хранения, только сухофруктов в мире консервируется свыше трех миллионов тонн в год, и объемы продолжают расти. Ввиду длительности и энергозатратности процесса, когда непосредственно на удаление влаги из продуктов тратиться почти 50 % энергии, оптимизация сушки представляет собой актуальную задачу. Целенаправленная и обоснованная оптимизация может быть осуществлена только при наличии общей математической модели оборудования и процессов сушки. Однако при моделировании процесса сушки, как правило, математическая модель оборудования не используется, что делает полученные результаты ограниченными для применения. Это является тем пробелом в знаниях, который призвано устранить предлагаемое авторами исследование. В статье представлены результаты разработки и идентификации параметров математической модели малогабаритного дегидратора, используемого в качестве экспериментальной установки для исследования процессов сушки пищевых продуктов. Целью исследования является разработка математической модели тепловой подсистемы дегидратора, учитывающей процессы тепло- и массопереноса. Для достижения поставленной цели были решены следующие задачи: проанализирована конструкция дегидратора и учтено

влияние на нее системы управления, построена математическая модель дегидратора в виде системы обыкновенных дифференциальных уравнений (ОДУ), разработана имитационная модель дегидратора в пакете Matlab/Simulink, проведены экспериментальные исследования для получения данных о температуре и потребляемой мощности, идентифицированы параметры математической модели, в том числе величины воздушного потока и коэффициент циркуляции. Полученная модель верифицирована путем сравнения результатов имитационного моделирования и эксперимента.

Материалы и методы. В качестве объекта моделирования был использован малогабаритный конвективный дегидратор, оснащенный оригинальной микропроцессорной системой управления. Данная система предназначена для обеспечения заданного температурного режима и сбора данных о параметрах процесса сушки: температуре, влажности, давлении воздуха и других. В системе было установлено три датчика: два датчика BME-280 и один датчик DS18B20. Телеметрические данные и управляющие команды передавались через бота на платформе Телеграм. Математическая модель дегидратора построена в классе нелинейных обыкновенных дифференциальных уравнений методом накопителей и потоков. Идентификация параметров математической модели осуществлялась как путем прямых измерений конструктивных элементов дегидратора, так и с использованием данных, полученных в ходе экспериментальных исследований. Для параметрической идентификации модели применен метод наименьших квадратов (МНК). Вычисления выполнены в программном пакете MATLAB.

Результаты исследования. Разработана математическая модель тепловых процессов в дегидраторе в виде системы обыкновенных нелинейных дифференциальных уравнений третьего порядка. Модель учитывает как поток воздуха, выходящий из дегидратора, так и циркуляцию воздуха внутри него. Также определен суммарный коэффициент теплопотерь через стенки дегидратора и показана его зависимость от разности температур внутри и снаружи установки. Разработанная модель представлена как в аналитическом виде, так и в виде модели в системе MATLAB/Simulink. Экспериментальная верификация модели показала высокую точность: максимальное отклонение расчетных температур от измеренных составило менее 0,5 °C. Методом идентификации определены ключевые параметры системы: объемный расход воздуха через нагреватель (14,1 л/с) и коэффициент циркуляции воздуха (11,3), что указывает на более чем десятикратное увеличение воздушного потока, проходящего через рабочую камеру. Установлено, что воздух совершает более 10 циклов внутри камеры перед выходом, что существенно интенсифицирует тепломассообмен. Коэффициент теплопередачи через стенки линейно зависит от разности температур, что согласуется с теорией естественной конвекции. Модель обеспечивает физическую интерпретируемость параметров и требует минимального объема экспериментальных данных.

Обсуждение. Разработанная математическая модель дегидратора на основе обыкновенных дифференциальных уравнений показала высокую точность в рабочем диапазоне температур. Предложенный в работе энергетический метод, базирующийся на анализе теплового баланса системы, позволил идентифицировать объемный расход воздуха и коэффициент циркуляции, которые невозможно измерить напрямую. В отличие от эмпирических и нейросетевых моделей, предложенный подход требует меньше экспериментальных данных и обеспечивает физическую интерпретируемость параметров. Модель создает основу для оптимизации процессов сушки пищевых продуктов.

Заключение. Разработанная и экспериментально верифицированная математическая модель тепловой подсистемы малогабаритного конвективного дегидратора обеспечивает точность измерения и позволяет идентифицировать труднодоступные параметры: объемный расход воздуха и коэффициент циркуляции. Результаты исследования могут быть основой для разработки комплексной модели процесса дегидратации пищевых продуктов и оптимизации режимов работы устройства. Модель применима для проектирования и совершенствования бытовых дегидраторов.

Ключевые слова: моделирование, конвективный дегидратор, идентификация, управление, поток, ОДУ

Благодарности. Авторы выражают благодарность редакции и рецензентам за внимательное отношение к статье и указанные замечания, устранение которых позволило повысить ее качество.

Финансирование. Финансовая поддержка исследований в части разработки системы управления дегидратором осуществлена в рамках гранта Российского научного фонда № 23-76-30006, https://rscf.ru/project/23-76-30006/

Для цитирования. Лукьянов А.Д., Журавлев А.Н., Петкович М.М., Филиппович В.С., Милетич Н.М., Донской Д.Ю. Математическая модель теплового режима малогабаритного конвективного дегидратора и идентификация его параметров. *Advanced Engineering Research (Rostov-on-Don).* 2026;26(1):2249. https://doi.org/10.23947/2687-1653-2026-26-1-2249

Introduction. Convective drying of food raw materials is one of the most common methods of canning, while dried fruits alone are produced in the world over three million tons annually, and volumes continue to grow [1, 2]. Due to the duration and energy consumption of the process, when less than 50% of energy is spent directly on moisture removal [3], optimization of drying is an urgent task. Targeted optimization is possible only if there is an adequate mathematical model of both the equipment and the drying process.

A significant number of models of food drying processes have been published in the scientific literature. The predominant approach is to approximate the kinetics of drying by various empirical functions: the Lewis model [4], modified exponential models of Page [5] and Henderson-Pabis [6], combined Yaldiz models [7], and polynomial approximations [8]. Researchers are analyzing the applicability of various models for specific products: in [9], an artificial neural network was used to study the kinetics of drying wild bitter watermelon, in [10], the drying of avocado peel was studied, in [11], convective dehydration of carrots was studied using a statistical approach to curve identification [12]. However, this approach is traditional, but "situational" and does not sufficiently reflect the physical patterns of heat and mass transfer during drying.

A more promising method is dynamic modeling based on differential equations, the parameters of which are better amenable to physical understanding [13, 14]. A critical analysis of the literature has revealed a significant gap: when modeling drying processes, the mathematical model of the equipment itself is usually not used or simplified, which limits the applicability of the results. The dehydrator model should describe the processes of heat transfer and air circulation, including such hard-to-reach parameters as volume flow and air circulation coefficient, which significantly affect the accuracy of modeling [15]. Despite the distributed nature of the processes [16], the use of ordinary differential equations ensures interpretability of the results while maintaining sufficient accuracy.

A significant number of scientific publications in recent years has been devoted to the use of artificial neural networks to study food dehydration processes, build mathematical models, and optimize parameters. A comprehensive review of the use of artificial neural networks in drying is presented in [17]. Among such works, it is worth mentioning [18], in which the authors use a neural network approach to improve the drying process of pear slices. In [19], a neural network model is used to simulate the drying process of zucchini slices. In [20], the authors apply a neural network approach to simulate the drying process of *Phyllanthus emblica* in a complex infrared drying process with ultrasonic activation. Another example of successful application of neural networks (ANN) in modeling complex multiparametric processes in food production is work [21]. Despite the promise of the neural network approach, traditional modeling can be more effective for deterministic technical systems due to a better understanding of physical processes and lower requirements for the amount of experimental data.

The objective of this study is to develop a mathematical model of the thermal subsystem of a small convective dehydrator based on ordinary differential equations with the identification of hard-to-reach parameters. To achieve the goal, the following tasks were set: to analyze the design of the dehydrator and the influence of the control system; to build a mathematical model in the form of an ODE system; to develop a simulation model in the MATLAB/Simulink package; to conduct experimental studies of temperature conditions and energy consumption; to identify model parameters, including air flow and circulation coefficient; to verify the model by comparing simulation and experimental results.

1. Materials and Methods

1.1 Design of a small-sized dehydrator

To build a laboratory installation designed to study drying processes, a household convective dehydrator with horizontal air movement and 12 trays for the dehydrated product was used (Fig. 1). The maximum power of the dehydrator was 800 watts, the air movement was provided by two propeller fans.

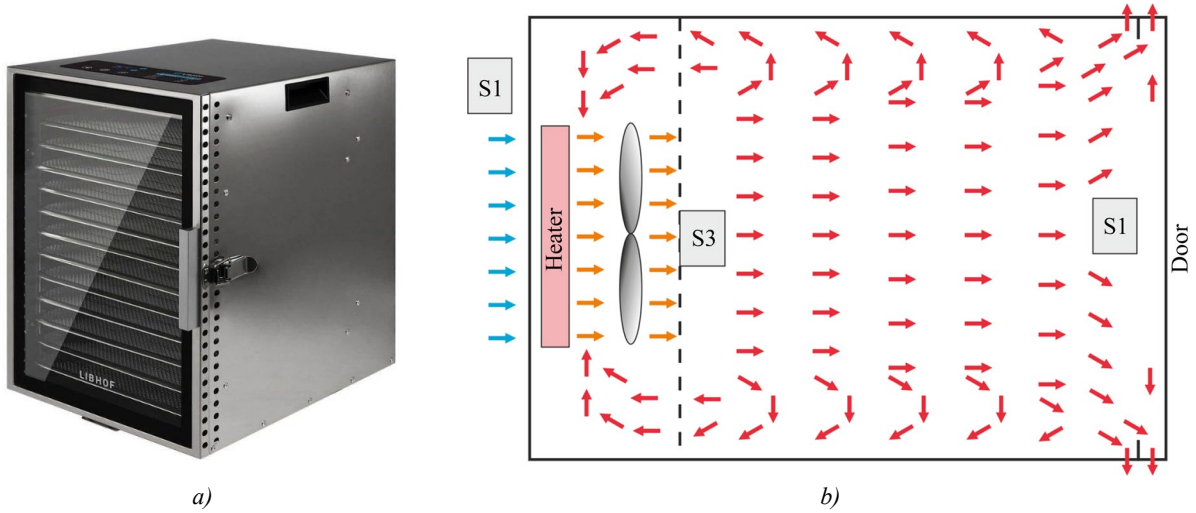

a) *b)*

Fig. 1 Household dehydrator used for experiments: *a* — appearance; *b* — placement of sensors and an approximate diagram of the air flow inside the dehydrator (cross section)

The design characteristics of the dehydrator (Fig. 1) are shown in Table 1.

Table 1

Design Characteristics of the Dehydrator

Parameter	Designation	Size	Dimension
Chamber volume	V	0.054	m^3
Side wall area	S_w	0.189	m^2
Floor and roof area	S_h	0.134	m^2
Door and rear wall area	S_g	0.140	m^2
Weight of internal elements of the dehydrator	m_d	3.348	kg
Weight of the heater	m_h	0.3	kg
Heater power	P_{max}	800	W

1.2 Microcontroller control and monitoring system

The temperature control system and timer present in the dehydrator were disabled, and the original microcontroller control system was installed instead. Figure 1 *b* shows the installation locations of the control system sensors: S1 — BME-280 sensor for outdoor air parameters; S2 — BME-280 sensor for hot air parameters at the outlet of the dehydrator chamber; S3 — DS18B20 sensor for air temperature after the heater.

The control system was independently developed, manufactured and implemented by a team of the authors. The structure of the system is shown in Figure 2. The system was based on the ESP32-WROOM-32 IoT microcontroller. BME-280 MEMS sensors were used to measure air parameters (temperature, humidity, pressure). A DS18B20 digital thermometer was used to control the air temperature after the heater. The fan and heater were controlled via OMRON G3MB-202P and JOTTA SSD-40DA solid-state relays, respectively[1].

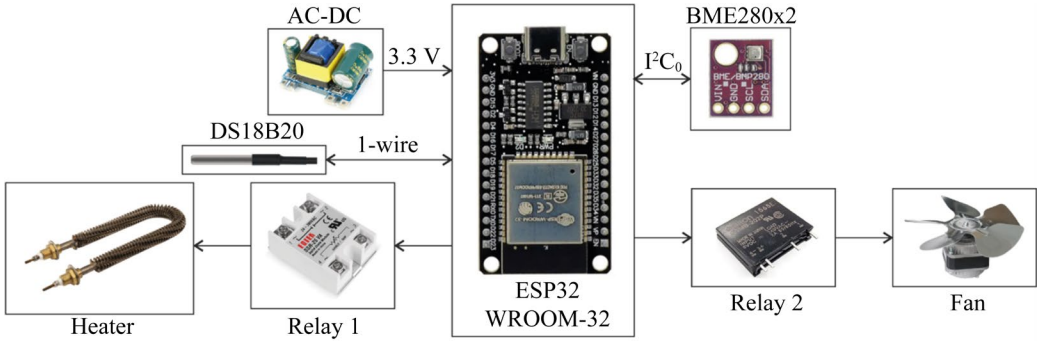

Fig. 2. Structure of the dehydrator control system based on the microcontroller

The microcontroller control system provided the following possibilities for controlling the dehydrator:

– regulation of the air temperature after the heater using a software PI controller in the range from 30 to 100°C with a discreteness of 0.25°C;

– measurement of temperature, relative humidity and air pressure with errors of 0.5°C, 3% and 1 gPa, respectively;

– the period of measuring the parameters of the dehydration process is at least 10 times per minute;

– information about the dehydration process is transmitted via the serial port to the connected computer and in parallel to the Telegram bot. The information transfer period is 1 minute;

– the BME280 sensors are temperature calibrated using a DS18B20 digital thermometer (as a reference) according to GOST 8.558–2009[2]. The calibration coefficients are entered into the program of the dehydrator control system;

– the dehydrator is controlled either directly by sending commands via the serial port of the connected computer, or remotely via a Telegram bot.

The use of the Telegram bot cloud technology provided a unique opportunity for both the Russian and Serbian teams to receive information about the operation of the experimental facility instantly and synchronously. The Telegram bot allows you to quickly receive telemetric information about the drying process, as well as remotely control and configure the dehydrator.

[1] All electronic components were purchased on electronic trading platforms, the country of origin is China.

[2] GOST 8.558–2009. *State verification scheme for temperature measuring instruments.* URL: https://meganorm.ru/Data2/1/4293795/4293795489.pdf (дата обращения: 26.01.2026).

The application of the developed dehydrator control system made it possible to implement a methodology for conducting experimental studies that provided online monitoring of the dehydration process, as well as to build and identify a mathematical model of the dehydrator.

1.3 Mathematical model of the dehydrator

The structure of the mathematical model of the dehydrator, based on a priori concepts of heat exchange processes and heat flows in it, is shown in Figure 3.

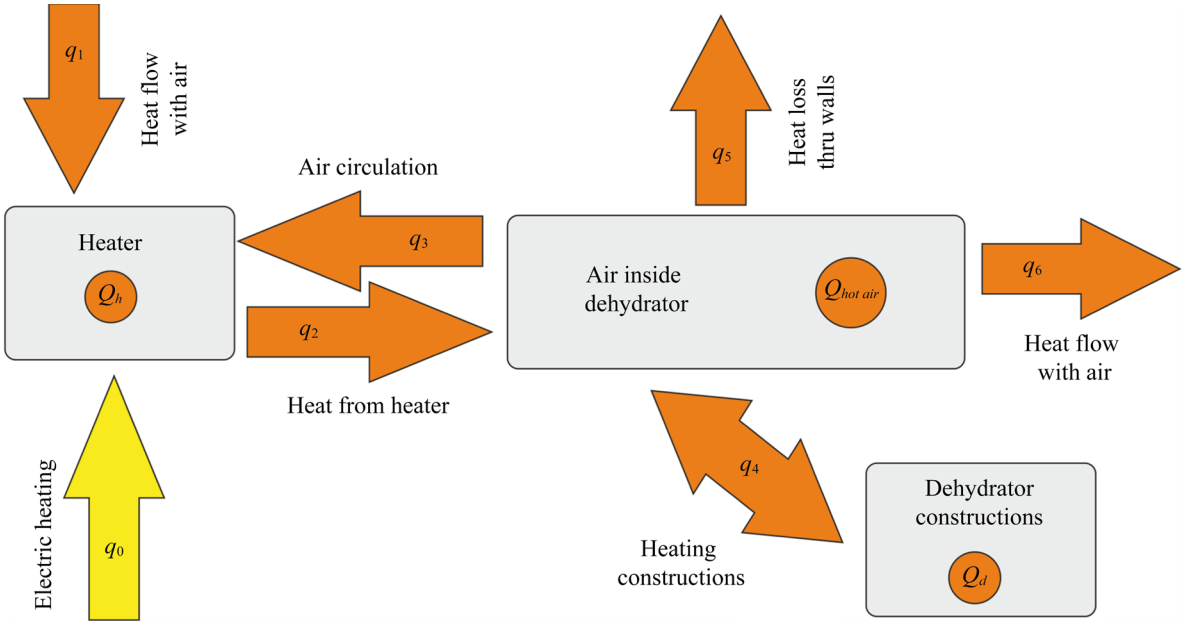

Fig. 3. Flowchart of the thermodynamic model of a small-sized dehydrator

The model includes three heat storage units – a heater, hot air inside the dehydrator, and structural elements of the dehydrator connected to each other and the external environment by seven heat streams. The model is created in the formalism of ordinary differential equations (ODEs) and is described by a system of three first-order differential equations (1):

$$\begin{cases} \frac{d}{dt}\vartheta_h = \frac{1}{m_h \cdot c_h}\left(P_{max}\cdot u(t) - c_{p,air}\cdot f_{air}\cdot\left(\vartheta_h - \vartheta_{ext\_air}\right) - k_{circ}\cdot c_{p,air}\cdot f_{air}\cdot\left(\vartheta_h - \vartheta_{hot\_air}\right)\right) \\ \frac{d}{dt}\vartheta_d = \frac{1}{m_d \cdot c_d} S_d \cdot \alpha_d \cdot \left(\vartheta_d - \vartheta_h\right) \\ \frac{d}{dt}\vartheta_{hot,air} = \frac{1}{V_d \cdot c_{p,air}}\left(k_{circ}\cdot c_{p,air}\cdot f_{air}\left(\vartheta_h - \vartheta_{hot\_air}\right) - \right. \\ \left. - S_{ext}\cdot\frac{A_{ext,0} + A_{ext,1}\cdot\left(\vartheta_h - \vartheta_{ext\_air}\right)}{d}\cdot\left(\vartheta_{ext\_air} - \vartheta_{hot\_air}\right) - S_d\cdot\alpha_d\cdot\left(\vartheta_h - \vartheta_d\right)\right) \end{cases}. \quad (1)$$

The following notation is used in equation (1) (Table 2):

Table 2

State Variables, External Influences, and Identifiable Model Parameters (1)

Parameter or variable	Designation	Value or range	Dimension
Heater temperature	ϑ_h	0–100	°C
Dehydrator element temperature	ϑ_d	0– 100	°C
Temperature of the hot air at the outlet of the dehydrator	$\vartheta_{hot,\ air}$	0–100	°C
Temperature external air	ϑ_{ext_air}	0–100	°C
Regulator duty	$u(t)$	0–1	dimentionless
Mass flow of air leaving the dehydrator	f_{air}	–	kg/s
Volumetric flow rate of air leaving the dehydrator	$f_{air,\ V}$	–	m^3/s
Air circulation coefficient inside the dehydrator chamber	k_{circ}	–	dimentionless

Heat transfer coefficient to the heater elements	α_d	–	W
Static part heat transfer coefficient through the wall	$A_{ext,\,0}$	–	W/(m^2·K)
Dynamic part heat transfer coefficient through the wall	$A_{ext,\,1}$	–	W·s/(m^2·K)

Considering the system of equations of model (1), it should be recognized that it is rather cumbersome and not very convenient for modeling. Therefore, we transform it to the form (2) and enter the coefficients of the equations in Table 3:

$$\begin{cases} \dfrac{d\vartheta_h}{dt} = a_{10}\left(P_{max}\cdot u(t) - a_{12}\cdot\left(\vartheta_h - \vartheta_{ext}\right) - a_{13}\cdot\left(\vartheta_h - \vartheta_{hot}\right)\right) \\ \dfrac{d\vartheta_d}{dt} = a_{21}\cdot\left(\vartheta_h - \vartheta_d\right) \\ \dfrac{d\vartheta_{hot}}{dt} = a_{30}\left(a_{31}\cdot\left(\vartheta_h - \vartheta_{hot}\right) - a_{32}\left(\vartheta_h - \vartheta_{ext}\right)\cdot\left(\vartheta_{ext} - \vartheta_{hot}\right) - a_{33}\cdot\left(\vartheta_h - \vartheta_d\right)\right) \end{cases}. \quad (2)$$

When converting system of equations (1) to form (2), it can be noted that $a_{21} = a_{33}$, $a_{31} = a_{12} = a_{13}/k_{circ}$. In addition, it should be noted that system (1) uses a mass flow rate of air f_{air}, and during the identification process, the value of the volume flow is obtained $f_{air,\,V}$. These quantities differ by the value of the air density, which depends on the temperature.:

$$f_{air} = f_{air,V}\cdot\rho_{air}\left(\vartheta_{hot}\right) = f_{air,V}\cdot\frac{p_{atm}\cdot M_{air}}{R_{air}\cdot\left(\vartheta_{hot} + 273{,}2\right)}. \quad (3)$$

The numerical values and expressions for the coefficients of the equation are given in Table 3

Table 3

Formulas and Values of the Coefficients of Equation (2)

Coefficient	Coefficient formula	Value
a_{10}	$1/(m_h\cdot c_h)$	0.0067
a_{12}	$c_{p,air}\cdot f_{air} = c_{p,air}\cdot f_{air,\,V}\cdot\rho(\vartheta_{hot})$	$0.011\cdot p_{atm}/(\vartheta_{hot} + 273.2)$
a_{13}	$a_{12}\cdot k_{circ}$	$0.111\cdot p_{atm}/(\vartheta_{hot} + 273.2)$
a_{21}	$1/(m_d\cdot c_d)$	$5.9737\cdot10^{-4}$
a_{30}	$1/(V_d\cdot c_{p,air})$	0,0184
a_{31}	$c_{p,air}\cdot f_{air} = c_{p,air}\cdot f_{air,\,V}\cdot\rho(\vartheta_{hot})$	$0.011\cdot p_{atm}/(\vartheta_{hot} + 273.2)$
a_{32}	$S_{ext}\cdot\dfrac{A_{ext,0} + A_{ext,1}\cdot\left(\vartheta_h - \vartheta_{ext\_air}\right)}{d}$	$0.0082\cdot(\vartheta_h - \vartheta_{ext\_air}) + 0.2351$
a_{33}	$1/(m_d\cdot c_d)$	$5.9737\cdot10^{-4}$

Table 4 shows additional model parameters measured or taken from reference books.

Table 4

Physical Parameters in the Dehydrator Model

Designation	Name	Value	Dimension
m_h	heater mass	0.3	kg
c_h	heat capacity of the heater, stainless steel	500	J/(kg·K)
m_d	weight dehydrator design	2.400	kg
c_d	heat capacity of the dehydrator material, stainless steel	500	J/(kg·K)
V_d	dehydrator internal volume	0.054	m^3
$c_{p,air}$	air heat capacity at constant pressure	1005	J/(kg·K)
S_d	dehydrator structural area	0.07	m^2
α_d	metal-air heat transfer coefficient	50	W/(m^2·K)
d	dehydrator wall thickness	0.75	mm
P_{max}	maximum heater power	800	W

Figure 4 shows the general structure of the dehydrator model in the Simulink mathematical package.

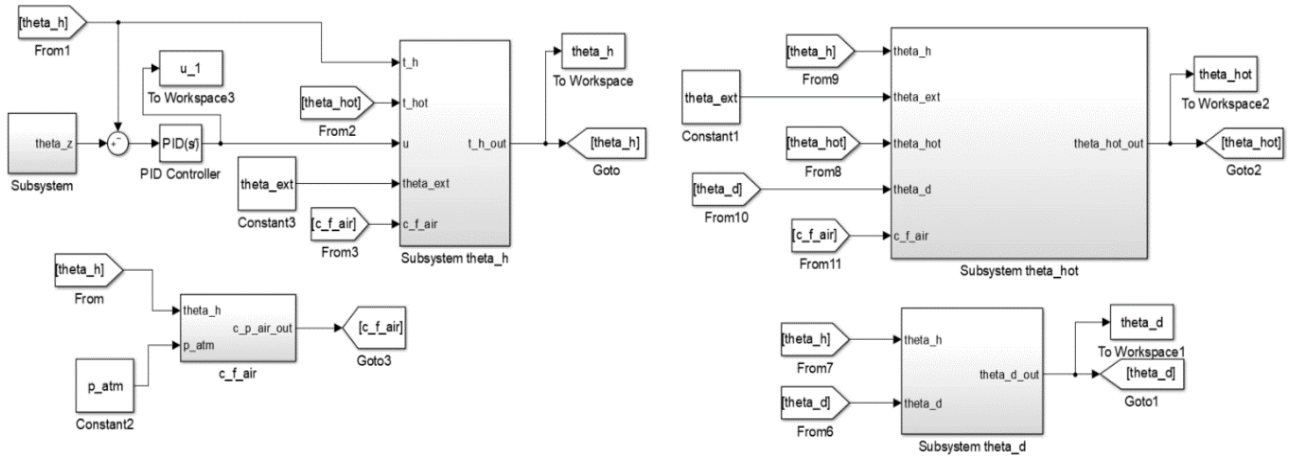

Fig. 4. Structure of the dehydrator model in Simulink

The model consists of three dynamic subsystems describing the dynamics of heat exchange with the heater, with the internal structures of the dehydrator and with the air inside the dehydrator. The fourth subsystem is used to calculate the heat flow carried out by air from the dehydrator.

Let us take a closer look at the following aspects. A priori information about the functioning of convective dehydrators of the considered design indicates the presence of convective air movement inside the dehydrator chamber. However, it is difficult to analytically estimate the "circulation coefficient", that is, how many times the air passes over the product before leaving the dehydrator. To account for this effect, a dimensionless circulation coefficient k_{circ} is introduced into the model, which will be estimated during the identification of model parameters.

Similarly, the heat transfer coefficient from the air to the structural elements of the dehydrator α_d is introduced into the model. Based on general physical considerations, this coefficient should have the following form (4):

$$\alpha_d = 5.6 + 4v, \tag{4}$$

where v — air velocity in m/s. However, based on the fact that this speed will be constant in the stationary operation of the dehydrator, and on the other hand, its measurement presents certain difficulties, we will consider this coefficient constant and identify it as a constant.

For the coefficients of heat transfer from the dehydrator chamber to the external environment through the walls, it is incorrect to assume the constancy of the transfer coefficient. Based on formula (4), it is necessary to take into account that the speed of the upward movement of the outside air along the wall of the dehydrator will depend on the temperature difference between the air inside and outside. That is, it is advisable to present this coefficient as (5) and identify it accordingly:

$$A_{ext,0} + A_{ext,1} \cdot \left(\vartheta_h - \vartheta_{ext\_air} \right). \tag{5}$$

However, the identification of the mass f_{air} (and volume $f_{air,v}$) air flow coming out of the dehydrator and carrying away heat and moisture is of the greatest practical interest. The mass and volume air flows leaving the dehydrator are related to the air density $\rho_{air}(\vartheta_{hot}, P_{atm})$ by the following ratio (6):

$$\rho_{air}\left(\vartheta_{hot}, P_{atm}\right) = \frac{P_{atm} \cdot M_{air}}{R_{air} \cdot \vartheta_{hot}}, \tag{6}$$

where M_{air} — molar mass of air, R_{air} — gas constant of air, and P_{atm} — atmospheric pressure.

The air flow from the dehydrator is determined by the excess air pressure on the inner front wall of the dehydrator chamber. The pressure is created by rotating fans. From general physical considerations, it seems that at a constant rotational speed, the volumetric air flow rate should not depend on the air temperature, since its value is determined by the geometric design of the fan blades and their rotational speed.

The authors have tested several physical approaches to measuring the amount of airflow:

– by directly measuring the flow velocity using an anemometer;

– by directly measuring the difference in air pressure inside and outside the dehydrator and estimating the air flow rate passing through the holes in the walls of the dehydrator using the Bernoulli formula;

– by the magnitude of the force acting on the dehydrator door (for indirect determination of the pressure drop), and then using the Bernoulli formula, as in the previous paragraph.

However, none of them, due to insufficient accuracy, allowed us to obtain a reliable and plausible estimate of the cost. For this reason, it was decided to estimate the amount of airflow based on energy considerations — based on the amount of electrical power that is consumed to heat an unknown amount of airflow with known physical characteristics. The procedure for identifying model parameters developed by the authors is discussed below. At the same time, the maximum possible number of parameter values was measured directly or taken from reference books. Thus, it is necessary to identify the following model parameters: flows f_{air} and $f_{air,v}$; total heat transfer coefficient $A_{ext,0} + A_{ext,1} \cdot (\vartheta_h - \vartheta_{ext\_air}) \cdot S_{ext}/d$; circulation coefficient k_{circ}.

Analyzing model (1), it can be seen that some of the identified parameters can be obtained from static equations, that is, from equations describing the steady-state operation of the dehydrator (7):

$$\begin{cases} 0 = P_{max} \cdot u(t) - c_{p,air} \cdot f_{air} \cdot \left(\vartheta_h - \vartheta_{ext\_air}\right) - k_{circ} \cdot c_{p,air} \cdot f_{air} \cdot \left(\vartheta_h - \vartheta_{hot\_air}\right) \\ 0 = \dfrac{1}{m_d \cdot c_d} S_d \cdot \alpha_d \cdot \left(\vartheta_h - \vartheta_d\right) \\ 0 = k_{circ} \cdot c_{p,air} \cdot f_{air} \left(\vartheta_h - \vartheta_{hot\_air}\right) - \\ -S_{ext} \cdot \dfrac{A_{ext,0} + A_{ext,1} \cdot \left(\vartheta_h - \vartheta_{ext\_air}\right)}{d} \cdot \left(\vartheta_{ext\_air} - \vartheta_{hot\_air}\right) - S_d \cdot \alpha_d \cdot \left(\vartheta_h - \vartheta_d\right) \end{cases}. \tag{7}$$

Moreover, it makes sense to analyze the first and third equations, whereas the second one turns out to be degenerate in the steady-state operation of the dehydrator. From the first equation, we can estimate the power carried away by the air flow and the air circulation coefficient k_{circ}:

$$P_{max} \cdot u(t) = -c_{p,air} \cdot f_{air} \cdot \left(\vartheta_h - \vartheta_{ext\_air}\right) - k_{circ} \cdot c_{p,air} \cdot f_{air} \cdot \left(\vartheta_h - \vartheta_{hot\_air}\right). \tag{8}$$

From the third equation, we can estimate the amount of heat loss through the walls of the dehydrator:

$$S_{ext} \cdot \frac{A_{ext}\left(\vartheta_h - \vartheta_{ext\_air}\right)}{d} = \frac{P_{max} \cdot u(t)\left(\vartheta_h - \vartheta_{ext\_air}\right)}{\left(\vartheta_{ext\_air} - \vartheta_{hot\_air}\right) \cdot \left(\left(\vartheta_h - \vartheta_{ext\_air}\right) + k_{circ}\left(\vartheta_h - \vartheta_{hot\_air}\right)\right)}, \tag{9}$$

where the heat transfer coefficient itself is understood as a linear function of the temperature difference inside and outside the dehydrator:

$$S_{ext} \cdot \frac{A_{ext}\left(\vartheta_h - \vartheta_{ext\_air}\right)}{d} = a \cdot \left(\vartheta_h - \vartheta_{ext\_air}\right) + b. \tag{10}$$

Identification is carried out based on the results of experimental measurements on a real dehydrator, during which the following parameters are recorded: ϑ_h — temperature of the air after the heater; ϑ_{hot_air} — temperature of the hot air at the outlet of the dehydrator chamber; ϑ_{ext_air} — temperature of the air outside the dehydrator (indoors); $u(t)$ — continuous operation of the heater under the control of the PID controller; P_{atm} — atmospheric air pressure.

A matrix implementation of the least squares method was used for identification:

$$\mathbf{\Theta} = \left(\mathbf{X}^T \times \mathbf{X}\right) \times \mathbf{X}^T \times \mathbf{Y}, \tag{11}$$

where $\mathbf{Y}$ — vector of experimental results, $\mathbf{X}$ — matrix of explanatory variables, and $\mathbf{\Theta}$ — vector of parameter estimates.

For the first equation, these values are formed as follows:

$$\mathbf{Y} = \begin{pmatrix} \dfrac{P_{max}}{c_{p,air}} u(0) \\ \vdots \\ \dfrac{P_{max}}{c_{p,air}} u(N) \end{pmatrix} \mathbf{X} = \begin{pmatrix} \vartheta_h(0) - \vartheta_{ext}(0) & \vartheta_h(0) - \vartheta_{hot}(0) \\ \vdots & \vdots \\ \vartheta_h(N) - \vartheta_{ext}(N) & \vartheta_h(N) - \vartheta_{hot}(N) \end{pmatrix} \mathbf{\Theta} = \begin{pmatrix} f_{air} \\ k_{circ} \cdot f_{air} \end{pmatrix}, \tag{12}$$

where N — sample length of the experimental data.

For the third equation:

$$\mathbf{Y} = \begin{pmatrix} \dfrac{P_{max} \cdot u(0)\left(\vartheta_h(0) - \vartheta_{ext}(0)\right)}{\left(\vartheta_{ext}(0) - \vartheta_{hot}(0)\right) \cdot \left(\left(\vartheta_h(0) - \vartheta_{ext}(0)\right) + k_{circ}\left(\vartheta_h(0) - \vartheta_{hot}(0)\right)\right)} \\ \vdots \\ \dfrac{P_{max} \cdot u(N)\left(\vartheta_h(N) - \vartheta_{ext}(N)\right)}{\left(\vartheta_{ext}(N) - \vartheta_{hot}(N)\right) \cdot \left(\left(\vartheta_h(N) - \vartheta_{ext}(N)\right) + k_{circ}\left(\vartheta_h(N) - \vartheta_{hot}(N)\right)\right)} \end{pmatrix} \quad (13)$$

$$\mathbf{X} = \begin{pmatrix} \vartheta_h(0) - \vartheta_{ext}(0) & 1 \\ \vdots & \vdots \\ \vartheta_h(N) - \vartheta_{ext}(N) & 1 \end{pmatrix} \mathbf{\Theta} = \begin{pmatrix} A_{ext,1} \\ A_{ext,0} \end{pmatrix} \cdot \frac{S_{ext}}{d},$$

The identification procedure was performed in the MATLAB mathematical package. The identification results will be described in the Results section, and the identification experiments will be described in the next section.

The internal design of the dehydrator assumes the presence of an air flow returning to the heater along the side walls of the dehydrator and losing some of the heat due to its transfer through the walls to the external environment (Fig. 1 *b*).

Accordingly, the first equation of system (1) contains a flow describing the process of returning circulating air to the heater:

$$\frac{d}{dt}\vartheta_h = \frac{1}{m_h \cdot c_h}\left(P_{max} \cdot u(t) - c_{p,air} \cdot f_{air} \cdot \left(\vartheta_h - \vartheta_{ext\_air}\right) - k_{circ} \cdot c_{p,air} \cdot f_{air} \cdot \left(\vartheta_h - \vartheta_{hot\_air}\right)\right), \quad (14)$$

where k_{circ} — coefficient showing how many times the air "wraps around" inside the dehydrator before leaving it.

The equation for calculating the amount of mass air flow will have the following form (15):

$$f_{air} = \frac{1}{c_{p,air}} \frac{P_{max} \cdot u(t)}{\left(\left(\vartheta_h - \vartheta_{ext\_air}\right) + k_{circ}\left(\vartheta_h - \vartheta_{hot\_air}\right)\right)}. \quad (15)$$

The conversion of mass flow into volume flow is carried out from formula (15) using formula (6):

$$f_v = \frac{f_{air}}{\rho_{air}} = \frac{1}{c_{p,air}} \frac{R_{air} \cdot \vartheta_{hot\_air}}{P_{atm} \cdot M_{air}} \frac{P_{max} \cdot u(t)}{\left(\left(\vartheta_h - \vartheta_{ext\_air}\right) + k_{circ}\left(\vartheta_h - \vartheta_{hot\_air}\right)\right)}. \quad (16)$$

It should be borne in mind that air circulation is "unobservable" and manifests itself only indirectly depending on the volume flow rate and temperature. However, if we perform a series of calculations of the dependence of volume flow on temperature for different values of the circulation coefficient, we can "choose"k the most plausible value that will give the best approximation $f_v(\vartheta_h)$ of a horizontal straight line (more precisely, a straight line with the smallest angle of inclination to the horizontal). The least squares method (LSM) can be used to obtain estimates of the coefficients of the equation of the approximating line:

$$f_v\left(\vartheta_h\right) = a \cdot \vartheta_h + b. \quad (17)$$

A two-stage search method was used to identify the circulation coefficient k_{circ}. At the first stage, when identifying the parameters of equation (8), values of k_{circ} in the range from 0 to 20 in increments of 1 were used. At the second stage, when a rough estimate of the suboptimal value of k_{circ} in the region of 10 was obtained, the range from 9 to 11 in increments of 0.1 was used. The optimal value of k_{circ} was considered to be the value at which the approximating line of dependence $f_{air,v}$ on temperature, had the minimum modulo tangent of the angle of inclination (was as close as possible to the horizontal line).

1.4 Description of experimental studies

Experimental studies on a small-sized dehydrator with a microcontroller control and monitoring system were carried out to identify the parameters of a mathematical model of the dehydrator thermal subsystem.

The dehydrator operation mode with a stepwise temperature change was used to identify the model. The air temperature sensor after the heater (DS18B20 thermometer) and BME-280 sensors (outdoor air parameter sensor and hot air parameter sensor at the outlet of the dehydrator) allow you to measure the air temperature immediately after the heater, as well as the temperature, relative humidity and air pressure outside the dehydrator and at the outlet of the chamber. The approximate location of the sensors is shown in Figure 1 *b*.

Standard stainless-steel trays (12 pieces) with a total weight of 2,450 kg are placed in the dehydrator chamber to increase its thermal inertia and reduce temperature fluctuations.

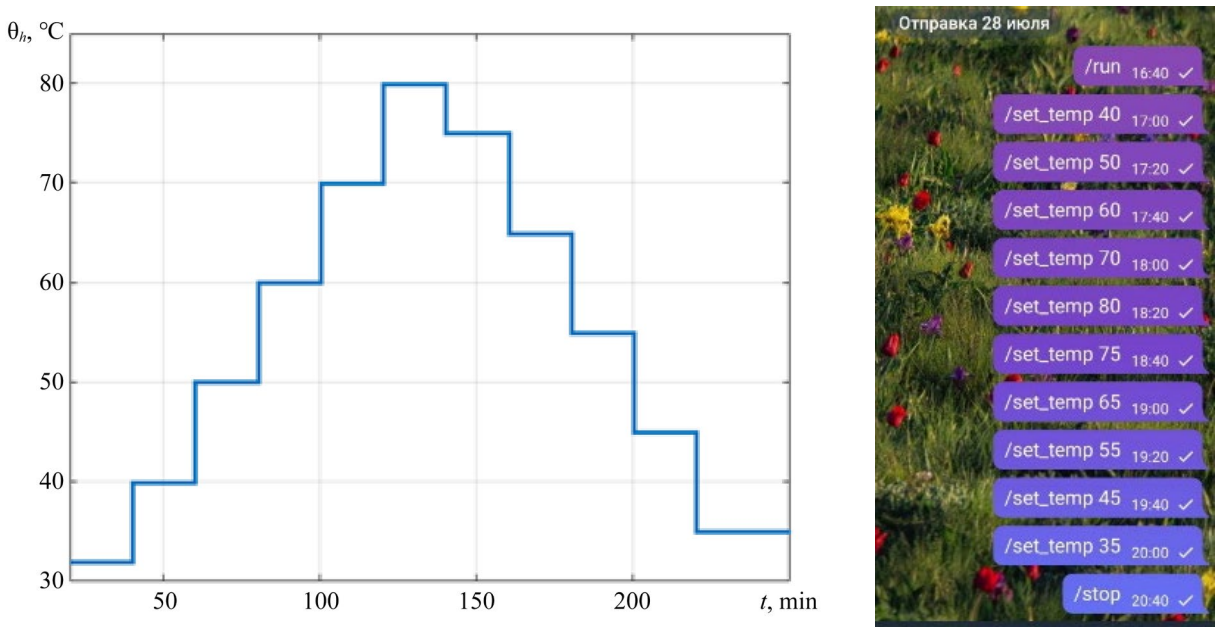

a) *b)*

Fig. 5. Temperature regime in experiments: *a* — graph of temperature changes; *b* — corresponding sequence of commands of the Telegram bot

Temperature control is performed programmatically, using a PID controller implemented in the program, the library of which is taken from the website[3]. The program graph of temperature changes set to the controller is shown in Figure 5. The experiments were carried out in automatic mode.

The programmed temperature change in the dehydrator was performed in steps of 10 degrees until the temperature reached 80°C. After reaching the maximum, the temperature was reduced programmatically in similar steps of 10 degrees, with an offset of 5 degrees relative to the increase stage (Fig. 5 *a*).

One cycle of the experiment looked like this:

1. Empty trays were loaded into the dehydrator at room temperature.

2. A temperature change program was set in the Telegram bot (as shown in Fig. 5 *b*). The initial temperature was set to 30 degrees, the coefficient of the integral component of the PID controller was set to 0.3, and the coefficient of the proportional component was set to 200.3. The drying process was started by a command from the Telegram bot.

4. The values of the air parameters from the three sensors and the current power of the regulator were automatically transmitted to the cloud service of the telegram bot every minute.

5. At the end of the experiment program, the dehydrator was automatically switched off. The data was uploaded from the cloud service to the computer and saved as a json file for further processing.

This design of the experiment made it possible to exclude any influence of the human factor and external effects.

2. Results

This section will present experimental and simulation results for the study of a mathematical model and the identification of its parameters using the methods described above.

2.1 Identification and investigation of the mathematical model

The dehydrator control program provides a stepwise increase and then decrease in temperature after the transient attenuation during experiments to identify the mathematical model.

2.1.1 Determination of the air flow through the dehydrator

Based on model (1) and taking into account its transformations (14)–(16), as well as using the data of the new experiment, which are presented in Figures 6-7, it is possible to calculate the value of the mass air flow through the dehydrator as a function of the air temperature after the heater (Fig. 9).

[3] GyverPID — PID Controller Library for Arduino. URL: https://github.com/GyverLibs/GyverPID://github.com/GyverLibs/GyverPID (date of access: 26.01.2026).

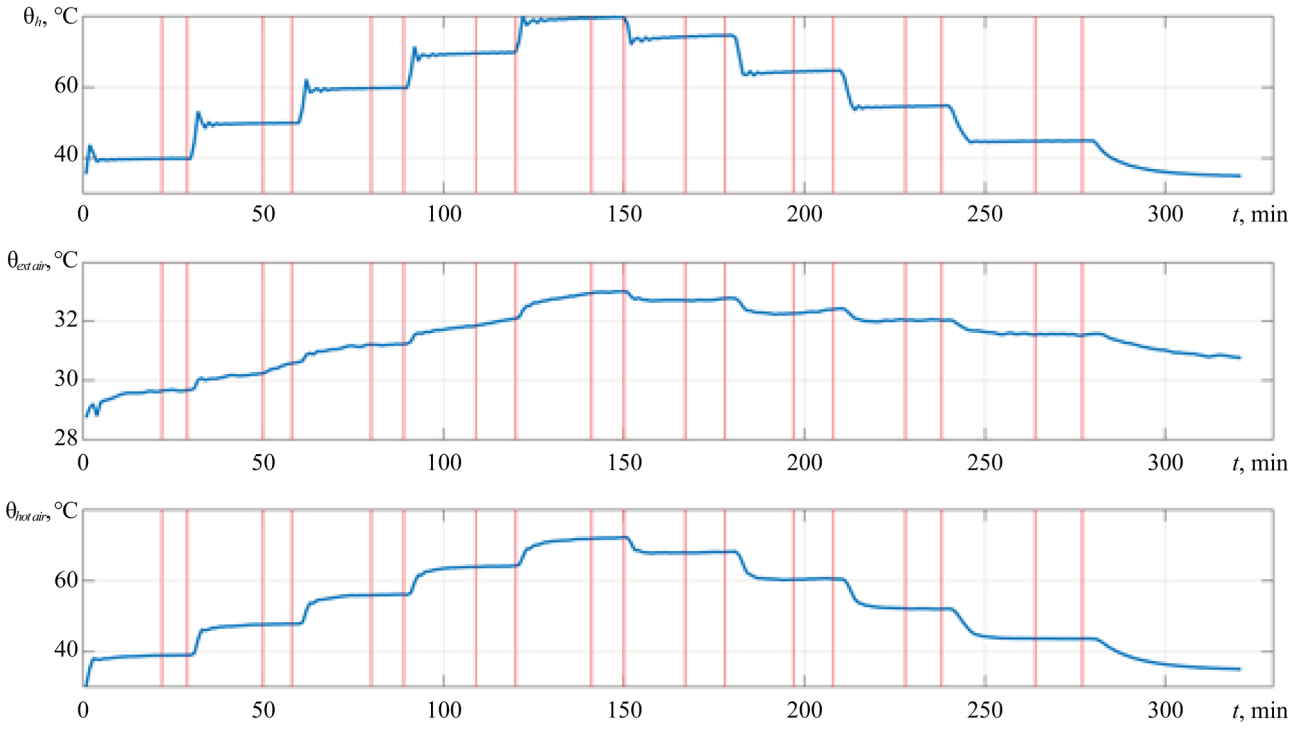

Fig. 6. Temperatures in the dehydrator according to sensors 1, 2 and 3

The upper graph shows the program for changing the air temperature immediately after the heater. Minor fluctuations are associated with the operation of the PI controller and the low thermal inertia of the empty dehydrator.

The middle graph shows the outside air temperature readings (Fig. 6). There is some instability, but it is only about 4 degrees when the air temperature changes by 40 degrees after the heater. This effect occurs due to the heating of the external air from the dehydrator housing.

In Figure 7, we see the instantaneous value of the heater power, calculated as the product of the maximum heater power and the borehole of its operation. Due to the operation of the PI controller in the microcontroller of the control system, fluctuations are observed after switching the temperature, but then the heater power stabilizes.

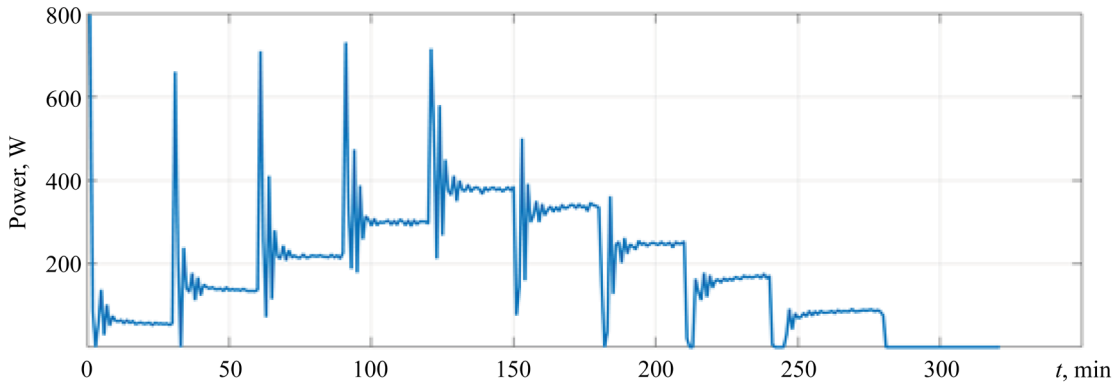

Fig. 7. Instantaneous power on the heater

In Figure 8: flow_{RAW} (f_{RAW}) — mass air flow calculated from the initial experimental data; flow_{m} (f_m) — mass air flow calculated after applying the intervals (Fig. 6, red vertical lines) in which the temperature, ϑ_h has stabilized; flow_{v} (f_v) — volume air flow calculated from f_m using formula (6).

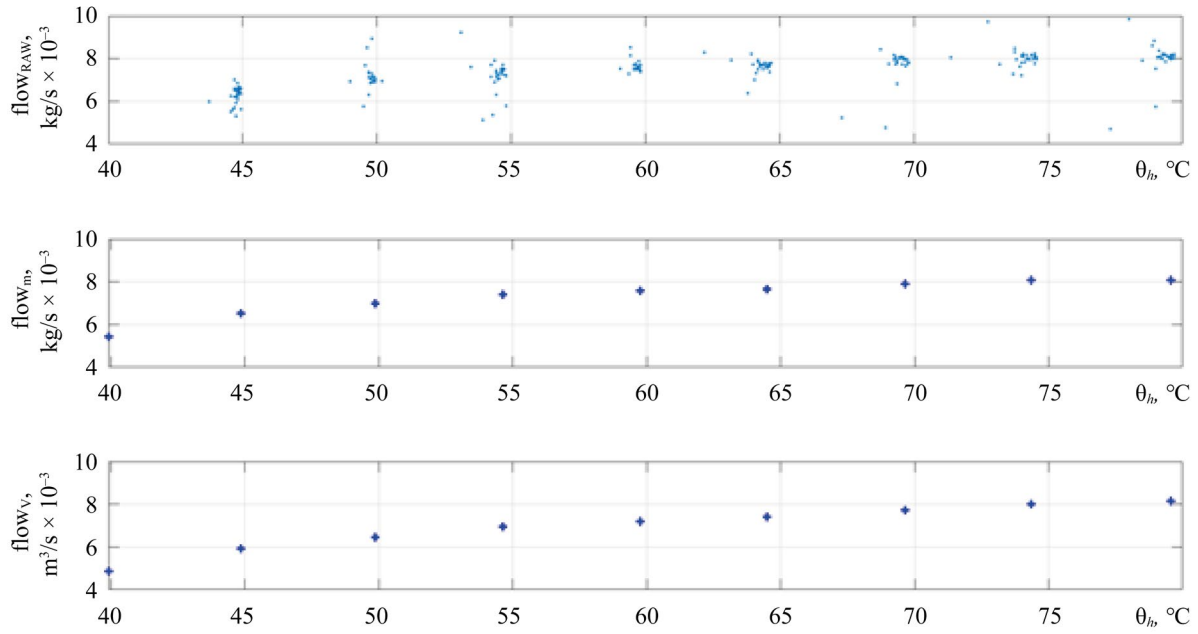

Figure 8. Estimation of flow values (from top to bottom): estimation based on initial data; interval estimation of mass flow; interval estimation of volume flow

2.1.2 Estimation of the circulation value

The results of the identification of the straight line (17) at values k_{circ} in the range from 7 to 15 are shown in Figure 9 *a, b*. The upper graph shows the dependence of the coefficient (the tangent of the angle of inclination of the straight line), and the lower graph shows the coefficient, the constant component of the flow.

Graph 9 *a* shows a calculated curve describing the dependence of the tangent of the angle of inclination of the approximating straight line on the value of the circulation coefficient. The point of its intersection with the axis of the abscissa allows you to determine the real value k_{circ} = 10.2.

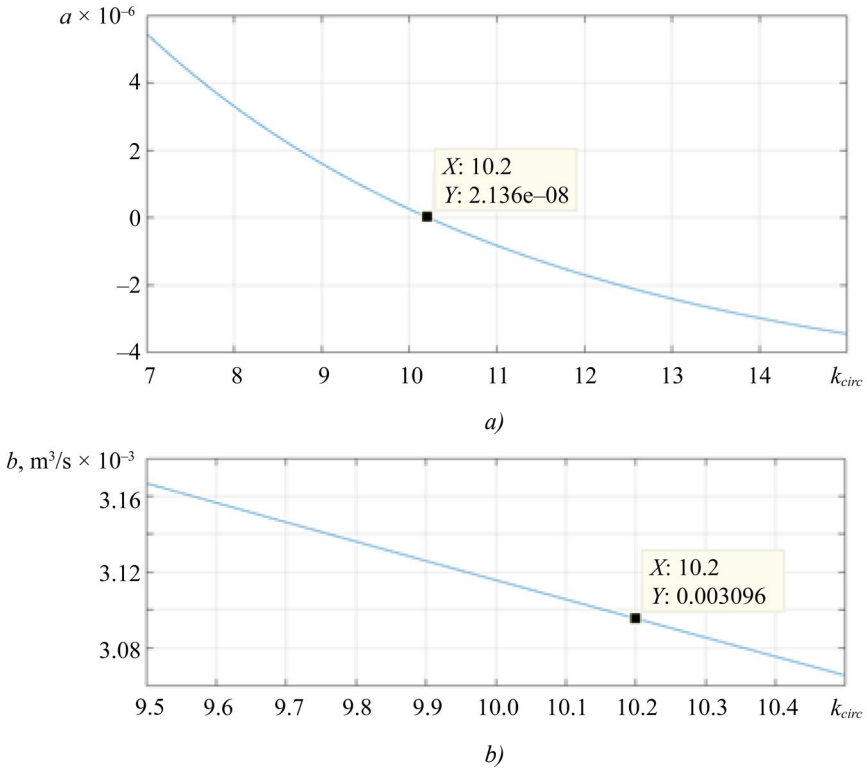

Fig. 9. Identification of the parameters of air movement: *a* — dependence of the tangent of the angle of inclination on value of k_{circ}; *b* — dependence of the displacement on value of k_{circ}

The straight line in Figure 9 *b* allows us to determine the volume flow rate for the obtained circulation coefficient. Value of k_{circ} =10.2 corresponds to volumetric flow rate f_v = 0.003096 m^3s^{-1}, or approximately 3.1 l/s.

2.1.3 Heat loss assessment

As the basis of an identifiable mathematical model of heat loss through the walls of the dehydrator, we take equation (8) and look for the value of the total heat transfer coefficient as a linear function of the temperature difference, according to expression (10).

The identification procedure is based on the same principle as for the identification of the parameters of the air flow equation. The temperature measurement results obtained by stepwise changing the controller setting were averaged over the intervals after the transient attenuation and processed using the least squares matrix method in form (10). The experimental results and the approximating line are shown in Figure 10.

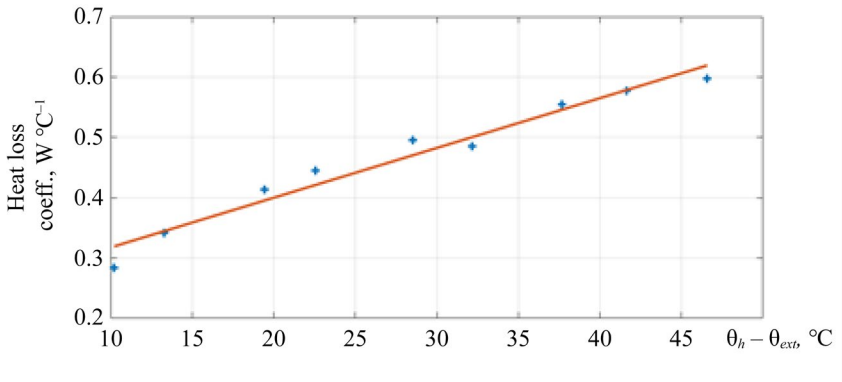

Fig. 10. Dependence of the coefficient of heat transfer to the external environment through the wall of the dehydrator on the temperature difference inside and outside the dehydrator

The actual calculated values of the coefficients of the approximating line are given in formula (18):

$$S_{ext} \cdot \frac{A_{ext}\left(\vartheta_h - \vartheta_{ext\_air}\right)}{d} = 0.0082 \cdot \left(\vartheta_h - \vartheta_{ext\_air}\right) + 0.2351. \quad (18)$$

Thus, an estimate of the heat transfer coefficient through the walls of the dehydrator chamber to the external environment was obtained. As expected, this coefficient depends on the temperature difference on different sides of the dehydrator wall, and this dependence is close to linear.

2.2 Model verification

To verify the model, an additional experiment was conducted using the methodology described in Section 1.4. The simulation of the dehydrator operation was also performed using the identified parameters of model (2) in the MATLAB/Simulink mathematical package (Fig. 4). To compare the results obtained, output temperature ϑ_{hot} and the heater temperature ϑ_h graphs synchronized at the beginning of the drying process were constructed. The graph for temperature ϑ_{hot}, as the most important for further study of the model, is shown in Figure 11.

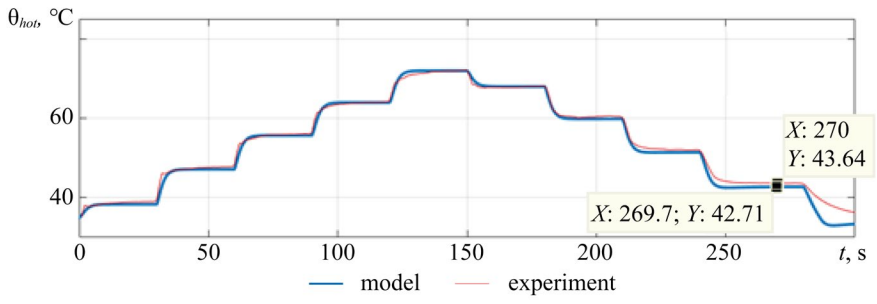

Fig. 11. Verification of the operation of the dehydrator. Comparison of experimental data with model data

The estimated deviation of the model data from the experimental data was less than 0.5°C with an increase in temperature from 35 to 80°C and with a decrease in temperature from a maximum to 50°C. With further cooling of the dehydrator, the error is about 1°C.

3. Discussion

The results of the study convincingly confirm the possibility of creating an adequate mathematical model of thermal processes in a small convective dehydrator using the apparatus of ordinary differential equations. The achieved modeling error, which does not exceed 0.5°C in the operating temperature range from 35 to 80°C, indicates a high accuracy of reproduction of real heat transfer processes in the equipment under study.

The main result of the research is the construction, identification and verification of a mathematical model of the thermal subsystem of the dehydrator. Analyzing the results obtained, attention should be paid to the following aspects:

– structure of the developed mathematical model and the selected ODE formalism for modeling;

– obtaining a numerical estimate of the amount of air flow from the dehydrator chamber based on indirect measurements;

– obtaining a numerical estimate of an unobservable but important parameter of the drying process – the air circulation coefficient inside the dehydrator chamber;

– ability to estimate the amount of heat loss through the walls of the drying chamber through the identified heat transfer coefficient;

– verification of model parameters and assessment of its applicability for modeling drying processes.

The development of numerical methods and programs for finite element modeling creates prerequisites for the widespread use of finite element models, including for modeling thermal systems. For example, in [22], the author provides a complex 3D model of a dehydrator for drying corn kernels. However, it seems that the thermal part of this model could be replaced not only by 2D (as the author does), but also by a one-dimensional concentrated model with minor errors. In [23], a finite element model of a dehydrator with horizontal air movement is also constructed, in which the calculated method shows the laminar movement of the air flow along the gratings, which is consistent with the assumptions accepted for modeling about the possibility of using a model with concentrated parameters and ODEs. The adequacy of the model is confirmed by the graph in Figure 11, which shows the air temperature at the outlet of the dehydrator chamber for the experiment and the model. There is a good qualitative and quantitative correspondence between the simulation and experimental results. Some discrepancy in the characteristics is observed at the end of the experiment, when the air temperature inside the dehydrator chamber approaches the ambient temperature. In this case, if the temperature difference inside and outside decreases, the air movement along the outer wall of the dehydrator becomes less stable, and heat transfer decreases compared to formula (1.8). As a result, the real dehydrator cools down more slowly than the simulated one. The deviation in steady-state mode was about 0.9 degrees.

Although the effect of internal air circulation is indeed used in a number of designs of domestic and industrial dehydrator designs, the authors failed to find a detailed analysis of this effect in the scientific literature. The processes of heat and mass transfer during drying, as well as their mathematical modeling, are considered, for example, in [24]. However, unlike the proposed model (1.1), the authors do not take into account the possibility of reverse air circulation in the dehydrator chamber. At the same time, this process is essential for the considered equipment (Fig. 1). A similar situation is described in [25], where only direct air flow is also considered. At the same time, the variability in air velocity is small, which leaves room for further experiments to optimize the drying process. In [26], detailed attention is paid to the processes of heat transfer using infrared radiation, but the convective component of the drying process is described in less detail. In [27], the design of an industrial dehydrator uses an external air flow circulation system, including one with a controlled inlet flow. It is shown that regulation of circulation makes it possible to increase the coefficient of productivity (COP) up to 39%, which underlines the importance and relevance of the presented studies. However, it is precisely the circulation coefficient (multiplicity of air passage over the product) that is not analyzed in [27], which distinguishes it from the presented study, that makes it possible to quantify this coefficient.

The study of the effect of the air velocity in the dehydrator on the intensity of moisture loss was performed in [28]. It shows that the effect of temperature is less significant at high air velocity. This once again confirms the importance of assessing the magnitude and circulation of the air flow inside the dehydrator. In [29], based on a study of the kinetics of drying tomato slices, it was concluded that an increase in the air flow velocity by one and a half times can increase the efficiency of water diffusion by up to 25%. This determines the prospects of controlling the air flow velocity during drying to increase energy efficiency and reduce drying time. At the same time, direct measurement of the air velocity inside the dehydrator is usually difficult. For this reason, the proposed method for estimating the amount of air flow based on energy characteristics seems to be practically promising. The margin of error can be estimated at no more than 10%.

Separately, we should mention work [30]. It is an experimental study of the drying process of apple slices, where two directions of air movement are considered: above the grate with samples and through the grate with samples. At the same time, it has been experimentally shown that when air moves through the grate at a lower speed than when moving over the grate (1.7 m/s versus 3.5 m/s), the drying time in the first case is 15% less than in the second. However, in this case, due to the design of the installation, the air passed through the dehydrated product once. The internal air circulation described and identified in our work should significantly improve the situation and increase the energy efficiency of drying.

Analyzing the heat loss in the drying chamber through the walls, and determining the value of the heat loss coefficient as a function of the temperature difference, make it possible to optimize drying modes in terms of energy efficiency, since it reflects “non-industrial” heat losses depending on the design and thermal insulation of the drying chamber. In our opinion, insufficient attention is paid to this heat flow in the works devoted to the energy optimization of the convective drying process [30, 31]. Although this dependence can serve as an optimization parameter when selecting drying modes.

It is necessary to point out certain limitations of the developed model. The model is based on the assumption of concentrated parameters and does not take into account the spatial heterogeneity of the temperature field inside the chamber. This simplification is justified for small-sized dehydrators with intensive air circulation. However, for large industrial installations, it may be required to switch to models with distributed parameters. In addition, the model has been identified for the product-free dehydrator operation mode. In the presence of a dewatered material, the thermal balance of the system will change due to energy consumption for moisture evaporation and modification of the nature of air flow.

The practical value of the results obtained is due to the possibility of using the identified model to optimize the drying modes of various products. Knowing the exact values of the air flow and circulation coefficient allows you to calculate the intensity of mass transfer, which is crucial for predicting the kinetics of drying. The model of heat transfer through walls makes it possible to evaluate the energy efficiency of the process and identify ways to increase it. It is noteworthy that when operating at the maximum temperature, heat loss through the enclosing structures accounts for about 24% of the heater power, which indicates the expediency of improving thermal insulation.

The prospects for further research are related to the expansion of the model by including mass transfer processes during the dehydration of specific types of food raw materials. The identified parameters of the dehydrator will serve as the basis for constructing a comprehensive drying model that includes equations of moisture balance, evaporation kinetics, and diffusion.

Conclusion

In the course of research on the development of a small convective dehydrator with a microcontroller control system, as well as the construction and identification of its mathematical model, the following significant scientific and practical results were obtained:

– a mathematical model of a small convective dehydrator has been developed and identified. The model is developed in the ODE formalism. Data has been obtained that the model is adequate in the range of drying temperatures from 50 to 70°C with an error of less than 0.5°C, in the range from 35 to 50°C – with an error of about 1°C;

– a model estimate of the air flow coming out of the drying chamber has been obtained. The volume flow was 3.1 l/s. It is shown that it is possible to model the value of the air outlet flow under conditions where its direct measurement is difficult;

– a model estimate of the air circulation coefficient inside the dehydrator chamber has been obtained. For the experimental conditions, it was 10.2 times. Varying this value by controlling the amount of the output stream provides a potential opportunity to optimize the drying process;

– an estimate of the amount of heat loss through the walls of the dehydrator chamber was obtained as a linear function of the air temperature difference inside and outside the dehydrator. This value makes it possible to evaluate the effectiveness of the thermal insulation of the dehydrator chamber. The assessment is applicable when the temperature difference inside and outside the dehydrator is above 15°C.

The studies performed and the results obtained will make it possible to effectively use the described small convective dehydrator as an experimental installation for studying convective drying processes. In addition, the obtained mathematical model of thermal and air mass transfer processes can serve as a basis for constructing models of the kinetics of drying products by supplementing the equations of evaporation and moisture mass transfer.

References

1. Miletić N, Lukyanov A, Petković M. Nonthermal Pretreatment Technologies to Improve Drying Efficiency and Quality in Fresh-Cut Fruits and Vegetables: A Comprehensive Review. *Foods.* 2026;15(3):568. https://doi.org/10.3390/foods15030568

2. Production Volume of Dried Fruit Worldwide from 2009/2010 to 2024/2025. *Statista.* URL: https://www.statista.com/statistics/1025671/total-dried-fruits-global-production/ (дата обращения: 16.01.2026).

3. Onwude DI, Hashim N, Janius RB, Nawi NM, Abdan K. Modeling the Thin-Layer Drying of Fruits and Vegetables: A Review. *Comprehensive Reviews in Food Science and Food Safety.* 2016;15(3):599–618.

4. Lewis WK. The Rate of Drying of Solid Materials. *Journal of Industrial and Engineering Chemistry*. 2021;13(5):427–432. https://doi.org/10.1021/ie50137a021

5. Page GE. *Factors Influencing the Maximum Rates of Airdrying Shelled Corn in Thin Layers*, MSc. Thesis. West Lafayette, IN: Purdue University. 2016;7(3):1949.

6. Henderson SM, Pabis S. Grain Drying Theory: Temperature Affection Drying Coefficient. *Journal of Agricultural Engineering Research.* 2016;8(2):169–170.

7. Yaldiz O, Ertekin C, Uzun HI. Mathematical Modeling of Thin Layer Solar Drying of Sultana Grapes. *Energy.* 2001;26(5):457–465. https://doi.org/10.1016/S0360-5442(01)00018-4

8. Jun Jiang, Leping Dang, Cheong Yuensin, Hongsing Tan, Bochen Pan, Hongyuan Wei. Simulation of Microwave Thin Layer Drying Process by a New Theoretical Model. *Chemical Engineering Science.* 2017;162:69–76. https://doi.org/10.1016/j.ces.2016.12.040

9. Gite SS, Kaushik A, Singh S. Artificial Neural Network Modeling of the Drying Kinetics of Wild Bitter Gourd During Hot Air Drying. *Journal of Biosystems Engineering*. 2025;50:310–328. https://doi.org/10.1007/s42853-025-00268-x

10. María del Carmen Razola-Díaz, Eduardo Jesús Guerra-Hernández, Ana María Gómez-Caravaca, Belén García-Villanova, Vito Verardo. Mathematical Modelling of Drying Kinetics of Avocado Peels and Its Influence on Flavan-3-ols Content and Antioxidant Activity. *LWT - Food Science and Technology*. 2023;176:114552. https://doi.org/10.1016/j.lwt.2023.114552

11. Filipović VS, Filipović JS, Petković MM, Filipović IB, Miletić NM, Đurović IB, et al. Modelling Convective Thin-Layer Drying of Carrot Slices and Quality. *Thermal Science.* 2022;26(3A):2187–2198.

12. Muchilwa IE, Hensel O, Matofari JW. Evaluating the Water Activity Simulation Consistency of Empirical Models for Shelled and Cobed Maize Drying. *International Journal of AgriScience.* 2014;4(3):177–188.

13. Dincer I, Sahin AZ. A New Model for Thermodynamic Analysis of a Drying Process. *International Journal of Heat and Mass Transfer.* 2004;47(4):645–652. https://doi.org/10.1016/j.ijheatmasstransfer.2003.08.013

14. José Vásquez, Alejandro Reyes, Nicolás Pailahueque. Modeling, Simulation and Experimental Validation of a Solar Dryer for Agro-Products with Thermal Energy Storage System. *Renewable Energy*. 2019;139:1375–1390. https://doi.org/10.1016/j.renene.2019.02.085

15. Makokha AB, Melly SC, Muchilwa IE. Dynamic Modelling of Low-Temperature Batch In-Bin Drying of Cobed Seed Maize: an Industrial Case Study. *Journal of Biosystems Engineering*. 2020;45:249–260. https://doi.org/10.1007/s42853-020-00065-8

16. Ateeque Md, Udayraj, Mishra RK, Chandramohan VP, Talukdar P. Numerical Modeling of Convective Drying of Food with Spatially Dependent Transfer Coefficient in a Turbulent Flow Field. *International Journal of Thermal Sciences*. 2014;78:145–157. https://doi.org/10.1016/j.ijthermalsci.2013.12.003.

17. Aghbashlo M, Hosseinpour S, Mujumdar AS. Application of Artificial Neural Networks (ANNs) in Drying Technology: A Comprehensive Review. *Drying Technology.* 2015;33(12):1397–1462. https://doi.org/10.1080/07373937.2015.1036288

18. Tepe TK, Tepe FB. Improvement of Pear Slices Drying by Pretreatments and Microwave-Assisted Convective Drying Method: Drying Characteristics, Modeling of Artificial Neural Network, Principal Component Analysis of Quality Parameters. *Journal of Thermal Analysis and Calorimetry*. 2024;149:7313–7328. https://doi.org/10.1007/s10973-024-13280-8

19. Tepe TK, Azarabadi N, Tepe FB. Convective Drying of the Zucchini Slices; Impact of Pretreatments on the Drying Characteristics and Color Properties, Evaluation of Artificial Neural Network Modeling and Thin-Layer Modeling. *The Black Sea Journal of Sciences*. 2024;14(1):168–193. https://doi.org/10.31466/kfbd.1373651

20. Wenyang Huang, Dan Huang, Yongjia Chen, Guiliang Gong, Feng Zhou, Shuai Huang, et al. Ultrasound-Assisted Medium-Wave Infrared Drying Performance of Phyllanthus Emblica and Artificial Neural Network Modeling. *International Communications in Heat and Mass Transfer*. 2024;159(A):108028. https://doi.org/10.1016/j.icheatmasstransfer.2024.108028

21. Lončar B, Kljakić AC, Arsenijević J, Petronijević M, Panić S, Mračević SD, et al. Valorization of Lemon, Apple, and Tangerine Peels and Onion Skins–Artificial Neural Networks Approach. *Separations*. 2026;13(1):9. https://doi.org/10.3390/separations13010009

22. Ostanek J, Ileleji K. Conjugate Heat and Mass Transfer Model for Predicting Thin-Layer Drying Uniformity in a Compact, Crossflow Dehydrator. *Drying Technology*. 2020;38(5-6):775–792. https://doi.org/10.1080/07373937.2019.1590394

23. Akpan K, Okon A, Akpan W, Nyaudo I. Optimization of Thermo-Flow in a Solar Food Dehydrator Using Computational Techniques. *Engineering and Technology Journal.* 2023;8(11):3061–3083. https://doi.org/10.47191/etj/v8i11.16

24. Muga FC, Marenya MO, Workneh TS. A Heat and Mass Transfer Model for Predicting the Drying of Beef During Biltong Processing Using Infrared-Assisted Hot Air Drying. *Journal of Biosystems Engineering.* 2021;46:273–285. https://doi.org/10.1007/s42853-021-00105-x

25. Sonmete MH, Mengeş HO, Ertekin C, Özcan MM. Mathematical Modeling of Thin Layer Drying of Carrot Slices by Forced Convection. *Journal of Food Measurement and Characterization.* 2017;11:629–638. https://doi.org/10.1007/s11694-016-9432-y

26. Gargari AN, Asefi N, Roufegarinejad L, Khodaei M. Investigation of Heat Transfer in Combined Infrared-Hot Air Drying: A Strategy for Evaluation in Potato Food Model. *Potato Research*. 2025;68:307–325. https://doi.org/10.1007/s11540-024-09730-3

27. Bowser TJ, Frazier RS, Raghavendra Rao Kakarala. Improvement of Efficiency and Environmental Impact of a Low-Cost Food Dehydrator. *The Open Food Science Journal*. 2011;5:37–41. https://doi.org/10.2174/1874256401105010037

28. Raka Noveriyan Putra1, Tri Ayodha Ajiwiguna. Influence of Air Temperature and Velocity for Drying Process. *Procedia Engineering*. 2017;170:516–519. https://doi.org/10.1016/j.proeng.2017.03.082

29. Mamouda Moussa Na Abou, Saïdou Madougou, Makinta Boukar. Effect of Drying Air Velocity on Drying Kinetics of Tomato Slices in a Forced-Convective Solar Tunnel Dryer. *Journal of Sustainable Bioenergy Systems*. 2019;9(2):64–78. https://doi.org/10.4236/jsbs.2019.92005

30. Nuñez Vega A-M, Rombach Ch, Hofacker W. Influence of Air Routing on the Drying Behavior of Air Dried Apple. In: *Proc. 19th International Drying Symposium*. France, Lyon, 2014. P. 24–27.

31. Pippia R, Narayanan R. Technical Analysis and Energy Efficiency Enhancement of a Ginger Dehydrator. *AIP Conference Proceedings*. 2021;2681:020023. https://doi.org/10.1063/5.0116121

About the Authors:

Alexandr D. Lukyanov, Cand.Sci. (Eng.), Associate Professor, Head of the Department of Automation of Production Processes, Don State Technical University (1, Gagarin Sq., Rostov-on-Don, 344010, Russian Federation), SPIN-code, ORCID, ScopusID, ResearcherID, ResearchGate, lex1998@rambler.ru

Alexander N. Zhuravlev, Owner and Scientific Director, Gruvior LLC (294/3 Sholokhov Ave., Rostov-on-Don, 344009, Russian Federation), mail@gruvior.ru

Marko Petković, PhD, Associate Professor of the Department of Technology of Plant Raw Materials, Čačak, University of Kragujevac (34, Car Dušan Str., Čačak, 32102, Serbia), ORCID, ScopusID, ResearchGate, marko.petkovic@kg.ac.rs

Vladimir Filipović, PhD, Principal Research Fellow, Faculty of Technology, University of Novi Sad (1, Car Lazar Boulevard, Novi Sad, 21101, Serbia), ORCID, ScopusID, ResearcherID, ResearchGate, vladaf@uns.ac.rs

Nemanja Miletić, PhD, Associate Professor of the Department of Technology of Plant Raw Materials, Čačak, University of Kragujevac (34, Car Dušan Str., Čačak, 32102, Serbia), ORCID, ScopusID, ResearchGate, n.m.miletic@kg.ac.rs

Danila Yu. Donskoy, Assistant Professor of the Department of Automation of Production Processes, Don State Technical University (1, Gagarin Sq., Rostov-on-Don, 344010, Russian Federation), SPIN-code, ORCID, ScopusID, ResearcherID, ResearchGate, dand22@bk.ru

Claimed Contributorship:

AD Lukyanov: supervision, methodology, writing – original draft preparation.
AN Zhuravlev: resources, visualization.
MM Petković: conceptualization, writing – review & editing.
VS Filippović: validation.
NM Miletić: formal analysis, data curation.
DYu Donskoy: software, data curation.

Conflict of Interest Statement: **the authors declare no conflict of interest.**

All authors have read and approved the final version of manuscript.

Об авторах:

Александр Дмитриевич Лукьянов, кандидат технических наук, доцент, заведующий кафедрой «Автоматизация производственных процессов» Донского государственного технического университета (344010, Российская Федерация, г. Ростов-на-Дону, пл. Гагарина, 1), SPIN-код, ORCID, ScopusID, ResearcherID, ResearchGate, lex1998@rambler.ru

Александр Николаевич Журавлев, владелец и научный руководитель компании «Грувиор» (344009, Российская Федерация, г. Ростов-на-Дону, пр. Шолохова, 294/3), mail@gruvior.ru

Марко Петкович, PhD, доцент кафедры «Технология растительного сырья» факультета агрономии Университета Крагуеваца (32102, Республика Сербия, г. Чачак, ул. Царя Душана, 34), ORCID, ScopusID, ResearchGate, marko.petkovic@kg.ac.rs

Владимир Филиппович, PhD, научный сотрудник технологического факультета Университета Нови-Сада (21101, Республика Сербия, г. Нови-Сад, бульвар Царя Лазаря, 1), ORCID, ScopusID, ResearcherID, ResearchGate, vladaf@uns.ac.rs

Неманья Милетич, PhD, доцент кафедры «Технология растительного сырья» факультета агрономии Университета Крагуеваца (32102, Республика Сербия, г. Чачак, ул. Царя Душана, 34), ORCID, ScopusID, ResearchGate, n.m.miletic@kg.ac.rs

Данила Юрьевич Донской, ассистент кафедры «Автоматизация производственных процессов» Донского государственного технического университета. (344010, Российская Федерация, г. Ростов-на-Дону, пл. Гагарина, 1), SPIN-код, ORCID, ScopusID, ResearcherID, ResearchGate, dand22@bk.ru

Заявленный вклад авторов:
Лукьянов А.Д.: научное руководство, разработка методологии, написание черновика рукописи.
Журавлев А.Н.: предоставление ресурсов, визуализация.
Петкович М.М.: разработка концепции, написание рукописи — внесение замечаний и исправлений.
Филиппович В.С.: валидация результатов.
Милетич Н.М.: формальный анализ, курирование данных.
Донской Д.Ю.: разработка программного обеспечения, курирование данных

Конфликт интересов: **авторы заявляют об отсутствии конфликта интересов.**

Все авторы прочитали и одобрили окончательный вариант рукописи.

Received / **Поступила в редакцию** 30.01.2026
Reviewed / **Поступила после рецензирования** 24.02.2026
Accepted / **Принята к публикации** 03.03.2026